Study of Heat Transfer in Stagnation Point Flows

By

Irfan Mustafa

Reg. No. 06-FBAS/PHDMA/F11

Department of Mathematics and Statistics
Faculty of Basic and Applied Sciences
International Islamic University, Islamabad
Pakistan

2016

1. Point processes

Study of Heat Transfer in Stagnation Point Flows

By

Irfan Mustafa

Supervised By

Dr. Tariq Javed

Department of Mathematics and Statistics
Faculty of Basic and Applied Sciences
International Islamic University, Islamabad
Pakistan
2016

Study of Heat Transfer in Stagnation Point Flows

A dissertation

submitted in the partial fulfillment of the

requirements for the degree of

DOCTOR OF PHILOSOPHY

IN

MATHEMATICS

Submitted By

Irfan Mustafa

Supervised By

Dr. Tariq Javed

Department of Mathematics and Statistics

Faculty of Basic and Applied Sciences

International Islamic University, Islamabad

Pakistan

2016

Author's Declaration

I, **Irfan Mustafa** Reg. No. **06-FBAS/PHDMA/F11** hereby state that my Ph.D. thesis titled: **Study of Heat Transfer in Stagnation Point Flows** is my own work and has not been submitted previously by my for taking any degree from this university, **International Islamic University, Sector H-10, Islamabad, Pakistan** or anywhere else in the country/world.

At any time if my statement is found to be incorrect even after my Graduate the university has the right to withdraw my Ph.D. degree.

Name of Student: **(Irfan Mustafa)**

Reg. No. **06-FBAS/PHDMA/F11**

Dated: **29-12-2016**

Plagiarism Undertaking

I solemnly declare that research work presented in the thesis titled: **Study of Heat Transfer in Stagnation Point Flows** is solely my research work with no significant contribution from any other person. Small contribution/help wherever taken has been duly acknowledged and that complete thesis has been written by me.

I understand the zero tolerance policy of the HEC and University, **International Islamic University, Sector H-10, Islamabad, Pakistan** towards plagiarism. Therefore, I as an Author of the above titled thesis declare that no portion of my thesis has been plagiarized and any material used as reference is properly referred/cited.

I undertake that if I am found guilty of any formal plagiarism in the above titled thesis even after award of Ph.D. degree, the university reserves the rights to withdraw/revoke my Ph.D. degree and that HEC and the University has the right to publish my name on the HEC/University Website on which names of students are placed who submitted plagiarized thesis.

Student/Author Signature: 

Name: **(Irfan Mustafa)**

Certificate of Approval

This is to certify that the research work presented in this thesis, entitled: **Study of Heat Transfer in Stagnation Point Flows** was conducted by **Mr. Irfan Mustafa,** Reg. No. **06-FBAS/PHDMA/F11** under the supervision of **Dr. Tariq Javed** no part of this thesis has been submitted anywhere else for any other degree. This thesis is submitted to the **Department of Mathematics & Statistics, FBAS, IIU, Islamabad** in partial fulfillment of the requirements for the degree of **Doctor of Philosophy in Mathematics, Department of Mathematics & Statistics, Faculty of Basic & Applied Science, International Islamic University, Sector H-10, Islamabad, Pakistan.**

Student Name: Irfan Mustafa **Signature:** _____

Examination Committee:

a) **External Examiner 1:**
Name/Designation/Office Address) **Signature:** Saleem Asghar
Prof. Dr. Saleem Asghar
Professor of Mathematics, COMSATS, IIT, Islamabad.

b) **External Examiner 2:**
Name/Designation/Office Address) **Signature:** _____
Prof. Dr. Tasawar Hayat
Professor of Mathematics, QAU, Islamabad.

c) **Internal Examiner:**
Name/Designation/Office Address) **Signature:** _____
Prof. Dr. Muhammad Sajid, TI
Professor of Mathematics, IIU, Islamabad.

Supervisor Name: **Signature:** _____
Dr. Tariq Javed

Name of Dean/HOD **Signature:** M. Arshad
Prof. Dr. Muhammad Arshad Zia

Dedicated

To

My beloved Parents

&

Other family members

who have been supportive and encouraging

in my accomplishments

Acknowledgement

To begin in the name of Allah who is most Merciful and Beneficent. All praise goes to Allah Almighty and only deserves to be worshipped due to Lord and creator of this universe. I am very thankful to Allah Almighty that with His blessing I was able to start the research work and successfully completed my PhD. The blessings of Allah be upon the last of the Holy Prophets, Hazrat Muhammad (PBUH) and I offer my humblest Darood to my beloved Holy Prophet (PBUH).

I pay gratitude to my kind nature and devoted supervisor **Dr. Tariq Javed** from core of my heart, who helped and guided me properly at every step whenever I faced a difficulty during the research work as well as in all aspects of life. I feel that he is one of the best teacher and researcher in his field because he is hard worker and involve with the research students till the completion of the task. I am very thankful to my external examiners **Prof. Dr. Saleem Asghar** and **Prof. Dr. Tasawar Hayat** for valuable comments and encouragement. I am also thankful to my respected teachers **Prof. Dr. Muhammad Arshad Zia, Prof Dr. Muhammad Sajid** and **Dr. Nasir Ali** as they guided me during the research work.

I am greatly indebted to my research fellows, **Hussain Ahmad** (Late) who left us when he was near completion of his Doctorate, **Muhammad Saleem Iqbal, Abid Majeed, Dr. Abuzar Ghaffari, Arshad Siddiqi, Ziafat Mehmood, Bilal Ahmed** and **Abdul Haleem** for detailed discussion and spend sleepless night together in research room and also indebted to my friends **Dr. Nayyar Mehmood, Niaz Ahmad, Muhammad Asif Javed, Dr. Arshad Riaz, Dr. Shafique ur Rehman, Dr. Ahmad Zeeshan, Mubashir Nazeer, Sohail Ahmad, Waqas Nazir, Zahid Mangral** and **Muhammad Azam**.

Now I pay special thanks and tribute to my beloved parents who loved me a lot and have been taking since my childhood and I cannot pay the reward for such kind and care. The completion of my education was not possible without their prayers and supports. I am also thankful to my wife for her support and help in writing this thesis. It is worthless if don't mention the role of my sisters and my brothers Shakaib Arslan Gursal, Rizwan Mustafa, Farhan Mustafa, Yahya Haleem, Usman Mustafa and Muhammad Ibrahim, because without their support it was not possible.

Finally I am grateful to my uncles Bashir Ahmad Malik and Sharf ud Din Shami whenever I meet them they always pray for my health and success.

Preface

In the field of science, a great importance has been given on the topic of heat transfer due to its numerous industrial applications. It is therefore, we focused our attentions on two things namely **temperature** and **flow of heat**. Temperature is represented as amount of thermal energy and the flow of heat explains the complete mechanism of the movement of such thermal energy within the body from one position at higher temperature to another position at lower temperature. There are many material properties which modulate the heat transferred involves specific heat, thermal conductivity, fluid velocity, viscosity and density etc. The mechanism of heat transfer can be divided into three modes namely conduction, convection and radiation. The second mode of heat transfer is further divided into three categories namely forced convection, natural convection and mixed convection. The main purpose of this thesis is to study the heat transfer analysis in stagnation point flows which also have numerous applications in engineering and industrial problems which are cooling of nuclear reactors during emergency shut down, heat exchangers placed in a low velocity environment, cooling of electronic devices by fans, solar central receivers exposed to wind currents and many more. Initially we studied the flow and heat transfer rates in stagnation point flow by considering Newtonian fluid such as water which has low thermal conductivity and heat transfer rate. To improve the thermal conductivity and heat transfer rate in such base fluid like water we extended the work by considering nanofluid which is a colloidal suspension of nano-size particles in a base fluid. Finally, we studied the heat transfer analysis in non-Newtonian fluid flow near the stagnation point due to its practical application in polymer industry. The resulting highly nonlinear ordinary and partial differential equations of the considered fluid models are solved numerically by using well known methods which are Keller Box and spectral collocation methods.

In chapter 1, some basic definitions, literature survey related to heat transfer analysis in stagnation point flow of different fluids on different geometries, mathematical models of Newtonian fluid, nanofluid and non-Newtonian fluid are discussed. I hope that on the basis of the information given in this chapter, a reader will be able to comprehend different flow problems discussed in forthcoming chapters relatively easily.

In chapter 2, heat transfer in stagnation point flow over an unsteady Wang's cylinder is discussed. The term unsteady Wang's cylinder represents to mean that the cylinder is assumed of the nature of having ability to expand radially and contract along its length at the

same time. To make the problem more interesting we further assume that the cylinder surface is subjected to the suction phenomenon. The problem is modeled in terms of partial differential equations which are transformed into nonlinear ordinary differential equations by using similarity transformation. The numerical solution of the problem is computed with the help of a very rapid convergent numerical method namely Chebyshev spectral collocation method. The ranges of the parameters for which unique, dual and triple solutions exist are explored. The effects of pertinent parameters namely Reynolds number, unsteadiness parameter, Prandtl number, suction parameter and velocity ratio parameter on velocity profile, temperature profile, skin friction coefficient and Nusselt number are discussed and shown through graphs. The analysis presented in this chapter has been published in **Asia Pacific Journal of Chemical Engineering, 10 (2015) 184-192.**

Chapter 3 deals with analysis of radiative heat transfer in unsteady mixed convection flow near forward stagnation point over a cylinder of elliptic cross section for both blunt and slender orientations. The governing partial differential equations are transformed into dimensionless partial differential equations by using suitable transformation and numerical solution is obtained with the help of implicit finite difference scheme known as Keller Box scheme. The effects of pertinent parameters namely Prandtl number, mixed convection parameter, thermal radiation parameter, surface temperature parameter and blunt/slender orientation parameter on the velocity and temperature profile and Nusselt number are shown graphically also the separation times for both orientations are presented through table. The contents of this chapter have been published in **Thermal Science, 21 (2017) 1-12.**

Chapter 4 presents the heat transfer analysis in MHD mixed convection stagnation point flow of a nanofluid over a vertical plate with viscous dissipation. It is assumed that the nanofluid contains two types of nano-size particles namely copper and alumina with water as a base fluid. The constitutive equations related to the nanofluid model are converted into a dimensionless nonlinear system of ordinary differential equations by using similarity transformation and numerical solution is obtained by using Keller Box scheme. The graphs of velocity profile, temperature profile, skin friction coefficient and local Nusselt number are plotted against different values of involving parameters namely magnetic parameter, Eckert number and volume fraction parameter with fixed value of Prandtl number. This work has been published in **Canadian Journal of Physics, 93 (2015) 1365-1374.**

In chapter 5, heat transfer analysis in three dimensional boundary layer stagnation point flow of the ferrofluid over a stretchable rotating disk in the presence of external

magnetic field is presented. The three types of ferroparticles are considered namely magnetite, cobalt ferrite and Mn-Zn ferrite. The governing partial differential equations are transformed into nonlinear ordinary differential equations and numerical solution is obtained by using same numerical method which is used in Chapter 4. The effects of pertinent parameters on radial and azimuthal velocity profiles, temperature profile, skin friction coefficients and local Nusselt number are discussed in detail and shown through graphs. The contents of this chapter have been published in the **Journal of Molecular Liquids, 219 (2016) 526-532.**

Chapter 6 presents the heat transfer analysis in stagnation point flow of a nanofluid over a nonlinearly permeable stretching/shrinking sheet in the presence of Newtonian heating effect. The physical problem is modeled by using Buongiorno model [58] and the resulting nonlinear ordinary differential equations are obtained after using similarity transformation. The dual solutions against shrinking parameter is obtained numerically by using the Chebyshev spectral collocation method. The effects of emerging parameters namely Prandtl number, Schmidt number, Brownian and thermophoresis parameters, conjugate parameter and velocity ratio parameter on velocity and temperature profiles, skin friction coefficient and local Nusselt number are shown graphically. The contents of this chapter have been submitted in **Applied Mathematics and Computation.**

Chapter 7, deals with the study of heat transfer in mixed convection stagnation point flow of a non-Newtonian third grade fluid on a vertical surface with slips and viscous dissipation effects. The governing equations related to third grade fluid model are transformed into nonlinear ordinary differential equations after using similarity transformation and numerical solution is obtained by using Chebyshev spectral collocation method. The main findings are velocity and temperature increase with increasing the viscous dissipation effects. The local skin friction coefficient and local Nusselt number decrease in opposing flow case and increase in assisting flow case with increasing mixed convection parameter. The contents of this chapter have been published in the **Journal of Applied Mechanics and Technical Physics, 57 (2016) 527-536.**

Contents

Chapter 1 8

Preliminaries 8

1.1 Heat 8

1.2 Heat transfer and its modes 8

1.2.1 Conduction 8

1.2.2 Convection 9

1.2.3 Radiation 10

1.3 Governing equations for fluid motion 11

1.3.1 Continuity equation 11

1.3.2 Momentum equation 11

1.3.3 Energy equation 12

1.3.4 Concentration equation 13

1.4 Literature survey 13

1.5 Methodology 21

1.5.1 Finite difference method 22

1.5.2 Spectral method 22

Chapter 2 23

Heat transfer in stagnation point flow over an unsteady expansion/contraction permeable cylinder 23

2.1 Mathematical formulation 23

2.2 Spectral collocation method 26

2.3 Results and discussion 28

2.4 Conclusions 40

Chapter 3 42

Radiative heat transfer in unsteady mixed convection flow near forward stagnation point over a cylinder of elliptic cross section 42

3.1 Mathematical formulation 42

3.1.1 Forward stagnation point flow 46

3.2 Keller Box method 47

3.3 Results and discussion 51

3.4 Conclusions 63

Chapter 4 64

Heat transfer in MHD mixed convection stagnation point flow of a nanofluid over a vertical plate with viscous dissipation 64

4.1 Mathematical formulation 64

4.2 Keller Box method 68

4.3 Results and discussion 71

4.4 Conclusions 88

Chapter 5 90

Heat transfer in MHD stagnation point flow of a ferrofluid over a stretchable rotating disk 90

5.1 Mathematical formulation 90

5.2 Results and discussion 93

5.3 Conclusions 103

Chapter 6 105

Heat transfer in stagnation point flow of a nanofluid over a nonlinearly permeable stretching/shrinking sheet with Newtonian heating 105

6.1 Mathematical formulation 105

6.2 Results and discussion 108

6.3 Conclusions 123

Chapter 7 124

Heat transfer in mixed convection stagnation point flow of a third grade fluid on a vertical surface with slip effects 124

7.1 Mathematical formulation 124

7.2 Spectral collocation method 127
7.3 Results and discussion 130
7.4 Conclusions 143
Bibliography 144

Nomenclature

$\mathbf{A}_1, \mathbf{A}_2, \mathbf{A}_3$	Rivlin Ericksen tensors
a, c	Straining and stretching/shrinking constants
b	Constant of temperature
$\mathbf{b}$	Body force
$b_1(t)$	Time dependent radius
B_0	Strength of uniform magnetic field
c/a	Velocity ratio parameter
a^* and b^*	Length of semi major and minor axes
c_p	Specific heat constant
C	Nanoparticle concentration
C_∞	Ambient nanoparticle concentration
$C_f, C_{fx}, C_{Fr}, C_{G\theta^*}$	Skin friction coefficient/local skin friction coefficients
C_w	Nanoparticle concentration at the wall
D_B	Brownian diffusion coefficient
D_T	Thermophoretic diffusion coefficient
e	Eccentricity
Ec	Eckert number
f	stream function in dimensionless form
g	Acceleration due to gravity
Gr, Gr_x	Grashof number, local Grashof number
h_s	Convection heat transfer coefficient
h_1, h_2, h_3, h_4	Physical parameters
h_{11}, h_{22}	Metric coefficient
k_f	Thermal conductivity of fluid/base fluid
k_p	Thermal conductivity of nanoparticle
k_s	Thermal conductivity of material
k_{nf}	Thermal conductivity of nanofluid
Sc	Schmidt number
M	Magnetic parameter
m	Exponent of nonlinear velocity
N	Number of grid points

n, j	Integers
Nb	Brownian motion parameter
Nt	Thermophoresis parameter
Nu, Nu_x, Nu_r	Nusselt number/local Nusselt number
Pr	Prandtl number
p, p^*	Pressure, modified pressure
q_m	Mass flux at the wall
q, q_w	Heat flux, heat flux at the wall
R_1, R_2, R_3	Residuals
R_d	Radiation parameter
Re	Reynolds number
Re_x, Re_z, Re_r	Local Reynolds numbers
S	Unsteadiness parameter
Sh_x	Sherwood number
$t, \overline{t}$	Time, dimensionless time
t_1, t_2	Critical points
T	Temperature of the fluid in the boundary layer
T_n	Basis function
T_∞	ambient fluid temperature
T_w	surface temperature
u_e, v_e	Potential velocities
u_w	stretching/shrinking velocity
U_∞	Free stream velocity
v_w	Suction velocity
u, v, w	Velocity components in dimensionless form
We	Weissenberg number
x, y	Cartesian coordinates
r, θ^*, z	Cylindrical coordinates
X	Distance along the surface of elliptical cylinder measured from the forward stagnation point
Y	Normal to the surface of elliptical cylinder

Greek symbols

α_f	Thermal diffusivity of fluid/base fluid

α_{nf}	Thermal diffusivity of nanofluid
α_r	Rosseland mean absorption coefficient
α_s	Scattering coefficient
β_f	Thermal expansion coefficient of fluid/base fluid
β_p	Thermal expansion coefficient of nanoparticle
$\alpha_1, \alpha_2, \beta_1, \beta_2, \beta_3$	Material parameters of fluid
ε	Third grade parameter
γ	Suction parameter
γ_1, γ_2	Velocity and thermal slip factors
γ^*	Angle measured from the forward stagnation point in streamwise direction
λ	Mixed convection parameter
ψ	Stream function
ψ^*	Dimensionless stream function
Ω	Angular velocity
ω	Dimensionless angular velocity
ω^*	Blunt/slender orientation parameter
γ_s	Newtonian heating parameter
γ_v, γ_t	Dimensionless velocity and thermal slip parameters
ρ_f	Density of fluid/base fluid
ρ_p	Nanoparticle density
ρ_{nf}	Nanofluid density
$(c_p)_f$	Specific heat
μ_f	Dynamic viscosity of fluid/base fluid
μ_{nf}	Dynamic viscosity of nanofluid
τ	Cauchy stress tensor
τ^*	Ratio of heat capacity of the nanoparticle and heat capacity of base fluid
$\tau_w, \tau_{xy}, \tau_{rz}, \tau_{\theta^* z}$	Wall shear stress/shear stresses
ν_f	Kinematic viscosity of fluid/base fluid

$(\rho c_p)_f$	Heat capacity of the fluid/base fluid
$(\rho c_p)_{nf}$	Heat capacity of the nanofluid
$(\rho c_p)_p$	Heat capacity of the nanoparticle
b_o, β^*	Constants
θ	Dimensionless temperature
θ_w	Surface temperature parameter
ϕ	Nanoparticle volume fraction
φ^*	Angle between outward normal from the cylinder and downward vertical
σ_f	Electricity conductivity of fluid/base fluid
σ^*	Stefan-Boltzmann constant
η, ξ	Dimensionless variables
η_∞	Physical infinity
ζ, γ^*	Elliptic coordinate

Chapter 1

Preliminaries

In this chapter, we introduced the readers with the basics of heat transfer, mathematical models of different fluids, and fundamental laws relevant to the studies presented in the upcoming chapters for better understanding.

1.1 Heat

Heat is a thermal form of energy which flows from hotter to cooler direction. The flow of heat in any body is in general due to the temperature difference between the two positions. Heat was the earlier form of energy that human being might have used in this world. Heat can be converted from one form to another form such as mechanical work or internal energy etc. First law of thermodynamics is the simple relation among these forms of energy [1].

"Amount of heat transferred to the system = change in internal energy of the system + work done by the system"

1.2 Heat transfer and its modes

In the study of heat transfer, it is explained that how energy will be transferred and with what rate, which is the most important phenomenon to understand. Thermodynamics deals only with the equilibrium state of a system but does not explain the rate with which the change occurred. Study of heat transfer based on three modes namely conduction, convection and radiation [2], which are explained as follows

1.2.1 Conduction

Conduction is one of the mode of heat transfer in which energy can be transferred through solid body and it is due to the temperature gradient within a body. Conduction normally takes place in solids because of bound atoms, which gains thermal energy and vibrates about a fixed point. Due to the motion of the atoms about a fixed point, the thermal energy is transferred to neighboring atom. The part of solid, which gains thermal energy, will vibrate faster and passes the vibration to the next atom and so on. The rate of transfer of heat *'q'* through conduction is given by the equation

$$q = -k_s \frac{dT}{dx}.$$

The above equation represents the Fourier's law of heat conduction, which is stated as heat flux 'q' (the rate of transfer of heat per unit area) is proportional to $\frac{dT}{dx}$ temperature gradient, where k_s is known as thermal conductivity of the material.

1.2.2 Convection

Convection is another mode of heat transfer where energy is transferred by mass motion of atoms or molecules in the body. The transfer of energy through convection is actually conduction in a thin fluid layer on the surface and mixing caused by the fluid flow. It is the transfer of energy by bulk flow and molecular diffusion. Such type of heat flow does not depend upon the properties of material but depends upon fluid properties. Convection plays a vital role in daily life e.g. the cooling phenomenon of different electronic components in computer, cooling of cutting tools in machining operations, the heating and cooling of buildings etc. Newton established a relationship for transfer of heat by convection usually known as law of cooling.

$$q = h_s(T_w - T_\infty),$$

which is stated as heat flux 'q' is proportional to the difference of wall temperature and ambient temperature of the fluid, where h_s is known as convection heat transfer coefficient and depends upon boundary layers conditions including surface geometry, nature of fluid motion, an assortment of fluid thermodynamics and the transport properties. Convection is further divided into three mechanisms, which are explained here

Forced convection

In forced convection, the transfer of heat is due to the motion of fluid occurring by some external source for example blower, fan, jet and nozzle etc. In such mechanism, a small amount of buoyancy force effect exists. In Fig. 1.1(a), it is seen that the motion of fluid around elliptic cylinder occurs due to external source in term of free stream velocity.

Free/Natural convection

In free convection, the transfer of heat is due to the motion of fluid, occurring by the body force which depends not only on the gravitational field but also the variation in fluid density due to

the temperature difference. The body force is usually called the buoyancy force. In different areas of engineering, this mode of heat transfer is used such are "cooling of electric transformers, room heaters and cooling of electronic devices" etc. In Fig. 1.1 (b), it is seen that motion of the fluid occurs due to body force only in term of buoyancy force.

Mixed convection

A combination of both free convection and forced convection is known as mixed convection. In such mechanism both external source of heat and buoyancy force act together. In Fig. 1.1 (c), it is seen that motion of the fluid occurs due to the external source (free steam velocity) and buoyancy force.

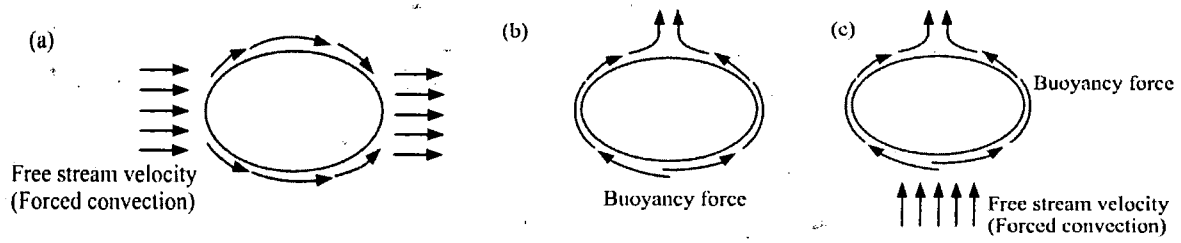

Figure 1.1: Transfer of heat in (a) Forced convection (b) Free convection (c) Mixed convection

1.2.3 Radiation

Radiation is the process of transfer of heat without any medium or source. Since, the conduction and convection require physical medium to transfer of heat but radiation can occur in vacuum. In thermodynamics, the electromagnetic radiations propagate as a result of temperature difference also known as thermal radiations. In Newtonian physics, Stephen-Boltzmann law explains the rate of energy radiated per unit area 'q' is proportional to the fourth power of temperature.

$$q = \sigma^* T^4,$$

where σ^* is the Stephen Boltzmann constant. The above equation is valid for black bodies which are an ideal absorber and ideal emitter also which is applicable for thermal radiation only. The above equation examines the radiations emitted by the black body [3].

1.3 Governing equations for fluid motion

The fluid is a substance that has an ability to deform continuously under the action of shear stress no matter how small it is. In fluid mechanics all the physical phenomena of the fluid flow can be expressed in mathematical model known as governing equations. The fundamental governing equations for the study of heat and mass transfer in the fluid flow based on three laws of conservation namely law of conservation of mass, law of conservation of momentum and law of conservation of energy. In general, these laws are written in term of partial differential equations. For different types of fluids these laws in term of governing equations are explained as follows:

1.3.1 Continuity equation

Law of conservation of mass is represented by equation of continuity, which states that mass cannot be created or destroyed. The equation of continuity for compressible fluid is

$$\frac{\partial \rho_f}{\partial t} + div(\rho_f \mathbf{V}) = 0, \tag{1.1}$$

where $\mathbf{V}(u,v,w)$ is the velocity vector, If the density ρ_f is constant (incompressible fluid) Eq. (1.1) becomes

$$div(\mathbf{V}) = 0. \tag{1.2}$$

In cylindrical coordinates, equation of continuity is

$$\frac{1}{r}\frac{\partial (ru)}{\partial r} + \frac{1}{r}\frac{\partial v}{\partial \theta} + \frac{\partial w}{\partial z} = 0. \tag{1.3}$$

1.3.2 Momentum equation

Law of conservation of momentum is represented by the momentum equation. Which describes the complete mechanism of fluid motion. The momentum equation for incompressible viscous fluid can be written as

$$\rho_f \left(\frac{\partial \mathbf{V}}{\partial t} + (\mathbf{V} \cdot \nabla)\mathbf{V} \right) = \nabla \cdot \boldsymbol{\tau} + \rho_f \mathbf{b}, \tag{1.4}$$

where ρ_f is density of the fluid, $\boldsymbol{\tau}$ is Cauchy stress tensor, which describes the nature of the fluid and $\mathbf{b}$ is the body force.

For **Newtonian fluid** the Cauchy stress tensor is defined as

$$\boldsymbol{\tau} = -p\mathbf{I} + \mu_f \mathbf{A}_1,$$

where p is the pressure, $\mathbf{I}$ is the identity tensor, μ_f is the dynamic viscosity and $\mathbf{A}_1$ is the first Rivlin Ericksen tensor defined by

$$\mathbf{A}_1 = \nabla\mathbf{V} + \nabla\mathbf{V}^{\mathrm{T}},$$

where $\nabla\mathbf{V}$ and $\nabla\mathbf{V}^{\mathrm{T}}$ represent the velocity gradient and its transpose.

For **Non-Newtonian fluid** (third order model), Cauchy stress tensor is defined as [4]

$$\boldsymbol{\tau} = -p\mathbf{I} + \mu\mathbf{A}_1 + \alpha_1\mathbf{A}_2 + \alpha_2\mathbf{A}_1^2 + \beta_1\mathbf{A}_3 + \beta_2\left(\mathbf{A}_2\mathbf{A}_1 + \mathbf{A}_1\mathbf{A}_2\right) + \beta_3\left(tr\mathbf{A}_1^2\right)\mathbf{A}_1,$$

where α_i $(i=1,2)$ and β_i $(i=1,2,3)$ are material constants. The Rivlin Erickson tensors $\mathbf{A}_n$ are defined as

$$\mathbf{A}_n = \left(\frac{\partial}{\partial t} + \mathbf{V}\cdot\nabla\right)\mathbf{A}_{n-1} + \mathbf{A}_{n-1}\left(\nabla\mathbf{V}\right) + \left(\nabla\mathbf{V}\right)^{\mathrm{T}}\mathbf{A}_{n-1}, \quad n = 2,3,\ldots$$

For third grade fluid the thermodynamic constraints are [5]

$$\mu_f \geq 0,\ \alpha_1 \geq 0,\ |\alpha_1 + \alpha_2| \leq \sqrt{24\mu_f\beta_3},$$
$$\beta_1 = \beta_2 = 0,\ \beta_3 \geq 0.$$

Cauchy stress tensor $\boldsymbol{\tau}$ becomes

$$\boldsymbol{\tau} = -p\mathbf{I} + \mu\mathbf{A}_1 + \alpha_1\mathbf{A}_2 + \alpha_2\mathbf{A}_1^2 + \beta_3\left(tr\mathbf{A}_1^2\right)\mathbf{A}_1.$$

Momentum equation for **nanofluid** in Tiwari-Das model [60] can be written as

$$\rho_{nf}\left(\frac{\partial\mathbf{V}}{\partial t} + (\mathbf{V}\cdot\nabla)\mathbf{V}\right) = \nabla\cdot\boldsymbol{\tau} + \rho_{nf}\mathbf{b}, \tag{1.5}$$

where ρ_{nf} is density of nanofluid. The Cauchy stress tensor in nanofluid is defined as

$$\boldsymbol{\tau} = -p\mathbf{I} + \mu_{nf}\mathbf{A}_1.$$

μ_{nf} is dynamic viscosity of nanofluid.

1.3.3 Energy equation

The analysis of heat transfer within the fluid is completely studied by energy equation, which can be derived using first law of thermodynamics under this statement that energy cannot be destroyed or created but can transform from one form to another. Energy equation in **Newtonian and non-Newtonian fluids** can be written as

$$\left(\frac{\partial T}{\partial t} + (\mathbf{V}\cdot\nabla)T\right) = \alpha_f\nabla\cdot\nabla T + \frac{1}{(\rho c_p)_f}\boldsymbol{\tau}:\nabla\mathbf{V} - \frac{1}{(\rho c_p)_f}\nabla\cdot\mathbf{q}_r, \tag{1.6}$$

where T is temperature, $(\rho c_p)_f$ is heat capacity, α_f is thermal diffusivity of the fluid, $\boldsymbol{\tau}:\nabla\mathbf{V}$ represents the term of viscous dissipation and $\mathbf{q}_r$ is radiative heat flux. By using the Rosseland

diffusion approximation $\mathbf{q}_r$ can be expressed as [3]

$$\mathbf{q}_r = -\frac{4\sigma^*}{3(\alpha_r + \alpha_s)}\nabla T^4,$$

where α_r is the Rosseland mean absorption coefficient and α_s is the scattering coefficient.

Energy equation for **nanofluid** in Tiwari-Das model is written as

$$\left(\frac{\partial T}{\partial t} + (\mathbf{V}\bullet\nabla)T\right) = \alpha_{nf}\nabla\bullet\nabla T + \frac{1}{(\rho c_p)_{nf}}\boldsymbol{\tau}:\nabla\mathbf{V}, \tag{1.7}$$

where $(\rho c_p)_{nf}$ is heat capacity and α_{nf} is thermal diffusivity of nanofluid.

Energy equation for **nanofluid** in Buongiorno model [58] is written as

$$\left(\frac{\partial T}{\partial t} + (\mathbf{V}\bullet\nabla)T\right) = \alpha_f\nabla\bullet\nabla T + \tau^*\left[D_B\nabla C\bullet\nabla T + \frac{D_T}{T_\infty}\nabla T\bullet\nabla T\right], \tag{1.8}$$

where $\tau^* = (\rho c_p)_p/(\rho c_p)_f$, is the ratio of heat capacity of nanoparticle and base fluid, D_B and D_T are the Brownian and thermophoretic diffusion coefficients, T_∞ is the ambient temperature of the fluid.

1.3.4 Concentration equation

The concentration equation for the nanoparticles in Buongiorno model is also known as continuity equation and in the absence of chemical reaction [58] is described as

$$\left(\frac{\partial C}{\partial t} + (\mathbf{V}\bullet\nabla)C\right) = D_B\nabla\bullet\nabla C + \frac{D_T}{T_\infty}\nabla\bullet\nabla T, \tag{1.9}$$

where C is the concentration of nanoparticle.

1.4 Literature survey

The analysis of heat transfer in stagnation point flow has received considerable attention since last few decades due to its abundant number of applications in several engineering and industrial problems. It includes cooling of nuclear reactors during emergency shut down, heat exchangers placed in a low velocity environment, cooling of electronic devices by fans, solar central receivers exposed to wind currents and many more. It is owing to the reasons that the stagnation point flow region encounters the highest pressure and highest heat transfer rate. In a flow field, stagnation point represents such point at which the velocity of the fluid become eventually zero. There are two types of stagnation point flow namely, orthogonal and non-

orthogonal. The non-orthogonal stagnation point flow is also known as oblique stagnation point flow in literature. It is the flow for which fluid impinges on a surface at an arbitrary angle other than 90°. However, in orthogonal stagnation point, the angle of strike of the fluids remain fixed at 90°. The study of two dimensional orthogonal stagnation point flow was first considered by Hiemenz [6]. Later on, Schlichting and Bussmann [7] provided a numerical solution of the Hiemenz [6] flow problem. Eckert [8] extended the work of Hiemenz [6] and analyzed the effects of heat transfer in the flow.

The study of fluid flow and heat transfer over a stretching/shrinking sheet has attracted attentions of many researchers. This phenomena remained important for many years for its analysis as it was needed to cope with several practical problems in the industry. Some of the problems are extrusion of a polymer in a melt spinning process, manufacturing plastic films, hot rolling and paper production, wire drawing and glass fiber production etc. Sakiadis [9, 10] was the first who studied the flow field over a moving surface with uniform linear velocity. After that, Crane [11] studied incompressible viscous fluid flow over a stretching sheet. The study of the fluid flow over a stretching cylinder was initiated by Wang [12], who investigated the steady flow and heat transfer characteristic outside of an infinite impermeable stretching cylinder. He obtained exact similarity solution of the governing Navier-Stoke equations of the problem. Later on, Ishak et al. [13] extended this work to the case of permeable cylinder. They found numerical solution of the governing equations and observed the fact that water is better cooling agent as compare to air. Again, Ishak et al. [14, 15] investigated the heat transfer effect on the flow over a stretching cylinder and heat transfer in MHD two dimensional flow over a stretching cylinder. K. Vajravelu et al. [16] studied the heat transfer analysis of axisymmetric electrically conducting flow of a viscous fluid induced by a non-isothermal stretching cylinder. Many other authors [17-20] have also worked on a stretching cylinder. The nature of the flow over a continuous shrinking surface is characterized by the fact that the flow over the surface is always directed towards a fixed point. Miklavcic and Wang [21] were the first, who studied the flow over a shrinking surface. Fang [22] studied boundary layer flow with power law velocity over the shrinking sheet. Fang and Zhang [23] calculated the exact solution of magneto-hydrodynamic viscous flow over a shrinking sheet. Sajid et al. [24] studied MHD rotating flow of a three dimensional viscous fluid over the surface which was assumed continuously shrinking towards the origin. Noor et al. [25] found non-perturbative solution for magneto-hydrodynamic viscous flow due to the shrinking sheet. Yao et al. [26] studied heat transfer analysis in a fluid flow over a generalized stretching shrinking wall with convective

boundary conditions. Mishra and Singh [27] found dual solutions of mixed convection flow over a permeable shrinking cylinder with momentum and thermal slip boundary conditions.

The combine study of stagnation point flow over a stretching/shrinking surface have been analyzed in detail by many researchers. Chiam [28] and Wang [29] were the first who studied stagnation point flow over a stretching and shrinking sheet. Bachok et al. [30] studied the decay of heat transfer in stagnation point flow of viscous fluid moving towards a stretching/shrinking sheet. Bhattacharyya [31] studied the heat and mass transfer rates with chemical reaction in a boundary layer stagnation point flow towards a stretching/shrinking surface. He obtained dual solutions of the governing nonlinear boundary value problem. Yacob et al. [32] extended the work of Bachok et al. [30] by considering micropolar fluid. Turkyilmazoglu and Pop [33] calculated exact analytical solutions of the governing problem for the flow and heat transfer in Jeffrey fluid near the stagnation point on a stretching/shrinking sheet. Weidman and Ali [34] investigated a stagnation point flow on a stretching cylinder. The analysis was presented for the flow in aligned and nonaligned radial direction and discussed the existence of unique and dual solution for wide range of shrinking parameter. Lok and Pop [35] studied the Wang's shrinking cylinder problem by considering it as permeable and of fixed radius with suction near a stagnation point. Lok et al. [36] considered mixed convection axisymmetric flow near the region of stagnation point on a stretching/shrinking cylinder. Najib et al. [37] investigated the diffusion of mass in stagnation point flow towards a stretching/shrinking cylinder with chemical reaction.

The analysis of unsteady flow has attracted considerable attention of many researchers due to its important practical applications due to time dependence. Such applications are to execute some devices in which time dependent motions are required, re-entry of space vehicles, fluid flow in vessels of human body in which reverse flow region may develop due to unsteadiness. Munawar et al. [38] studied the unsteady flow over an oscillatory stretching cylinder with time dependent oscillation and obtained the numerical solution of the governing equations by using an implicit finite difference scheme. Fang et al. [39] investigated unsteady viscous flow over an expanding stretching cylinder. They analyzed that the velocity decreases with the increase of Reynolds number and more rapidly expanding stretching cylinder slowly penetrate into the ambient fluid. Zaimi et al. [40] studied the mass transfer analysis of unsteady viscous flow over a shrinking cylinder and found unique and dual solutions for the specific range of unsteadiness parameter. They indicated that skin friction coefficient reduces with the enhancement in unsteadiness parameter. In **chapter 2**, the work of Lok and Pop [35] is extended by considering the flow near the stagnation point over an expanding/contracting

Wang's cylinder as an unsteady flow. The cylinder is assumed as permeable to analyze the suction phenomena while the cylinder is stretched or shrunk along the axis of the cylinder.

In the study of heat transfer analysis, mixed convection flows have gained considerable attentions of the researchers due to its many industrial and technological applications of solar central receivers placed in winds, with maximum cooling of nuclear reactors during emergency shutdown, cooling of electronic devices by fans and other heat exchangers placed in a low velocity environment etc. A careful literature review reveals that an intensive works have been done on convective boundary layer flow over a horizontal circular cylinder. Merkin [41] was the first who initiated the study of mixed convection flow near the lower stagnation point over a horizontal circular cylinder in which, he found that the separation point delays in case of heated cylinder and it comes earlier in cooling cylinder case. Further, a detail works on mixed convection flow along the same cylinder have been done in different investigations [42-47] by considering the flow of Newtonian and different non Newtonian fluids around it. The circular cylinder is a special case of an elliptic cylinder when major and minor axes are assumed equal.

The study of heat transfer analysis inside the flow around an elliptic cylinder has gained great importance due to the fact that it offers less resistance to the flow and heat transfer as compared to that of circular cylinders. The study of boundary layer flow over an elliptic cylinder is again initiated by Merkin [48]. In which, he investigated the free convection flow by considering CWT and CHF and problem was solved using Blasius series and Gortler type expansion techniques. In literature, few studies of mixed convection flow over an elliptic circular cylinder have been analyzed for both Newtonian\non-Newtonian fluids in [49-52].

The analysis of unsteady flow and heat transfer whose applications are mentioned earlier over a cylinder with elliptic cross section was investigated by Alessio [53]. In this study, he investigated the steady and unsteady flow over an inclined elliptic cylinder for the range of Reynolds numbers Re from 40 to 70 with Prandtl number at 1 and observed that the unsteady flow converges to steady state for small values of Re. Williams [54] studied analytically unsteady free convection flow from an inclined elliptic cylinder. Jaman and Hossain [55] found the influence of fluctuating in surface temperature with small amplitude on natural convection flow over an elliptic cylinder and obtained the numerical solution of the governing equation for eccentric angle in the range $0 \leq \alpha \leq 180^{\circ}$. The time dependent flow of combined natural and forced convection near the forward stagnation point region was first considered by Jamaludin et al. [56]. They solved the governing equations related to the flow problem numerically by using an implicit scheme of finite difference technique for both blunt and slender orientations. They found that separation times come early in case of opposing flow for slender orientation.

In **chapter 3**, the effects of thermal radiation on unsteady mixed convection flow near the forward stagnation point region over an elliptic cylinder is analyzed because thermal radiation in mixed convection flow has many practical applications such as the thermal energy storage devices, gas turbines and nuclear power plants etc.

In the preceding studies, a complete analysis on heat transfer have been made by the researchers by considering the fluids which have low thermal conductivity. Such fluids are water, air, oil, and ethylene glycol mixture which are poor in heat transfer. In many industrial and engineering problems, heat transfer rate plays an important role in term of highest heat transfer rate which can improve the efficiency of many processes in electronic cooling and heat exchangers. For improving the heat transfer rate and thermal conductivity of the fluids a huge effort has been made by the researchers. According to the experimental studies, the thermal conductivity of fluids can be increased when nano-size solid particles with length up to 100 nm are suspended in the base fluid, and this mixture is called a nanofluid introduced by Choi [57]. Various materials are considered, such as *Cu*, *Ag*, *Au* metals, *CuO*, Al_2O_3 and TiO_2 for making nanoparticles of different shapes. As a result, it is noted that the thermal conductivity of the obtained nanofluid is larger than that of the base fluid. Buongiorno [58] studied comprehensively the convective transport in nano-fluids and considered seven mechanisms such as Inertia, Thermophoresis, Brownian diffusion, gravity settling, fluid draining, Diffusiophoresis and Magnus effect. He observed that the absolute velocity of nanoparticle can be considered as sum of the velocity of the base fluid and relative velocity. Among these mechanisms, he found that only two mechanisms are very important namely Brownian diffusion and Thermophoresis. Investigation on the topic of heat transfer in nanofluids was done by many researchers, namely, Abu Nada [59], Tiwari and Das [60], Maiga et al. [61], Oztop and Abu Nada [62], and Nield and Kuznetsov [63, 64], Jaluria et al. [65], and Mahian et al. [66].

Mustafa et al. [67] were the first who studied two-dimensional flow of a nanofluid near the stagnation point region over the stretching sheet. They used the Buongiorno model and considered the important two Brownian motion and thermophoresis effects and solved governing equations analytically using homotopy analysis method. Nazar et al. [68] analyzed the stagnation point flow of a nanofluid past a shrinking sheet. They obtained a dual solution for the specific values of shrinking parameter. Bachok et al. [69] studied stagnation point flow of a nanofluid over a stretching-shrinking sheet. They considered three types of nano-size particles: *Cu*, TiO_2 and Al_2O_3 suspended in a base fluid like water. Kumar and Bandari [70] studied melting heat transfer in the flow of nanofluid with *Cu* and *Ag* (silver) as nano-size

particles suspended in water as a based fluid over a stretching/shrinking sheet near the stagnation point region. They noted that the heat transfer rate decreases with the increase of melting parameter. Khalili et al. [71] studied numerically the stagnation point flow and heat transfer of a nanofluid over a linear stretching/shrinking sheet. They considered three nano-size particles: Cu, Al_2O_3, and TiO_2, and found that the values of skin friction coefficient and heat transfer rate are higher for Cu-water nanofluid as compared to that of Al_2O_3 and TiO_2. In another studies, Zaimi et al. [72] investigated stagnation point flow of a nanofluid over a stretching/shrinking permeable sheet for both nanoparticles and gyrotactic microorganisms. They calculated dual solutions for specific values of stretching-shrinking parameter and found that the skin friction coefficient, Nusselt number, Sherwood number, and density of the motile microorganisms increase in case of suction.

The effects of magnetic field on the electrically conducting fluid flow problem have attained more importance due to its numerous applications in engineering problems such as geothermal energy extractions, magneto-hydrodynamic generators, plasma studies and nuclear reactors etc. Ibrahim et al. [73] investigated the two-dimensional stagnation point flow of a nanofluid towards a stretching sheet in the presence of magnetic field. Khalili et al. [74] studied MHD effects on stagnation point flow of nanofluids through a porous medium over a stretching/shrinking permeable plate. The effects of magneto-hydrodynamic on mixed convection flow of a nanofluid in the region of stagnation point flow over a convectively heated stretching/shrinking sheet was studied by Makinde et al. [75]. They presented dual solutions for the specific values of stretching-shrinking parameter. Yazdi et al. [76] analyzed the effects of thermal radiation in the presence of uniform magnetic field on mixed convection stagnation point flow along a vertical plate. The nanofluid was considered with Cu, Al_2O_3, and TiO_2 as nanoparticles in a base fluid. The flow was assumed through an isotropic porous medium sticked with vertical plate. The plate was assumed as stretching with small pores on it. They observed that the magnitude of skin friction coefficient and local Nusselt number increase with the increase of nanoparticle volume fraction for both assisting and opposing flow cases. Tamim et al. [77] presented the analysis of opposing and assisting flow cases on mixed convection stagnation point flow of a nanofluid along a vertical sheet without considering the effects of magneto-hydrodynamic. In **chapter 4**, the work of Tamim et al. [77] is extended by considering the combine effects of magneto-hydrodynamic and viscous dissipation because viscous dissipation plays an important role as an energy source and affects the heat transfer rates, which was ignored in all of the preceding studies.

Ferro or magnetic fluids are also known as a special type of nanofluids. Which is a colloidal suspension of magnetic nanoparticles namely; magnetite Fe_3O_4, hematite Fe_2O_3, cobalt Ferrite $CoFe_2O_4$ and many other compounds contain iron with nano-size about 10 to 100nm and dispersed in a base fluid [78]. Ferrofluid was first discovered in 1963 by NASA. The scientist Papell [79] found that "ferrofluid as a liquid rocket fuel that could be drawn toward a pump inlet in a weightless environment by applying magnetic field". Ferrofluids have a several applications in biomedicine and engineering fields. In biomedicine field, drug delivery is targeted magnetically up to a certain area of human body, in-vivo monitoring in the human brain for chemical activity, removal of toxin from the body and destruction of tumors [80, 81]. In engineering field, ferrofluid are extensively used in sealing of hard drives, rotating shafts, rotating X-ray tubes, rods and sink float systems for separation of materials, lubrication in bearing and dumpers, heat controller in electric motors and in hi-fi speakers [82] etc. A few studies on ferrofluid in the presence of external magnetic field were performed by the researchers [83–86]. Literature survey reveals that there are few studies in which ferrofluid over a rotating disk was considered. Ram et al. [87–89] studied the flow analysis of ferrofluid through the porous medium over rotating disk. After it, Ram and Sharma [90, 91] investigated the rotation and MHD effects on ferrofluid with rotating disk. To the best of the literature review, study of stagnation point flow of ferrofluid over a stretchable rotating disk was not considered by any other authors, therefore, in **chapter 5**, such analysis is presented in the presence of external magnetic field. For the general purpose of the study, we have studied three different magnetic nanoparticles namely, magnetite (Fe_3O_4), cobalt ferrite ($CoFe_2O_4$) and Mn-Zn ferrite ($Mn\text{-}ZnFe_2O_4$) and which become paramagnetic on the nanoscale (around 10nm) level.

All the above mentioned studies have been performed for linear stretching/shrinking sheet. Since, practically the rate of heat transfer at the stretching/shrinking sheet plays an important role for determining the quality of the final product. Therefore during the process, the kinematics of both stretching/shrinking and cooling/heating have major influence on the quality of the final product. It is, therefore, Vajravelu [92] studied viscous flow over a non-linear stretching sheet. Again, Vajravelu and Cannon [93] investigated the fluid flow over a non-linearly stretching sheet. Cortell [94] extended the work of Vajravelu [92] in the presence of viscous dissipation by considering two different cases of surface temperature namely constant and prescribed surface temperatures. Bataller [95] investigated the heat transfer analysis of quiescent fluid flow due to nonlinear stretching sheet and obtained the similarity solution of the problem in the presence of viscous dissipation and thermal radiation terms in

the equations. Two cases were considered namely prescribed surface temperature and prescribed heat flux. Hayat et al. [96] studied MHD effects on stagnation point flow of a micropolar fluid towards a non-linear stretching surface. Further, some very important studies on stagnation point flow towards a non-linear stretching/shrinking sheet have been made by the researchers [97-100].

A detail studies on the boundary layer flow of nanofluid in the stagnation point region over a linear stretching/shrinking sheet have been mentioned earlier. However, few studies of nanofluid over non-linear stretching/shrinking sheet have been presented by the researchers. Firstly, Rana and Bhargave [101] obtained the numerical solution of the boundary layer flow of nanofluid over non-linear stretching sheet. They used Buongiorno model and discussed the effects of thermophoresis and Brownian motion. Hady et al. [102] studied the heat transfer analysis of viscous fluid flow of a nanofluid over a non-linear stretching sheet in the presence of radiation effect with variable wall temperature. Some studies related to nonlinearly stretching/shrinking sheet have been considered by the researchers [103-106].

Boundary conditions play a vital role in material processing technologies and significantly modify the characteristic of manufactured products. In the above studies, two types of boundary conditions were considered namely prescribed surface heat flux (PHF) and prescribed surface temperature (PST). There is another type of boundary condition known as Newtonian heating (conjugate convective flows [107]) in which, heat is transported to the convective fluid passing near the boundary surface having finite heat capacity. Newtonian heating occurs in some important engineering devices such as heat exchangers in which the conduction in the solid wall is effected by convection in fluid [108]. Salleh et al. [109] investigated the effect of Newtonian heating on boundary layer flow and heat transfer over a stretching sheet. They solved non-linear boundary layer equations numerically by using finite difference scheme along with two cases "constant wall temperature (CWT)" and "constant heat flux (CHF)". Mohammed et al. [110] studied stagnation point flow over a stretching sheet with Newtonian heating. A number of studies with Newtonian and convective boundary conditions have been considered by many researchers [111-114]. Therefore, in **chapter 6**, the effect of Newtonian heating in nanofluid near the stagnation point over a non-linear permeable stretching/shrinking sheet is investigated.

The adherence of the fluid to a solid boundary is known as no slip velocity i.e., the velocity of the fluid at the solid boundary is zero. All the above studies were considered with no slip boundary condition but physically the no slip boundary condition does not hold. Beavers and Joseph [115] studied the fluid flow over a permeable wall with slip effects. They showed

that a boundary layer region induce within the permeable material. The slip flow under different flow geometries have been discussed by many researchers [116-122].

The aforementioned studies were considered for the complete analysis of the flow structure of Newtonian fluids. A study of heat transfer analysis in Non-Newtonian fluids have been considered by the researchers due to its numerous important practical application in industries, such as artificial fibers and plastic films. A few number of practical Non-Newtonian fluids such as food staff, molten plastic and polymers etc. Rajagopal et al. [123] investigated the flow analysis over a stretching sheet of second order viscoelastic fluid. They obtained fourth order highly nonlinear ordinary differential equation in which the order of boundary conditions was one less than the order of nonlinear differential equation and solved it numerically by using augmented boundary condition. Ariel [124] and Andersson [125] provided a closed form analytical solutions of same order highly nonlinear differential equations of second grade fluid and viscoelastic Walter's B fluid by considering magneto-hydrodynamic effects. Liu [126] investigated diverse physical effects on the flow of viscoelastic second grade fluid. Sahoo and Sharma [127] investigated the flow and heat transfer analysis of second grade fluid over a stretching sheet in which fluid was considered an electrically conducting. Afterwards, Cortell [128] considered second grade incompressible fluid and analyzed flow and heat transfer characteristic over a stretching sheet. A detail studies on second grade fluid reveals that it exhibits normal stress only for steady state flow but it cannot predict the shear thinning/thickening properties. Another models of Non-Newtonian fluids are third and fourth grade [129, 130] fluids models which can predict shear thinning/thickening properties. Therefore, in **chapter 7**, the slip effects on mixed convection orthogonal stagnation point flow of third grade fluid over a vertical plate is presented.

All the governing equations of the considered problems in this thesis are nonlinear ordinary/partial differential equations subject to different boundary conditions. The solution procedure used for these problems are discussed in the following section.

1.5 Methodology

For nonlinear differential equations, different analytical methods like homotopy analysis method, and Adomian decomposition method with Pade approximations developed in last decade have been used by researchers. Although these methods are efficient but are time consuming. Similarly, numerical methods like finite difference method and spectral method are also in great use of the researchers for this purpose. Since, we will be dealing with very

complex equations in this study; we prefer to use these numerical methods instead of analytical methods. The brief summary of these methods is as follows:

1.5.1 Finite difference method

The finite difference explicit/implicit schemes are one of the oldest schemes to solve any ordinary/partial differential equation. These schemes are based on the replacement of ordinary/partial derivatives of the equation with the appropriate forward/backward/central difference approximation: As a result, a system of algebraic equations is achieved, which can easily be solved by using any standard technique. Keller Box method is one of the implicit finite difference method, in which the higher order differential equations are first transformed into a system of first order differential equations and then converted to the system of algebraic equations. Since the flow problems regarding the boundary layer stagnation point flow are always nonlinear, so it is necessary to reduce the nonlinear differential equation to a system of 1^{st} order linear differential equations as per criteria of Keller Box method and then these linear differential equations are reduced to algebraic equations and then solved. This finite difference scheme is very famous scheme [131]. The details about this method for different equations have been presented in **chapters 3 and 4**.

1.5.2 Spectral method

Spectral method has developed rapidly in the past four decades and has been applied successfully to numerical simulations in many fields, such as heat conduction, fluid dynamics, quantum mechanics, turbulence theory and metrology. Spectral method [132] is one of the best method for the numerical solutions of PDE's. The basic theme of this method is to represent the solution of the nonlinear equation as a sum of certain trial/basis functions with unknown coefficients to be found subject to satisfy the differential equation at different nodes and boundary condition. The main feature of the spectral method is to take various orthogonal systems of infinitely differentiable global functions as trial functions. It is noted that the different trial functions lead to different spectral approximations. For instance, "trigonometric polynomials" are chosen for bounded periodic problems, "Legendre and Chebyshev polynomials" are for non-periodic problems, "Laguerre polynomials" are for problems on the half line, and "Hermite polynomials" are for problems on the whole line. The details about this method for different equations have been presented in **chapters 2 and 7**.

Chapter 2

Heat transfer in stagnation point flow over an unsteady expansion/contraction permeable cylinder

This chapter deals with the study of heat transfer analysis in unsteady boundary layer stagnation point flow of an incompressible viscous fluid over an expanding/contracting permeable cylinder. The mathematical model of the problem is made in terms of nonlinear partial differential equations which is further reduced to a system of nonlinear ordinary differential equations by using similarity transformation. The numerical solution of system of nonlinear ordinary differential equations is calculated by using Chebyshev spectral collocation method. There exist unique, dual and triple solutions in different ranges of unsteadiness parameter S and for different values of velocities ratio parameter. The ranges for which the unique, dual and triple solutions exist are shown through graphs and in tabular form. It is observed that the temperature and thermal boundary layer thickness decrease by increasing the absolute values of S in expanding cylinder case. However, this behavior is opposite in contracting cylinder case.

2.1 Mathematical formulation

Consider a laminar boundary layer axisymmetric stagnation point flow of an incompressible viscous fluid over a cylinder of time dependent radius $r = b_1(t) = b_0\sqrt{1-\beta^* t}$. It is assumed that the surface of the cylinder is permeable and its radius is kept flexible as to contract or expand. For negative values of β^*, the radius of the cylinder increases which is a case of expanding cylinder and for positive values of β^*, the radius of the cylinder decreases which is a case of contracting cylinder. Fig. 2.1 shows the geometrical description of the problem in which cylinder described by $r = b_1(t)$, and z and r are the cylindrical polar coordinates measured along axial and radial directions respectively. It is further assumed that the cylinder is stretched or shrunk with time dependent velocity $u_w = \dfrac{2cz}{1-\beta^* t}$, which is linearly proportional to the axial distance from its origin. It is clear that, the stretching or shrinking velocity of the surface

accelerates or decelerates for positive and negative values of β^*. The stagnation point is taken at $r = b_0$ and $z = 0$ with wall temperature T_w, uniform ambient temperature T_∞ and velocity of potential flow outside the boundary layer u_e. The flow is considered here is like axisymmetric about the z-axis, which enforces the azimuthal component of velocity to zero. The equations representing the laws of conservation of mass, momentum and energy in cylindrical coordinate system are

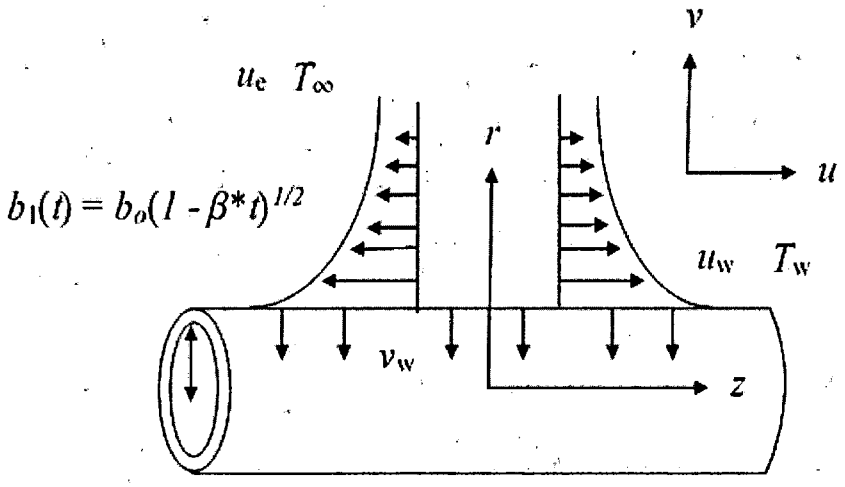

Figure 2.1: The physical model and coordinate system.

$$\frac{1}{r}\frac{\partial(rv)}{\partial r} + \frac{\partial u}{\partial z} = 0, \tag{2.1}$$

$$\frac{\partial v}{\partial t} + v\frac{\partial v}{\partial r} + u\frac{\partial v}{\partial z} = \frac{-1}{\rho_f}\frac{\partial p}{\partial r} + \nu_f\left(\frac{\partial^2 v}{\partial r^2} + \frac{1}{r}\frac{\partial v}{\partial r} + \frac{\partial^2 v}{\partial z^2} - \frac{v}{r^2}\right), \tag{2.2}$$

$$\frac{\partial u}{\partial t} + v\frac{\partial u}{\partial r} + u\frac{\partial u}{\partial z} = \frac{-1}{\rho_f}\frac{\partial p}{\partial z} + \nu_f\left(\frac{\partial^2 u}{\partial r^2} + \frac{1}{r}\frac{\partial u}{\partial r} + \frac{\partial^2 u}{\partial z^2}\right), \tag{2.3}$$

$$\frac{\partial T}{\partial t} + v\frac{\partial T}{\partial r} + u\frac{\partial T}{\partial z} = \alpha_f\left(\frac{\partial^2 T}{\partial r^2} + \frac{1}{r}\frac{\partial T}{\partial r} + \frac{\partial^2 T}{\partial z^2}\right), \tag{2.4}$$

where u and v are the components of velocity in z and r directions respectively, ν_f is the kinematic viscosity and T is the temperature of the fluid. The assumed boundary conditions for the problem are given by

$$\left.\begin{aligned} &v = v_w,\ u = u_w,\ T = T_w \text{ at } r = b_1(t) \\ &v \to v_e,\ u \to u_e,\ T \to T_\infty \text{ as } r \to \infty \end{aligned}\right\}. \tag{2.5}$$

The suction velocity v_w, stretching/shrinking velocity u_w and potential flow velocity u_e are defined as follows:

$$u_w = \frac{2cz}{1-\beta^* t}, v_w = \frac{-ab_0\gamma}{\sqrt{1-\beta^* t}} \text{ and } u_e = \frac{2az}{1-\beta^* t}, \tag{2.6}$$

where a and $c > 0$ (stretching) and $c < 0$ (shrinking) are the constants of dimension s^{-1}. After using the boundary layer approximations, Eqs. (2.2-2.4) reduce to the form

$$\frac{\partial u}{\partial t} + v\frac{\partial u}{\partial r} + u\frac{\partial u}{\partial z} = \frac{-1}{\rho_f}\frac{\partial p}{\partial z} + \nu_f\left(\frac{\partial^2 u}{\partial r^2} + \frac{1}{r}\frac{\partial u}{\partial r}\right), \tag{2.7}$$

$$\frac{\partial p}{\partial r} = 0, \tag{2.8}$$

$$\frac{\partial T}{\partial t} + v\frac{\partial T}{\partial r} + u\frac{\partial T}{\partial z} = \alpha_f\left(\frac{\partial^2 T}{\partial r^2} + \frac{1}{r}\frac{\partial T}{\partial r}\right). \tag{2.9}$$

For eliminating the pressure gradient, the boundary condition $r \to \infty$ is used in Eq. (2.7) (potential flow velocity outside the edge of the boundary layer) which reduces to

$$\frac{\partial u}{\partial t} + v\frac{\partial u}{\partial r} + u\frac{\partial u}{\partial z} = \frac{\partial u_e}{\partial t} + u_e\frac{\partial u_e}{\partial z} + \nu_f\left(\frac{\partial^2 u}{\partial r^2} + \frac{1}{r}\frac{\partial u}{\partial r}\right). \tag{2.10}$$

Upon using the following similarity variable

$$\left.\begin{aligned} v = \frac{-ab_0}{\sqrt{1-\beta^* t}\sqrt{\eta}} f(\eta),\ u = \frac{2az}{1-\beta^* t} f'(\eta) \\ \theta(\eta) = \frac{T-T_\infty}{T_w - T_\infty},\ \eta = \left(\frac{r}{b_0}\right)^2 \frac{1}{1-\beta^* t} \end{aligned}\right\}, \tag{2.11}$$

the governing partial differential Eqs. (2.10, 2.9) and boundary conditions Eq. (2.5) become

$$\eta f''' + \mathrm{Re}(ff'' - f'^2 + 1) + f'' + S(1-(f' + \eta f'')) = 0, \tag{2.12}$$

$$\eta\theta'' + (1 + \mathrm{Pr}\,\mathrm{Re}\, f - S\,\mathrm{Pr}\,\eta)\theta' = 0, \tag{2.13}$$

$$\left.\begin{aligned} f(1) = \gamma,\ f'(1) = \frac{c}{a},\ \theta(1) = 1 \\ f'(\eta) \to 1,\ \theta(\eta) \to 0 \text{ as } \eta \to \infty \end{aligned}\right\}, \tag{2.14}$$

where

$$\mathrm{Re} = \frac{ab_0^2}{2\nu_f}, S = \frac{\beta^* b_0^2}{4\nu_f} \text{ and } \mathrm{Pr} = \frac{\nu_f}{\alpha_f},$$

and prime denotes the differentiation w.r.t η, Re is the Reynolds number, S is the unsteadiness parameter, Pr is the Prandtl number, $\gamma > 0$ is the suction parameter, and c/a is the ratio of the constant of stretching/shrinking velocity and the free stream velocity, which represents stretching phenomenon when $c/a > 0$ and shrinking phenomenon when $c/a < 0$.

The physical quantities of interest are the skin friction coefficient and Nusselt number, which are defined as

$$C_f = \frac{\tau_w}{\rho_f u_e^2/2}, \quad Nu = \frac{b_0 q_w}{k_f (T_w - T_\infty)}, \tag{2.15}$$

where k_f is the thermal conductivity of the fluid, τ_w is the wall shear stress and q_w is the heat flux from the surface, which are defined as

$$\tau_w = \mu_f \left(\frac{\partial u}{\partial r}\right)_{r=b_1(t)}, \quad q_w = -k_f \left(\frac{\partial T}{\partial r}\right)_{r=b_1(t)}. \tag{2.16}$$

After using the Eqs. (2.11) and (2.16) into the Eq. (2.15), the skin friction coefficient and Nusselt number take the new form as follows:

$$\frac{C_f \mathrm{Re}_z}{\sqrt{1-\beta^* t}} = f''(1), \quad Nu\sqrt{1-\beta^* t} = -2\theta'(1). \tag{2.17}$$

2.2 Spectral collocation method

In order to solve nonlinear boundary value problem given in Eqs. (2.12) and (2.13) subject to the boundary conditions Eq. (2.14) against the applicable range of involved physical parameters, a highly accurate Chebyshev spectral collocation method is used. In this method, the solutions $f(\xi)$ and $\theta(\xi)$ are approximated by sum of N+1 basis functions T_n with unknown coefficients a_n and b_n are written as

$$f(\xi) \approx f_N(\xi) = \sum_{n=0}^{N} a_n T_n(\xi), \tag{2.18}$$

$$\theta(\xi) \approx \theta_N(\xi) = \sum_{n=0}^{N} b_n T_n(\xi). \tag{2.19}$$

To obtain the highly accurate solution, the basis functions are chosen as Chebyshev polynomial of degree n and defined in the interval $-1 \le \xi \le 1$ as

$$T_n(\xi) = \cos\left(n \cos^{-1} \xi\right).$$

Since the physical domain of the flow under consideration is $[1,\infty)$. The following transformation is used to convert the physical domain into the same domain as that of basis functions is $[-1,1]$ by

$$\xi = 2\frac{\eta - 1}{\eta_\infty - 1} - 1, \tag{2.20}$$

where η_∞ represents the physical infinity, i.e., the edge of the boundary layer. After using the above transformation, the obtained boundary value problem will take the form

$$\begin{aligned} &8\left\{1+\frac{(\eta_\infty-1)(\xi+1)}{2}\right\}\frac{d^3f}{d\xi^3}+4(\eta_\infty-1)\frac{d^2f}{d\xi^2}+ \\ &\mathrm{Re}\left\{4(\eta_\infty-1)f\frac{d^2f}{d\xi^2}-4(\eta_\infty-1)\left(\frac{df}{d\xi}\right)^2+(\eta_\infty-1)^3\right\} \\ &+S\left\{(\eta_\infty-1)^3-2(\eta_\infty-1)^2\frac{df}{d\xi}-4\left(1+\frac{(\eta_\infty-1)(\xi+1)}{2}\right)(\eta_\infty-1)\frac{d^2f}{d\xi^2}\right\}=0, \end{aligned} \tag{2.21}$$

$$4\left\{1+\frac{(\eta_\infty-1)(\xi+1)}{2}\right\}\frac{d^2\theta}{d\xi^2}+2\left\{\begin{array}{c}(\eta_\infty-1)+\mathrm{PrRe}(\eta_\infty-1)f- \\ S\,\mathrm{Pr}(\eta_\infty-1)\left(1+\frac{(\eta_\infty-1)(\xi+1)}{2}\right)\end{array}\right\}\frac{d\theta}{d\xi}=0, \tag{2.22}$$

and boundary conditions become

$$\left.\begin{array}{l} f(\xi)=\gamma,\ \dfrac{df}{d\xi}=(\eta_\infty-1)\dfrac{c}{2a},\ \theta(\xi)=1 \text{ at } \xi=-1 \\ \\ \dfrac{df}{d\xi}=\dfrac{\eta_\infty-1}{2},\ \theta(\xi)=0 \text{ at } \xi=1 \end{array}\right\}. \tag{2.23}$$

After substituting the assumed solutions (2.18, 2.19) into Eqs. (2.21, 2.22), the following non-zero residues R_1 and R_2

$$\begin{aligned} R_1 = &\frac{8}{\left(1-\xi^2\right)^{5/2}}\left(1+\frac{(\eta_\infty-1)(\xi+1)}{2}\right)\sum_{n=0}^{N}na_n\left(\begin{array}{c}-3n\xi\sqrt{1-\xi^2}\cos(n\cos^{-1}\xi) \\ +\sin(n\cos^{-1}\xi)-n^2\sin(n\cos^{-1}\xi) \\ +2\xi^2\sin(n\cos^{-1}\xi)+n^2\xi^2\sin(n\cos^{-1}\xi)\end{array}\right) \\ &+\frac{4(\eta_\infty-1)}{(-1+\xi^2)}\sum_{n=0}^{N}na_n\left(n\cos(n\cos^{-1}\xi)-\xi\frac{\sin(n\cos^{-1}\xi)}{\sqrt{1-\xi^2}}\right)+ \\ &S\left(\begin{array}{c}(\eta_\infty-1)^3-2(\eta_\infty-1)^2\sum_{n=0}^{N}\dfrac{na_n\sin(n\cos^{-1}\xi)}{\sqrt{1-\xi^2}}-4\left(1+\dfrac{(\eta_\infty-1)(\xi+1)}{2}\right) \\ \dfrac{(\eta_\infty-1)}{\left(-1+\xi^2\right)}\sum_{n=0}^{N}na_n\left(n\cos(n\cos^{-1}\xi)-\xi\dfrac{\sin(n\cos^{-1}\xi)}{\sqrt{1-\xi^2}}\right)\end{array}\right)+ \end{aligned}$$

$$\mathrm{Re}\left(\begin{array}{l}(\eta_\infty-1)^3-4(\eta_\infty-1)\left(\sum_{n=0}^{N}\frac{na_n\sin(n\cos^{-1}\xi)}{\sqrt{1-\xi^2}}\right)^2+4\frac{(\eta_\infty-1)}{(-1+\xi^2)}\\ \sum_{n=0}^{N}a_n\cos(n\cos^{-1}\xi)\sum_{n=0}^{N}na_n\left(n\cos(n\cos^{-1}\xi)-\xi\frac{\sin(n\cos^{-1}\xi)}{\sqrt{1-\xi^2}}\right)\end{array}\right) \tag{2.24}$$

and

$$R_2=\frac{4}{(-1+\xi^2)}\left(1+\frac{(\eta_\infty-1)(\xi+1)}{2}\right)\sum_{n=0}^{N}nb_n\left(n\cos(n\cos^{-1}\xi)-\xi\frac{\sin(n\cos^{-1}\xi)}{\sqrt{1-\xi^2}}\right)+$$
$$2(\eta_\infty-1)\left(1-\mathrm{Pr}\left(1+\frac{(\eta_\infty-1)(\xi+1)}{2}\right)S+\mathrm{PrRe}\sum_{n=0}^{N}a_n\cos(n\cos^{-1}\xi)\right)\times \tag{2.25}$$
$$\sum_{n=0}^{N}\frac{nb_n\sin(n\cos^{-1}\xi)}{\sqrt{1-\xi^2}},$$

will be left due to the fact that the proposed solutions of Eqs. (2.12) and (2.13) are not the exact solutions of the problem. To find the coefficients a_n and b_n in such a way that these residues R_1 and R_2 are minimized throughout the domain. In the present work, collocation point method is used in which the residues are forced to become exactly equal to zero at the set of N+1 collocation points. These points are called Gauss-Lobatto collocation points [132] defined as:

$$\xi_j=\cos(j\pi/N);\qquad j=0,1,2,...,N. \tag{2.26}$$

In this way, two systems of N+1 linear algebraic equations are obtained with N+1 unknowns constant coefficients each for a_n and b_n respectively and Newton's iteration method [133] is used for this purpose. The self-built code in MATLAB is used to compute the solution. It is observed that the grid independent solution is achieved when N = 52 is chosen for all values of the parameters in the discussion.

2.3 Results and discussion

For the validity of obtained result, a comparison for the values of $f''(1)$ with the work of Lok and Pop [35] is shown in Table 2.1 for distinct values of Re and γ as a limiting case when $S=0$ and $c/a=-0.5$. It is observed that the computed solution is in good agreement with the previous work in which the solution was obtained both analytically and numerically. Figs. 2.2(a-c) and 2.3(a-c) show the graphical values of skin friction coefficient and Nusselt number as a function of velocity ratio parameter $c/a<0$ for shrinking cylinder case for different

values of Re when $\gamma = 0.5$ and Pr = 0.7 are fixed. It is observed that the boundary value problem Eq. (2.12) subject to the boundary conditions Eq. (2.14) satisfies the solution of spiral like shape for these values of the parameters for $S = 0$ and $S = 0.04$ as shown in Fig. 2.2(a), which is evident from the previous study [35] for $S = 0$. It is further noticed that when $S = 0$, this spiral ends very near to the point (-1, 0) as shown in Fig. 2.2(b), but in the presence of unsteadiness parameter $S = 0.04$, this spiral ends at the different points for different values of Reynolds number Re as shown in Fig. 2.2(c). In other words, one can say that there exist triple solutions of boundary value problem Eq. (2.12) subject to the boundary conditions Eq. (2.14) for different values of velocity ratio parameter c/a for shrinking cylinder case as shown through Tables 2.2 and 2.3. It is further observed that the solution of the problem does not exist when $c/a < t_1$ for both $S = 0$ and $S = 0.04$. The ranges of parameters c/a for which unique, dual and triple solutions exist are mentioned in Tables 2.2 and 2.3 for $S = 0$ and $S = 0.04$ respectively. The points t_1 and t_2 are turning points where dual and triple solutions are found. One can easily observe from these figures that $t_2 < c/a < 0$ is the unique solution region for all given values of Reynolds number Re and unsteadiness parameter S, which is in fact the continuation of the solution for stretching case ($c/a > 0$). As in the paper of Riley and Weidman [134] and Lok and Pop [35], the upper branch solution of the triple solutions as that for which $f''(1)$ is greatest for a given value of c/a. Similarly the other solutions are known as lower branch solutions. Wilks and Bramley [135] and Merkin [136] performed the stability analysis of dual solutions for the same boundary value problem and it was revealed that the solution along the upper branch (first solution) was linearly stable however, the solution along the lower branch (second solution) was linearly unstable. Similar discussion can be found on the multiplicity of solution of boundary value problems in the paper of Riley and Weidman [134] and Wang [29]. Unsteadiness parameter further helps to decrease the skin friction coefficient for all values of Reynolds number Re as shown in Fig. 2.2(a) for first solution and by increasing the value of Re in presence of unsteadiness parameter the skin friction coefficient increases. Similar behavior was mentioned in [35] in the absence of unsteadiness parameter. Fig. 2.3(a-c) shows the variation in the values of Nusselt number against c/a with different values of Reynolds number Re for shrinking cylinder case. It is observed that for the upper branch solution, the value of Nusselt number decreases with the increase in the magnitude of c/a till the critical points for both $S = 0$ and $S = 0.04$ as shown in Fig. 2.3(a). It shows that the transfer of heat from the surface of cylinder to the fluid decreases for shrinking case. It is

also observed that the induction of unsteadiness parameter further reduces the heat transfer rate from cylinder to the fluid. In case of second solution, the Nusselt number increases with the increase in magnitude of c/a. Finally for $S=0$, the Nusselt number ends near the point (-1, 0) as shown in Fig. 2.3(b) as reported in [35] but for $S=0.04$, it ends at different points depending upon the values of Re as shown in Fig. 2.3(c). Fig. 2.4 shows the velocity profile for different values of velocity ratio parameter c/a (shrinking cylinder) with suction parameter $\gamma=0.5$, Reynolds number Re = 1 and unsteadiness parameter $S=0.04$ are fixed. It is observed that for the first solution velocity decreases and boundary layer thickness increases by increasing the absolute values of c/a. In the second solution for the starting values of η velocity decreases but for large values of η velocity increases and boundary layer thickness decreases with the increase of absolute values of c/a. Fig. 2.5 shows the velocity profile for various values of mass suction parameter and Reynolds number Re with $c/a=-1.2$ and $S=0.04$. It is seen that velocity increases and boundary layer thickness decreases by increasing the values of γ. The lower branch solution attains its minimum value near the wall, which gives the negative velocity gradient and causes the reverse flow. Physically, the velocity gradient will be considered positive when fluid will exert drag forces on the wall and will be opposite in negative velocity gradient. Fig. 2.6 shows the effects of various values of Re, Pr and γ on the temperature profile when $c/a=-1.2$ and $S=0.04$ are fixed. It is observed that thermal boundary layer thickness increases by increasing the values of Prandtl Pr. Figs. 2.7(a, b) and 2.8(a, b) show the velocity and temperature profiles for various values of unsteadiness parameter with $c/a=-0.5$, $\gamma=2$, Pr = 0.7 and Re = 1 are fixed. In Fig. 2.7(a), it is seen that velocity increases by increasing the absolute values of unsteadiness parameter S (expanding cylinder) but it produces apposite effects on boundary layer thickness. On the other hand velocity decreases and boundary layer thickness increases by increasing the unsteadiness parameter for contracting cylinder case as shown in Fig. 2.7(b). Fig. 2.8(a) shows that the temperature and thermal boundary layer thickness decrease by increasing the absolute values of S (expanding cylinder). However, behavior of temperature and thermal boundary layer thickness is found opposite against unsteadiness parameter for contracting cylinder as shown in Fig. 2.8(b). Figs. (2.9–2.12) show the streamlines for stretching and shrinking cylinder with $\gamma=0.5$, Re = 1 and $S=0.04$ are fixed. Figs. (2.10-2.12) show the streamlines of the first, second and third solution for the shrinking cylinder case.

Table 2.1: Numerical values of $f''(1)$ for distinct values of Re with $c/a = -0.5$.

	$\gamma = 0.5$			$\gamma = 1.5$		
	Lok and Pop [35]		Present work	Lok and Pop [35]		Present work
Re	Analytical	Numerical	Numerical	Analytical	Numerical	Numerical
0.5	1.7297	1.6800	1.6800	2.1975	2.1794	2.1794
1	2.4038	2.3709	2.3709	3.4421	3.4406	3.4406
5	6.3380	6.3331	6.3331	12.6513	12.6579	12.6579
10	10.5448	10.5456	10.5456	23.9478	23.9515	23.9515
50	41.4347	41.4368	41.4368	113.9897	113.9900	113.9900
100	79.1703	79.1714	79.1714	226.4949	226.4950	226.4950

(a)

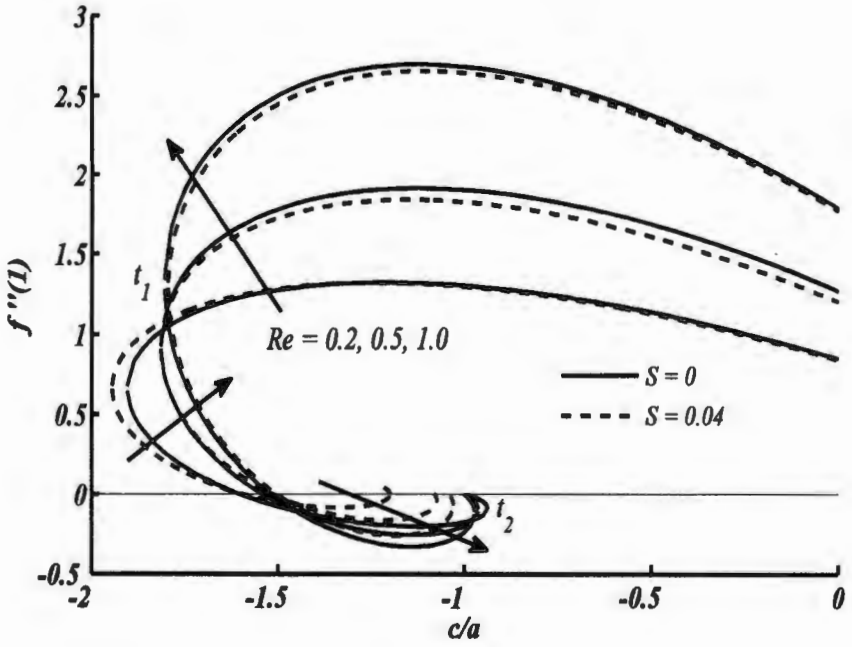

(b)

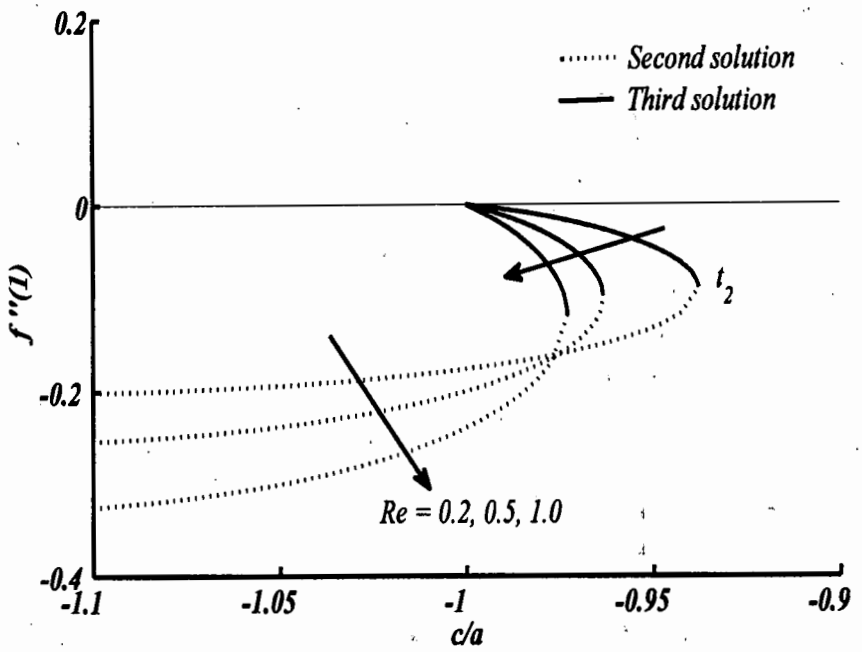

(c)

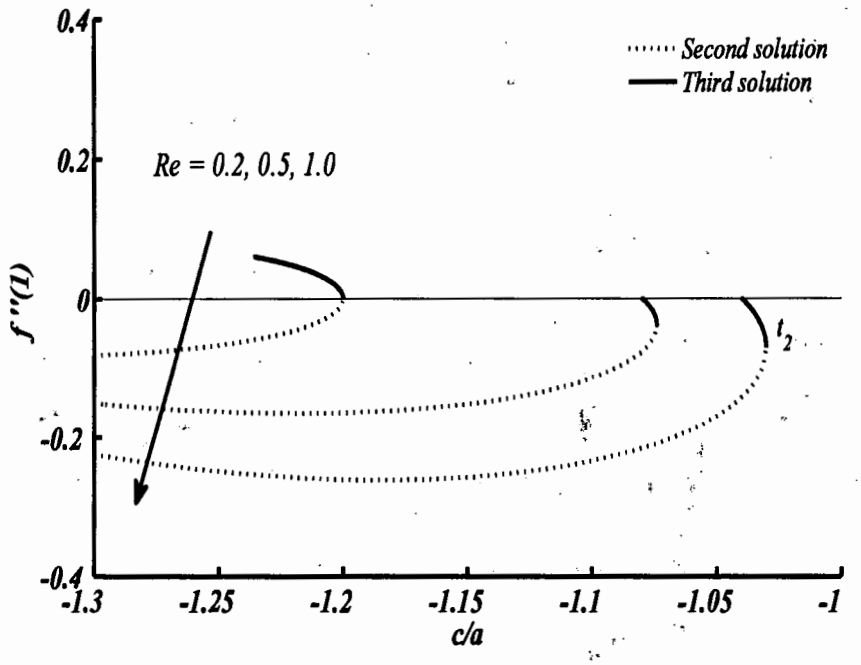

Figure 2.2(a-c): Variation of the skin friction coefficient with c/a for distinct values of Re (a) when $\gamma = 0.5$ (b) when $\gamma = 0.5$ and $S = 0$ (c) when $\gamma = 0.5$ and $S = 0.04$.

(a)

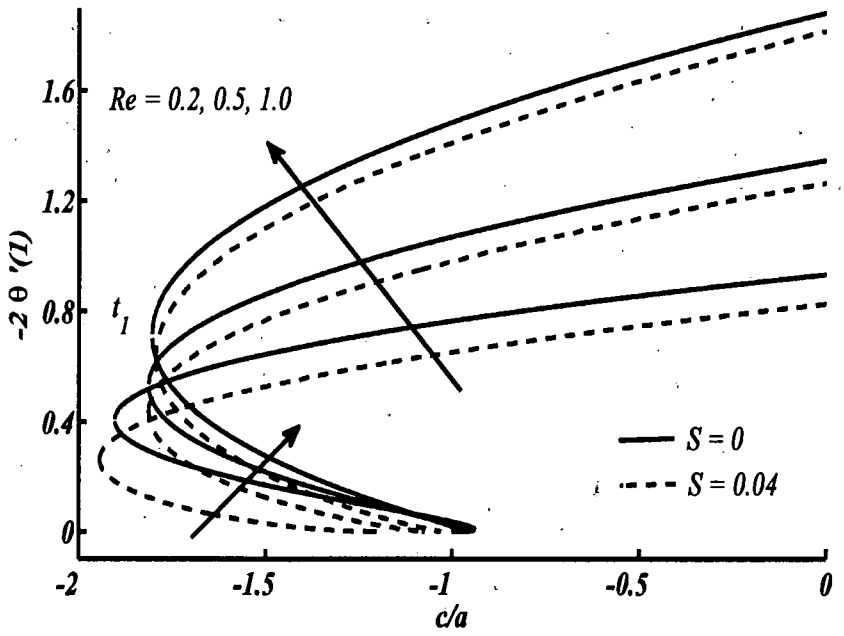
Re = 0.2, 0.5, 1.0
t_1
S = 0
S = 0.04
-2 θ '(1)
c/a
1.6
1.2
0.8
0.4
0
-2
-1.5
-1
-0.5
0

(b)

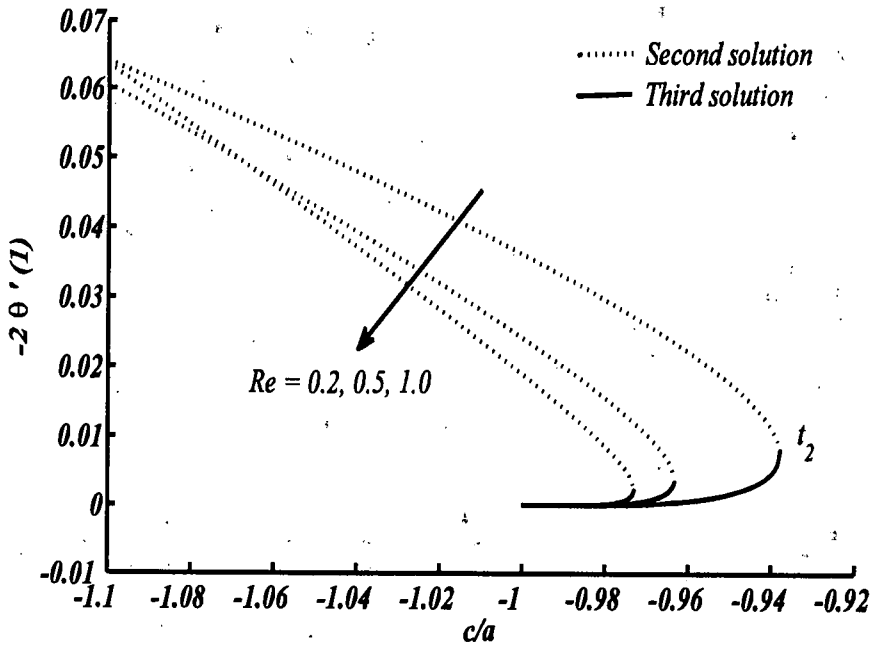
Second solution
Third solution
Re = 0.2, 0.5, 1.0
t_2
-2 θ '(1)
c/a
0.07
0.06
0.05
0.04
0.03
0.02
0.01
0
-0.01
-1.1
-1.08
-1.06
-1.04
-1.02
-1
-0.98
-0.96
-0.94
-0.92

(c)

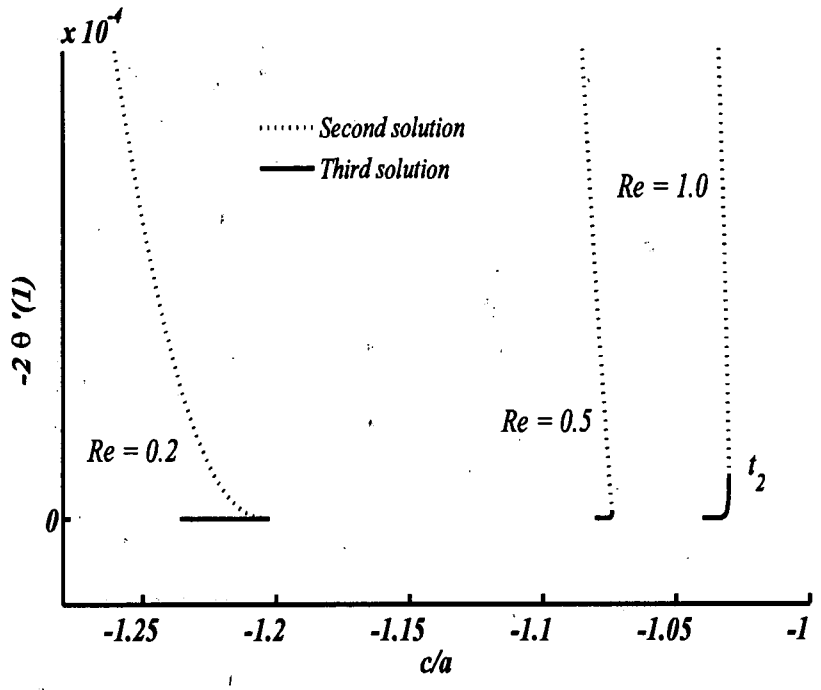

Figure 2.3(a-c): Variation of Nusselt number with c/a for distinct values of Re (a) when Pr = 0.7 and $\gamma = 0.5$ (b) when $S = 0$, Pr = 0.7 and $\gamma = 0.5$ (c) when $S = 0.04$, Pr = 0.7 and $\gamma = 0.5$.

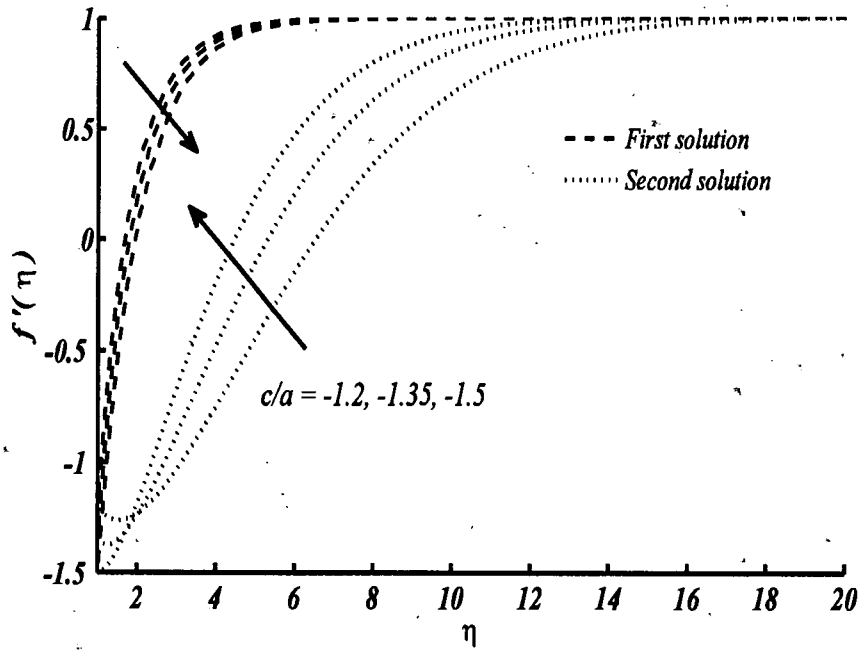

Figure 2.4: Velocity profile $f'(\eta)$ for distinct values of c/a when Re = 1, $S = 0.04$ and $\gamma = 0.5$.

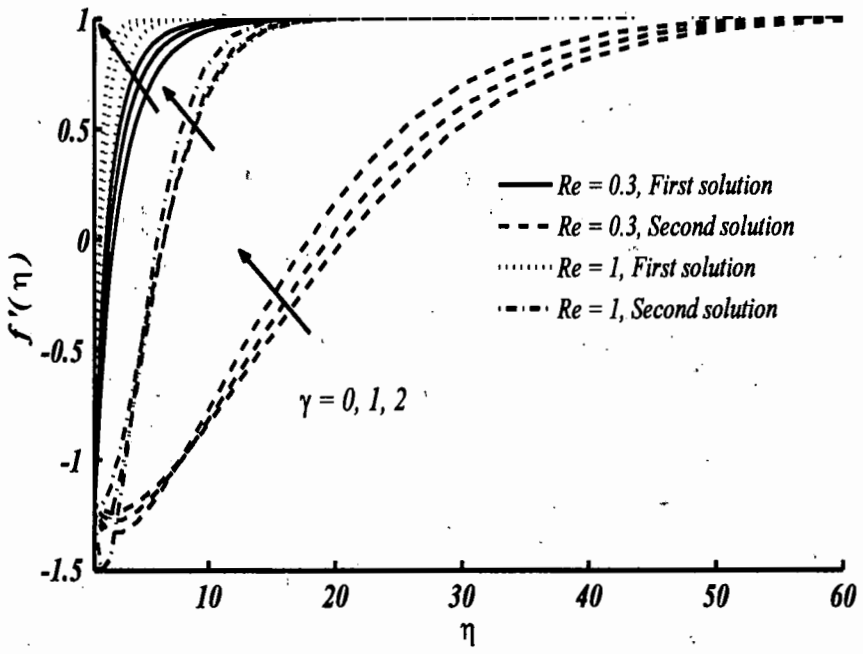

Figure 2.5: Velocity profile $f'(\eta)$ for distinct values of γ when c/a = -1.2 and S = 0.04.

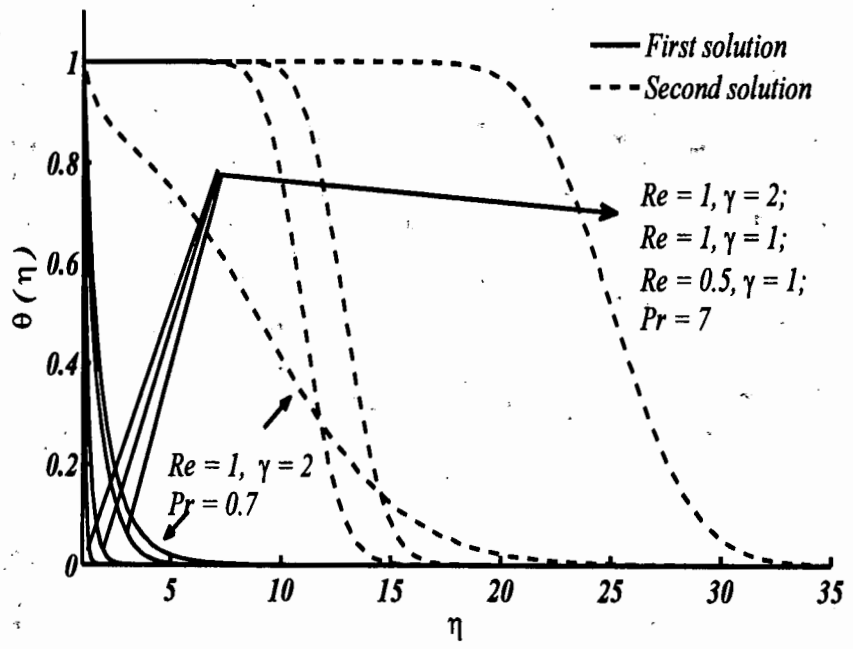

Figure 2.6: Temperature profile $\theta(\eta)$ when c/a = -1.2 and S = 0.04.

(a)

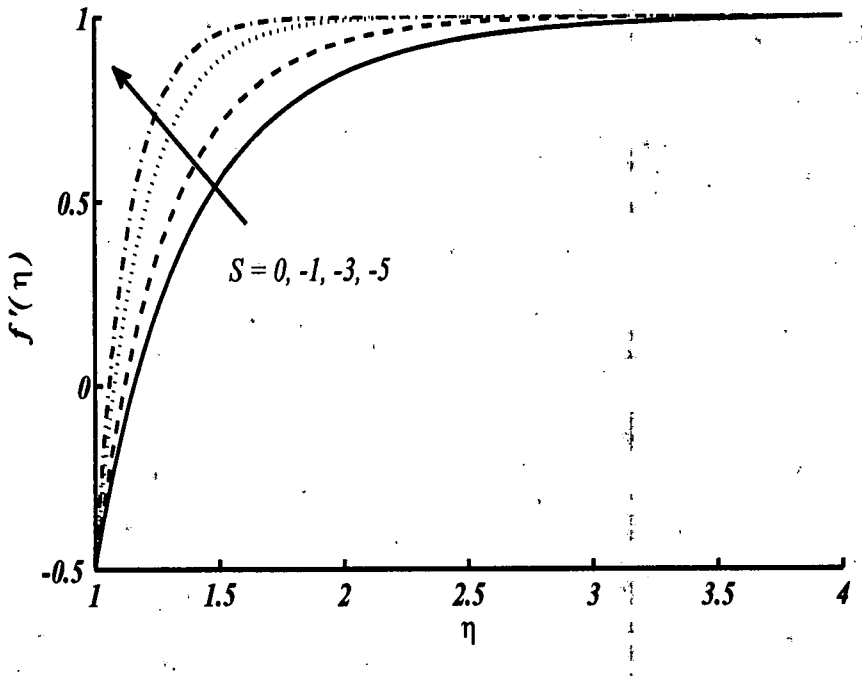

(b)

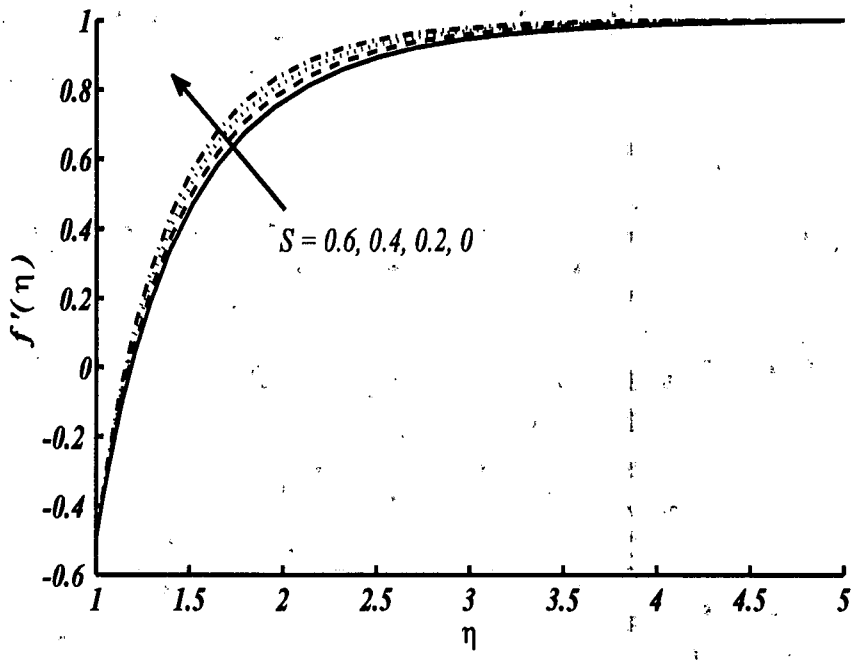

Figure 2.7(a, b): Velocity profile $f'(\eta)$ for distinct values of S when Re = 1, c/a = -0.5 and $\gamma = 2$.

(a)

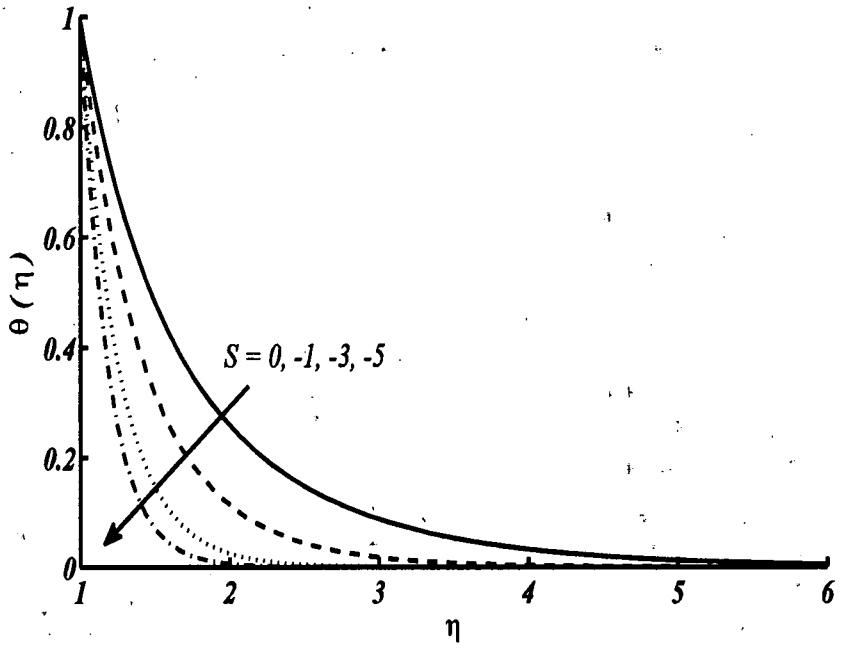

(b)

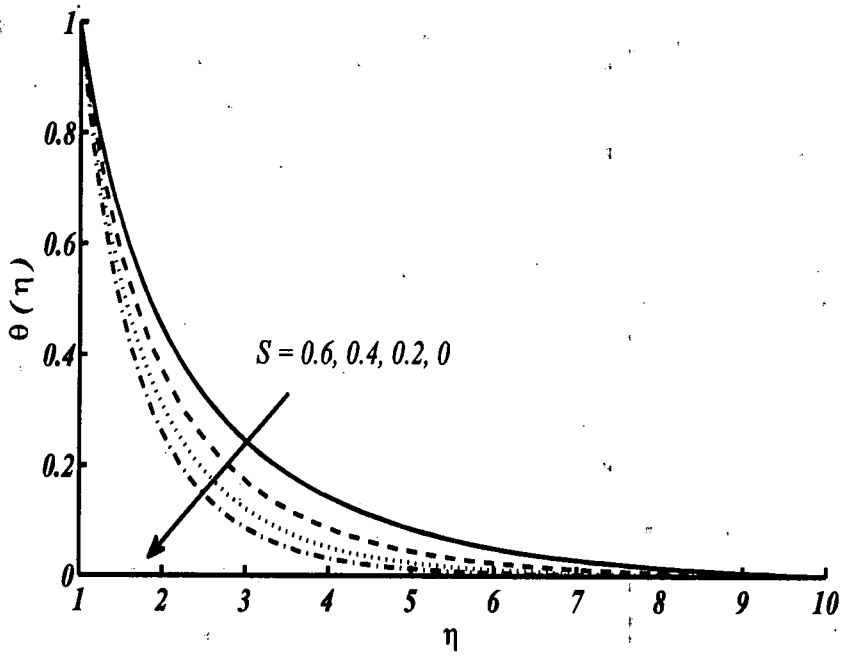

Figure 2.8(a, b): Temperature profile $\theta(\eta)$ for distinct values of S when Re = 1, c/a = -0.5, Pr = 0.7 and $\gamma = 2$.

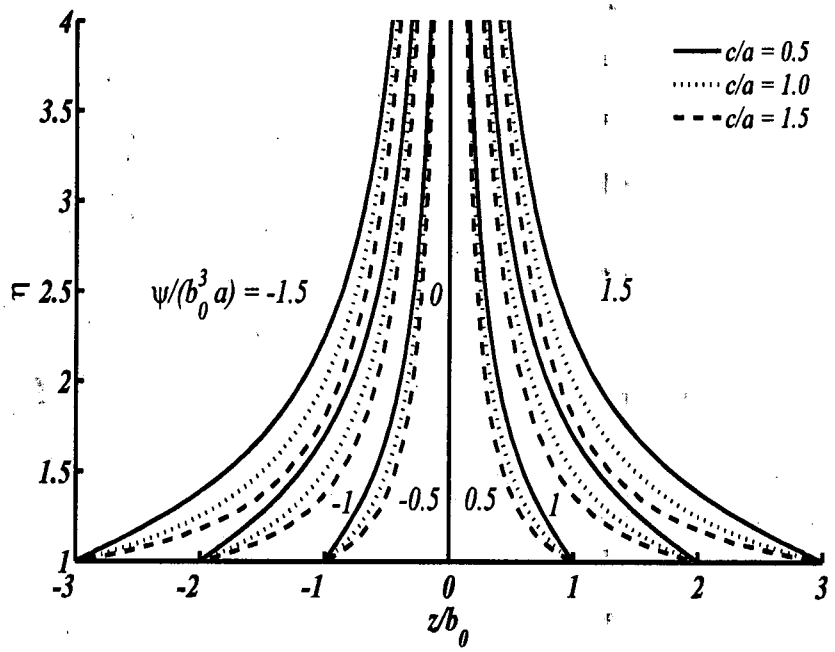

Figure 2.9: Streamlines for distinct values of stretching parameter c/a when Re = 1, $S = 0.04$ and $\gamma = 0.5$.

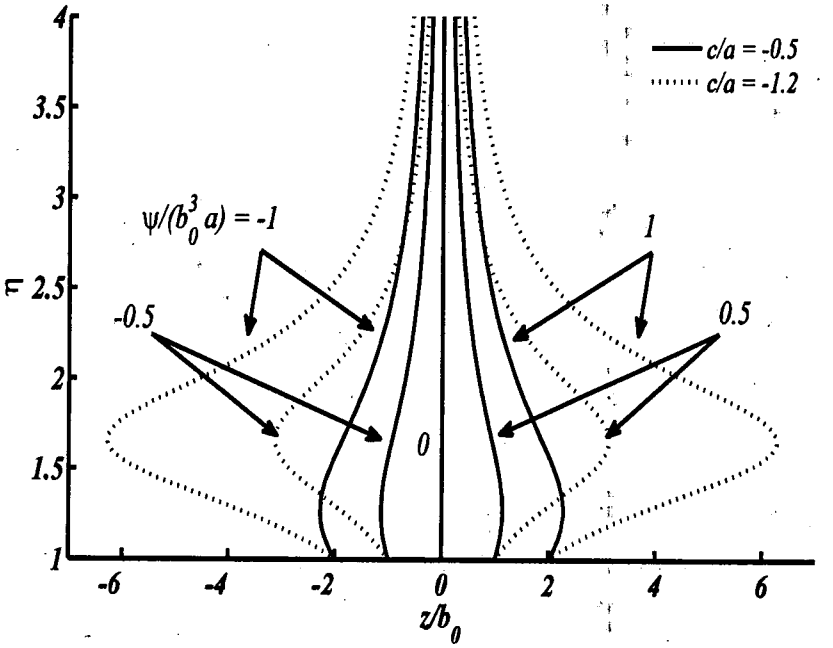

Figure 2.10: Streamlines for distinct values of shrinking parameter c/a when Re = 1, $S = 0.04$ and $\gamma = 0.5$ (first solution).

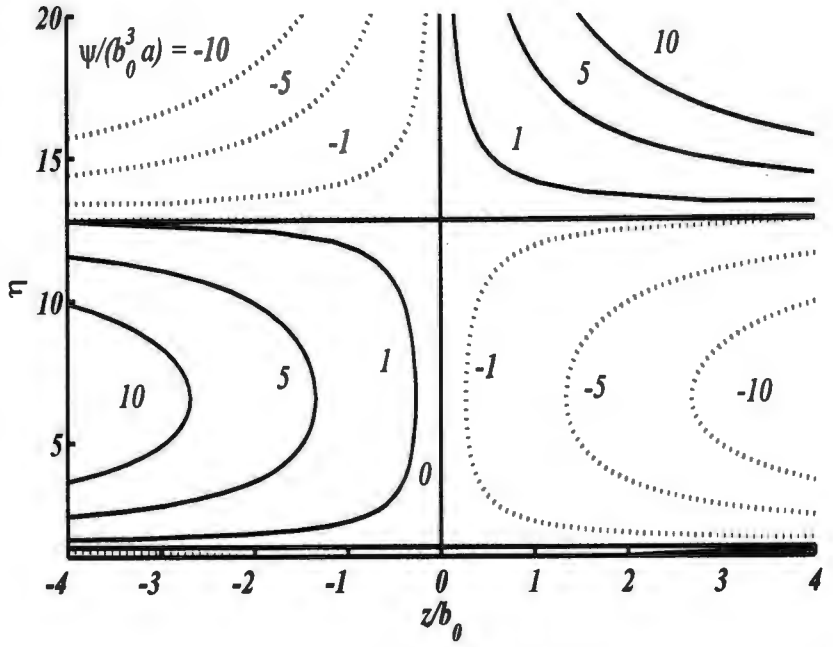

Figure 2.11: Streamlines for shrinking parameter $c/a = -1.2$ when Re = 1, $S = 0.04$ and $\gamma = 0.5$ (second solution).

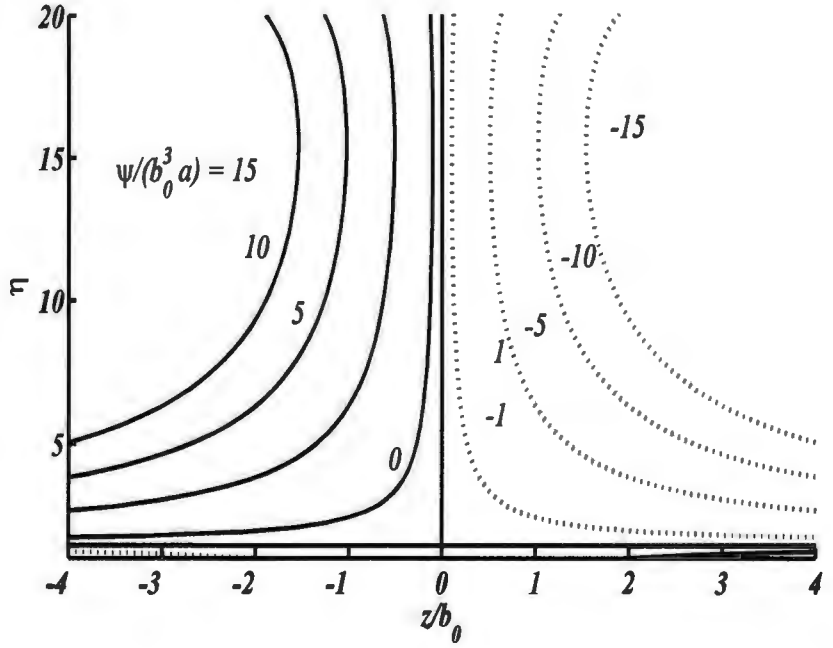

Figure 2.12: Streamlines for shrinking parameter $c/a = -1.0383$ when Re = 1, $S = 0.04$ and $\gamma = 0.5$ (third solution).

Table 2.2: The regions for which three solutions exist related to the Fig. 2.2 and Fig. 2.3 for distinct values of Re when $\gamma = 0.5$ and $S = 0$.

Lok and Pop [35] ($S = 0$)			
Re	0.2	0.5	1.0
1st solution	$-0.9377 < c/a < 0$	$-0.9633 < c/a < 0$	$-0.9731 < c/a < 0$
2nd solution	$-1.9042 < c/a < -1$	$-1.8138 < c/a < -1$	$-1.8047 < c/a < -1$
3rd solution	$-1 < c/a < -0.9377$	$-1 < c/a < -0.9633$	$-1 < c/a < -0.9731$
Present work ($S = 0$)			
1st solution	$-0.93779 < c/a < 0$	$-0.96339 < c/a < 0$	$-0.97319 < c/a < 0$
2nd solution	$-1.904169 < c/a < -1$	$-1.81379 < c/a < -1$	$-1.80469 < c/a < -1$
3rd solution	$-1 < c/a < -0.93779$	$-1 < c/a < -0.96339$	$-1 < c/a < -0.97319$

Table 2.3: The regions for which three solutions exist related to the Fig. 2.2 and Fig. 2.3 for distinct values of Re when $\gamma = 0.5$ and $S = 0.04$.

Present work ($S = 0.04$)			
Re	1st solution	2nd solution	3rd solution
0.2	$-1.2 < c/a < 0$	$-1.9444 < c/a < -1.236$	$-1.236 < c/a < -1.2$
0.5	$-1.0741112 < c/a < 0$	$-1.8144 < c/a < -1.0803$	$-1.0803 < c/a < -1.0741112$
1.0	$-1.03022 < c/a < 0$	$-1.795 < c/a < -1.04005$	$-1.04005 < c/a < -1.03022$

2.4 Conclusions

In this study, the effect of unsteadiness parameter on the fluid flow near the stagnation point region over an expanding/contracting permeable cylinder is investigated. The positive value of unsteadiness parameter corresponds to contracting cylinder and negative value corresponds to expanding cylinder. The governing partial differential equations are modeled as to describe the considered flow problem which is then reduced to system of nonlinear ordinary differential equations. The solution of the obtained system is computed with the help of highly accurate Chebyshev spectral collocation method. The Chebyshev polynomial are used as a basis function over the Gauss Lobatto points as grid points in the domain. The computed solution is first validated by comparing the values of the obtained solution as a limiting case with the results available in the literature. It is ensured that the computed solution is highly accurate, so the analysis presented in this chapter are valid. The dual and triple solutions of the present problem are obtained in the specific ranges of the parameters. In the case of expanding cylinder,

velocity increases and temperature decreases by increasing the absolute values of unsteadiness parameter. On the other hand velocity and thermal boundary layer thickness decrease due to it. The opposite behavior is observed in the case of contracting cylinder case.

Chapter 3

Radiative heat transfer in unsteady mixed convection flow near forward stagnation point over a cylinder of elliptic cross section

In this chapter, the effect of thermal radiation on unsteady mixed convection boundary layer flow near a forward stagnation point over a cylinder of elliptic cross section is presented. The governing partial differential equations contain three independent variables are converted into dimensionless partial differential equations by using a suitable transformation and become partial differential equations with two independent variables for the case of forward stagnation point and then solved numerically by using an implicit finite difference scheme. The detail about the solution procedure for the obtained partial differential equations are elaborated in this chapter. This method is commonly known as Keller Box method and the accuracy of the results is verified by comparing the obtained results with that of previous studies available in the literature. It is shown that the results are highly accurate and are in good agreement. The separation times for both blunt and slender orientations in the presence of thermal radiation are shown in tabular form. Moreover, the effects of pertinent parameters including Prandtl number Pr, mixed convection parameter λ, thermal radiation parameter R_d, surface temperature parameter θ_w and blunt/slender orientation parameter ω^* on the velocity profile, temperature profile and Nusselt number are shown graphically and discussed in detail. From the present study, it is observed that boundary layer separation occurs early due to presence of thermal radiation and Nusselt number increases for both blunt and slender orientations of the elliptic cylinder.

3.1 Mathematical formulation

Consider a two dimensional unsteady mixed convection flow of an incompressible viscous fluid over an elliptic cylinder near the region of forward stagnation point. It is assumed that the heat is transferring through the boundary layer due to both external agent and buoyancy effects called mixed convection in the presence of thermal radiation. A uniform temperature T_w is

considered at the surface of the elliptic cylinder and T_∞ is temperature of the fluid away from the cylinder.

Coordinate system: The relation between Cartesian coordinate (x, y) and elliptic coordinate (ζ, γ^*) is defined as [137]

$$x = a^* e \cosh\zeta \cos\gamma^*, \quad y = a^* e \sinh\zeta \sin\gamma^*$$

The surface of an ellipse can be defined by $\zeta = \zeta_o$, so

$$\tanh\zeta_o = b^*/a^*,$$

and the metric coefficients of elliptic coordinate system are defined as

$$h_{11} = h_{22} = a^* e\sqrt{\sinh^2\zeta + \sin^2\gamma^*},$$

where a^* is semi major axis, e is eccentricity and γ^* is angle measured in the streamwise direction from the forward stagnation point.

Governing equations: For the study of fluid flow and heat transfer around the surface of elliptic cylinder, it is convenient to use a local coordinate system in which X-coordinate is measured in the streamwise direction along the surface of the elliptic cylinder from the forward stagnation point and Y-coordinate is taken normal to the surface as shown in Fig. 3.1. The free stream velocity is considered as $1/2U_\infty$ as taken by Merkin [41], very far from the cylinder which impulsively starts in vertically upward direction. After using the boundary layer approximations, the governing equations of the flow problem can be written as

$$\frac{\partial u}{\partial X} + \frac{\partial v}{\partial Y} = 0, \tag{3.1}$$

$$\frac{\partial u}{\partial t} + u\frac{\partial u}{\partial X} + v\frac{\partial u}{\partial Y} = u_e(X)\frac{du_e(X)}{dX} + \nu_f \frac{\partial}{\partial Y}\left(\frac{\partial u}{\partial Y}\right) + \beta_f g\left(T - T_\infty\right)\sin\left(\varphi^*\right), \tag{3.2}$$

$$\frac{\partial T}{\partial t} + u\frac{\partial T}{\partial X} + v\frac{\partial T}{\partial Y} = \frac{1}{(\rho c_p)_f}\frac{\partial}{\partial Y}\left[\left\{k_f + \frac{16\sigma^* T^3}{3(\alpha_r + \alpha_s)}\right\}\frac{\partial T}{\partial Y}\right], \tag{3.3}$$

subject to the initial and boundary conditions

$$\begin{aligned} t<0:&\ u(X,Y) = v(X,Y) = 0,\ T(X,Y) = T_\infty \text{ for any } X, Y \\ t\geq 0:&\ u(X,0) = v(X,0) = 0,\ T(X,0) = T_w \text{ and} \\ &\ u(X,Y) \to u_e(X), T(X,Y) \to T_\infty \text{ as } Y \to \infty, \end{aligned} \tag{3.4}$$

where u and v are the velocity components in X and Y directions respectively and φ^* is the angle between outward normal from the cylinder with downward vertical axis, $\left(\rho c_p\right)_f$ is the

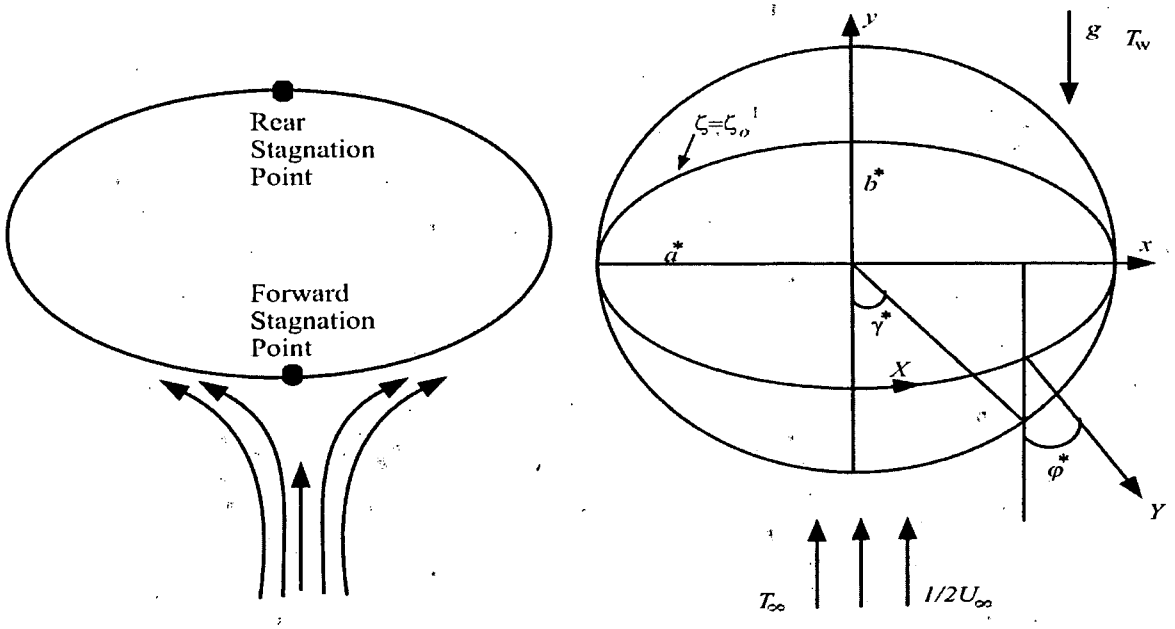

Figure 3.1: The physical model and coordinate system.

heat capacity of the fluid, β_f is the thermal expansion coefficient, g is the acceleration due to gravity and u_e is the velocity of potential flow. The radiation effect in Eq. (3.3) is considered by using the Rosseland diffusion approximation [3]. Under this approximation, the solution is not valid for situations where scattering is expected to be non-isotropic as well as in the immediate vicinity of the surface of the cylinder. Now introducing the non-dimensional variables as reported by Ali et al. [138]

$$\bar{x}=\frac{X}{a^*},\bar{y}=\frac{\mathrm{Re}^{1/2}}{a^*}Y,\bar{u}=\frac{u}{U_\infty},\bar{v}=\mathrm{Re}^{1/2}\left(\frac{v}{U_\infty}\right),\bar{t}=\frac{U_\infty}{a^*}t,\theta=\frac{T-T_\infty}{T_w-T_\infty}, \tag{3.5}$$

where $\mathrm{Re}=a^*U_\infty/\nu_f$ is the Reynolds number. Using Eq. (3.5) into the Eqs. (3.1–3.3), the non-dimensional form of governing equations are

$$\frac{\partial\bar{u}}{\partial\bar{x}}+\frac{\partial\bar{v}}{\partial\bar{y}}=0, \tag{3.6}$$

$$\frac{\partial\bar{u}}{\partial\bar{t}}+\bar{u}\frac{\partial\bar{u}}{\partial\bar{x}}+\bar{v}\frac{\partial\bar{u}}{\partial\bar{y}}=\bar{u}_e(\bar{x})\frac{d\bar{u}_e(\bar{x})}{d\bar{x}}+\frac{\partial}{\partial\bar{y}}\left(\frac{\partial\bar{u}}{\partial\bar{y}}\right)+\lambda\theta\sin(\varphi^*), \tag{3.7}$$

$$\frac{\partial\theta}{\partial\bar{t}}+\bar{u}\frac{\partial\theta}{\partial\bar{x}}+\bar{v}\frac{\partial\theta}{\partial\bar{y}}=\frac{1}{\mathrm{Pr}}\frac{\partial}{\partial\bar{y}}\left[\left\{1+\frac{4}{3}R_d\left(1+(\theta_w-1)\theta\right)^3\right\}\frac{\partial\theta}{\partial\bar{y}}\right], \tag{3.8}$$

where $\lambda = Gr/\mathrm{Re}^2$ is the mixed convection parameter, $R_d = 4\sigma^* T^3{}_\infty / k_f(\alpha_r + \alpha_s)$ is the radiation parameter, $Gr = g\beta_f(T_w - T_\infty)a^{*3}/\nu_f{}^2$ is the Grashof number and $\theta_w = T_w/T_\infty$ is the surface temperature parameter. It is necessary to mention here that $\lambda > 0$ corresponds to assisting flow when $T_w > T_\infty$ and $\lambda < 0$ corresponds to opposing flow when $T_w < T_\infty$. The initial and boundary conditions (3.4) take the new form as

$$\begin{aligned} &\bar{t} < 0: \ \bar{u}(\bar{x},\bar{y}) = \bar{v}(\bar{x},\bar{y}) = 0, \ \theta(\bar{x},\bar{y}) = 0 \text{ for any } \bar{x},\bar{y} \\ &\bar{t} \geq 0: \ \bar{u}(\bar{x},0) = \bar{v}(\bar{x},0) = 0, \ \theta(\bar{x},0) = 1, \\ &\bar{u}(\bar{x},\bar{y}) \to \bar{u}_e(\bar{x}), \theta(\bar{x},\bar{y}) \to 0 \text{ as } \bar{y} \to \infty. \end{aligned} \tag{3.9}$$

Now introduce the following transformation stated below

$$\psi^* = \bar{t}^{1/2}\bar{u}_e(\bar{x}) f(\bar{x},\eta,\bar{t}), \theta = \theta(\bar{x},\eta,\bar{t}), \eta = \frac{\bar{y}}{\bar{t}^{1/2}}, \tag{3.10}$$

where ψ^* is a dimensionless stream function, defined by the relationship $u = \dfrac{\partial \psi^*}{\partial \bar{y}}$ and $v = -\dfrac{\partial \psi^*}{\partial \bar{x}}$. Using Eq. (3.10) into the Eqs. (3.7-3.8), the system of dimensionless partial differential equations is obtained as follows

$$\begin{aligned} \frac{\partial^3 f}{\partial \eta^3} + \frac{\eta}{2}\frac{\partial^2 f}{\partial \eta^2} + \bar{t}\frac{\partial \bar{u}_e}{\partial \bar{x}}\left(1 - \left(\frac{\partial f}{\partial \eta}\right)^2 + f\frac{\partial^2 f}{\partial \eta^2}\right) &= \bar{t}\frac{\partial^2 f}{\partial \eta \partial \bar{t}} - \bar{t}\lambda\theta\frac{\sin(\varphi^*)}{\bar{u}_e} \\ &+ \bar{t}\,\bar{u}_e\left(\frac{\partial f}{\partial \eta}\frac{\partial^2 f}{\partial \eta \partial \bar{x}} - \frac{\partial f}{\partial \bar{x}}\frac{\partial^2 f}{\partial \eta^2}\right), \end{aligned} \tag{3.11}$$

$$\begin{aligned} \frac{1}{\mathrm{Pr}}\frac{\partial}{\partial \eta}\left[\left\{1 + \frac{4}{3}R_d\left(1 + (\theta_w - 1)\theta\right)^3\right\}\frac{\partial \theta}{\partial \eta}\right] + \bar{t}\frac{\partial \bar{u}_e}{\partial \bar{x}} f\frac{\partial \theta}{\partial \eta} + \frac{\eta}{2}\frac{\partial \theta}{\partial \eta} \\ = \bar{t}\left(\frac{\partial \theta}{\partial \bar{t}} + \bar{u}_e\left(\frac{\partial f}{\partial \eta}\frac{\partial \theta}{\partial \bar{x}} - \frac{\partial f}{\partial \bar{x}}\frac{\partial \theta}{\partial \eta}\right)\right). \end{aligned} \tag{3.12}$$

Initial and boundary conditions Eq. (3.9) take the form as

$$\begin{aligned} &\bar{t} < 0: \ f = \frac{\partial f}{\partial \eta} = 0, \ \theta = 0 && \text{for any } \bar{x} \text{ and } \eta \\ &\bar{t} \geq 0: \ f = \frac{\partial f}{\partial \eta} = 0, \ \theta = 1 && \text{at } \eta = 0, \\ &\frac{\partial f}{\partial \eta} \to 1, \theta \to 0 && \text{as } \eta \to \infty. \end{aligned} \tag{3.13}$$

Blunt orientation of the cylinder: The blunt orientation of the cylinder is defined as when the major axis of the cylinder remain parallel to the axis.

Slender orientation of the cylinder: When the major axis of the cylinder remain parallel to the y-axis, the orientation of cylinder is called slender orientation.

Here $\bar{x}$ and $\sin(\varphi^*)$ in terms of angle γ^* for blunt and slender orientations are

$$\bar{x} = \int_0^{\gamma^*} \left(1 - e^2 \sin^2 s\right)^{1/2} ds, \quad \sin(\varphi^*) = \frac{b^*}{a^*} \frac{\sin\gamma^*}{\left(1 - e^2 \sin^2 \gamma^*\right)^{1/2}}, \tag{3.14}$$

$$\bar{x} = \int_0^{\gamma^*} \left(1 - e^2 \cos^2 s\right)^{1/2} ds, \quad \sin(\varphi^*) = \frac{\sin\gamma^*}{\left(1 - e^2 \cos^2 \gamma^*\right)^{1/2}}, \tag{3.15}$$

respectively, where a^* and b^* are the length of semi major and minor axes and e is the eccentricity which is given by $e^2 = 1 - (b^*/a^*)^2$. In case of blunt orientation $\omega^* = b^*/a^*$ is considered less than 1 and in slender orientations $\omega^* = (a^*/b^*)^2$ is considered greater than 1.

3.1.1 Forward stagnation point flow

The present study is concerned to investigate the flow and heat transfer near forward stagnation point ($\bar{x} = 0$) over an elliptic cylinder. The term on the R.H.S. of Eq. (3.11), $\sin(\varphi^*)/\bar{u}_e$ approaches ω^* when $\bar{x}$ approaches zero. The potential velocity $\bar{u}_e(\bar{x}) = \sin(\bar{x})$ as reported by Ingham and Merkin [139] becomes zero in case of forward stagnation point and $\partial\bar{u}_e/\partial\bar{x} = 1$. The governing partial differential Eqs. (3.11, 3.12) near the forward stagnation point become

$$\frac{\partial^3 f}{\partial\eta^3} + \frac{\eta}{2}\frac{\partial^2 f}{\partial\eta^2} + \bar{t}\left(1 - \left(\frac{\partial f}{\partial\eta}\right)^2 + f\frac{\partial^2 f}{\partial\eta^2}\right) = \bar{t}\frac{\partial^2 f}{\partial\eta\partial\bar{t}} - \bar{t}\lambda\theta\omega^*, \tag{3.16}$$

$$\frac{1}{\Pr}\frac{\partial}{\partial\eta}\left[\left\{1 + \frac{4}{3}R_d\left(1 + (\theta_w - 1)\theta\right)^3\right\}\frac{\partial\theta}{\partial\eta}\right] + \bar{t}f\frac{\partial\theta}{\partial\eta} + \frac{\eta}{2}\frac{\partial\theta}{\partial\eta} = \bar{t}\left(\frac{\partial\theta}{\partial\bar{t}}\right), \tag{3.17}$$

and the boundary conditions become

$$\begin{aligned} &\bar{t} \geq 0: \ f = \frac{\partial f}{\partial\eta} = 0, \ \theta = 1 && \text{at } \eta = 0, \\ &\frac{\partial f}{\partial\eta} \to 1, \ \theta \to 0 && \text{as } \eta \to \infty. \end{aligned} \tag{3.18}$$

The relation of local skin friction coefficient and Nusselt number are written as

$$C_f = \frac{\tau_w}{(\rho_\infty)_f U_\infty^2}, \quad Nu = \frac{aq_w}{k_f(T_w - T_\infty)}, \tag{3.19}$$

where τ_w and q_w are defined as

$$\tau_w = \mu_f \left(\frac{\partial u}{\partial Y}\right)_{Y=0}, \quad q_w = -\left[\left(k_f + \frac{16\sigma^* T^3}{3(\alpha_r + \alpha_s)}\right)\frac{\partial T}{\partial Y}\right]_{Y=0}. \tag{3.20}$$

After using Eq. (3.20) into Eq. (3.19), the skin friction coefficient and Nusselt number take the form

$$C_f \,\mathrm{Re}^{1/2} = \frac{1}{\sqrt{\bar{t}}}\bar{u}_e \frac{\partial^2 f(0,\bar{t})}{\partial \eta^2},$$

$$Nu\,\mathrm{Re}^{-1/2} = -\left(1 + \frac{4}{3}R_d \theta_w^{\ 3}\right)\frac{1}{\sqrt{\bar{t}}}\frac{\partial \theta(0,\bar{t})}{\partial \eta}.$$

The skin friction coefficient $C_f \,\mathrm{Re}^{1/2}$ vanishes as $\bar{u}_e(\bar{x}) = 0$ at forward stagnation point.

3.2 Keller Box method

The system of partial differential Eqs. (3.16, 3.17) is nonlinear in nature and the solution of this system subject to the boundary conditions Eq. (3.18) is hardly possible through analytical methods. Therefore, a numerical method is used known as Keller Box method which is second order accurate method and converges rapidly [131].

Initially these differential equations are reduced to the system of first order differential equations by introducing the new variables using U, V, P and Q defined as

$$f' = U, U' = V, \theta = P \text{ and } \theta' = Q \tag{3.21}$$

Eqs. (3.16, 3.17) and boundary conditions Eq. (3.18) take new form as

$$V' + \frac{\eta}{2}V + \bar{t}\left(1 - U^2 + fV\right) = \bar{t}\frac{\partial U}{\partial \bar{t}} - \bar{t}\lambda P\omega^*, \tag{3.22}$$

$$Q' + \mathrm{Pr}\frac{\eta}{2}Q + \mathrm{Pr}\,\bar{t}fQ + \frac{4}{3}R_d\left(1 + (\theta_w - 1)P\right)^3 Q' + 4R_d(\theta_w - 1)\left(1 + (\theta_w - 1)P\right)^2 Q^2 = \mathrm{Pr}\,\bar{t}\frac{\partial P}{\partial \bar{t}} \tag{3.23}$$

$$f(0,\bar{t}) = U(0,\bar{t}) = 0, P(0,\bar{t}) = 1, \quad U(\infty,\bar{t}) = 1, P(\infty,\bar{t}) = 0. \tag{3.24}$$

A grid net on the plane $(\eta, \bar{t})$ is defined as

$$\eta_0 = 0, \eta_j = \eta_{j-1} + \Delta\eta, \eta_J = \eta_\infty,\ j = 1,2,\ldots J-1, \quad \bar{t}^0 = 0, \bar{t}^n = \bar{t}^{n-1} + \Delta\bar{t},\ n = 1,2,\ldots, \tag{3.25}$$

where n and j are positive integers, $\Delta\eta$ and $\Delta\bar{t}$ are widths of meshing variables on $(\eta, \bar{t})$ plane. The approximate quantities of functions f, U, V, P and Q at the net point $(\eta_j, \bar{t}^n)$ are

known as net functions whose derivatives in η and $\bar{t}$ - directions are replaced by the central difference formulae and functions itself are replaced by average centered at the midpoint $(\eta_{j-1/2}, \bar{t}^{n-1/2})$ defined as

$$\left(\frac{\partial f}{\partial \bar{t}}\right)_j^{n-1/2} = \frac{1}{\Delta \bar{t}}(f_j^n - f_j^{n-1}), f'^{n}_{j-1/2} = \frac{1}{\Delta \eta}(f_j^n - f_{j-1}^n), \text{and} f_j^{n-1/2} = \frac{1}{2}(f_j^n + f_j^{n-1}),$$

$$f_{j-1/2}^n = \frac{1}{2}(f_j^n + f_{j-1}^n).$$

After discretization, the system of nonlinear partial differential Eqs. (3.22) and (3.23) are converted to the system of difference equations written as

$$\frac{V_j^n - V_{j-1}^n}{\Delta \eta} + \left(\frac{\eta_j + \eta_{j-1}}{4}\right)\left(\frac{V_j^n + V_{j-1}^n}{2}\right) - 2\frac{\bar{t}^{n-1/2}}{\Delta \bar{t}}\left(\frac{U_j^n + U_{j-1}^n}{2}\right) + \bar{t}^{n-1/2}\lambda\omega^*\left(\frac{P_j^n + P_{j-1}^n}{2}\right)$$
$$+\bar{t}^{n-1/2}\left(\left(\frac{f_j^n + f_{j-1}^n}{2}\right)\left(\frac{V_j^n + V_{j-1}^n}{2}\right) - \left(\frac{U_j^n + U_{j-1}^n}{2}\right)^2\right) = r_{j-1/2}^{n-1}, \tag{3.26}$$

$$\frac{Q_j^n - Q_{j-1}^n}{\Delta \eta} + \Pr\left(\frac{\eta_j + \eta_{j-1}}{4}\right)\left(\frac{Q_j^n + Q_{j-1}^n}{2}\right) + \Pr \bar{t}^{n-1/2}\left(\frac{f_j^n + f_{j-1}^n}{2}\right)\left(\frac{Q_j^n + Q_{j-1}^n}{2}\right) +$$
$$\frac{4}{3}R_d\left\{(1-\theta_w)^3\left(\frac{P_j^n + P_{j-1}^n}{2}\right)^3 + 3(1-\theta_w)\left(\frac{P_j^n + P_{j-1}^n}{2}\right) + 3(1-\theta_w)^2\left(\frac{P_j^n + P_{j-1}^n}{2}\right)^2\right\}$$
$$\left(\frac{Q_j^n - Q_{j-1}^n}{\Delta \eta}\right) + 4R_d(1-\theta_w)^2\left\{(1-\theta_w)\left(\frac{P_j^n + P_{j-1}^n}{2}\right)^2 + (P_j^n + P_{j-1}^n)\right\}\left(\frac{Q_j^n + Q_{j-1}^n}{2}\right)^2 \tag{3.27}$$
$$-\Pr \bar{t}^{n-1/2}\left(\frac{P_j^n + P_{j-1}^n}{\Delta \bar{t}}\right) = m_{j-1/2}^{n-1},$$

Eq. (3.21) become

$$f_j^n - f_{j-1}^n = \frac{\Delta \eta}{2}(U_j^n + U_{j-1}^n), \tag{3.28}$$

$$U_j^n - U_{j-1}^n = \frac{\Delta \eta}{2}(V_j^n + V_{j-1}^n), \tag{3.29}$$

$$P_j^n - P_{j-1}^n = \frac{\Delta \eta}{2}(Q_j^n + Q_{j-1}^n). \tag{3.30}$$

Where

$$r_{j-1/2}^{n-1} = -\left(\frac{V_j^{n-1} - V_{j-1}^{n-1}}{\Delta \eta}\right) - \left(\frac{\eta_j + \eta_{j-1}}{4}\right)\left(\frac{V_j^{n-1} + V_{j-1}^{n-1}}{2}\right) -$$
$$\bar{t}^{n-1/2}\left(2 + \left(\frac{f_j^{n-1} + f_{j-1}^{n-1}}{2}\right)\left(\frac{V_j^{n-1} + V_{j-1}^{n-1}}{2}\right) - \left(\frac{U_j^{n-1} + U_{j-1}^{n-1}}{2}\right)^2\right) -$$

$$2\frac{\bar{t}^{n-1/2}}{\Delta\bar{t}}\left(\frac{U_j^{n-1}+U_{j-1}^{n-1}}{2}\right)-\bar{t}^{n-1/2}\lambda\omega^*\left(\frac{P_j^{n-1}+P_{j-1}^{n-1}}{2}\right), \tag{3.31}$$

$$m_{j-1/2}^{n-1}=-\left(\frac{Q_j^{n-1}-Q_{j-1}^{n-1}}{\Delta\eta}\right)-\Pr\left(\frac{\eta_j+\eta_{j-1}}{4}\right)\left(\frac{Q_j^{n-1}+Q_{j-1}^{n-1}}{2}\right)-$$
$$\Pr\bar{t}^{n-1/2}\left(\frac{P_j^{n-1}+P_{j-1}^{n-1}}{\Delta\bar{t}}\right)-\Pr\bar{t}^{n-1/2}\left(\frac{f_j^{n-1}+f_{j-1}^{n-1}}{2}\right)\left(\frac{Q_j^{n-1}+Q_{j-1}^{n-1}}{2}\right)-$$
$$\frac{4}{3}R_d\left\{\begin{array}{c}1+(1-\theta_w)^3\left(\frac{P_j^{n-1}+P_{j-1}^{n-1}}{2}\right)^3\\+3(1-\theta_w)\left(\frac{P_j^{n-1}+P_{j-1}^{n-1}}{2}\right)+3(1-\theta_w)^2\left(\frac{P_j^{n-1}+P_{j-1}^{n-1}}{2}\right)^2\end{array}\right\}\left(\frac{Q_j^{n-1}-Q_{j-1}^{n-1}}{\Delta\eta}\right)-$$
$$4R_d(1-\theta_w)\left\{\begin{array}{c}1+(1-\theta_w)^2\left(\frac{P_j^{n-1}+P_{j-1}^{n-1}}{2}\right)^2\\+(1-\theta_w)(P_j^{n-1}+P_{j-1}^{n-1})\end{array}\right\}\left(\frac{Q_j^{n-1}+Q_{j-1}^{n-1}}{2}\right)^2 \tag{3.32}$$

The boundary condition Eq. (3.24) become

$$f_0^n=U_0^n=0,P_0^n=1,U_J^n=1,P_J^n=0. \tag{3.33}$$

The above nonlinear algebraic Eqs. (3.26) and (3.27) are linearized by using Newton method by introducing $(i+1)^{th}$ iterates as

$$f_j^{n(i+1)}=f_j^{n(i)}+\delta f_j^{n(i)}, \tag{3.34}$$

similarly it is same for all other variables in which $f_j^{n(i)}$ is known for $0\le j\le J$ as an initial guess and $\delta f_j^{n(i)}$ is unknown. After using the Newton linearization process and neglecting the terms containing square and higher order of $\delta f_j^{n(i)},\delta U_j^{n(i)},\delta V_j^{n(i)},\delta P_j^{n(i)}$ and $\delta Q_j^{n(i)}$ the system of linear algebraic equations is obtained as follows

$$\delta f_j^n-\delta f_{j-1}^n-\frac{\Delta\eta}{2}(\delta U_j^n+\delta U_{j-1}^n)=(r_1)_j,$$
$$(s_1)_j\delta f_j^n+(s_2)_j\delta f_{j-1}^n+(s_3)_j\delta U_j^n+(s_4)_j\delta U_{j-1}^n+(s_5)_j\delta V_j^n+(s_6)_j\delta V_{j-1}^n+$$
$$(s_7)_j\delta T_j^n+(s_8)_j\delta T_{j-1}^n=(r_2)_j,$$
$$(s_9)_j\delta T_j^n+(s_{10})_j\delta T_{j-1}^n+(s_{11})_j\delta Q_j^n+(s_{12})_j\delta Q_{j-1}^n=(r_3)_j,$$
$$\delta U_j^n-\delta U_{j-1}^n-\frac{\Delta\eta}{2}(\delta V_j^n+\delta V_{j-1}^n)=(r_4)_j,$$
$$\delta P_j^n-\delta P_{j-1}^n-\frac{\Delta\eta}{2}(\delta Q_j^n+\delta Q_{j-1}^n)=(r_5)_j.$$

The boundary conditions Eq. (3.33) take the form as

$$\delta f_0^n=\delta U_0^n=0,\delta P_0^n=0,\delta U_J^n=0,\delta P_J^n=0.$$

Finally, the above system of linear algebraic equations with boundary conditions will be written in matrix vector form. The coefficients in momentum and energy equations of unknown functions $\delta f_j^n, \delta U_j^n, \delta V_j^n, \delta P_j^n$ and δQ_j^n and non-homogeneous parts are given as

Coefficient of momentum equation:

$$\delta f_j^n = (s_1)_j = \bar{t}^{\,n-1/2}\frac{(V_j^n + V_{j-1}^n)}{4}, \delta f_{j-1}^n = (s_2)_j = (s_1)_j,$$

$$\delta U_j^n = (s_3)_j = -\bar{t}^{\,n-1/2}\frac{(U_j^n + U_{j-1}^n)}{2} - \frac{\bar{t}^{\,n-1/2}}{\Delta \bar{t}}, \delta U_{j-1}^n = (s_4)_j = (s_3)_j,$$

$$\delta V_j^n = (s_5)_j = \frac{1}{\Delta\eta} + \frac{(\eta_j + \eta_{j-1})}{8} + \bar{t}^{\,n-1/2}\frac{(f_j^n + f_{j-1}^n)}{4},$$

$$\delta V_{j-1}^n = (s_6)_j = -\frac{1}{\Delta\eta} + \frac{(\eta_j + \eta_{j-1})}{8} + \bar{t}^{\,n-1/2}\frac{(f_j^n + f_{j-1}^n)}{4},$$

$$\delta P_j^n = (s_7)_j = \frac{\bar{t}^{\,n-1/2}\lambda\omega^*}{2}, \delta P_{j-1}^n = (s_8)_j = (s_7)_j,$$

Coefficient of energy equation:

$$\delta P_j^n = (s_9)_j = \frac{4}{3}R_d\left\{3(\theta_w - 1)^3\frac{(P_j^n + P_{j-1}^n)^2}{8} + \frac{3(\theta_w - 1)}{2} + 3\frac{(\theta_w - 1)^2}{2}(P_j^n + P_{j-1}^n)\right\}\frac{(Q_j^n - Q_{j-1}^n)}{\Delta\eta} +$$

$$R_d(\theta_w - 1)\left\{\frac{(\theta_w - 1)^2}{2}(P_j^n + P_{j-1}^n) + (\theta_w - 1)\right\}(Q_j^n + Q_{j-1}^n)^2 - \Pr\frac{\bar{t}^{\,n-1/2}}{\Delta\bar{t}}, \delta P_{j-1}^n = (s_{10})_j = (s_9)_j,$$

$$\delta Q_j^n = (s_{11})_j = \frac{1}{\Delta\eta} + \frac{\Pr(\eta_j + \eta_{j-1})}{8} + \Pr\bar{t}^{\,n-1/2}\frac{(f_j^n + f_{j-1}^n)}{4} +$$

$$\frac{4}{3\Delta\eta}R_d\left\{1 + (\theta_w - 1)^3\frac{(P_j^n + P_{j-1}^n)^3}{8} + \frac{3(\theta_w - 1)}{2}(P_j^n + P_{j-1}^n) + 3\frac{(\theta_w - 1)^2}{4}(P_j^n + P_{j-1}^n)^2\right\} +$$

$$+2R_d(\theta_w - 1)\left\{1 + (\theta_w - 1)^2\frac{(P_j^n + P_{j-1}^n)^2}{4} + (\theta_w - 1)(P_j^n + P_{j-1}^n)\right\}(Q_j^n + Q_{j-1}^n),$$

$$\delta Q_{j-1}^n = (s_{12})_j = -\frac{1}{\Delta\eta} + \frac{\Pr(\eta_j + \eta_{j-1})}{8} + \Pr\bar{t}^{\,n-1/2}\frac{(f_j^n + f_{j-1}^n)}{4} -$$

$$\frac{4}{3\Delta\eta}R_d\left\{1 + (\theta_w - 1)^3\frac{(P_j^n + P_{j-1}^n)^3}{8} + \frac{3(\theta_w - 1)}{2}(P_j^n + P_{j-1}^n) + 3\frac{(\theta_w - 1)^2}{4}(P_j^n + P_{j-1}^n)^2\right\} +$$

$$2R_d(\theta_w - 1)\left\{1 + (\theta_w - 1)^2\frac{(P_j^n + P_{j-1}^n)^2}{4} + (\theta_w - 1)(P_j^n + P_{j-1}^n)\right\}(Q_j^n + Q_{j-1}^n),$$

Non-homogenous terms:

$$(r_1)_j = (f_{j-1}^n - f_j^n) + \frac{\Delta\eta}{2}(U_j^n + U_{j-1}^n),$$

$$(r_2)_j = -\frac{(V_j^n - V_{j-1}^n)}{\Delta\eta} - \frac{(\eta_j + \eta_{j-1})}{4}\frac{(V_j^n + V_{j-1}^n)}{2} - \frac{\bar{t}^{n-1/2}}{4}\left\{-(U_j^n + U_{j-1}^n)^2 + \frac{(f_j^n + f_{j-1}^n)}{2}\frac{(V_j^n + V_{j-1}^n)}{2}\right\} +$$

$$\frac{\bar{t}^{n-1/2}}{\Delta\bar{t}}(U_j^n + U_{j-1}^n - U_j^{n-1} - U_{j-1}^{n-1}) - \bar{t}^{n-1/2}\lambda\omega^*\frac{(P_j^n + P_{j-1}^n)}{2} - \frac{(V_j^{n-1} - V_{j-1}^{n-1})}{\Delta\eta} - \frac{(\eta_j + \eta_{j-1})}{4}\frac{(V_j^{n-1} + V_{j-1}^{n-1})}{2} -$$

$$\bar{t}^{n-1/2}\left\{2 - \frac{(U_j^{n-1} + U_{j-1}^{n-1})^2}{4} + \frac{(f_j^{n-1} + f_{j-1}^{n-1})}{2}\frac{(V_j^{n-1} + V_{j-1}^{n-1})}{2}\right\} - \bar{t}^{n-1/2}\lambda\omega^*\frac{(P_j^{n-1} + P_{j-1}^{n-1})}{2},$$

$$(r_3)_j = -\frac{(Q_j^n - Q_{j-1}^n)}{\Delta\eta} - \frac{\Pr(\eta_j + \eta_{j-1})}{8}(Q_j^n + Q_{j-1}^n) - \Pr\bar{t}^{n-1/2}\frac{(f_j^n + f_{j-1}^n)(Q_j^n + Q_{j-1}^n)}{4} -$$

$$\frac{4}{3\Delta\eta}R_d\left\{1 + (\theta_w - 1)^3\frac{(P_j^n + P_{j-1}^n)^3}{8} + \frac{3(\theta_w - 1)}{2}(P_j^n + P_{j-1}^n) + 3\frac{(\theta_w - 1)^2}{4}(P_j^n + P_{j-1}^n)^2\right\}(Q_j^n - Q_{j-1}^n) -$$

$$R_d(\theta_w - 1)\left\{1 + (\theta_w - 1)^2\frac{(P_j^n + P_{j-1}^n)^2}{4} + (\theta_w - 1)(P_j^n + P_{j-1}^n)\right\}(Q_j^n + Q_{j-1}^n)^2 +$$

$$\Pr\frac{\bar{t}^{n-1/2}}{\Delta\bar{t}}(P_j^n + P_{j-1}^n - P_j^{n-1} - P_{j-1}^{n-1}) - \frac{(Q_j^{n-1} - Q_{j-1}^{n-1})}{\Delta\eta} - \frac{\Pr(\eta_j + \eta_{j-1})}{8}(Q_j^{n-1} + Q_{j-1}^{n-1}) -$$

$$\Pr\bar{t}^{n-1/2}\frac{(f_j^{n-1} + f_{j-1}^{n-1})(Q_j^{n-1} + Q_{j-1}^{n-1})}{4} - \frac{4}{3\Delta\eta}R_d\left\{\begin{array}{l}1 + (\theta_w - 1)^3\dfrac{(P_j^{n-1} + P_{j-1}^{n-1})^3}{8} + \\ \dfrac{3(\theta_w - 1)}{2}(P_j^{n-1} + P_{j-1}^{n-1}) + 3\dfrac{(\theta_w - 1)^2}{4}(P_j^{n-1} + P_{j-1}^{n-1})^2\end{array}\right\}\times$$

$$(Q_j^{n-1} - Q_{j-1}^{n-1}) - R_d(\theta_w - 1)\left\{1 + (\theta_w - 1)^2\frac{(P_j^{n-1} + P_{j-1}^{n-1})^2}{4} + (\theta_w - 1)(P_j^{n-1} + P_{j-1}^{n-1})\right\}(Q_j^{n-1} + Q_{j-1}^{n-1})^2,$$

$$(r_4)_j = (U_{j-1}^n - U_j^n) + \frac{\Delta\eta}{2}(V_j^n + V_{j-1}^n),$$

$$(r_5)_j = (P_{j-1}^n - P_j^n) + \frac{\Delta\eta}{2}(Q_j^n + Q_{j-1}^n).$$

The resulting matrix vector form is solved by using block-tridiagonal elimination technique, which consists on two sweeps namely forward sweep and backward sweep. The edge of the boundary layer η_∞ and step sizes $\Delta\eta$ and $\Delta\bar{t}$ in η and $\bar{t}$ respectively are set for different range of parameters involved in the problem.

3.3 Results and discussion

The effects of pertinent parameters like mixed convection parameter λ, blunt and slender orientations parameter ω^*, Prandtl number Pr, radiation parameter R_d and surface temperature parameter θ_w on the flow behavior are shown graphically by plotting velocity, temperature profiles and Nusselt number. For the validation of our results, the values of separation times near a forward stagnation point are compared with that of the work of Jamaludin et al. [56], as

shown in Tables 3.1 for the particular values of $\omega^*, \lambda, \Pr, R_d$ and θ_w. It is found that the computed results are in good agreement with the previous study and hence it is accurate. Table 3.1 presents the separation times along the elliptic cylinder near a forward stagnation point in absence as well as in presence of thermal radiation for both blunt and slender orientations with the fixed values of other parameters like $\Pr = 1$ and $\lambda = -3$ (opposing flow). In blunt orientation, separation times do not occur for values of parameter $\omega^* = 0.1, 0.25$ and 0.5. In slender orientation, separation time reduces with the increase of ω^*. It is also seen that separation time in blunt orientation is higher than that of the slender orientation. It is further observed that, in the presence of thermal radiation, separation times of the boundary layer flow reduce. The variation in separation time near forward stagnation point against mixed convection parameter λ in the absence as well as in the presence of thermal radiation is shown in Fig. 3.2. It is noticed that separation time decreases with the increase of absolute values of mixed convection parameter λ. Further, the separation time reduces due to the presence of thermal radiation. The effects of involving parameters on velocity and temperature profiles for both orientations are given in Figs. 3.3–3.8. Figs. (3.3–3.6) show the velocity and temperature profiles for specific values of time $\bar{t}$ in the absence as well as in the presence of thermal radiation in which dashed lines represent the thermal radiation effect. Fig. 3.3(a, b) shows velocity profiles in assisting flow case for blunt orientation $(\omega^* = 0.5)$ and slender orientation $(\omega^* = 4)$ in (a) and (b) respectively. The Fig. 3.3(a, b) depicts that the velocity increases with the increase of time $\bar{t}$ in both blunt and slender orientations. It can be further verified through the figure that velocity profile increases due to the effect of thermal radiation. Fig. 3.4(a, b) shows the variation in velocity profile in opposing flow case for both orientations. It is seen that velocity profile in the boundary layer increases in blunt orientation and decreases in slender orientations with the increase of time $\bar{t}$. It is further seen that velocity reduces in the presence of thermal radiation for both blunt and slender orientation cases. The momentum boundary layer thickness in blunt orientation decreases with the increase of time $\bar{t}$. Fig. 3.5(a, b) presents the temperature profiles for different values of time $\bar{t}$ in assisting flow for both blunt and slender orientations. It is seen that temperature and thermal boundary layer thickness decrease with the increase of time $\bar{t}$ in both orientations but the values of temperature become higher in the presence of thermal radiation. Fig. 3.6(a, b) is drawn to show the behavior of temperature in opposing flow case for different values of time. Fig. 3.6(a, b) shows the same behavior as

observed in Fig. 3.5(a, b). The effect of thermal radiation parameter R_d on velocity and temperature profiles for both opposing and assisting flow cases are shown in Figs. 3.7(a, b) and 3.8(a, b), when $\Pr = 1$ and $\bar{t} = 0.04$ are fixed. The dashed and solid lines represent the behavior of blunt ($\omega^* = 0.5$) orientation and slender ($\omega^* = 4$) orientation respectively. Fig. 3.7(a) depicts that velocity decreases in both blunt and slender orientations with the increase of thermal radiation in opposing flow case ($\lambda = -3$). Fig. 3.7(b) shows that velocity increases in both blunt and slender orientations with the increase of thermal radiation in assisting flow case ($\lambda = 2$). Fig. 3.8(a, b) shows that temperature and thermal boundary layer thicknesses increase by increasing the thermal radiation parameter R_d for both orientations. Also the values of temperature in both orientations are very close. In opposing flow, the values of temperature in blunt orientation become smaller as compare to slender orientation and opposite behavior is observed in assisting flow case. The effects of pertinent parameters on Nusselt number are shown in Figs. 3.9(a, b) and 3.10(a, b). Fig. 3.9(a, b) illustrates the variation in Nusselt number against $\bar{t}$ for various values of ω^* when $\Pr = 1$ is fixed for both orientations in opposing flow ($\lambda = -3$). Fig. 3.9(a) shows that Nusselt number decreases in blunt orientation with the increase of ω^* in the presence as well as in the absence of radiation effect. The transition in Nusselt number become smooth from initial unsteady state to steady state flow, but for $\omega^* = 0.75$ the value of Nusselt number truncates up to a certain value of $\bar{t}$ due to the separation. It is seen that radiation effect further enhances the values of Nusselt number for all values of $\bar{t}$. In Fig. 3.9(b), Nusselt number decreases in slender orientation up to certain values of $\bar{t}$ with the increase of ω^* due to the separation time, and the values of heat transfer rate increase due to thermal radiation. Fig. 3.10(a, b) demonstrates the variation in Nusselt number against $\bar{t}$ for various values of thermal radiation parameter R_d for both opposing ($\lambda = -3$) and assisting ($\lambda = 2$) flow cases. Nusselt number increases with the increase of thermal radiation for both blunt and slender orientations. This is because increasing values of R_d help to enhance the interaction of radiation with the thermal boundary layer and as a result, the heat absorption intensity of the fluid increases. In Fig. 3.10(a), the values of Nusselt number in blunt orientation become smooth from initial unsteady state flow to final steady state flow. In slender orientation, the values of Nusselt number for each values of R_d truncate up to certain values of $\bar{t}$ due to the separation. In Fig. 3.10(b) for assisting flow, the values of Nusselt number become smooth

from initial unsteady state flow to final steady state flow in both orientations. It is further seen that heat transfer rate in slender orientation is greater than that in blunt orientation.

Table 3.1: The separation times $\bar{t}_s$ at $(\bar{x}=0)$ over elliptic cylinder for $\mathrm{Pr}=1$ and $\lambda=-3$ (opposing flow).

		Slender orientation $\omega^* = (a^*/b^*)^2$				Blunt orientation $\omega^* = b^*/a^*$			
		100	16	4	1.7778	0.75	0.5	0.25	0.1
$R_d=0.0$	[56] $\bar{t}_s$	0.0033	0.0215	0.0954	0.2652	1.521	-	-	-
	present $\bar{t}_s$	0.0033	0.0215	0.0958	0.2652	1.521	-	-	-
$R_d=0.5$ $\theta_w=0.8$	present $\bar{t}_s$	0.0031	0.0199	0.0877	0.23902	1.2215	-	-	-

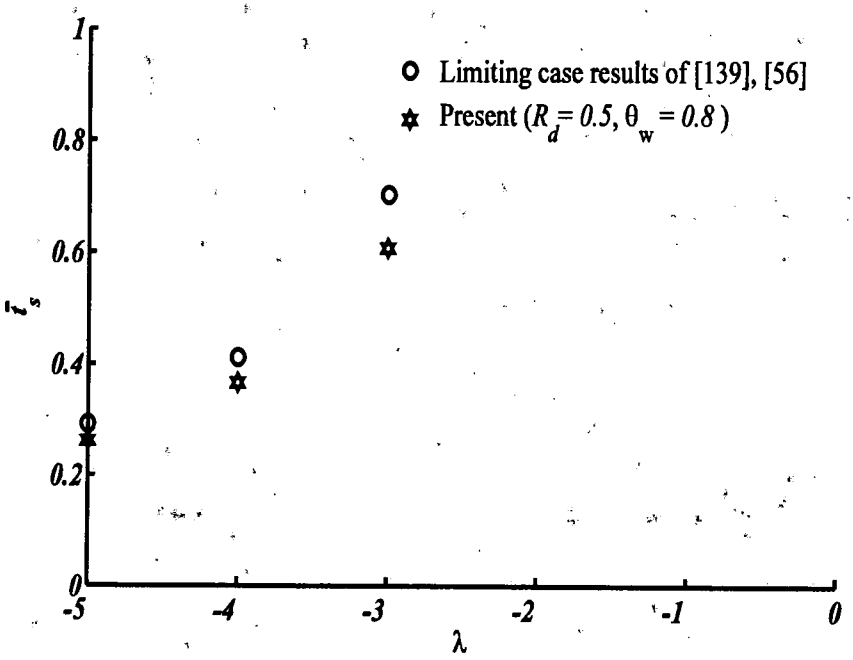

Figure 3.2: Separation times at $(\bar{x}=0)$ when $\mathrm{Pr}=1$ and $\omega^*=1$.

(a)

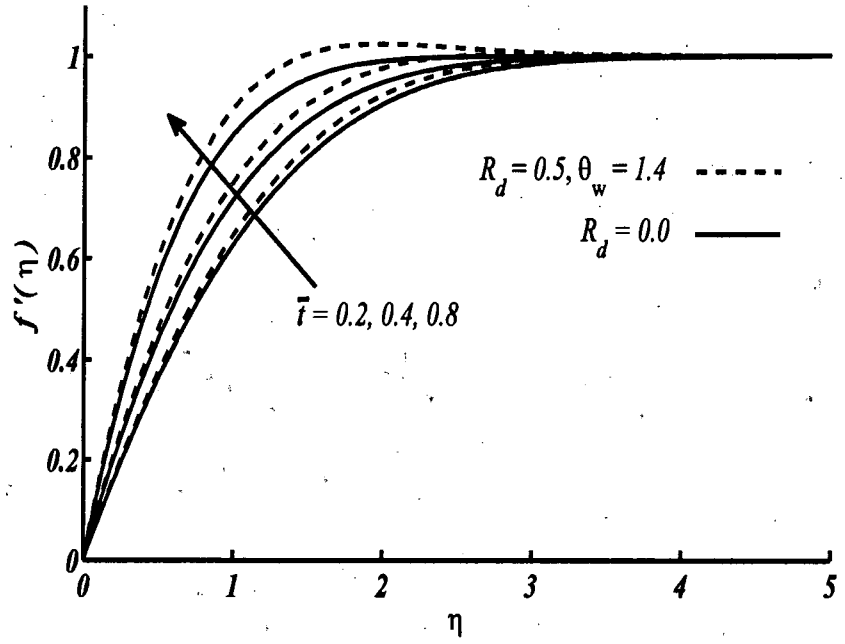

(b)

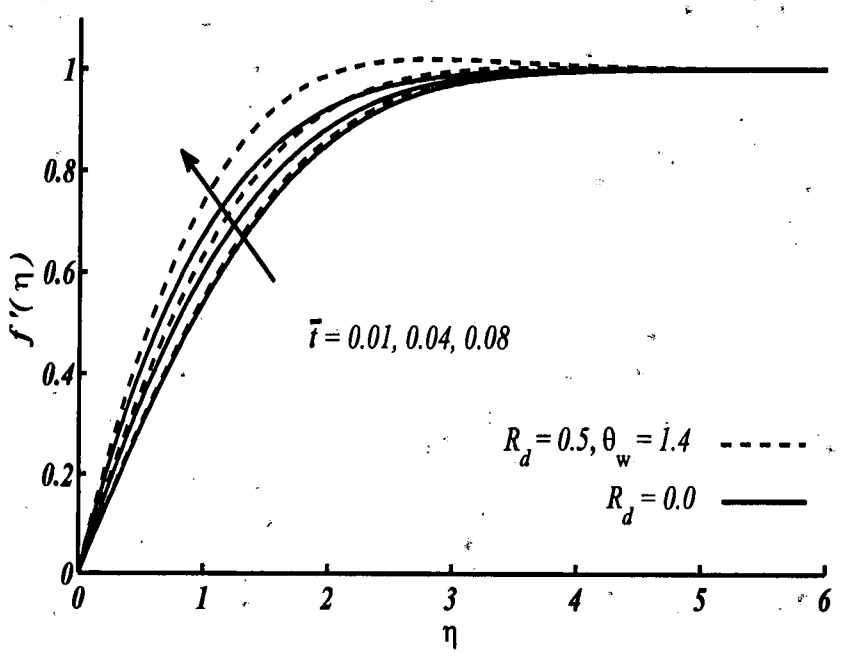

Figure 3.3(a, b): Velocity profiles for assisting flow for different time steps $\bar{t}$ at $(\bar{x} = 0)$ when $\Pr = 1$ and $\lambda = 2$ in (a) blunt orientation $\omega^* = 0.5$ (b) slender orientation $\omega^* = 4$.

(a)

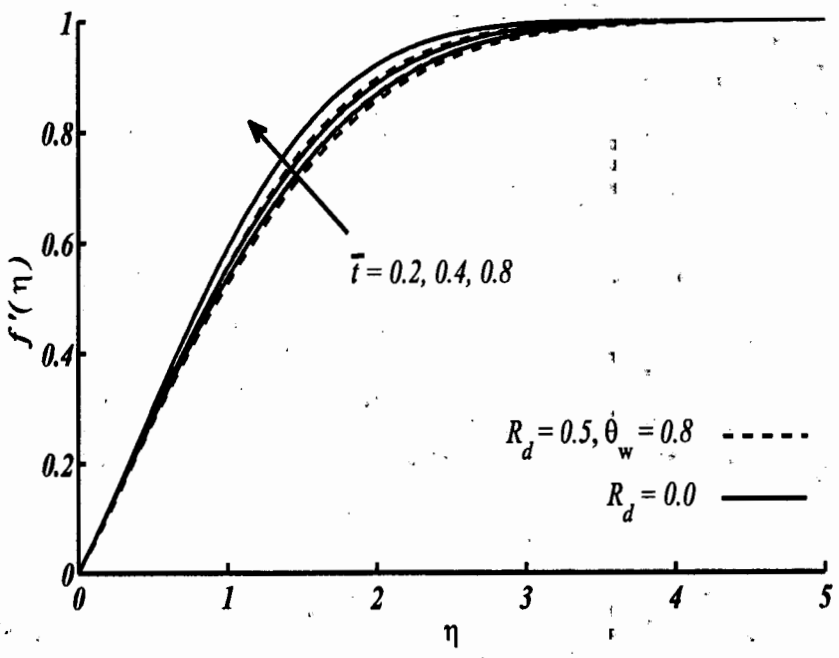

(b)

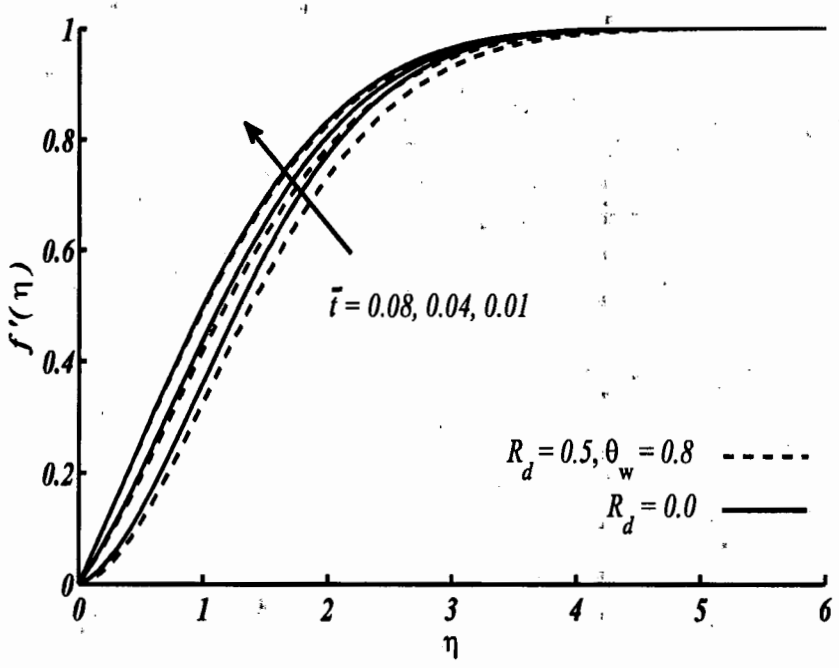

Figure 3.4(a, b): Velocity profiles for opposing flow for different time steps $\bar{t}$ at $(\bar{x} = 0)$ when $\mathrm{Pr} = 1$ and $\lambda = -3$ in (a) blunt orientation $\omega^* = 0.5$ (b) slender orientation $\omega^* = 4$.

(a)

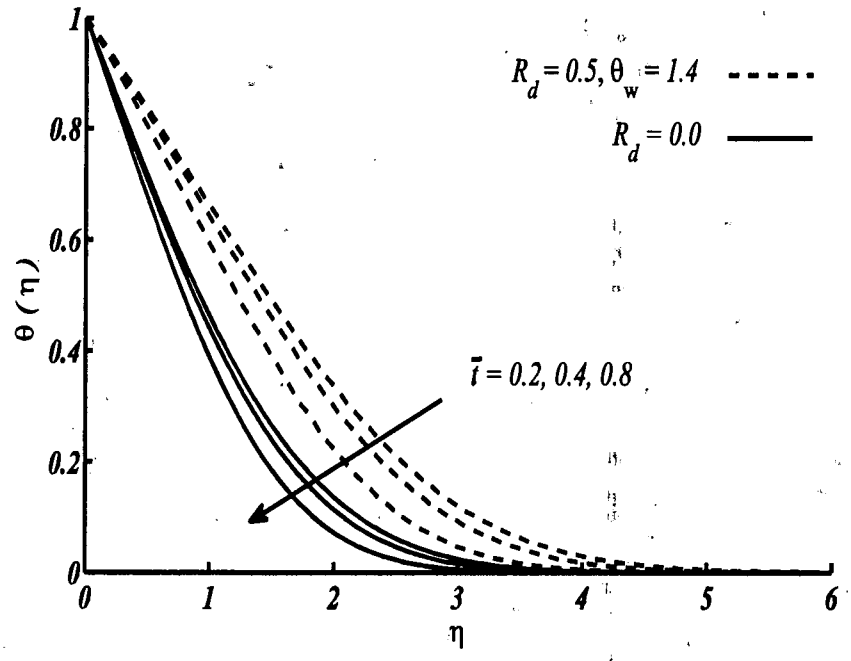

(b)

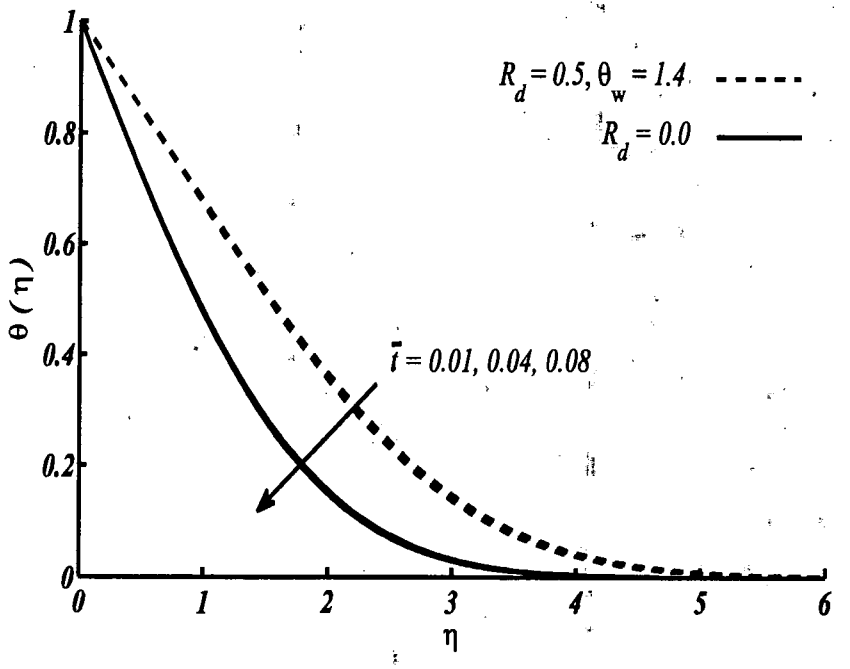

Figure 3.5(a, b): Temperature profiles for assisting flow for different time steps $\bar{t}$ at $(\bar{x} = 0)$ when $\Pr = 1$ and $\lambda = 2$ in (a) blunt orientation $\omega^* = 0.5$ (b) slender orientation $\omega^* = 4$.

(a)

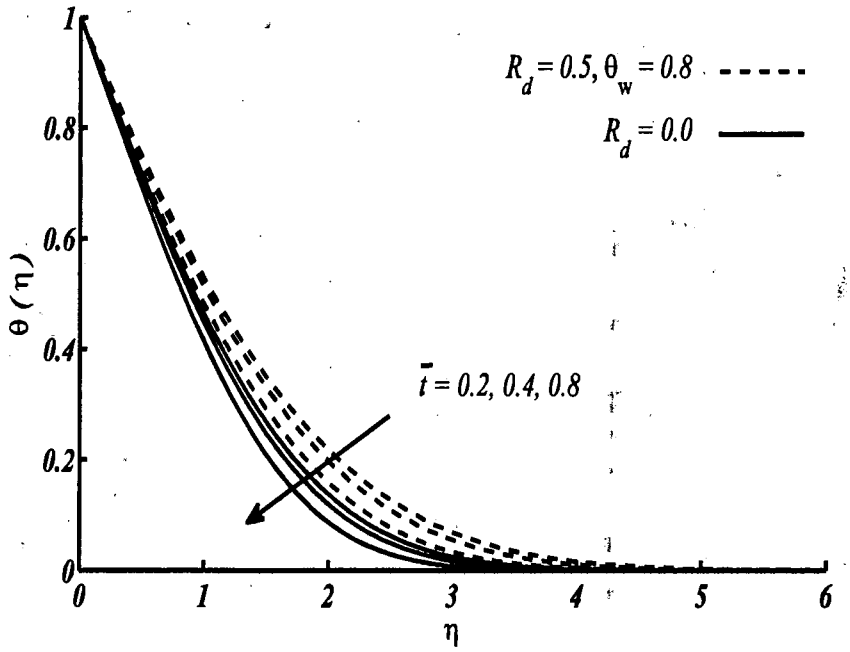

(b)

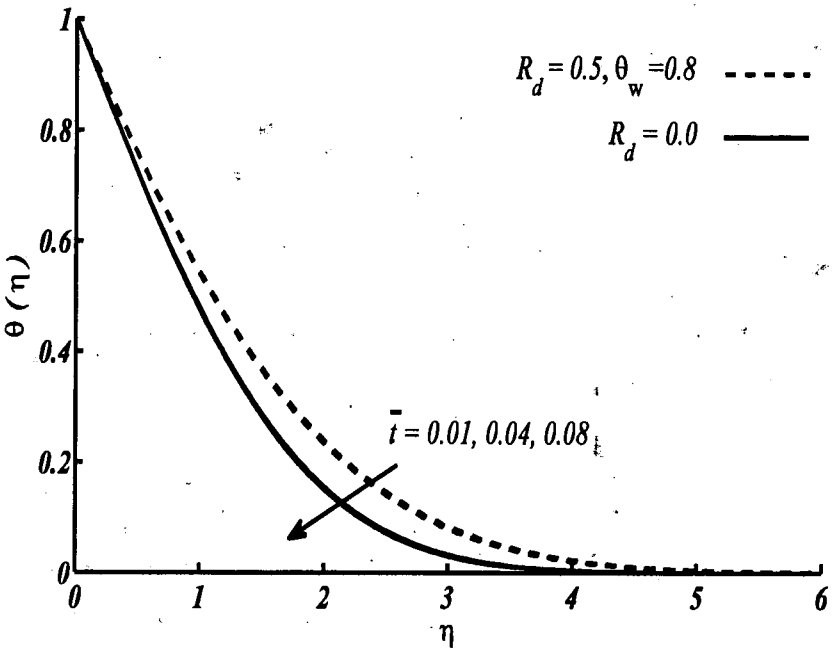

Figure 3.6(a, b): Temperature profiles for opposing flow for different time steps $\bar{t}$ at $(\bar{x} = 0)$ when $\Pr = 1$ and $\lambda = -3$ in (a) blunt orientation $\omega^* = 0.5$ (b) slender orientation $\omega^* = 4$.

(a)

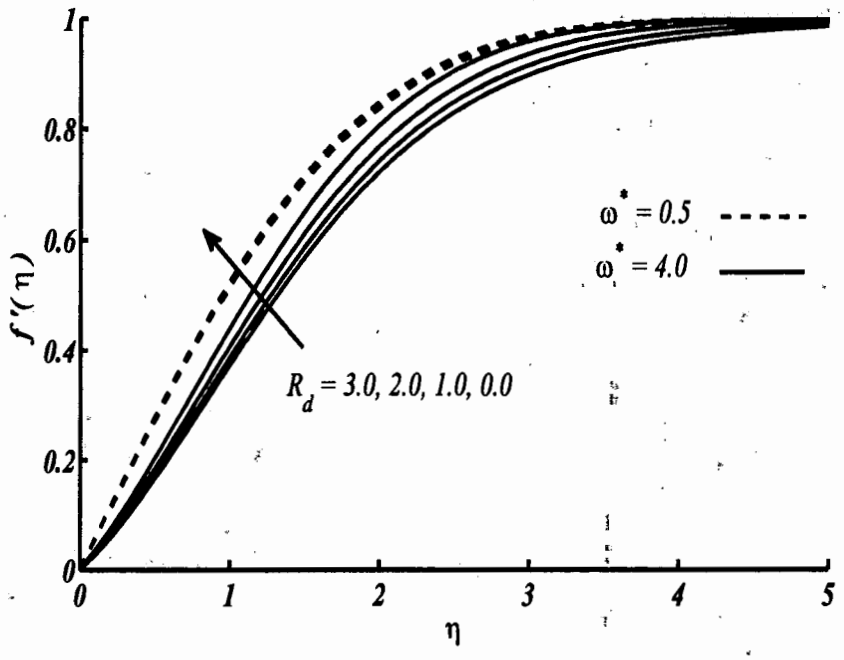

(b)

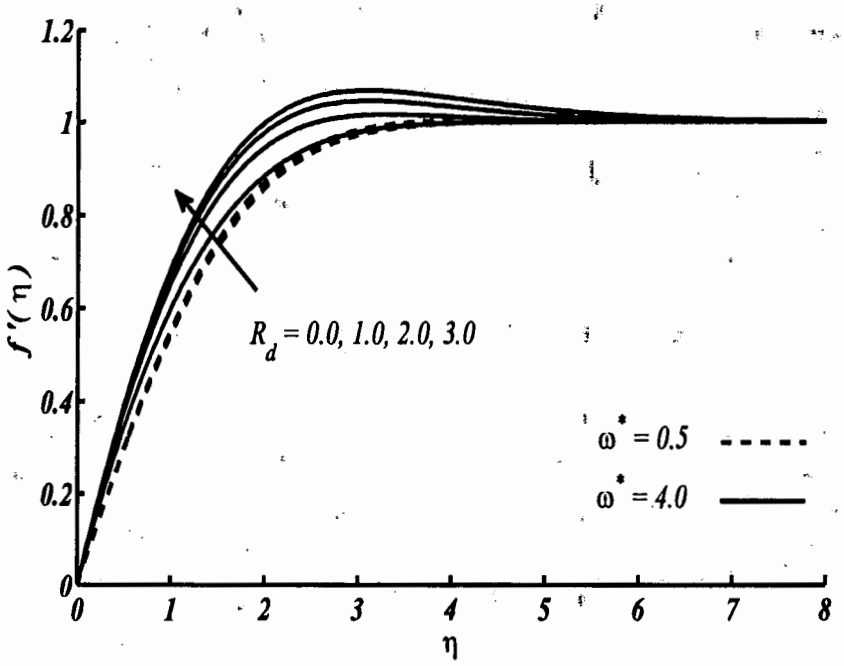

Figure 3.7(a, b): Velocity profiles for distinct values of R_d at $(\bar{x} = 0)$ when $\mathrm{Pr} = 1$ and $\bar{t} = 0.04$ in (a) opposing flow $\lambda = -3, \theta_w = 0.8$ (b) assisting flow $\lambda = 2, \theta_w = 1.4$.

(a)

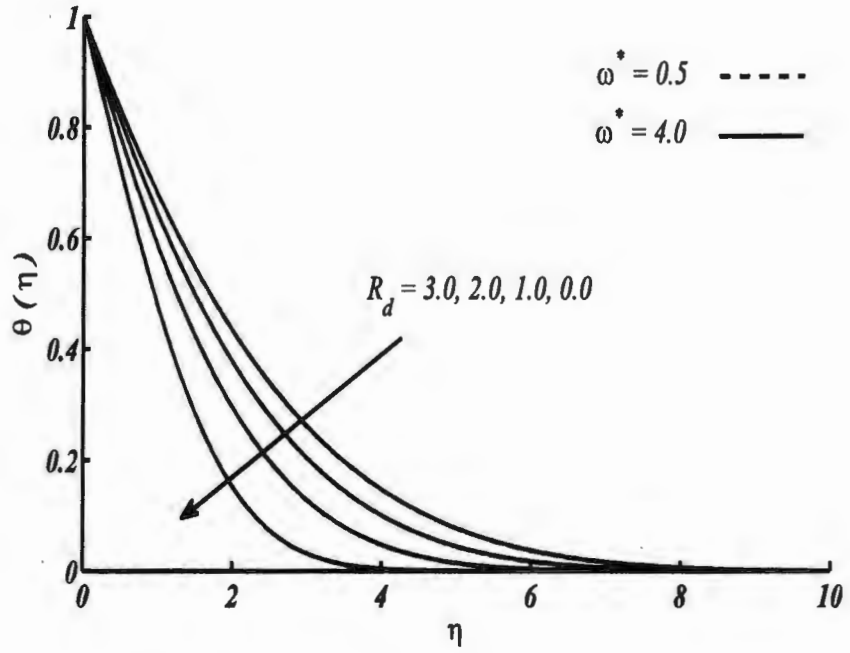

(b)

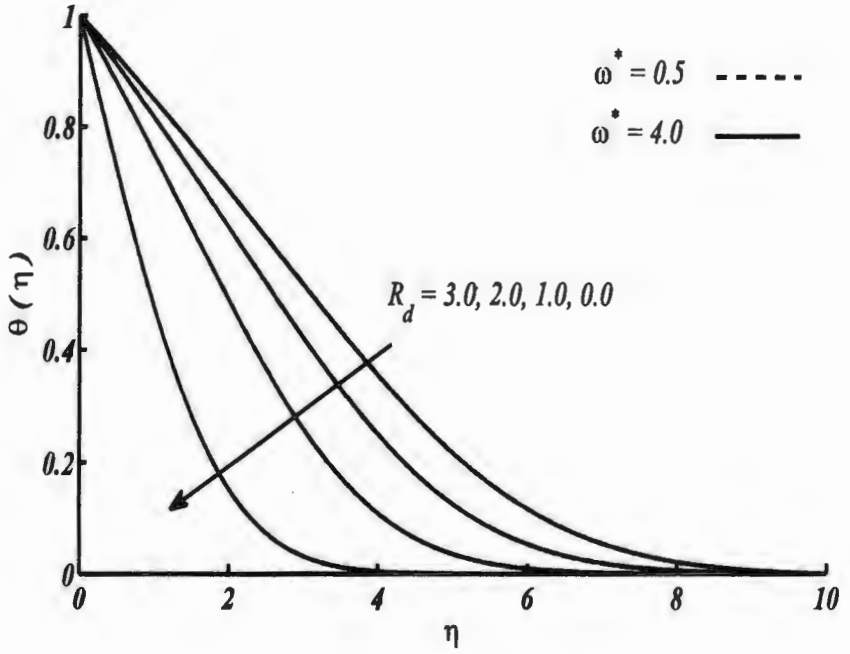

Figure 3.8(a, b): Temperature profiles for distinct values of R_d at $(\overline{x}=0)$ when $\overline{t}=0.04$ and $\mathrm{Pr}=1$ in (a) opposing flow $\lambda=-3, \theta_w=0.8$ (b) assisting flow $\lambda=2, \theta_w=1.4$.

(a)

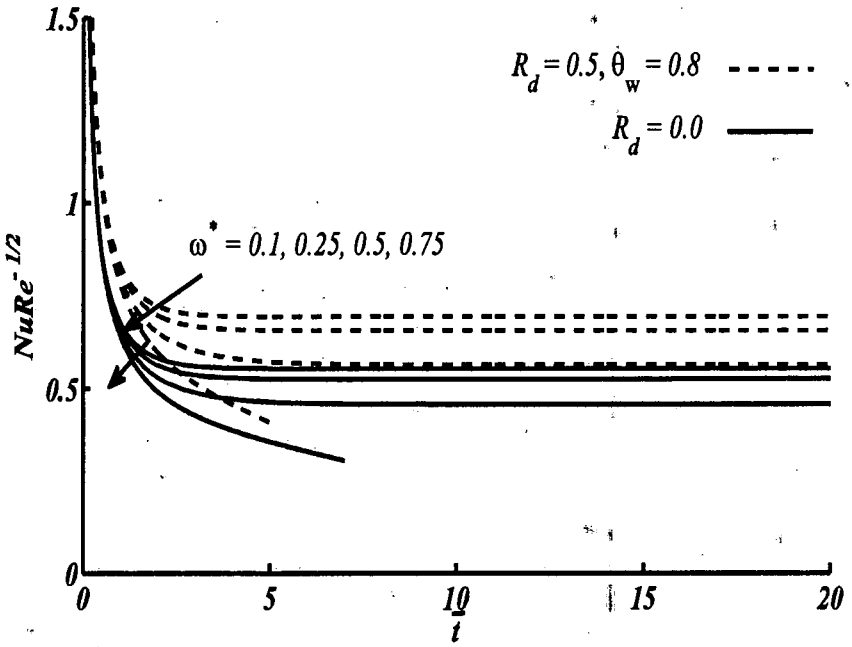

(b)

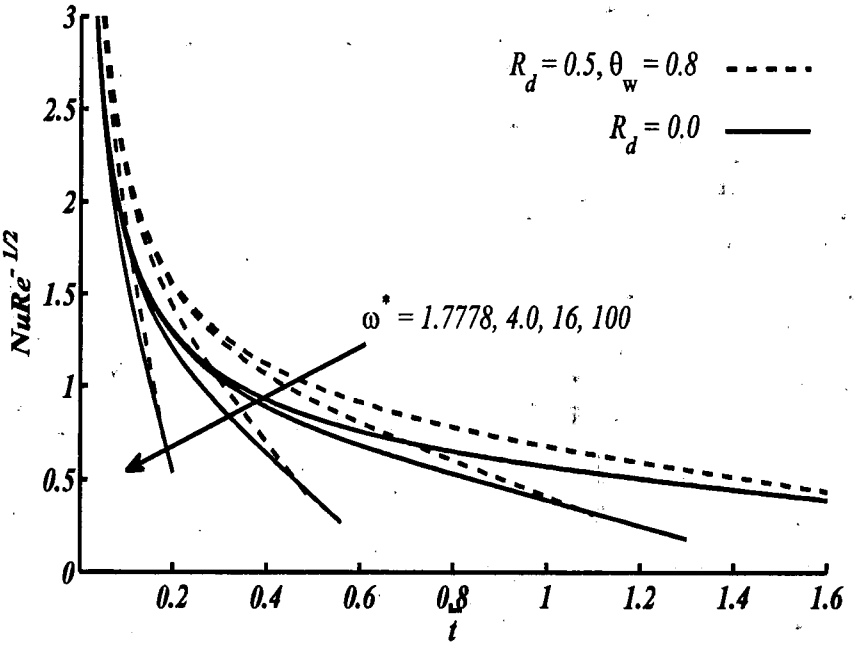

Figure 3.9(a, b): Variation in Nusselt number against $\bar{t}$ at $(\bar{x} = 0)$ for distinct values of ω^* when $\Pr = 1$ and $\lambda = -3$ in (a) blunt orientation (b) slender orientation.

(a)

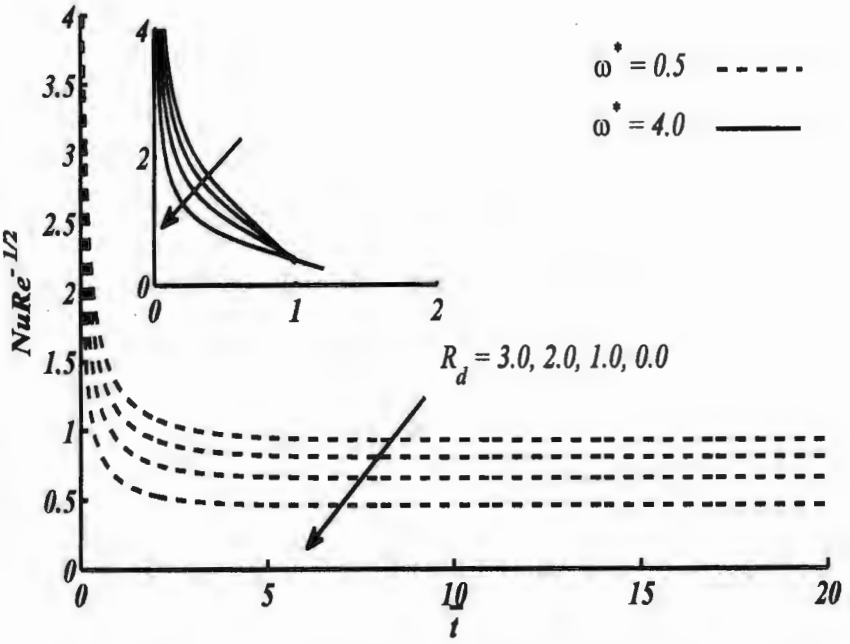

(b)

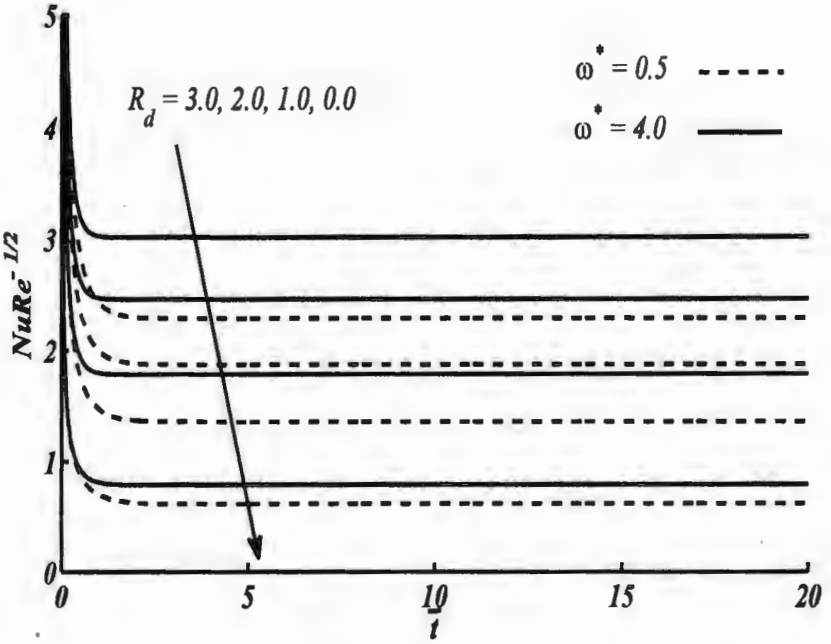

Figure 3.10(a, b): Variation in Nusselt number against $\bar{t}$ at $(\bar{x} = 0)$ for distinct values of R_d when $\Pr = 1$ in (a) opposing flow $\lambda = -3, \theta_w = 0.8$ (b) assisting flow $\lambda = 2, \theta_w = 1.4$.

3.4 Conclusions

In this chapter, the study of the effect of thermal radiation on unsteady mixed convection flow near a forward stagnation point over an elliptic cylinder is investigated. The analysis is made for both orientations of the elliptic cylinder and focused only on flow near the region of forward stagnation point. Separation times in both orientations in the presence of thermal radiation are calculated by using implicit scheme of finite difference method and shown in Tabular and graphical forms. It is observed that boundary layer separation occurs early due to thermal radiation and the value of $C_f \, \mathrm{Re}^{1/2}$ become zero at $(\bar{x} = 0)$. In opposing flow, the values of velocity in blunt orientation become higher than the values in slender orientation due to thermal radiation. However, the values of temperature profile in blunt orientation become smaller than the values in slender orientation. An opposite behavior is observed in assisting flow case. In opposing flow, for both orientations, heat transfer rate increases due to thermal radiation. The heat transfer rate in blunt orientation become higher than that of slender orientation in the presence of thermal radiation in opposing flow case but an opposite behavior is observed in assisting flow case.

Chapter 4

Heat transfer in MHD mixed convection stagnation point flow of a nanofluid over a vertical plate with viscous dissipation

In this chapter, magnetohydrodynamic effects on the mixed convection stagnation point flow of electrically conducting nanofluid over a vertical plate in the presence of viscous dissipation is presented. The nanofluid consists of *Cu* (copper) and Al_2O_3 (alumina) nano-particles with water as base fluid. Tiwari and Das model [60] is used to develop the mathematical formulation of nanofluid flow in terms of governing equations. The developed governing equations are then reduced to the system of ordinary differential equations by using similarity transformations. The solution of the resulting system of ordinary differential equations is obtained numerically by using Keller Box method. The developed numerical code is validated through a comparison of computed results with previous studies is shown in tabular form. The effects of pertinent parameters like magnetic parameter M, Eckert number Ec, and volume fraction parameter ϕ on velocity, temperature, skin friction coefficient and local Nusselt number with fixed value of Prandtl number Pr = 6.2 are shown graphically and discussed in detail. These results show that by increasing M and Ec, the skin friction coefficient increases for both nanoparticles in both assisting and opposing flow cases. However, the heat transfer rate increases in opposing flow case and decreases in assisting flow case due to these parameters. Similarly, by increasing the volume fraction parameter ϕ of the nanoparticles, the skin friction coefficient increases in both assisting and opposing flow cases, and the value of skin friction coefficient become maximum for *Cu* nanoparticle as that of Al_2O_3 nanoparticle. The same behavior is observed for local Nusselt number in opposing flow as in skin friction coefficient, but in assisting flow the local Nusselt number decreases with the increase of ϕ in the presence of magnetic and viscous dissipation effects and the values of local Nusselt number in *Cu* nanoparticle become smaller than that of Al_2O_3 nanoparticle.

4.1 Mathematical formulation

Consider a two-dimensional steady-stable laminar mixed convection boundary layer flow of

an incompressible electrically conducting nanofluid in the vicinity of stagnation point over a vertical flat plate. The geometry of the flow problem is shown in Fig. 4.1 in which the x–axis and y–axis are taken along and normal to the plate. The velocity of potential flow outside the boundary layer and wall temperature are considered as a linear functions of x in the form of

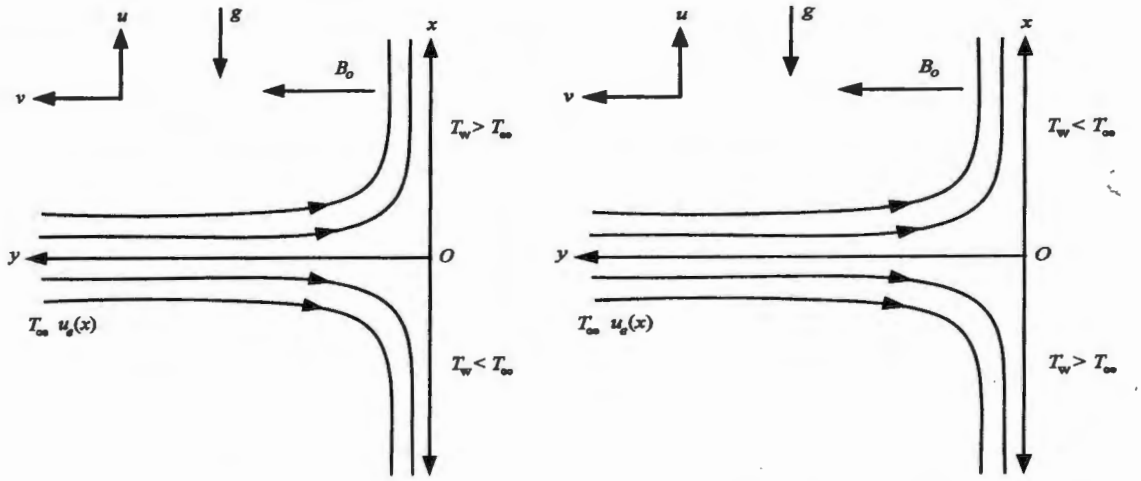

(a) (b)

Figure 4.1: The physical model of the flow towards a vertical plate near stagnation point region for (a) assisting flow (b) opposing flow.

$u_e(x) = ax$ and $T_w = T_\infty + bx$, respectively, where a and b are constants in which $b > 0$ corresponds to assisting flow case ($T_w > T_\infty$) and $b < 0$ corresponds to opposing flow case ($T_w < T_\infty$). The case for $b > 0$ occurs when the upper half of the vertical plate is heated and lower half is cooled. On the other hand, the case of $b < 0$ occurs when upper half of the plate is taken as cooled and lower half is heated and x is the distance from the stagnation point on the vertical

Table 4.1: Thermophysical properties of base fluid and nanoparticles.

Properties	*Cu*	Al_2O_3	Fluid
c_p (J/kgK)	385	765	4179
k(W/mK)	400	40	0.613
ρ(kg/m^3)	8933	3970	997.1
$\beta\times10^{-5}$(1/K)	1.67	0.85	21

plate. It is further assumed that the nanoparticles and base fluid are in thermal equilibrium and the thermophysical properties of base fluid and nanoparticles are given in Table 4.1. A uniform magnetic field is applied perpendicular to the flow in the direction normal to the surface under

the assumption that induced magnetic field is negligible as compared to applied magnetic field. All the physical properties of the fluid are assumed to be independent of temperature except the density, which varies linearly with temperature in the body force according to the Boussinesq's hypothesis. Tiwari and Das model [60] has been chosen to model the governing equations for the present flow problem and using the boundary layer approximations, the simplified form of the governing equations with MHD and viscous dissipation effects are written as

$$\frac{\partial u}{\partial x}+\frac{\partial v}{\partial y}=0, \tag{4.1}$$

$$u\frac{\partial u}{\partial x}+v\frac{\partial u}{\partial y}=u_e\frac{du_e}{dx}+\frac{\mu_{nf}}{\rho_{nf}}\left(\frac{\partial^2 u}{\partial y^2}\right)+\frac{\phi\rho_p\beta_p+(1-\phi)\rho_f\beta_f}{\rho_{nf}}g(T-T_\infty)+\frac{\sigma_f B_0^{\,2}}{\rho_{nf}}(u_e-u), \tag{4.2}$$

$$u\frac{\partial T}{\partial x}+v\frac{\partial T}{\partial y}=\alpha_{nf}\frac{\partial^2 T}{\partial y^2}+\frac{\mu_{nf}}{(\rho c_p)_{nf}}\left(\frac{\partial u}{\partial y}\right)^2, \tag{4.3}$$

where u and v are the velocity components in x and y directions, respectively, μ_{nf} is the dynamic viscosity of the nanofluid, which was introduced by Brinkman [140], β_p and β_f are the thermal expansion coefficients of the nanoparticles and base fluid, respectively, g is the acceleration due to gravity, σ_f is the electric conductivity of base fluid, B_0 is the strength of uniform magnetic field and T is the temperature of nanofluid. The relations of $\mu_{nf}, \rho_{nf}, \alpha_{nf}$ and $(\rho c_p)_{nf}$ are described as follows:

$$\begin{gathered}\mu_{nf}=\frac{\mu_f}{(1-\phi)^{2.5}},(\rho c_p)_{nf}=(1-\phi)(\rho c_p)_f+\phi(\rho c_p)_p,\rho_{nf}=(1-\phi)\rho_f+\phi\rho_p,\\ \alpha_{nf}=\frac{k_{nf}}{(\rho c_p)_{nf}},\ \frac{k_{nf}}{k_f}=\frac{(k_p+2k_f)-2\phi(k_f-k_p)}{(k_p+2k_f)+\phi(k_f-k_p)}.\end{gathered} \tag{4.4}$$

where μ_f is the dynamic viscosity of the base fluid, ϕ is the solid volume fraction of nanoparticles, $\rho_f,(\rho c_p)_f,k_f$ and $\rho_p,(\rho c_p)_p,k_p$ are the densities, heat capacities and thermal conductivities of the base fluid and nanoparticles, respectively and k_{nf} is the thermal conductivity of the nanofluid, which was described by Maxwell-Garnett model [141]. The boundary conditions of the problems are

$$\begin{gathered}u(x,0)=0,\ v(x,0)=0,\ T(x,0)=T_w(x)=T_\infty+bx,\\ u(x,y)\to u_e(x)=ax,\ T(x,y)\to T_\infty\quad \text{as } y\to\infty.\end{gathered} \tag{4.5}$$

After reducing the equations in term of stream function ψ by using the relations $u=\frac{\partial\psi}{\partial y}$ and $v=-\frac{\partial\psi}{\partial x}$, the following similarity transformation

$$\eta=\left(\frac{a}{\nu_f}\right)^{1/2} y,\psi(x,y)=x\sqrt{a\nu_f}\,f(\eta),\theta(\eta)=\frac{T-T_\infty}{T_w-T_\infty}, \tag{4.6}$$

is used in Eqs. (4.2) and (4.3) to get

$$f'''+h_1\left(ff''-f'^2+1+\frac{h_5}{h_2}\lambda\theta+\frac{M}{h_2}(1-f')\right)=0, \tag{4.7}$$

$$\theta''+\frac{k_f}{k_{nf}}\Pr h_3\left(f\theta'-f'\theta+\frac{1}{h_4}Ecf''^2\right)=0, \tag{4.8}$$

where prime denotes the differentiation with respect to η, ν_f is the kinematic viscosity of the base fluid, Gr_x is a local Grashof number, Re_x is a local Reynolds number, M is the magnetic parameter and Ec is the Eckert number. Where h_1, h_2, h_3, h_4, h_5 and other physical parameter are given by

$$h_1=(1-\phi)^{2.5}\left[1-\phi+\phi\left(\frac{\rho_p}{\rho_f}\right)\right], h_2=\left[1-\phi+\phi\left(\frac{\rho_p}{\rho_f}\right)\right], h_3=\left[1-\phi+\phi\frac{(\rho c_p)_p}{(\rho c_p)_f}\right],$$

$$h_4=(1-\phi)^{2.5}\left[1-\phi+\phi\frac{(\rho c_p)_p}{(\rho c_p)_f}\right], \lambda=\frac{Gr_x}{\mathrm{Re}_x^2}, Gr_x=\frac{g\beta_f(T_w-T_\infty)x^3}{\nu_f^2},$$

$$h_5=\left[1-\phi+\phi\left(\frac{\rho_p\beta_p}{\rho_f\beta_f}\right)\right], \mathrm{Re}_x=\frac{xu_e}{\nu_f}, M=\frac{\sigma_f B_0^2}{\rho_f a}, Ec=\frac{u_e^2}{(c_p)_f(T_w-T_\infty)}, \Pr=\frac{\nu_f}{\alpha_f}.$$

The values of λ and Ec are considered positive or negative according to assisting and opposing flows, respectively. The boundary conditions Eq. (4.5) take the new form as

$$\begin{aligned} &f(0)=0, f'(0)=0, \theta(0)=1, \\ &f'(\infty)=1, \theta(\infty)=0. \end{aligned} \tag{4.9}$$

The relation of skin friction coefficient and local Nusselt number and written as

$$C_f=\frac{\tau_w}{\rho_f u_e^2/2}, \quad Nu_x=\frac{xq_w}{k_f(T_w-T_\infty)}, \tag{4.10}$$

where τ_w and q_w are defined as

$$\tau_w=\mu_{nf}\left(\frac{\partial u}{\partial y}\right)_{y=0}, \quad q_w=-k_{nf}\left(\frac{\partial T}{\partial y}\right)_{y=0}. \tag{4.11}$$

After inserting Eq. (4.11) into Eq. (4.10), the skin friction coefficient and local Nusselt number take the form

$$C_f \operatorname{Re}_x^{1/2} = \frac{2}{(1-\phi)^{2.5}} f''(0), Nu_x \operatorname{Re}_x^{-1/2} = -\frac{k_{nf}}{k_f}\theta'(0). \tag{4.12}$$

4.2 Keller Box method

To obtain the numerical solution of the system of nonlinear boundary value problem (4.7-4.9) an implicit finite difference method is used known as Keller Box method, which has been used for the solution of the system of partial differential equations in previous chapter. The details of the method for the system of nonlinear ordinary differential Eqs. (4.7, 4.8) subject to boundary condition Eq. (4.9) are explained as follows:

Initially these higher order system of ordinary differential equations are transformed into system of first order ordinary differential equations by introducing the new variables using U, V, P and Q defined as

$$f' = U, U' = V, \theta = P \text{ and } \theta' = Q. \tag{4.13}$$

Eqs. (4.7), (4.8) and boundary conditions Eq. (4.9) take new form as

$$V' + h_1\left(1 - U^2 + fV + \frac{h_5}{h_2}\lambda P + \frac{M}{h_2}(1-U)\right) = 0, \tag{4.14}$$

$$Q' + \Pr\frac{k_f}{k_{nf}}h_3\left(fQ - UP + \frac{1}{h_4}EcV^2\right) = 0, \tag{4.15}$$

$$f(0) = U(0) = 0, P(0) = 1, U(\infty) = 1, P(\infty) = 0. \tag{4.16}$$

A net on η is defined as

$$\eta_0 = 0, \eta_j = \eta_{j-1} + \Delta\eta, \eta_J = \eta_\infty,\ j = 1, 2, ..., J-1 \tag{4.17}$$

where j is positive integer and $\Delta\eta$ is the width of meshing variables on η. The approximate quantities of functions f, U, V, P and Q at the net point η_j are known as net functions whose derivatives in η - direction are replaced by the central difference formulae and functions itself are replaced by average centered at the midpoint $\eta_{j-1/2}$ defined as

$$f'_{j-1/2} = \frac{1}{\Delta\eta}(f_j - f_{j-1}), \text{and } f_{j-1/2} = \frac{1}{2}(f_j + f_{j-1}).$$

After discretization, the system of first order nonlinear ordinary differential Eqs. (4.13-4.15) are converted to difference equations in terms of nonlinear algebraic equations written as

$$\frac{V_j - V_{j-1}}{\Delta\eta} + h_1\left(\begin{array}{c}\left(\frac{f_j + f_{j-1}}{2}\right)\left(\frac{V_j + V_{j-1}}{2}\right) - \left(\frac{U_j + U_{j-1}}{2}\right)^2 \\ + \frac{h_5}{h_2}\frac{\lambda}{2}\left(P_j + P_{j-1}\right) - \frac{M}{2h_2}\left(U_j + U_{j-1}\right)\end{array}\right) = -h_1\left(1 + \frac{M}{h_2}\right), \tag{4.18}$$

$$\frac{Q_j - Q_{j-1}}{\Delta\eta} + \Pr\frac{k_f}{k_{nf}}h_3\left(\begin{array}{c}\left(\frac{f_j + f_{j-1}}{2}\right)\left(\frac{Q_j + Q_{j-1}}{2}\right) - \left(\frac{U_j + U_{j-1}}{2}\right)\left(\frac{P_j + P_{j-1}}{2}\right) \\ + \frac{Ec}{h_4}\left(\frac{V_j + V_{j-1}}{2}\right)^2\end{array}\right) = 0. \tag{4.19}$$

Eq. (4.13) becomes

$$f_j - f_{j-1} = \frac{\Delta\eta}{2}(U_j + U_{j-1}), \tag{4.20}$$

$$U_j - U_{j-1} = \frac{\Delta\eta}{2}(V_j + V_{j-1}), \tag{4.21}$$

$$P_j - P_{j-1} = \frac{\Delta\eta}{2}(Q_j + Q_{j-1}). \tag{4.22}$$

The above nonlinear algebraic Eqs. (4.18) and (4.19) are linearized using Newton method by introducing $(i+1)^{th}$ iterates as

$$f_j^{(i+1)} = f_j^{(i)} + \delta f_j^{(i)}, \tag{4.23}$$

similarly it is same for all other variables in which $f_j^{(i)}$ is known for $0 \le j \le J$ as an initial guess and $\delta f_j^{(i)}$ is unknown. After using the Newton linearization process and neglecting the terms containing square and higher order of $\delta f_j^{(i)}$, $\delta U_j^{(i)}$, $\delta V_j^{(i)}$, $\delta P_j^{(i)}$ and $\delta Q_j^{(i)}$, the system of linear algebraic equations is obtained as follows:

$$\delta f_j - \delta f_{j-1} - \frac{\Delta\eta}{2}(\delta U_j + \delta U_{j-1}) = (r_1)_j,$$

$$(s_1)_j\delta f_j + (s_2)_j\delta f_{j-1} + (s_3)_j\delta U_j + (s_4)_j\delta U_{j-1} + (s_5)_j\delta V_j + (s_6)_j\delta V_{j-1} + (s_7)_j\delta T_j + (s_8)_j\delta T_{j-1} = (r_2)_j,$$

$$(s_9)_j\delta T_j + (s_{10})_j\delta T_{j-1} + (s_{11})_j\delta Q_j + (s_{12})_j\delta Q_{j-1} = (r_3)_j,$$

$$\delta U_j - \delta U_{j-1} - \frac{\Delta\eta}{2}(\delta V_j + \delta V_{j-1}) = (r_4)_j,$$

$$\delta P_j - \delta P_{j-1} - \frac{\Delta\eta}{2}(\delta Q_j + \delta Q_{j-1}) = (r_5)_j.$$

The boundary conditions Eq. (4.16) take the form as

$$\delta f_0 = \delta U_0 = 0, \delta P_0 = 0, \delta U_J = 0, \delta P_J = 0.$$

Finally, the above system of linear algebraic equations with boundary conditions are written in matrix vector form. The coefficients in momentum and energy equations of unknown functions $\delta f_j, \delta U_j, \delta V_j, \delta P_j$ and δQ_j and non-homogeneous parts are given as

Coefficient of momentum equation:

$$\delta f_j = (s_1)_j = \frac{h_1}{4}(V_j + V_{j-1}), \delta f_{j-1} = (s_2)_j = (s_1)_j,$$

$$\delta U_j = (s_3)_j = -h_1\left(\frac{(U_j + U_{j-1})}{2} + \frac{M}{2h_2}\right), \delta U_{j-1} = (s_4)_j = (s_3)_j,$$

$$\delta V_j = (s_5)_j = \frac{1}{\Delta\eta} + \frac{h_1}{4}(f_j + f_{j-1}),$$

$$\delta V_{j-1} = (s_6)_j = -\frac{1}{\Delta\eta} + \frac{h_1}{4}(f_j + f_{j-1}),$$

$$\delta P_j = (s_7)_j = \frac{h_5}{h_2}\frac{h_1\lambda}{2}, \delta P_{j-1} = (s_8)_j = (s_7)_j,$$

Coefficient of energy equation:

$$\delta P_j = (s_9)_j = \frac{-k_f}{4k_{nf}}\Pr h_3(U_j + U_{j-1}), \delta P_{j-1} = (s_{10})_j = (s_9)_j,$$

$$\delta Q_j = (s_{11})_j = \frac{1}{\Delta\eta} + \Pr\frac{k_f h_3}{k_{nf}}\frac{(f_j + f_{j-1})}{4},$$

$$\delta Q_{j-1} = (s_{12})_j = \frac{-1}{\Delta\eta} + \Pr\frac{k_f h_3}{k_{nf}}\frac{(f_j + f_{j-1})}{4}.$$

Non-homogenous terms:

$$(r_1)_j = (f_{j-1} - f_j) + \frac{\Delta\eta}{2}(U_j + U_{j-1}),$$

$$(r_2)_j = -\frac{(V_j - V_{j-1})}{\Delta\eta} - h_1\left(\begin{array}{c}\left(\frac{f_j + f_{j-1}}{2}\right)\left(\frac{V_j + V_{j-1}}{2}\right) - \left(\frac{U_j + U_{j-1}}{2}\right)^2 + \frac{h_5}{h_2}\frac{\lambda}{2}\left(P_j + P_{j-1}\right) - \\ \frac{M}{2h_2}\left(U_j + U_{j-1}\right) + 1 + \frac{M}{h_2}\end{array}\right),$$

$$(r_3)_j = -\frac{(Q_j - Q_{j-1})}{\Delta\eta} - \frac{\Pr k_f h_3}{k_{nf}}\left\{\left(\frac{f_j + f_{j-1}}{2}\right)\left(\frac{Q_j + Q_{j-1}}{2}\right) - \left(\frac{U_j + U_{j-1}}{2}\right)\left(\frac{P_j + P_{j-1}}{2}\right) + \frac{Ec}{h_4}\left(\frac{V_j + V_{j-1}}{2}\right)^2\right\},$$

$$(r_4)_j = (U_{j-1} - U_j) + \frac{\Delta\eta}{2}(V_j + V_{j-1}),$$

$$(r_5)_j = (P_{j-1} - P_j) + \frac{\Delta\eta}{2}(Q_j + Q_{j-1}).$$

For solving the above system of linear algebraic equations the same procedure is used as discussed in chapter 3.

4.3 Results and discussion

Numerical solution of nonlinear boundary value problem as a system of ordinary differential equations is obtained for important values of involving parameters M, Ec, Pr, λ and ϕ in the presence of nanoparticles for both assisting and opposing flow cases by using Keller Box method. The results are shown through graphs in terms of velocity, temperature profiles, skin friction coefficient $C_f \, \mathrm{Re}_x^{1/2}$ and local Nusselt number $Nu_x \, \mathrm{Re}_x^{-1/2}$. Two types of nanoparticles, namely, Cu (copper) and Al_2O_3 (alumina) are considered with water as a base fluid. The value of Prandtl number is taken Pr = 6.2 (water) as considered by Oztop and Abu Nada [62] and Tamim et al. [77]. To ensure the accuracy and validity of the numerical code, a comparison of the computed values of $C_f \, \mathrm{Re}_x^{1/2}$ and $Nu_x \, \mathrm{Re}_x^{-1/2}$ for limiting case is made with the work of Tamim et al. [77] and presented in Table 4.2 for various values of volume fraction parameter ϕ and mixed convection parameter λ. It is found that the computed results are in good agreement with Tamim et al. [77] and hence the code is valid and computed results are accurate. Table 4.3 shows the values of $Nu_x \, \mathrm{Re}_x^{-1/2}$ for different values of ϕ when mixed convection parameter λ is considered equal to 1 (assisting flow) and -1 (opposing flow). It is observed that heat transfer rate for assisting flow case decreases for both nanoparticles and the quite opposite behavior is observed for opposing flow. Figs. 4.2 to 4.5 show the velocity and temperature profiles for both assisting and opposing flows in which solid line represents the results of Tamim et al. [77] and dashed line represents the present work in which magnetic and viscous dissipation effects are taken into account. Figs. 4.2 and 4.3 show the velocity and temperature profiles against various values of volume fraction parameter ϕ for Cu-water nanofluid. It is seen that velocity and temperature profiles increase in the boundary layer region with the increase of volume fraction parameter ϕ from 0 to 0.2 for both assisting and opposing flow cases. This phenomena physically shows that when the amount of Cu nanoparticle is increased, the thermal conductivity increases and consequently thermal boundary layer thickness increases. It is also seen that the values of velocity become higher in the presence of magnetic field and viscous dissipation for both assisting and opposing flow cases. In Figs. 4.3(a) and 4.3(b), the values of temperature increase in assisting flow and decrease in opposing flow because of magnetic and viscous dissipation effects also the thermal boundary layer thickness increases in assisting flow and decreases in opposing flow. Figs. 4.4 and 4.5 display the effects of particular nanoparticles on velocity and temperature profiles respectively. It is seen through Figs. 4.4(a) and 4.4(b) that the velocity in Cu-water nanofluid become higher as compared to

Al_2O_3-water nanofluid both for assisting and opposing flow cases. The values of velocity in the presence of magnetic field and viscous dissipation for both types of nanofluids become higher than that in the absence of these effects. Fig. 4.5 shows that magnetic and viscous dissipation effects increase the temperature in both nanofluids for assisting flow case because these effects generate additional heat in the boundary layer region. However, the opposite behavior is observed in opposing flow case. Figs. 4.6 to 4.9 present the velocity and temperature profiles for different values of magnetic parameter and Eckert number in which solid and dashed lines represent the results for *Cu*-water and Al_2O_3-water nanofluids, respectively. In Fig. 4.6(a, b), it is seen that velocity increases with increasing the magnetic parameter M for both nanofluids. Physically this behavior occurs because in this case Lorentz force assists the flow and consequently velocity increases as M increases and hence flow rate increases. It is further seen that the values of velocity become higher for *Cu*-water nanofluid than that of Al_2O_3-water nanofluid in both assisting and opposing flow cases and opposite behavior is observed for momentum boundary layer thickness. Fig. 4.7(b) shows that temperature decreases with the increase of magnetic parameter M for both nanofluids, but in Fig. 4.7(a), temperature increases near the surface of the plate ($\eta = 0$), but for large values of η it decreases. Figs. 4.8 and 4.9 illustrate the velocity and temperature profiles against η for various values of Eckert number *Ec*. Figs. 4.8(a) and 4.8(b) depict that velocity increases and momentum boundary layer thickness decreases in both nanofluids for both assisting and opposing flows by increasing the absolute values of *Ec*. In Figs. 4.9(a) and 4.9(b), it is seen that temperature increases in assisting flow case but decreases in opposing flow case by increasing the absolute values of *Ec*. This is because the combined effects of viscous dissipation and magnetic field generate additional heat in the boundary layer region. Also the values of temperature for *Cu*-water nanofluid become smaller than that of Al_2O_3-water nanofluid. Figs. 4.10 and 4.11 show the effects of magnetic field and viscous dissipation on $C_f \, \mathrm{Re}_x^{1/2}$ and $Nu_x \, \mathrm{Re}_x^{-1/2}$ against volume fraction parameter ϕ for both types of nanofluids. The solid line represents the pervious study, which was investigated by Tamim et al. [77] and dashed line represents the present study. In Figs. 4.10(a) and 4.10(b), it is seen that the $C_f \, \mathrm{Re}_x^{1/2}$ increases for both nanofluids with the increase of volume fraction parameter ϕ for both assisting and opposing flow cases. It is further seen that the inclusion of magnetic and viscous dissipation effects enhance the values of $C_f \, \mathrm{Re}_x^{1/2}$ against ϕ in both nanofluids for both assisting and opposing flow cases. On the other hand, the effects of magnetic and viscous dissipation help to reduce the values of local Nusselt number against

ϕ in the assisting flow case and increase the values of $Nu_x \, \mathrm{Re}_x^{-1/2}$ in the opposing flow case as shown in Fig. 4.11(a, b). In assisting flow, it is noted that a lower heat transfer rate is obtained for *Cu*-water nanofluid than that of Al_2O_3-water nanofluid in the presence of magnetic and viscous dissipation effects. In other cases, the heat transfer rate for *Cu*-water nanofluid become higher than that of Al_2O_3-water nanofluid. This is because *Cu* has higher thermal conductivity as compared to Al_2O_3. Figs. 4.12 to 4.15 show the variations in $C_f \, \mathrm{Re}_x^{1/2}$ and $Nu_x \, \mathrm{Re}_x^{-1/2}$ against ϕ for both types of nanofluids at different values of magnetic parameter and Eckert number. Figs. 4.12(a) and 4.12(b) depict that $C_f \, \mathrm{Re}_x^{1/2}$ increases for both nanofluids in both assisting and opposing flow cases by increasing the magnetic parameter. It is also observed that the value of $C_f \, \mathrm{Re}_x^{1/2}$ for *Cu*-water nanofluid in both assisting and opposing flows become higher in magnitude than that of Al_2O_3-water nanofluid. In Fig. 4.13(a), it is seen that $Nu_x \, \mathrm{Re}_x^{-1/2}$ decreases by increasing the magnetic parameter and the values of $Nu_x \, \mathrm{Re}_x^{-1/2}$ become smaller in magnitude for *Cu*-water nanofluid than that of Al_2O_3-water nanofluid. In Fig. 4.13(b), quite opposite behavior is observed in case of opposing flow as compared to assisting flow. Fig. 4.14(a) and 4.14(b) show that $C_f \, \mathrm{Re}_x^{1/2}$ increases in both assisting and opposing flows for both nanofluids by increasing the absolute values of Eckert *Ec*. It is important to note that the value of $C_f \, \mathrm{Re}_x^{1/2}$ become higher in magnitude for *Cu*-water nanofluid than that of Al_2O_3-water nanofluid. Fig. 4.15(a) depicts that for nonzero Eckert number ($Ec \neq 0$), $Nu_x \, \mathrm{Re}_x^{-1/2}$ decreases by increasing the volume fraction parameter ϕ and for $Ec = 0$, it becomes an increasing function of ϕ. It is also observed that the values of $Nu_x \, \mathrm{Re}_x^{-1/2}$ become smaller in magnitude for *Cu*-water nanofluid than that of Al_2O_3-water nanofluid for $Ec \neq 0$. For opposing flow, as shown in Fig. 4.15(b), $Nu_x \, \mathrm{Re}_x^{-1/2}$ increases by increasing the absolute values of *Ec* and it values become higher in magnitude for *Cu*-water nanofluid than that of Al_2O_3-water nanofluid.

(a)

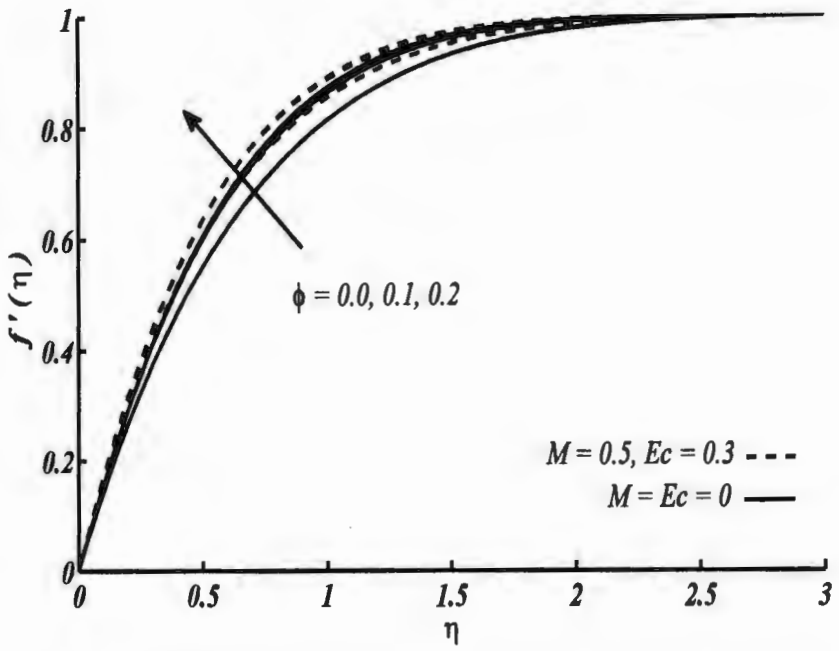

(b)

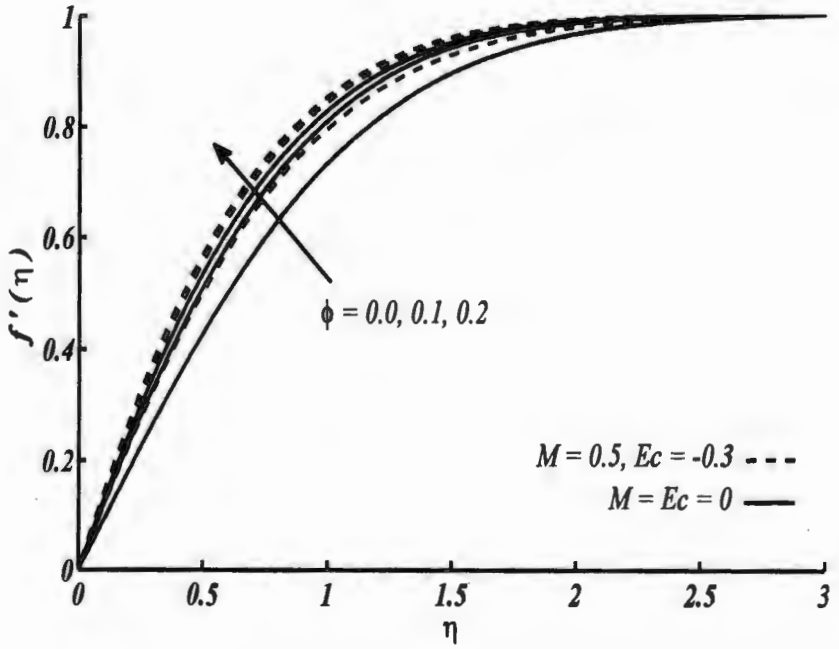

Figure 4.2(a, b): Velocity profile (*Cu*-water nanofluid) for distinct values of ϕ when Pr = 6.2 for (a) assisting flow $\lambda = 1$ (b) opposing flow $\lambda = -1$.

(a)

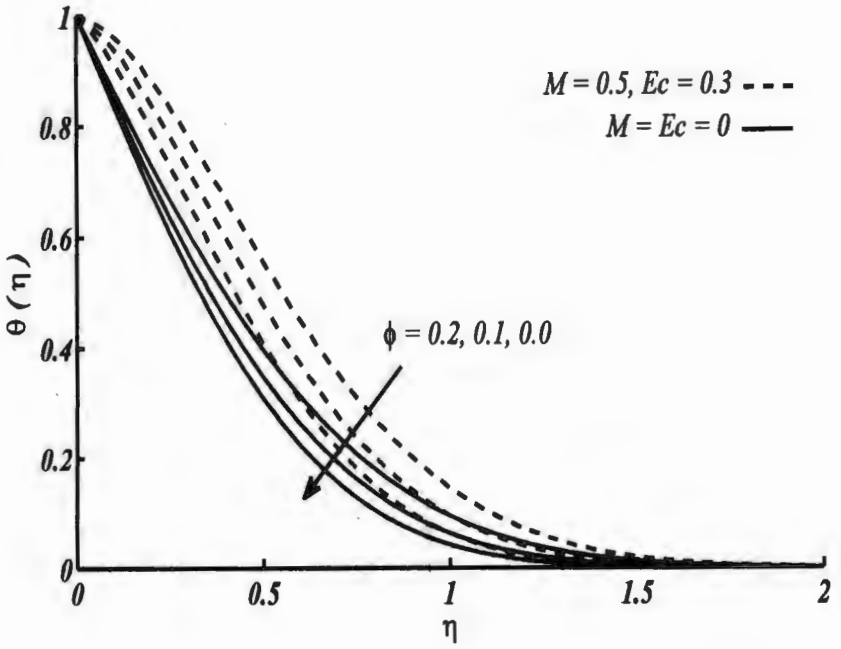

(b)

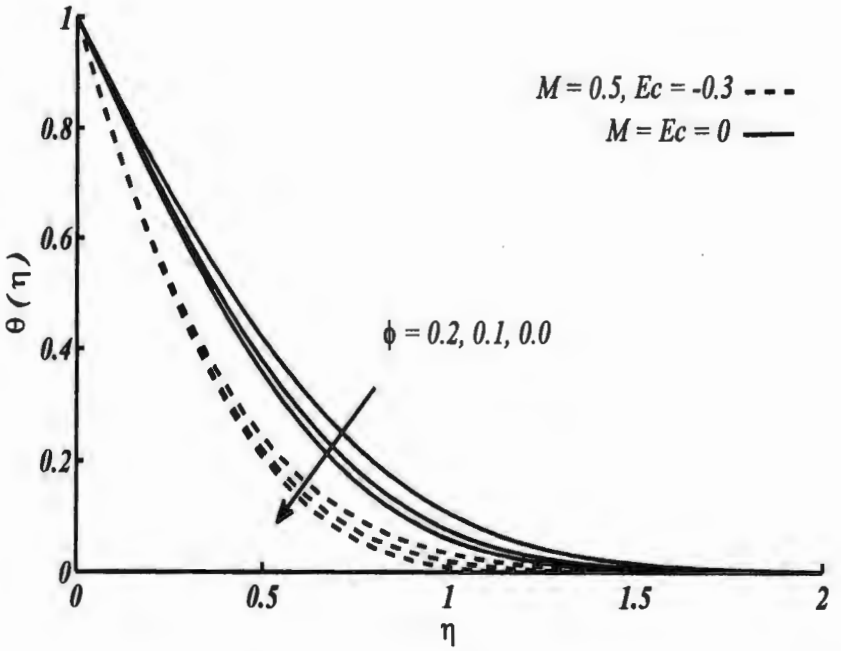

Figure 4.3(a, b): Temperature profile (*Cu*-water nanofluid) for distinct values of ϕ when Pr = 6.2 for (a) assisting flow $\lambda = 1$ (b) opposing flow $\lambda = -1$.

(a)

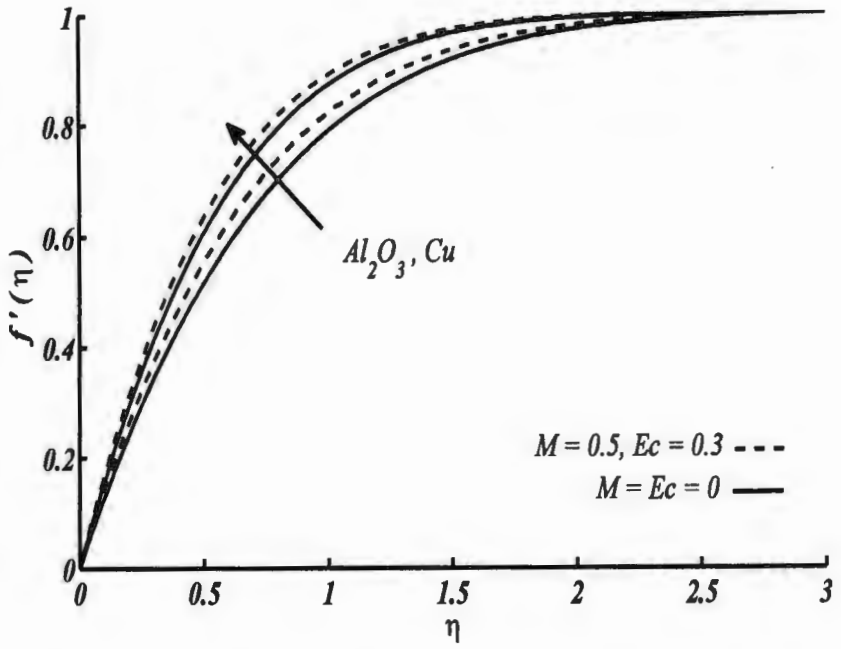

(b)

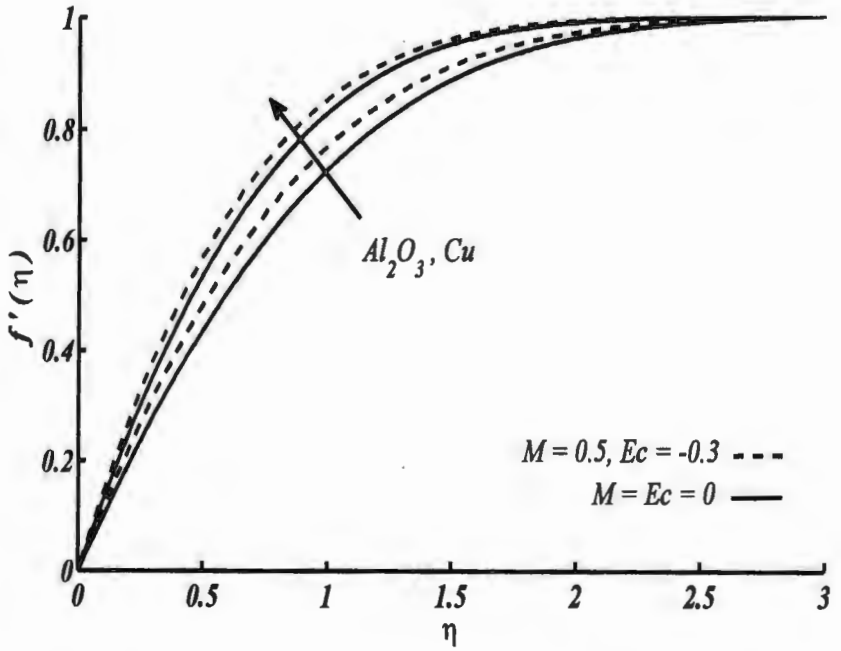

Figure 4.4(a, b): Velocity profile for different nanoparticles when $\phi = 0.2$ and Pr = 6.2 for (a) assisting flow $\lambda = 1$ (b) opposing flow $\lambda = -1$.

(a)

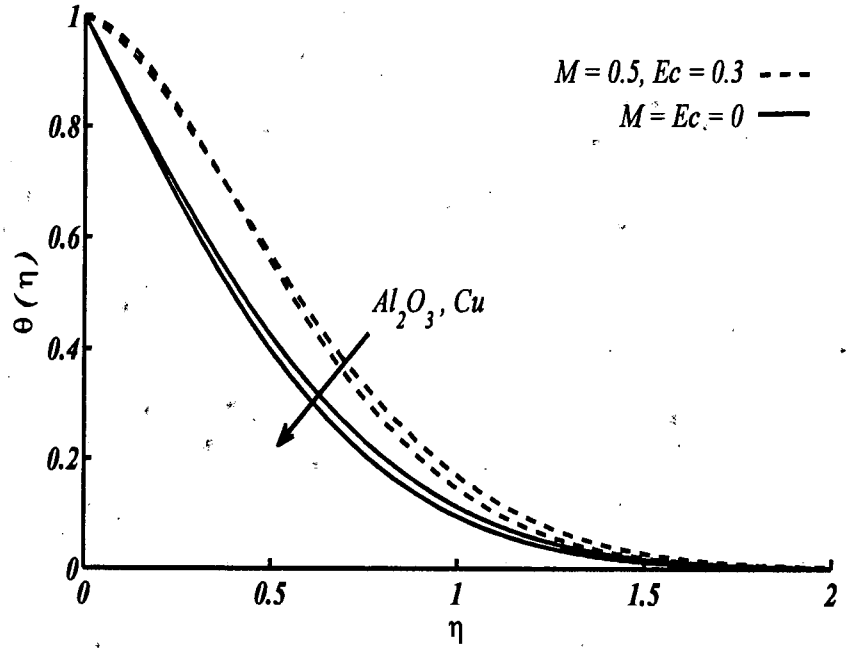

(b)

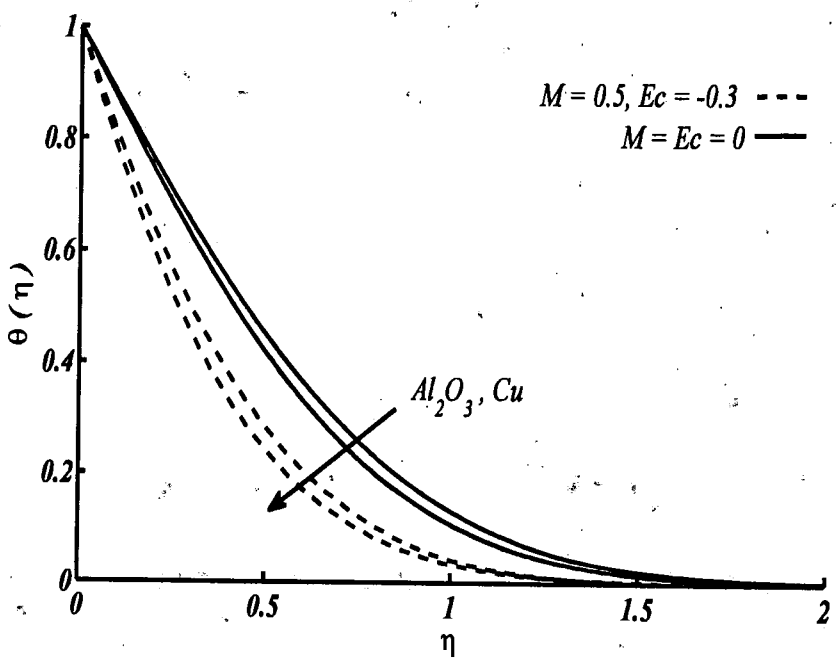

Figure 4.5(a, b): Temperature profile for different nanoparticles when $\phi = 0.2$ and Pr = 6.2 for (a) assisting flow $\lambda = 1$ (b) opposing flow $\lambda = -1$.

(a)

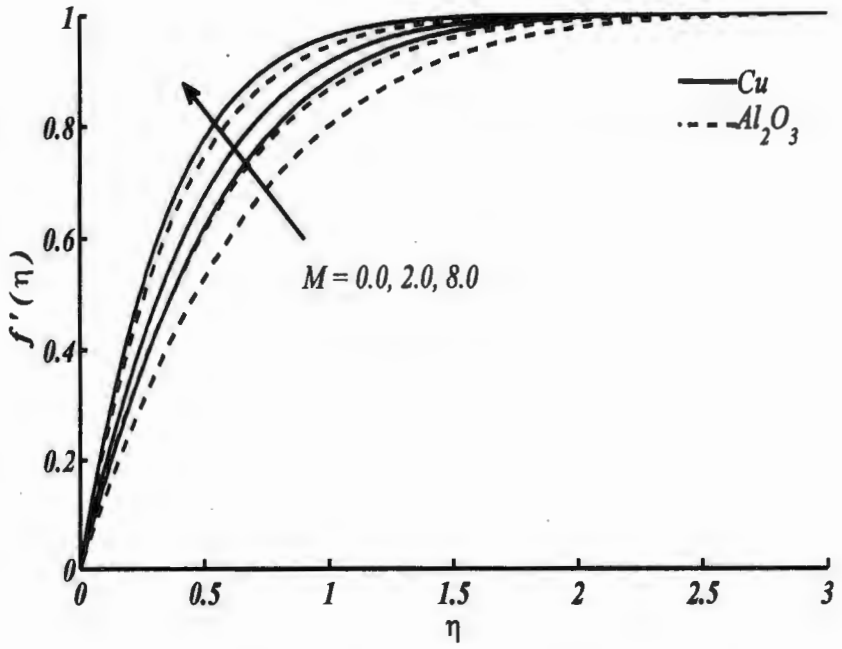

(b)

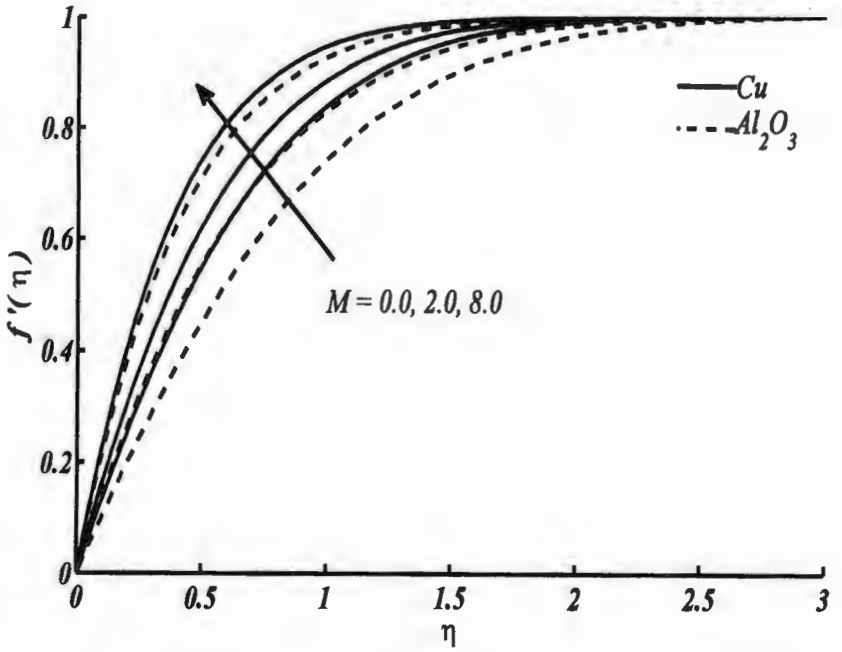

Figure 4.6(a, b): Velocity profile for distinct values of M when $\phi = 0.2$ and Pr = 6.2 for (a) assisting flow $\lambda = 1$ and $Ec = 0.3$ (b) opposing flow $\lambda = -1$ and $Ec = -0.3$.

(a)

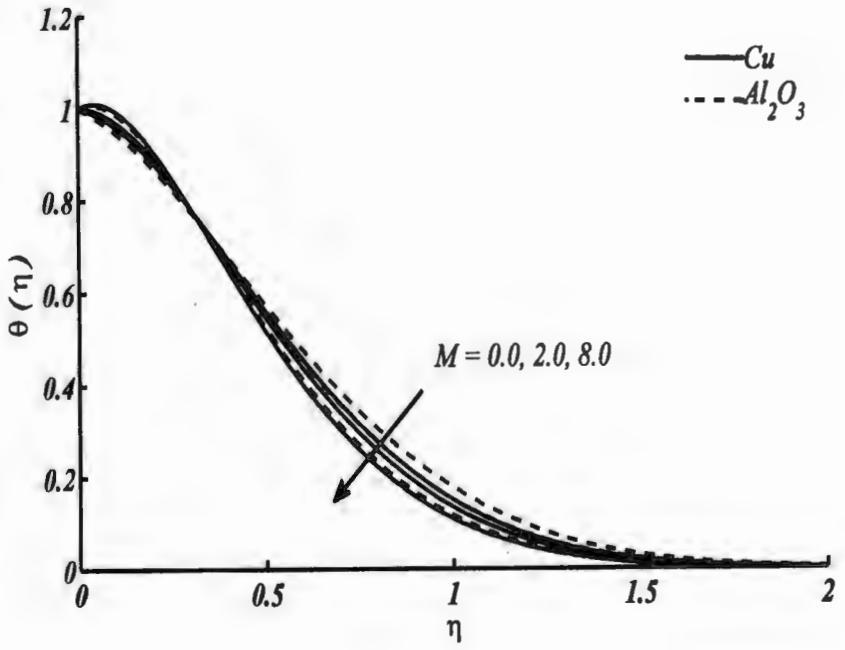

(b)

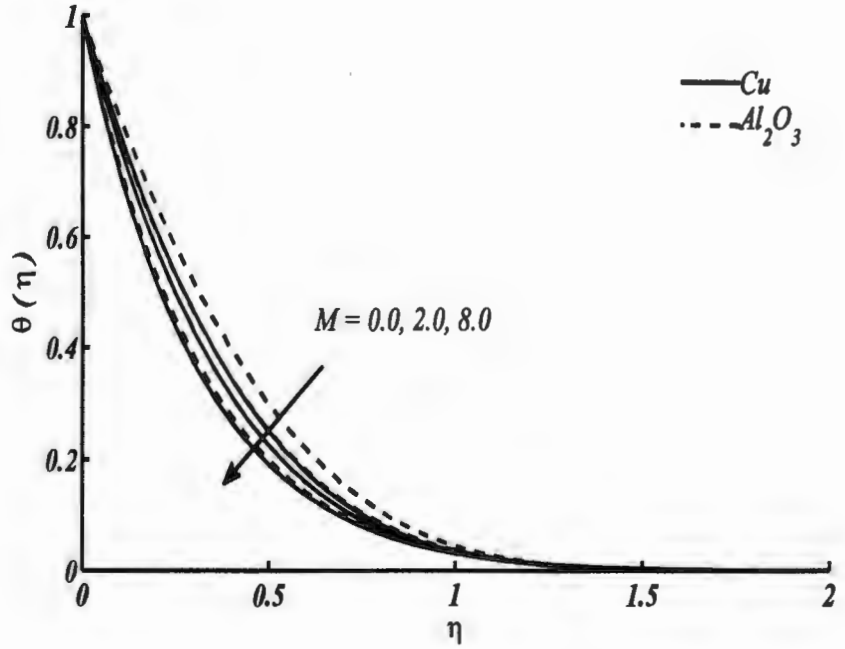

Figure 4.7(a, b): Temperature profile for distinct values of M when $\phi = 0.2$ and Pr = 6.2 for (a) assisting flow $\lambda = 1$ and $Ec = 0.3$ (b) opposing flow $\lambda = -1$ and $Ec = -0.3$.

(a)

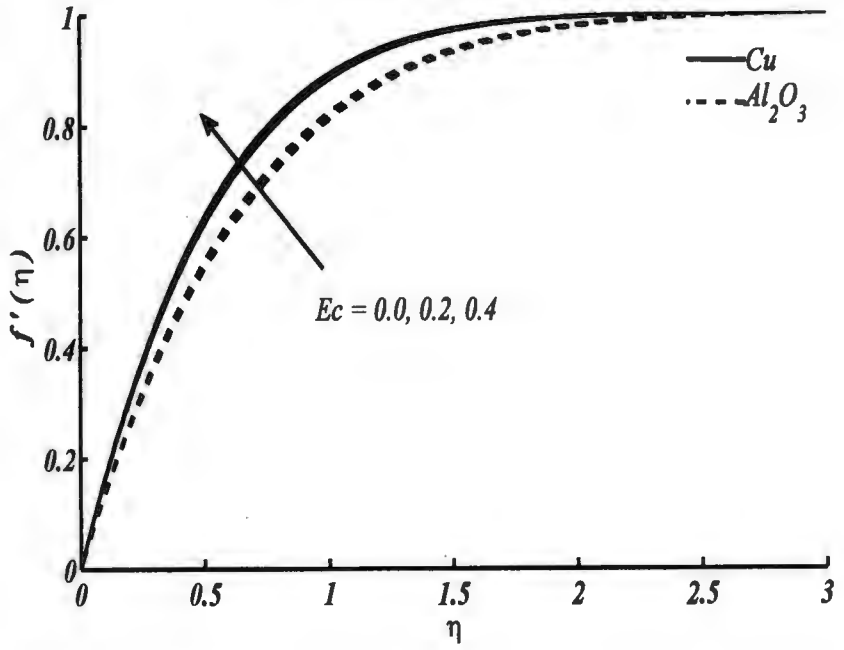

(b)

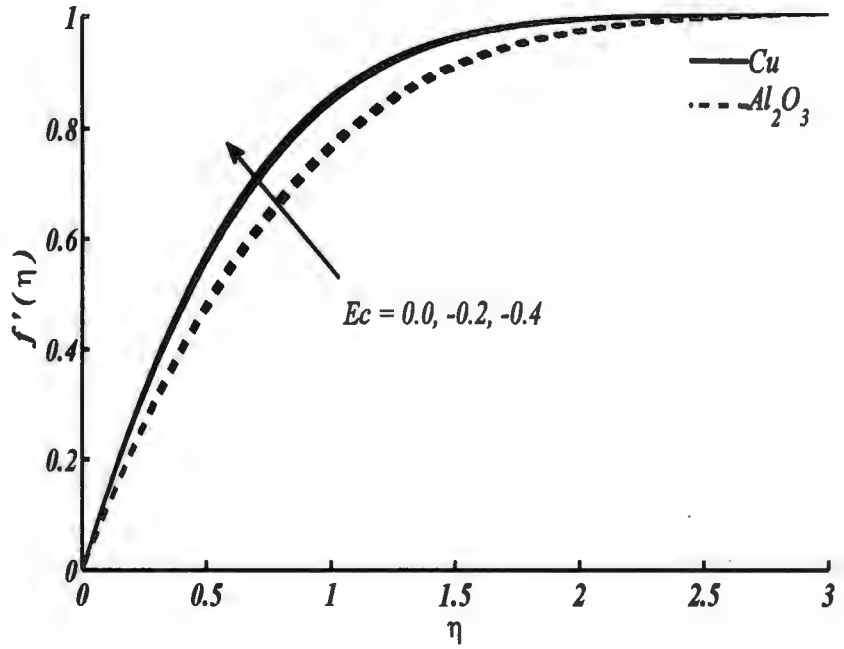

Figure 4.8(a, b): Velocity profile for distinct values of *Ec* when $\phi = 0.2$, $M = 0.5$, and Pr = 6.2 for (a) assisting flow $\lambda = 1$ (b) opposing flow $\lambda = -1$.

(a)

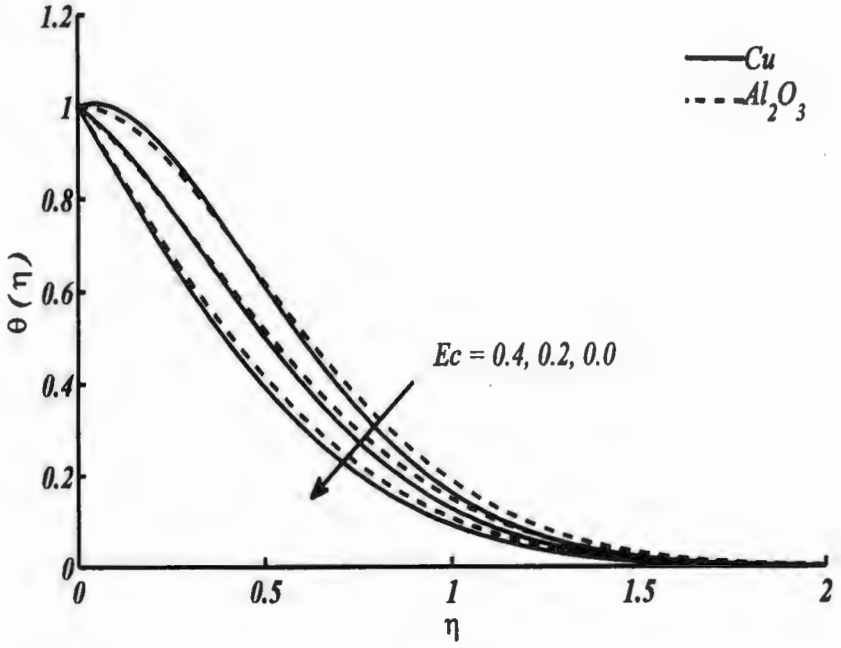

(b)

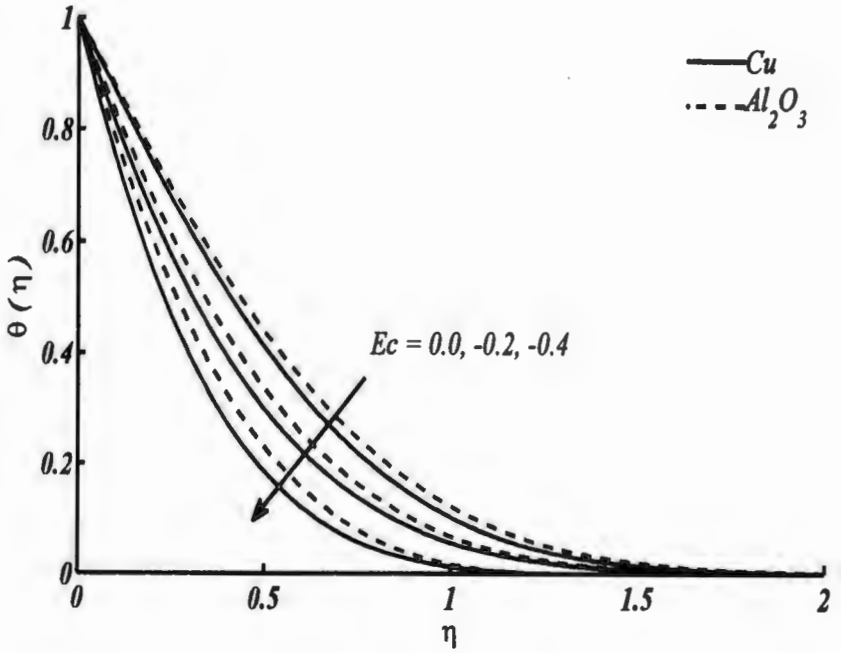

Figure 4.9(a, b): Temperature profile for distinct values of Ec when $\phi = 0.2$, $M = 0.5$, and Pr = 6.2 for (a) assisting flow $\lambda = 1$ (b) opposing flow $\lambda = -1$.

(a)

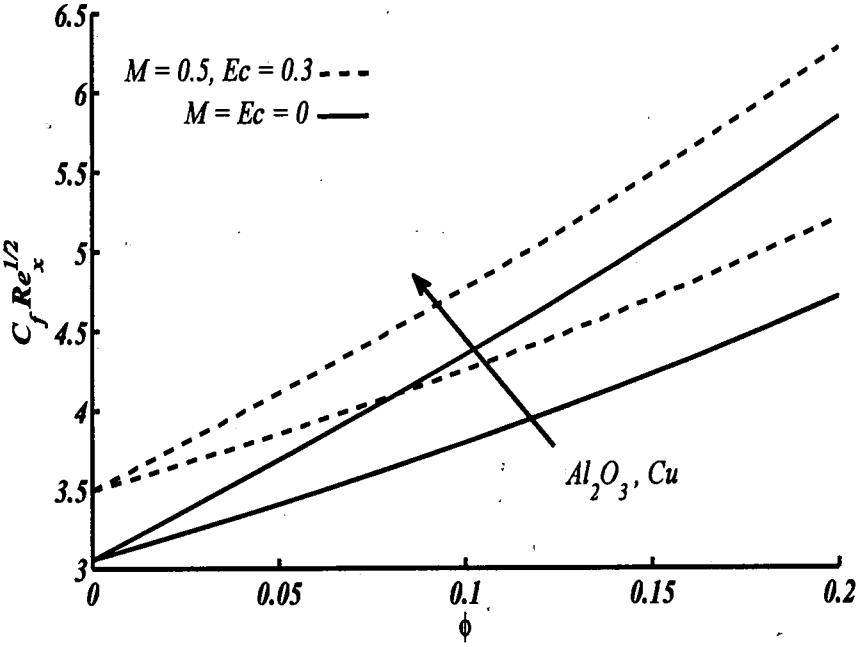

(b)

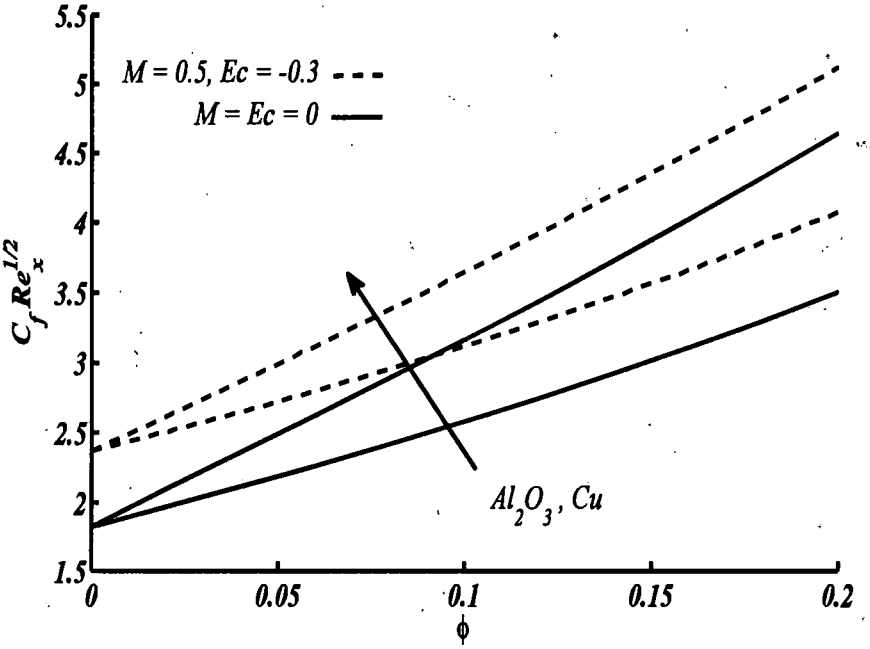

Figure 4.10(a, b): Skin friction coefficient against ϕ for different nanoparticles when Pr = 6.2 for (a) assisting flow $\lambda = 1$ (b) opposing flow $\lambda = -1$.

(a)

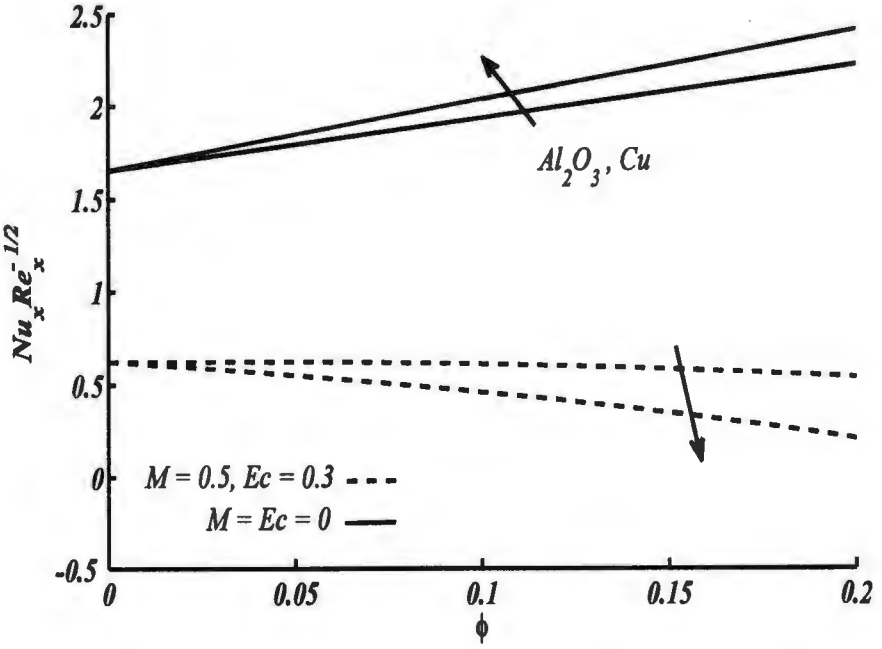

(b)

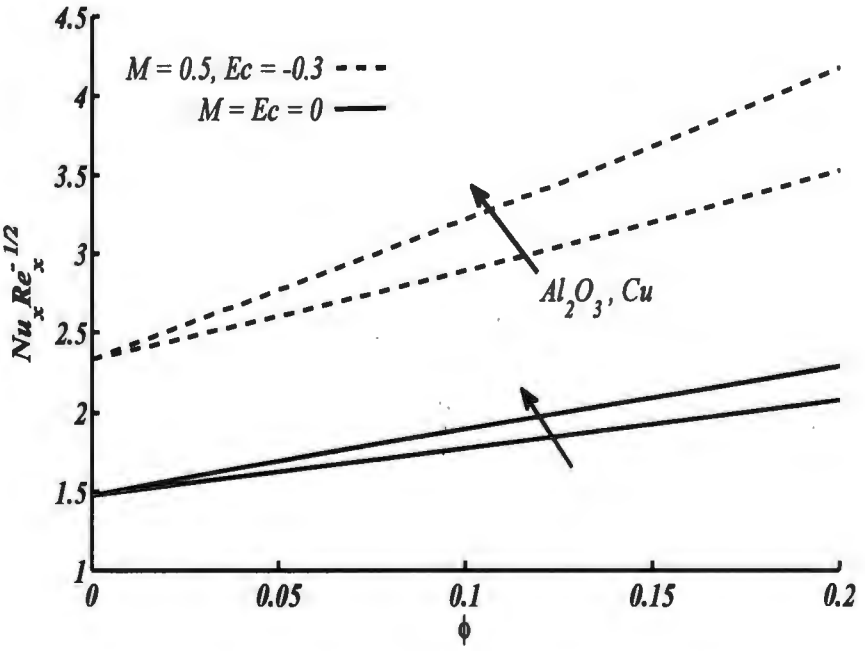

Figure 4.11(a, b): Local Nusselt number against ϕ for different nanoparticles when Pr = 6.2 for (a) assisting flow $\lambda = 1$ (b) opposing flow $\lambda = -1$.

(a)

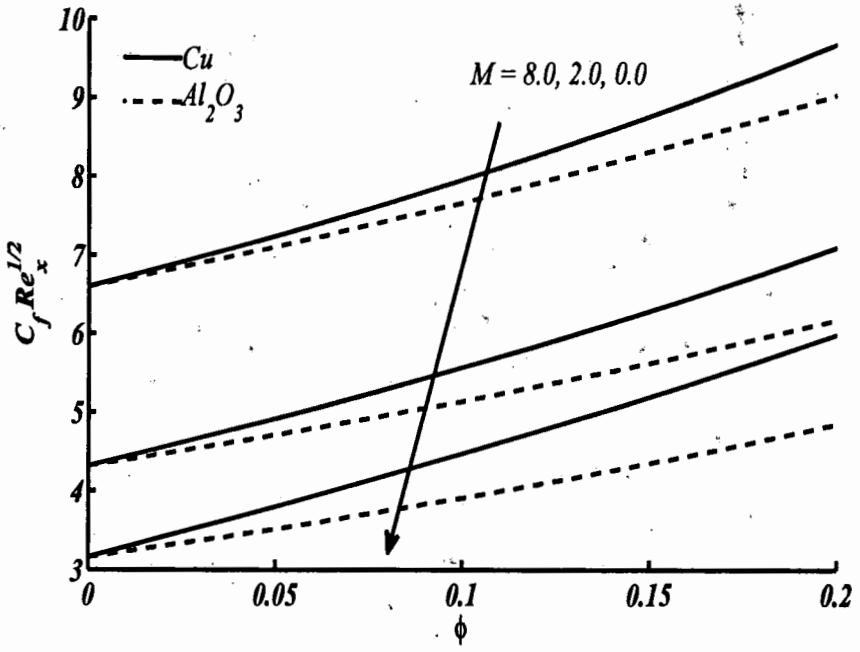

(b)

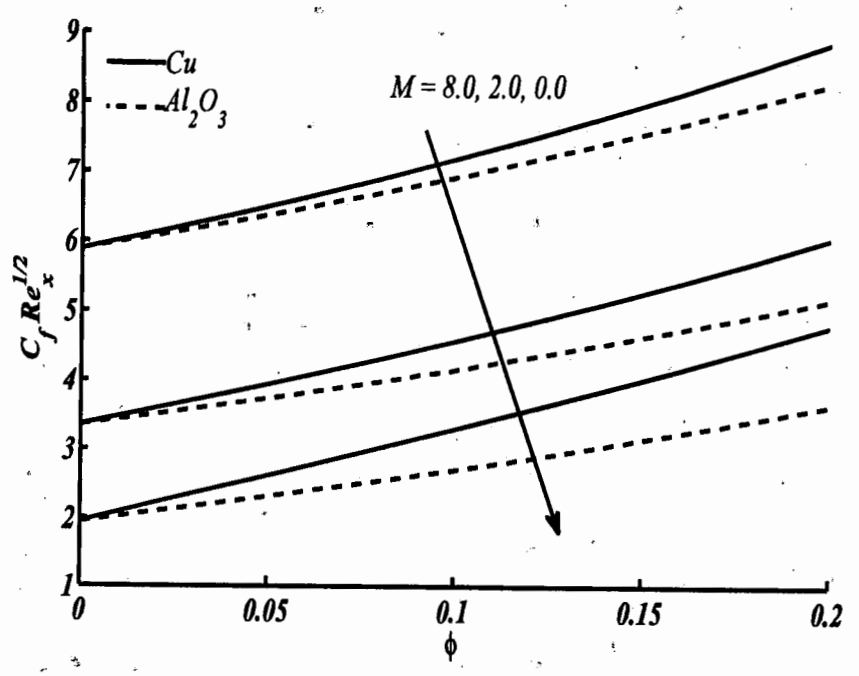

Figure 4.12(a, b): Skin friction coefficient against ϕ for distinct values of M when Pr = 6.2 for (a) assisting flow $\lambda = 1$ and $Ec = 0.3$ (b) opposing flow $\lambda = -1$ and $Ec = -0.3$.

(a)

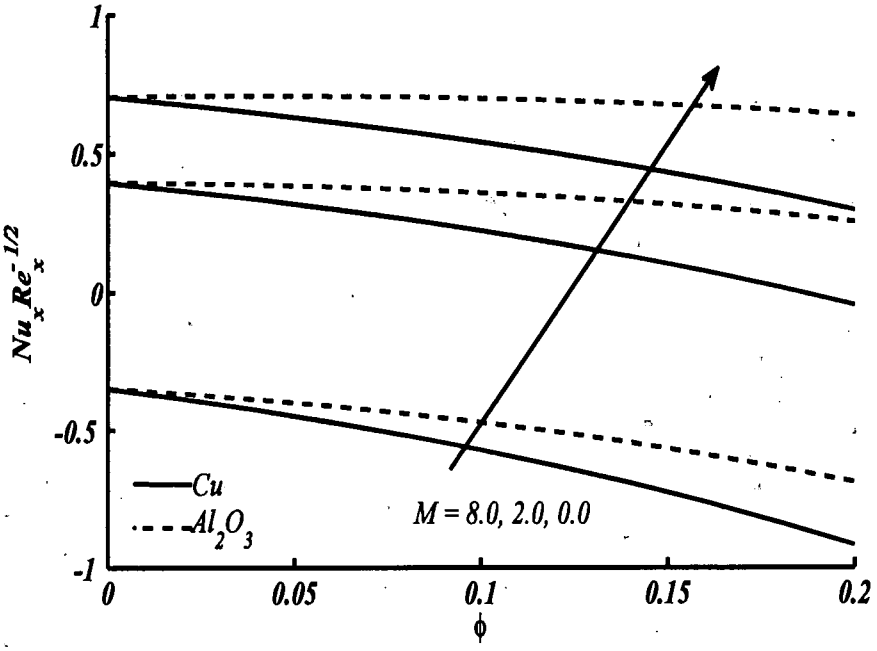

(b)

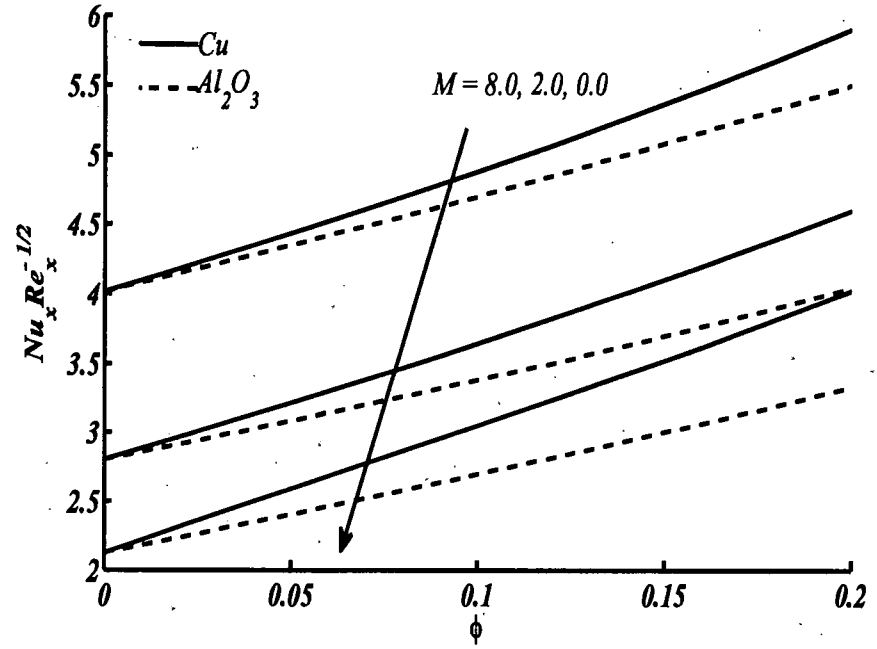

Figure 4.13(a, b): Local Nusselt number against ϕ for distinct values of M when Pr = 6.2 for (a) assisting flow $\lambda = 1$ and $Ec = 0.3$ (b) opposing flow $\lambda = -1$ and $Ec = -0.3$.

(a)

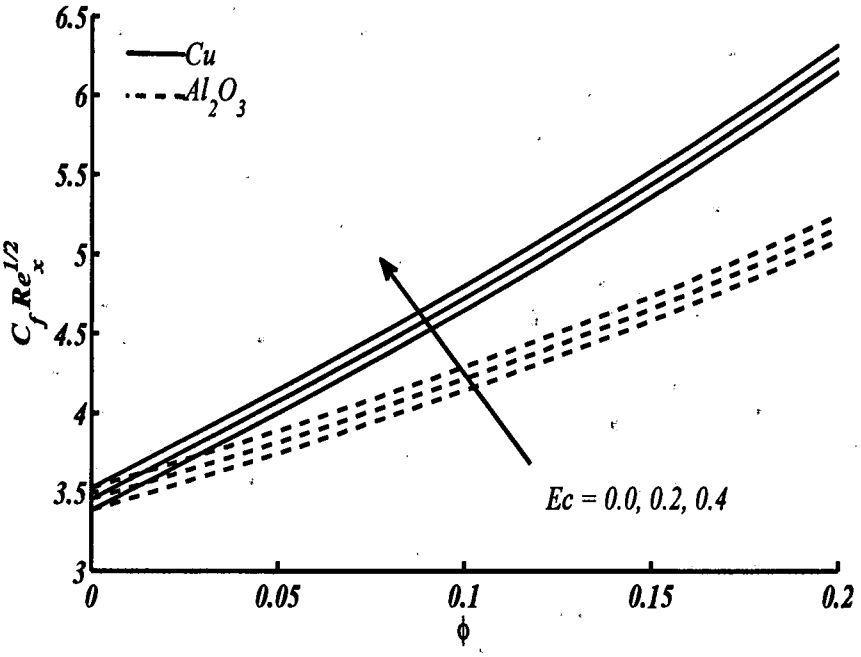

(b)

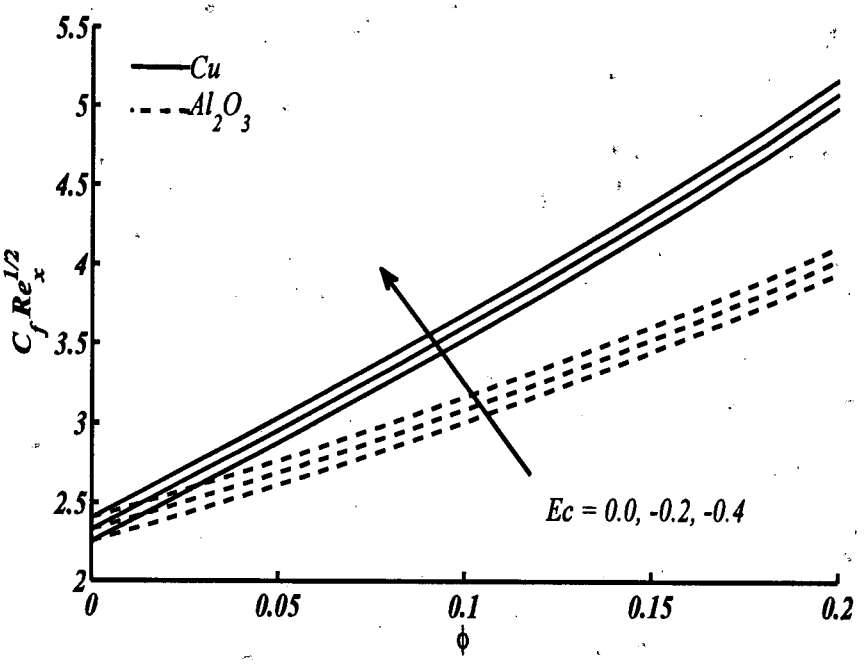

Figure 4.14(a, b): Skin friction coefficient against ϕ for distinct values of Ec when $M = 0.5$ and Pr = 6.2 for (a) assisting flow $\lambda = 1$ (b) opposing flow $\lambda = -1$.

(a)

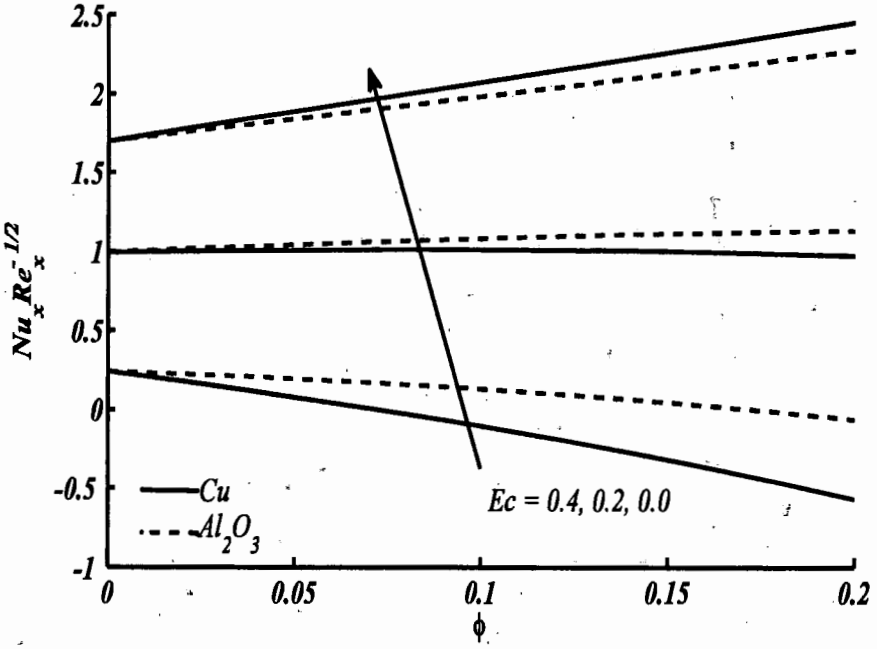

(b)

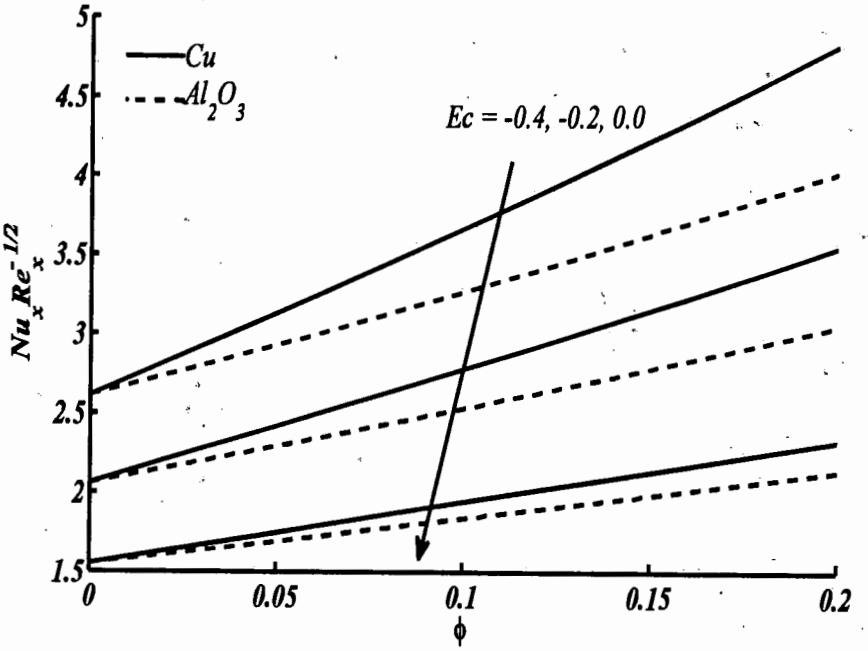

Figure 4.15(a, b): Local Nusselt number against ϕ for distinct values of Ec when $M = 0.5$ and Pr = 6.2 for (a) assisting flow $\lambda = 1$ (b) opposing flow $\lambda = -1$.

Table 4.2: The effects of ϕ on $C_f \mathrm{Re}_x^{1/2}$ and $Nu_x \mathrm{Re}_x^{-1/2}$ for different nanoparticles, when Pr = 6.2, $h_5/h_2 = 1$ and $M = Ec = 0$ are fixed.

ϕ	Tamim et al. [77] $\lambda = 1$		Present result $\lambda = 1$		Tamim et al. [77] $\lambda = -1$		Present result $\lambda = -1$	
	$C_f \mathrm{Re}_x^{1/2}$	$Nu_x \mathrm{Re}_x^{-1/2}$	$C_f \mathrm{Re}_x^{1/2}$	$Nu_x \mathrm{Re}_x^{-1/2}$	$C_f \mathrm{Re}_x^{1/2}$	$Nu_x \mathrm{Re}_x^{-1/2}$	$C_f \mathrm{Re}_x^{1/2}$	$Nu_x \mathrm{Re}_x^{-1/2}$
Nanoparticle *Cu* (Copper)								
0	3.0535	1.6524	3.0539	1.6525	1.8262	1.4779	1.8269	1.4781
0.05	3.9183	1.8728	3.9184	1.8728	2.2207	1.6562	2.2210	1.6563
0.10	4.8153	2.0834	4.8154	2.0834	2.6168	1.8265	2.6170	1.8265
0.15	5.7758	2.2901	5.7758	2.2901	3.0346	1.9939	3.0347	1.9940
0.20	6.8274	2.4964	6.8274	2.4964	3.4906	2.1617	3.4907	2.1617
Nanoparticle Al_2O_3 (Alumina)								
0	3.0535	1.6524	3.0539	1.6525	1.8262	1.4779	1.8269	1.4781
0.05	3.5180	1.8065	3.5184	1.8066	2.0542	1.6076	2.0549	1.6078
0.10	4.0276	1.9606	4.0280	1.9607	2.3042	1.7372	2.3052	1.7375
0.15	4.5929	2.1153	4.5935	2.1154	2.5829	1.8676	2.5843	1.8680
0.20	5.2269	2.2715	5.2277	2.2716	2.8982	1.9996	2.9004	2.0002

Table 4.3: Numerical values of $Nu_x \mathrm{Re}_x^{-1/2}$ for distinct values of nanoparticle volume fraction parameter ϕ, when Pr = 6.2 and M =0.5 are fixed.

ϕ	Nanoparticle *Cu* (Copper)		Nanoparticle Al_2O_3 (Alumina)	
	$Ec = 0.3, \lambda = 1$	$Ec = -0.3, \lambda = -1$	$Ec = 0.3, \lambda = 1$	$Ec = -0.3, \lambda = -1$
0.0	0.6225	2.3309	0.6225	2.3309
0.05	0.5482	2.7670	0.6210	2.6026
0.10	0.4570	3.2116	0.6074	2.8889
0.15	0.3445	3.6755	0.5795	3.1933
0.20	0.2057	4.1679	0.5346	3.5196

4.4 Conclusions

A numerical study on MHD mixed convection stagnation point flow of a nanofluid over a vertical flat plate is investigated. Tiwari and Das model [60] has been used to develop the

mathematical formulation in terms of the governing equations. Similarity transformation is used to convert governing system of partial differential equations into a system of ordinary differential equations along with boundary conditions. The Keller Box method is used to compute the numerical solution and detail procedure involved in this scheme for system of ordinary differential equations are explained in this chapter. Analysis is carried out to investigate these effects on two types of nanoparticles, namely, *Cu* and Al_2O_3. From the result and discussion, it is observed that velocity increases for both nanofluids in the presence of magnetic and viscous dissipation effects in assisting and opposing flow cases. In assisting flow, temperature increases because of the combined effects of magnetic and viscous dissipation for both nanofluids, and opposite behavior is observed in opposing flow. Both magnetic and viscous dissipation effects help to enhance $C_f \, \mathrm{Re}_x^{1/2}$ for both nanofluids in assisting and opposing flow cases. The heat transfer rate decreases in assisting flow case and increases in opposing flow case for both nanofluids in the presence of combined effects. However, the values of $Nu_x \, \mathrm{Re}_x^{-1/2}$ for *Cu*-water nanofluid become smaller than that of Al_2O_3-water nanofluid in assisting flow because of the combined effects of magnetic and viscous dissipation.

Chapter 5

Heat transfer in MHD stagnation point flow of a ferrofluid over a stretchable rotating disk

In this chapter, analysis of three dimensional boundary layer stagnation point flow of an incompressible viscous ferrofluid and heat transfer over a stretchable rotating circular disk in the presence of uniform external magnetic field is presented. For this purpose, three different types of ferroparticles namely, magnetite (Fe_3O_4), cobalt ferrite ($CoFe_2O_4$) and Mn-Zn ferrite ($Mn\text{-}ZnFe_2O_4$) are considered with water as a base fluid. The mathematical modelling of the considered problem is made in terms of nonlinear partial differential equations which are then reduced to nonlinear ordinary differential equations after using similarity transformation [142]. The solution of obtained equations are computed numerically using Keller Box method, the detail procedure of this method has been explained in previous chapters both for partial and ordinary differential equations. The effects of pertinent parameters namely, volume fraction parameter of magnetic nanoparticle, rotating parameter, magnetic parameter, velocity ratio parameter and Prandtl number on both radial and azimuthal velocity profiles, temperature profile, skin friction coefficients and local Nusselt number are computed and shown through graphs and tables. For magnetite ferroparticle (Fe_3O_4) radial velocity decreases and azimuthal velocity and temperature increase with increasing the value of volume fraction parameter ϕ. The values of skin friction coefficient in radial direction and local Nusselt number of magnetite ferroparticle (Fe_3O_4) become higher than that of other ferroparticles due to its maximum density and thermal conductivity.

5.1 Mathematical formulation

Consider a three dimensional stagnation point flow of an incompressible electrically conducting ferrofluid over a stretchable rotating disk as shown in Fig. 5.1. The flow is considered as axisymmetric and steady flow. Let (r, θ^*, z) be the cylindrical co-ordinates and the disk rotates about z-axis with a constant angular velocity Ω. The disk is stretched in radial direction at a constant rate c with velocity $u_w = cr$. Due to axisymmetric flow, the variation w.r.t. θ^* is ignored. It is assumed that a uniform external magnetic field of strength B_0 is applied normal to the circular disk along z-axis and consequently the ferrofluid becomes

strongly magnetized due to the reason that ferrofluids do not maintain magnetization in the absence of an external applied magnetic field. The induced magnetic field is considered negligible under the assumption of small magnetic Reynolds number. Further, it is assumed that velocity outside the boundary layer is prescribed as $u_e = ar$ (potential flow) and uniform surface temperature at the rotating disk is T_w, ambient fluid temperature is T_∞ under the assumption $T_w > T_\infty$. The thermophysical properties of base fluid and magnetic nanoparticles are shown in Table 5.1 and are taken as independent of temperature. The continuity, momentum and energy equations of the flow problem in cylindrical co-ordinate system can be written as

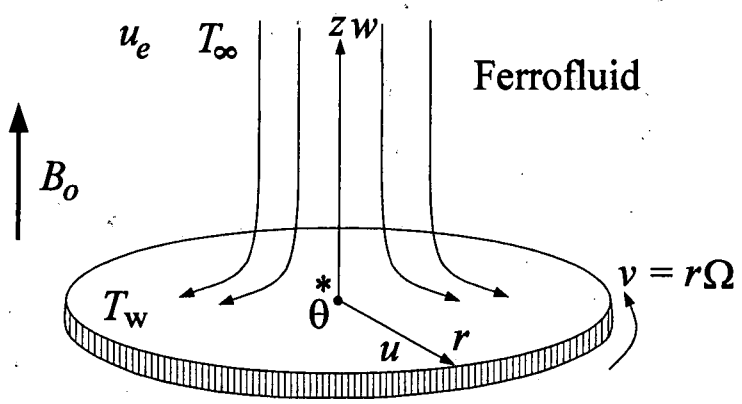

Figure 5.1: The physical model of the flow towards a rotating disk near stagnation point region.

$$\frac{\partial u}{\partial r}+\frac{u}{r}+\frac{\partial w}{\partial z}=0, \tag{5.1}$$

$$u\frac{\partial u}{\partial r}-\frac{v^2}{r}+w\frac{\partial u}{\partial z}=-\frac{1}{\rho_{nf}}\frac{\partial p}{\partial r}+\frac{\mu_{nf}}{\rho_{nf}}\left(\frac{\partial^2 u}{\partial r^2}+\frac{1}{r}\frac{\partial u}{\partial r}-\frac{u}{r^2}+\frac{\partial^2 u}{\partial z^2}\right)-\frac{\sigma_f B_0^{\,2}}{\rho_{nf}}u, \tag{5.2}$$

$$u\frac{\partial v}{\partial r}+\frac{uv}{r}+w\frac{\partial v}{\partial z}=\frac{\mu_{nf}}{\rho_{nf}}\left(\frac{\partial^2 v}{\partial r^2}+\frac{1}{r}\frac{\partial v}{\partial r}-\frac{v}{r^2}+\frac{\partial^2 v}{\partial z^2}\right)-\frac{\sigma_f B_0^{\,2}}{\rho_{nf}}v, \tag{5.3}$$

$$u\frac{\partial w}{\partial r}+w\frac{\partial w}{\partial z}=-\frac{1}{\rho_{nf}}\frac{\partial p}{\partial z}+\frac{\mu_{nf}}{\rho_{nf}}\left(\frac{\partial^2 w}{\partial r^2}+\frac{1}{r}\frac{\partial w}{\partial r}+\frac{\partial^2 w}{\partial z^2}\right), \tag{5.4}$$

$$u\frac{\partial T}{\partial r}+w\frac{\partial T}{\partial z}=\alpha_{nf}\left(\frac{\partial^2 T}{\partial r^2}+\frac{1}{r}\frac{\partial T}{\partial r}+\frac{\partial^2 T}{\partial z^2}\right). \tag{5.5}$$

In which u, v and w represent the velocity vector components in the direction of r, θ^* and z respectively. The relevant boundary conditions of the problem are

$$u = u_w = cr,\ v = r\Omega,\ w = 0,\ T = T_w \quad \text{at } z = 0,$$
$$u \to u_e = ar,\ v \to v_e = 0,\ w \to w_e = -2az,\ T \to T_\infty \quad \text{as } z \to \infty. \tag{5.6}$$

Using the boundary layer approximations, the Eqs. (5.1–5.5) take the form as

$$\frac{\partial u}{\partial r} + \frac{u}{r} + \frac{\partial w}{\partial z} = 0, \tag{5.7}$$

$$u\frac{\partial u}{\partial r} - \frac{v^2}{r} + w\frac{\partial u}{\partial z} = -\frac{1}{\rho_{nf}}\frac{\partial p}{\partial r} + \frac{\mu_{nf}}{\rho_{nf}}\left(\frac{\partial^2 u}{\partial z^2}\right) - \frac{\sigma_f B_0^{\,2}}{\rho_{nf}}u, \tag{5.8}$$

$$u\frac{\partial v}{\partial r} + \frac{uv}{r} + w\frac{\partial v}{\partial z} = \frac{\mu_{nf}}{\rho_{nf}}\left(\frac{\partial^2 v}{\partial z^2}\right) - \frac{\sigma_f B_0^{\,2}}{\rho_{nf}}v, \tag{5.9}$$

$$\frac{\partial p}{\partial z} = 0, \tag{5.10}$$

$$u\frac{\partial T}{\partial r} + w\frac{\partial T}{\partial z} = \alpha_{nf}\left(\frac{\partial^2 T}{\partial z^2}\right). \tag{5.11}$$

For eliminating the pressure gradient, the boundary condition $z \to \infty$ is used in Eq. (5.8) (potential flow velocity outside the edge of the boundary layer) which reduces to

$$u\frac{\partial u}{\partial r} - \frac{v^2}{r} + w\frac{\partial u}{\partial z} = u_e\frac{du_e}{dr} + \frac{\mu_{nf}}{\rho_{nf}}\left(\frac{\partial^2 u}{\partial z^2}\right) + \frac{\sigma_f B_0^{\,2}}{\rho_{nf}}(u_e - u), \tag{5.12}$$

After using the following suitable transformation [142]

$$\eta = \left(\frac{c}{\nu_f}\right)^{1/2} z,\ u(r,z) = crF(\eta),\ v(r,z) = crG(\eta),\ w(r,z) = \sqrt{c\nu_f}H(\eta),$$
$$\theta(\eta) = \frac{T - T_\infty}{T_w - T_\infty}, \tag{5.13}$$

into Eqs. (5.7, 5.9, 5.11, 5.12), the following system of ordinary differential equations are obtained

$$H' + 2F = 0, \tag{5.14}$$

$$F''' + h_1\left(-F^2 + G^2 - HF' + \frac{M}{h_2}\left(\frac{a}{c} - F\right) + \left(\frac{a}{c}\right)^2\right) = 0, \tag{5.15}$$

$$G'' - h_1\left(2FG + HG' + \frac{M}{h_2}G\right) = 0, \tag{5.16}$$

$$\theta'' - \frac{k_f}{k_{nf}}\Pr h_3 H\theta' = 0, \tag{5.17}$$

where F, G and H are dimensionless velocities in radial, azimuthal and axial directions respectively, the symbol prime denotes the differentiation w.r.t. η and a/c is the velocities ratio parameter. The boundary conditions Eq. (5.6) take the new form as

$$\begin{aligned} &F(0)=1, H(0)=0, G(0)=\omega, \theta(0)=1, \\ &F(\infty)=\frac{a}{c}, G(\infty)=0, \theta(\infty)=0. \end{aligned} \tag{5.18}$$

where $\omega=\dfrac{\Omega}{c}$ is the rotation parameter. The skin friction coefficients in radial and azimuthal directions and local Nusselt number are defined as

$$C_{Fr}=\frac{\tau_{rz}}{\rho_f (cr)^2}, C_{G\theta^*}=\frac{\tau_{\theta^* z}}{\rho_f (cr)^2}, Nu_r=\frac{rq_w}{k_f\left(T_w-T_\infty\right)}, \tag{5.19}$$

in which $\tau_{rz}, \tau_{\theta^* z}$ are the radial and azimuthal shear stresses at wall and q_w are defined as

$$\tau_{rz}=\mu_{nf}\left(\frac{\partial u}{\partial z}+\frac{1}{r}\frac{\partial w}{\partial \theta^*}\right)_{z=0}, \tau_{\theta^* z}=\mu_{nf}\left(\frac{\partial v}{\partial z}+\frac{1}{r}\frac{\partial w}{\partial \theta^*}\right)_{z=0}, \quad q_w=-k_{nf}\left(\frac{\partial T}{\partial z}\right)_{z=0}. \tag{5.20}$$

Using Eq. (5.20) into Eq. (5.19), the skin friction coefficients and local Nusselt number take the form

$$\begin{aligned} &C_{Fr}\,\mathrm{Re}_r^{1/2}=\frac{1}{(1-\phi)^{2.5}}F'(0), C_{G\theta^*}\,\mathrm{Re}_r^{1/2}=\frac{1}{(1-\phi)^{2.5}}G'(0), \\ &Nu_r\,\mathrm{Re}_r^{-1/2}=-\frac{k_{nf}}{k_f}\theta'(0). \end{aligned} \tag{5.21}$$

5.2 Results and discussion

The numerical solution of the system of nonlinear ordinary differential Eqs. (5.14–5.17) subject to the boundary conditions Eq. (5.18) is obtained using Keller Box method. The details of this method for the system of nonlinear ordinary differential equations have been described in chapter 4. The variation of skin friction coefficient in radial direction $C_{Fr}\,\mathrm{Re}_r^{1/2}$ and Nusselt number $Nu_r\,\mathrm{Re}_r^{-1/2}$ for water base ferrofluid against volume fraction parameter of magnetic nanoparticle ϕ, rotation parameter ω and magnetic parameter M are given in Tables 5.2 and 5.3. It is observed that the values of $C_{Fr}\,\mathrm{Re}_r^{1/2}$ and $Nu_r\,\mathrm{Re}_r^{-1/2}$ are smaller in the absence of magnetic field and become higher in the presence of magnetic field. It is due to the reason that the magnetic field aligns the magnetic nanoparticles in order. It is also observed that by increasing the rotation of the disk, the values of $C_{Fr}\,\mathrm{Re}_r^{1/2}$ and $Nu_r\,\mathrm{Re}_r^{-1/2}$ enhance for all

ferroparticles. It is moreover seen that the values of $C_{Fr}\,\mathrm{Re}_r^{1/2}$ and $Nu_r\,\mathrm{Re}_r^{-1/2}$ for magnetite (Fe_3O_4) ferroparticle are greater than that of other ferroparticles. When the values of volume fraction parameter of magnetic nanoparticle $\phi = 0$ (pure fluid) and velocity ratio parameter $a/c = 0$ are considered, the present problem becomes a limiting case of Turkyilmazoglu [142] which was solved numerically using classical fourth-order Runge-Kutta scheme. A comparison of the present study with the work of Turkyilmazoglu [142] is shown in Table 5.4 for various values of rotation parameter ω. It is found that our results are valid and in good agreement. The effects of pertinent parameters namely magnetic parameter M, velocity ratio parameter a/c rotation parameter ω, volume fraction parameter of magnetic nanoparticle ϕ and Prandtl number Pr on velocity and temperature profiles, skin friction coefficients and local Nusselt number are shown graphically through Figs. 5.2–5.13. The effects of magnetic parameter M for various values of ϕ on radial and azimuthal velocities and temperature profiles for magnetite ferroparticle (Fe_3O_4) are shown in Figs. (5.2–5.4). Fig. 5.2 depicts that radial velocity is maximum in the absence of magnetite ferroparticle (Fe_3O_4) i.e. $\phi = 0$ and decreases by increasing the values of volume fraction parameter of magnetic nanoparticle ϕ for both values of magnetic parameter $M = 3$ and 6. It is because of the reason that due to the enhancement of volume fraction of magnetic nanoparticle ϕ, the viscosity of ferrofluid increases as predicted by Brinkman [140] by using theoretical model for viscosity and consequently momentum diffusivity within the boundary layer increases. In Fig. 5.2, it is further seen that radial velocity increases and momentum boundary layer thickness decreases by increasing the values of M because, in this case Lorentz force assists the flow (the sign of Lorentz force is +ve in momentum Eq. 5.15) and helps to control the boundary layer. In Fig. 5.3, the effects of volume fraction parameter ϕ on azimuthal velocity show an opposite behavior as observed in Fig. 5.2. Both azimuthal velocity and boundary layer thickness decrease by increasing the values of M because in this case Lorentz force retards the flow (the sign of Lorentz force is -ve in momentum Eq. 5.16). Fig. 5.4 shows that temperature and thermal boundary layer thickness increase by increasing the values of magnetic nanoparticle volume fraction parameter ϕ for both values of magnetic parameter $M = 3$ and 6, which is interpreted physically as when the amount of magnetite (Fe_3O_4) ferroparticle is increased, the thermal conductivity increases as reported by Choi [57] using thermal conductivity model known as Maxwell model [141] and consequently thermal boundary layer thickness increases. It is observed that temperature of the fluid become smaller in the presence of high magnetic field ($M = 6$) as compared to low magnetic field ($M = 3$). Figs. (5.5–5.7) show the effect of rotation parameter ω on radial and

azimuthal velocities and temperature profile for magnetite ferroparticle (Fe_3O_4). Fig. 5.5 depicts that the radial velocity increases and momentum boundary layer thickness decreases by increasing the values of rotation parameter ω respectively. It physically shows that ferrofluid particles are pushed in the radial direction due to the existence of centrifugal force. As a result, the velocity in this direction increases. Figs. 5.6 and 5.7 show that the azimuthal velocity enhances and temperature reduces by increasing the values of rotation parameter ω. It is also noted that the thermal boundary layer thickness decreases due to increase in the rotation of the disk. In Figs. (5.8–5.10), the values of skin friction coefficient in radial and azimuthal directions and local Nusselt number are plotted against magnetic nanoparticle volume fraction parameter ϕ for different values of magnetic parameter in the presence of ferroparticles considered in this problem. Fig. 5.8 shows that the skin friction coefficient in the radial direction increases by increasing the magnetic nanoparticle volume fraction parameter ϕ because the viscosity of ferrofluids becomes higher due to the enhancement of magnetic nanoparticle concentration in the base fluid. It is further seen that the values of skin friction coefficient for magnetite ferroparticle (Fe_3O_4) are greater than that of other ferroparticles, because of its higher density as compared to other ferroparticles (see Table 5.1). It is also seen that skin friction coefficient increases in the presence of magnetic field. In Fig. 5.9 the result of skin friction coefficient in the azimuthal direction shows an opposite behavior as observed in Fig. 5.8. Fig. 5.10 depicts that the local Nusselt number increases by increasing the magnetic nanoparticle volume fraction parameter ϕ because the thermal conductivity of ferrofluids becomes higher due to the enhancement of magnetic nanoparticle concentration in the base fluid. It is observed that local Nusselt number in magnetite (Fe_3O_4) ferroparticle is greater than that of other ferroparticles due to the higher thermal conductivity of magnetite (Fe_3O_4) ferroparticle (see Table 5.1). It is also observed that local Nusselt number increases in the presence of magnetic field. The effects of rotation parameter ω on skin friction coefficient in radial and azimuthal directions and local Nusselt number for three different ferroparticles are plotted against magnetic nanoparticle volume fraction parameter ϕ and shown in Figs. (5.11–5.13). Fig. 5.11 shows that skin friction coefficient in radial direction increases by increasing the values of rotation parameter ω due to the existence of centrifugal force, which pushes the ferrofluid particles in radial direction, therefore, the flow rate increases in this direction. In Fig. 5.12, the skin friction coefficient in azimuthal direction shows an opposite behavior as observed in Fig 5.11. Fig. 5.13 depicts that the local Nusselt number increases by increasing the rotation parameter ω and magnetic nanoparticle volume fraction parameter ϕ. This is due to the fact that the rotation parameter reduces the temperature within the boundary layer.

Table 5.1: Thermophysical properties of base fluid and magnetic nanoparticles [143].

Properties	Fe_3O_4	$CoFe_2O_4$	$Mn\text{-}ZnFe_2O_4$	Fluid
c_p (J/kgK)	670	700	800	4179
k(W/mK)	9.7	3.7	5	0.613
ρ(kg/m^3)	5180	4907	4900	997.1

Table 5.2: The values of $C_{Fr}\,\mathrm{Re}_r^{1/2}$ at $a/c = 1.5$.

		$M=0$			$M=2$		
Ferroparticles	ϕ	$\omega=0$	$\omega=0.5$	$\omega=1.0$	$\omega=0$	$\omega=0.5$	$\omega=1.0$
magnetite (Fe_3O_4)	0.02	1.0688	1.1120	1.2409	1.2866	1.3229	1.4315
	0.1	1.3605	1.4155	1.5796	1.5763	1.6242	1.7675
	0.2	1.7942	1.8667	2.0831	2.0171	2.0821	2.2764
cobalt ferrite ($CoFe_2O_4$)	0.02	1.0661	1.1092	1.2378	1.2843	1.3205	1.4287
	0.1	1.3473	1.4018	1.5643	1.5649	1.6122	1.7538
	0.2	1.7673	1.8387	2.0519	1.9932	2.0570	2.2479
Mn-Zn ferrite ($Mn\text{-}ZnFe_2O_4$)	0.02	1.0660	1.1091	1.2377	1.2843	1.3204	1.4287
	0.1	1.3470	1.4014	1.5639	1.5646	1.6119	1.7535
	0.2	1.7666	1.8379	2.0511	1.9926	2.0564	2.2471

Table 5.3: The values of $Nu_r\,\mathrm{Re}_r^{-1/2}$ when Pr = 6.2 and $a/c = 1.5$.

		$M=0$			$M=2$		
Ferroparticles	ϕ	$\omega=0$	$\omega=0.5$	$\omega=1.0$	$\omega=0$	$\omega=0.5$	$\omega=1.0$
magnetite (Fe_3O_4)	0.02	3.0484	3.0521	3.0629	3.0699	3.0727	3.0808
	0.1	3.3507	3.3549	3.3670	3.3701	3.3733	3.3830
	0.2	3.7420	3.7467	3.7604	3.7595	3.7634	3.7748
cobalt ferrite ($CoFe_2O_4$)	0.02	3.0286	3.0322	3.0430	3.0500	3.0528	3.0608
	0.1	3.2482	3.2521	3.2639	3.2670	3.2701	3.2795
	0.2	3.5245	3.5288	3.5417	3.5411	3.5447	3.5554
Mn-Zn ferrite ($Mn\text{-}ZnFe_2O_4$)	0.02	3.0393	3.0429	3.0537	3.0608	3.0635	3.0716
	0.1	3.3044	3.3084	3.3204	3.3236	3.3268	3.3363
	0.2	3.6451	3.6496	3.6629	3.6623	3.6660	3.6771

Table 5.4: Comparison of the present results with the published work Turkyilmazoglu [142] for $a/c = \phi = 0$ and Pr = 1.

	ω	$F'(0)$		$-G'(0)$		$-\theta'(0)$	
		Present result	[142]	Present result	[142]	Present result	[142]
$M = 0$	0	-1.1737	-1.1737	0.0000	0.0000	0.8520	0.8520
	1	-0.9483	-0.9483	1.4870	1.4870	0.8757	0.8757
	2	-0.3263	-0.3262	3.1278	3.1278	0.9304	0.9304
	5	3.1937	3.1937	9.2536	9.2535	1.1292	1.1291
	10	12.7206	12.7209	22.9139	22.9134	1.4260	1.4259
	20	40.9056	40.9057	59.6895	60.0129	1.8743	1.8944
$M = 2$	0	-1.8305	-1.8305	0.0000	0.0000	0.7261	0.7261
	1	-1.6635	-1.6634	2.0239	2.0239	0.7422	0.7422
	2	-1.1754	-1.1753	4.1135	4.1135	0.7854	0.7854
	5	1.8928	1.8929	11.1407	11.1406	0.9803	0.9803
	10	10.8329	10.8334	25.7231	25.7225	1.2993	1.2992
	20	38.1857	38.1880	64.0635	64.0604	1.7974	1.7973

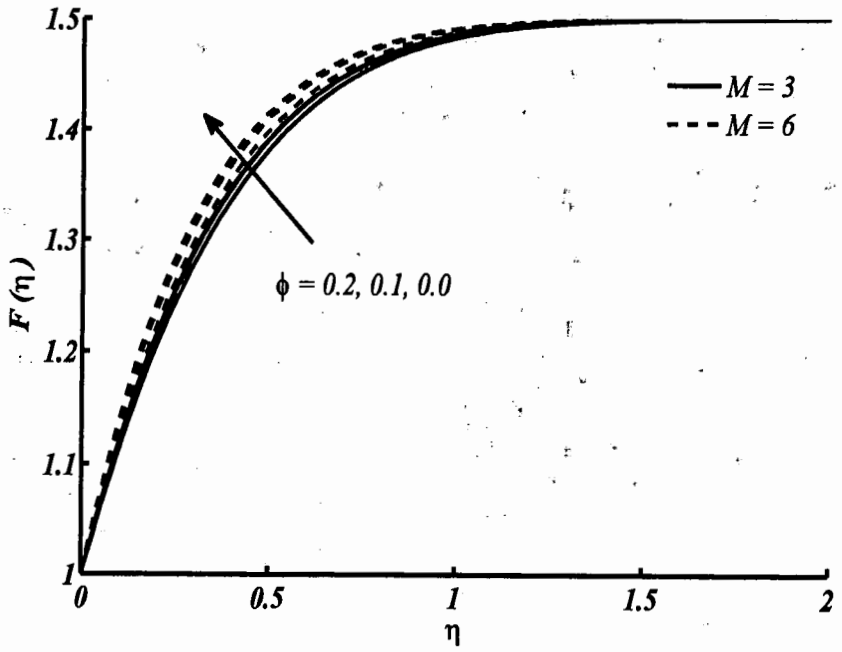

Figure 5.2: Radial velocity profile for magnetite (Fe_3O_4) water ferrofluid for distinct values of ϕ when $\omega = 0.5$ and $a/c = 1.5$.

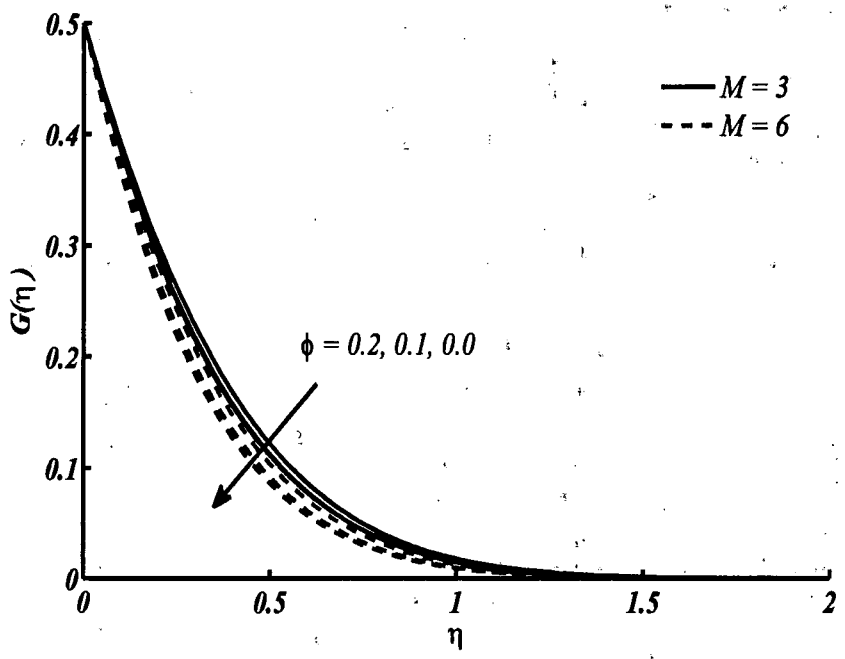

Figure 5.3: Azimuthal velocity profile for magnetite (Fe_3O_4) water ferrofluid for distinct values of ϕ when $\omega = 0.5$ and $a/c = 1.5$.

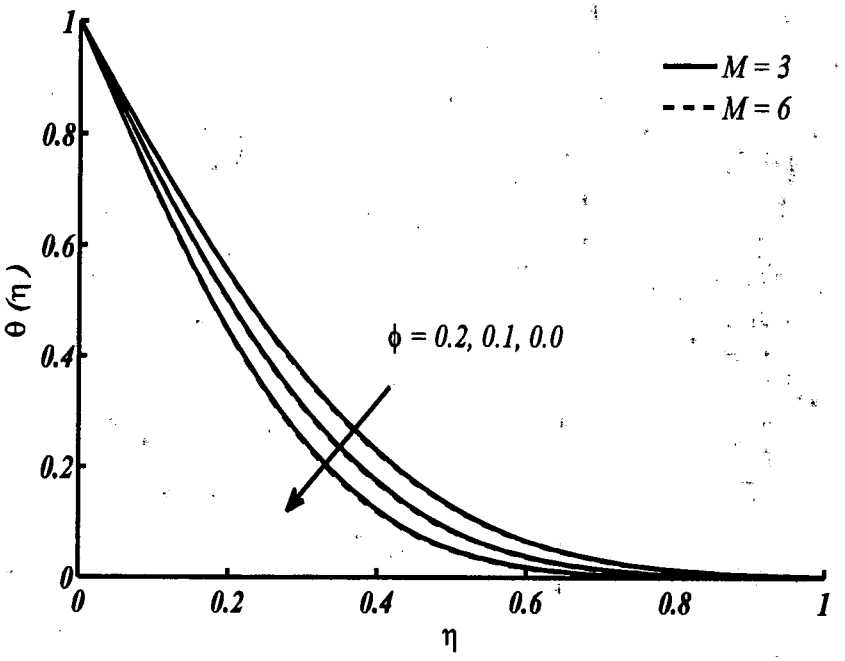

Figure 5.4: Temperature profile for Magnetite (Fe_3O_4) water ferrofluid for distinct values of ϕ when $\omega = 0.5$, Pr = 6.2 and $a/c = 1.5$.

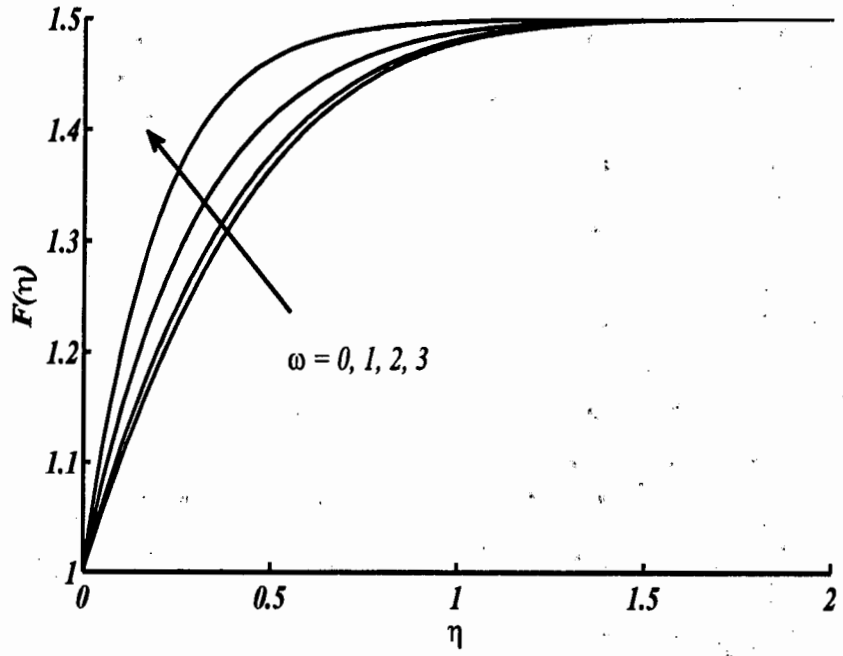

Figure 5.5: Radial velocity profile for Magnetite (Fe_3O_4) water ferrofluid for distinct values of ω when $\phi = 0.2$, $M = 1$ and $a/c = 1.5$.

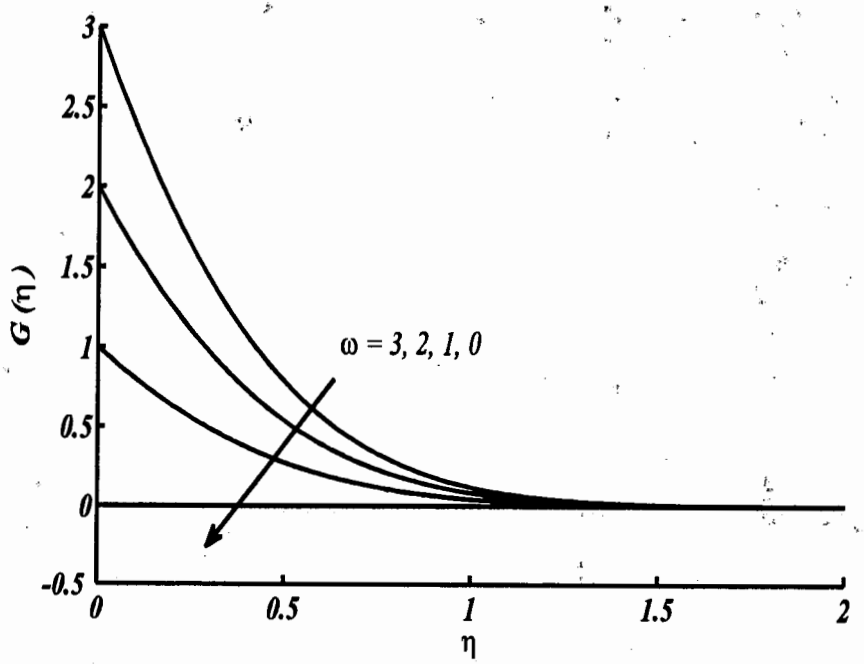

Figure 5.6: Azimuthal velocity profile for Magnetite (Fe_3O_4) water ferrofluid for distinct values of ω when $\phi = 0.2$, $M = 1$ and $a/c = 1.5$.

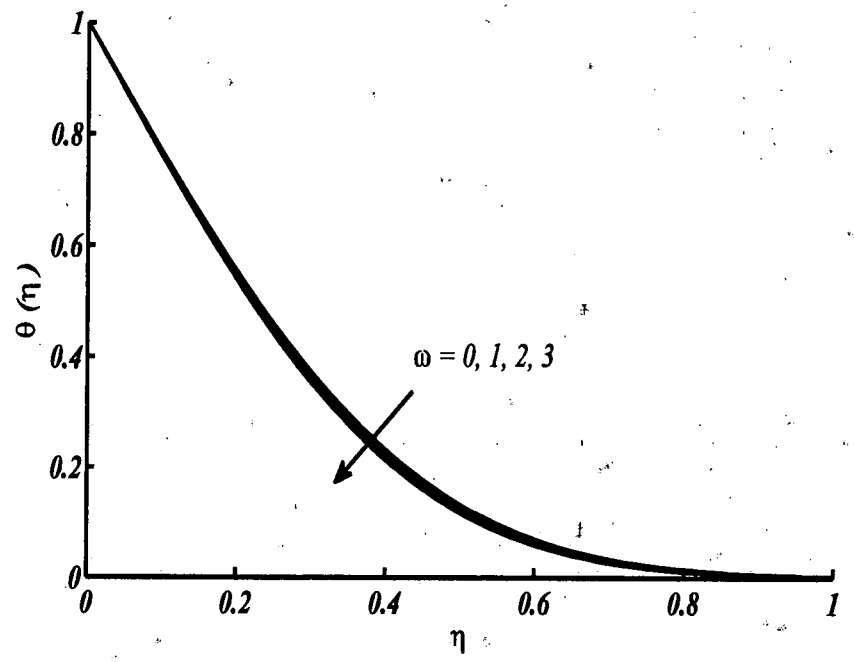

Figure 5.7: Temperature profile for Magnetite (Fe_3O_4) water ferrofluid for distinct values of ω when $\phi = 0.2$, Pr = 6.2, $M = 1$ and $a/c = 1.5$.

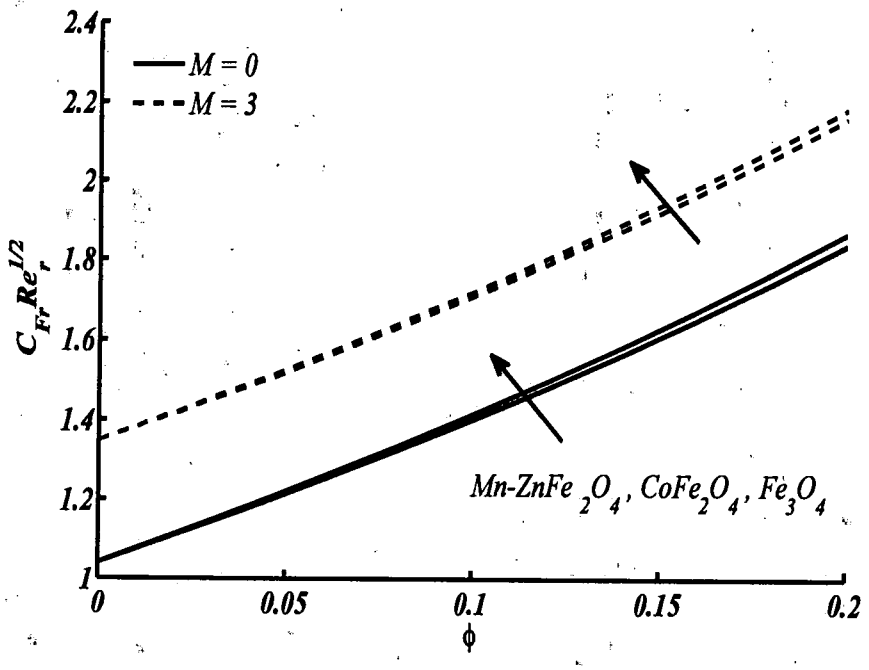

Figure 5.8: Skin friction coefficient in radial direction for distinct values of M when $\omega = 0.5$ and $a/c = 1.5$.

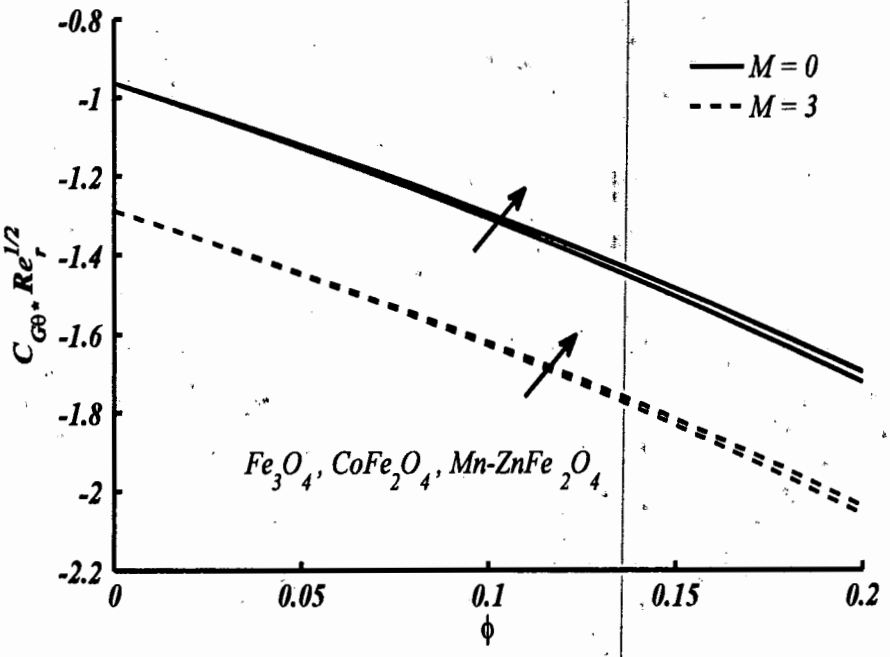

Figure 5.9: Skin friction coefficient in azimuthal direction for distinct values of M when ω = 0.5 and a/c = 1.5.

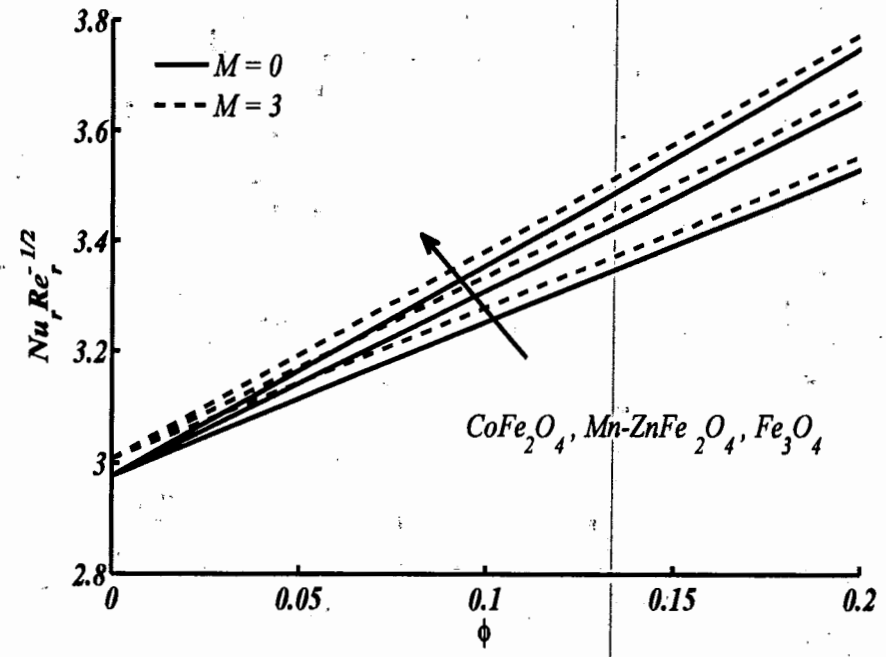

Figure 5.10: Local Nusselt number for distinct values of M when ω = 0.5, Pr = 6.2 and a/c = 1.5.

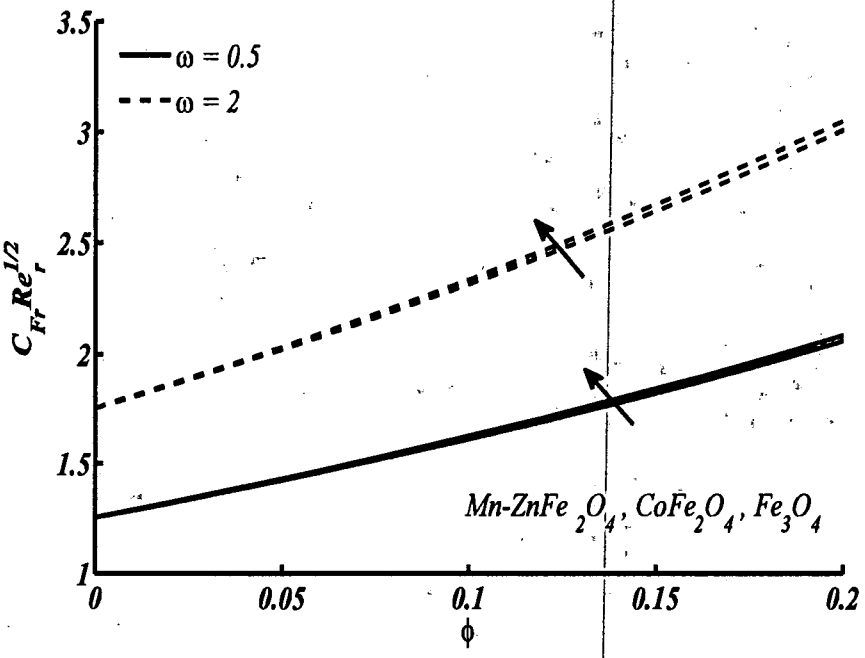

Figure 5.11: Skin friction coefficient in radial direction for distinct values of ω when $M = 2$ and $a/c = 1.5$.

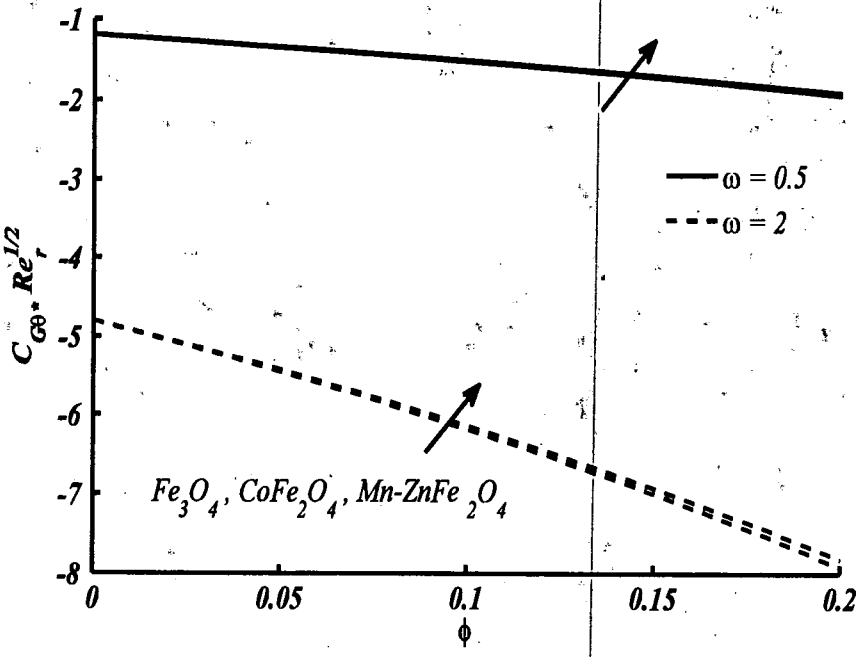

Figure 5.12: Skin friction coefficient in azimuthal direction for distinct values of ω when $M = 2$ and $a/c = 1.5$.

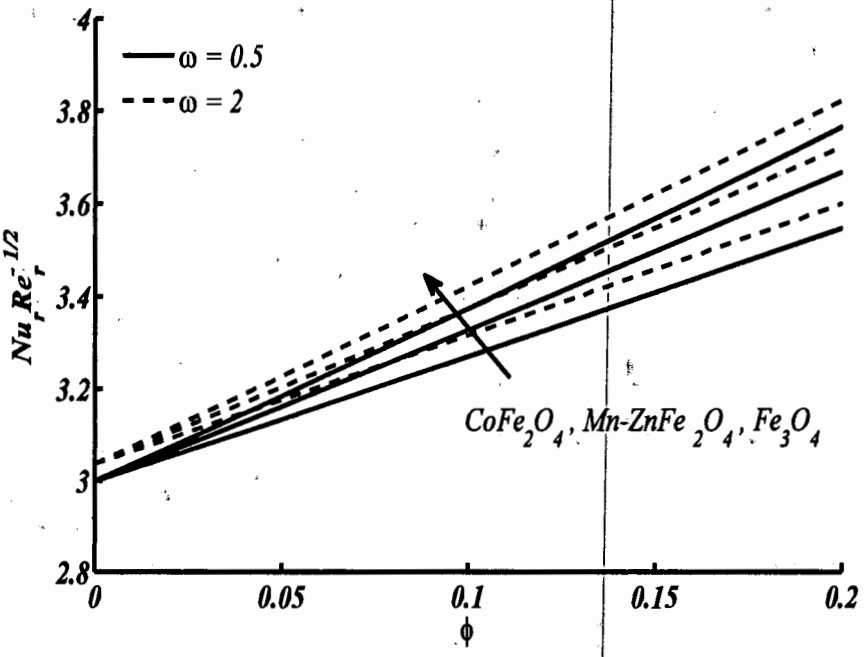

Figure 5.13: Local Nusselt number for distinct values of ω when $M = 2$, Pr = 6.2 and $a/c = 1.5$.

5.3 Conclusions

A study on heat transfer analysis in boundary layer flow of ferrofluid near the stagnation point region over a stretchable rotating disk in the presence of external magnetic field is investigated. The governing equations are modeled in terms of system of nonlinear partial differential equations which are later reduced to four nonlinear ordinary differential equations. The Keller Box method is again used to compute its solution in terms of velocity, temperature, skin friction coefficients and local Nusselt number. The effects of pertinent parameters namely, volume fraction parameter of nanofluid, magnetic parameter, rotation parameter on velocity profiles in radial and azimuthal directions, temperature profile, skin friction coefficients and local Nusselt number are examined through graphs. It is observed that for magnetite ferroparticle (Fe_3O_4), the radial velocity decreases and the velocity in azimuthal direction and temperature increase by increasing the volume fraction parameter ϕ. The effects of magnetic parameter on velocity profiles in both radial and azimuthal directions and temperature profile show an opposite behavior as observed against volume fraction parameter ϕ. For magnetite ferroparticle (Fe_3O_4), the velocities in both radial and azimuthal directions increase and temperature decreases by increasing the effects of rotation parameter. The values of skin friction coefficient in radial direction and local Nusselt number of magnetite ferroparticle (Fe_3O_4) are higher than that of

other ferroparticles. An opposite behavior is observed in azimuthal direction. Skin friction coefficient in radial direction and local Nusselt number increase by increasing rotation parameter and skin friction coefficient decreases in azimuthal direction.

Chapter 6

Heat transfer in stagnation point flow of a nanofluid over a nonlinearly permeable stretching/shrinking sheet with Newtonian heating

In this chapter, the heat transfer analysis in nanofluid flow near the region of stagnation point over a non-linear permeable stretching/shrinking sheet in the presence of Newtonian heating is presented. The two very important mechanism on the transportation of nanoparticles in base fluid are discussed, which are known as Brownian (*Nb*) and Thermophoresis (*Nt*) parameters. This physical problem is modeled using Buongiorno [58] model under the boundary layer assumption and similarity solution is calculated through numerical scheme using Chebyshev spectral collocation method. Dual solution is reported against shrinking parameter and ranges of these solutions are affected by suction parameter which are discussed through graphs and table. The effects of emerging dimensionless parameters on velocity, temperature and concentration profiles as well as skin friction coefficient, local Nusselt number and Sherwood number are shown through graphs. For the validity of the computed results, a comparison is established with published studies in limiting case. Through the results, the enhancement in temperature and concentration profiles is observed in the presence of Newtonian heating.

6.1 Mathematical formulation

A boundary layer steady flow of viscous incompressible nanofluid in the region of stagnation point towards a non-linear stretching/shrinking horizontal permeable sheet is discussed. The sheet is stretched or shrunk non-linearly along x–axis keeping O fixed as a stagnation point and y–axis is taken normal to the sheet as shown in Fig. 6.1. The non-linear stretching/shrinking velocity and straining velocity in potential flow are assumed as $u_w(x) = cx^m$ and $u_e(x) = ax^m$ respectively, where a is +ve constant and c is the constant in wall velocity, which is considered less than zero ($c < 0$) in shrinking case and greater than zero ($c > 0$) in stretching case. Using the Buongiorno model the governing equations of the problem under the boundary layer approximations can be written in the simplified form as

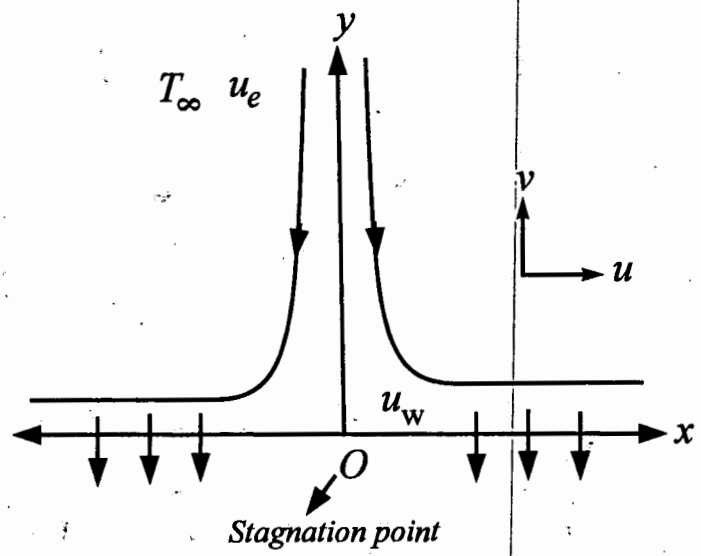

Figure 6.1: The physical geometry of the flow model near the region of stagnation point.

$$\frac{\partial u}{\partial x}+\frac{\partial v}{\partial y}=0, \tag{6.1}$$

$$u\frac{\partial u}{\partial x}+v\frac{\partial u}{\partial y}=u_e(x)\frac{du_e(x)}{dx}+\nu_f\frac{\partial^2 u}{\partial y^2}, \tag{6.2}$$

$$u\frac{\partial T}{\partial x}+v\frac{\partial T}{\partial y}=\alpha_f\frac{\partial^2 T}{\partial y^2}+\tau^*\left[D_B\frac{\partial C}{\partial y}\frac{\partial T}{\partial y}+\frac{D_T}{T_\infty}\left(\frac{\partial T}{\partial y}\right)^2\right], \tag{6.3}$$

$$u\frac{\partial C}{\partial x}+v\frac{\partial C}{\partial y}=D_B\frac{\partial^2 C}{\partial y^2}+\frac{D_T}{T_\infty}\frac{\partial^2 T}{\partial y^2}, \tag{6.4}$$

with boundary conditions

$$\begin{gathered}u=u_w(x)=cx^m, v=v_w(x), -k_f\frac{\partial T}{\partial y}=h_s T, C=C_w \text{ at } y=0,\\ u\to u_e(x)=ax^m, T\to T_\infty, C\to C_\infty \text{as } y\to\infty.\end{gathered} \tag{6.5}$$

The components of velocity along and normal to the surface are u and v respectively, C is the nanoparticle concentration, α_f is the thermal diffusivity of base fluid, v_w is suction velocity at the wall along y-axis, which exhibits suction in case of less than zero ($v_w < 0$) or injection in case of greater than zero ($v_w > 0$), h_s is the heat transfer coefficient, $m \neq 1$ is a nonlinear parameter, C_w and C_∞ are nanoparticle concentrations at the wall and far away from the wall. Now introducing the similarity transformation [101]

$$u = ax^m f'(\eta), v = -\sqrt{\frac{av_f(m+1)}{2}}x^{(m-1)/2}\left[f(\eta)+\frac{m-1}{m+1}\eta f'(\eta)\right],$$
$$\eta = y\sqrt{\frac{a(m+1)}{2v_f}}x^{(m-1)/2}, \theta = \frac{T-T_\infty}{T_\infty}, \varphi = \frac{C-C_\infty}{C_w-C_\infty}, \quad (6.6)$$

where differentiation with respect to η is denoted by prime. For similarity solution of the governing equations, a suction or injection velocity v_w is assumed as

$$v_w = -\sqrt{\frac{av_f(m+1)}{2}}x^{(m-1)/2}\gamma,$$

where γ is a constant and stand for suction when γ is greater than zero ($\gamma > 0$) and injection when γ is less than zero ($\gamma < 0$). Using the similarity transformation (6.6) into the Eqs. (6.2–6.4), the dimensionless form of ordinary differential equations is obtained as

$$f''' + ff'' + \frac{2m}{m+1}\left(1-f'^2\right) = 0, \quad (6.7)$$

$$\theta'' + \Pr\left(f\theta' + Nb\theta'\varphi' + Nt\theta'^2\right) = 0, \quad (6.8)$$

$$\varphi'' + Scf\varphi' + \frac{Nt}{Nb}\theta'' = 0, \quad (6.9)$$

with boundary conditions Eq. (6.5) reduce to

$$f(0) = \gamma, f'(0) = \frac{c}{a}, \theta'(0) = -\gamma_s\left(1+\theta(0)\right), \varphi(0) = 1,$$
$$f'(\infty) = 1, \theta(\infty) = 0, \varphi(\infty) = 0, \quad (6.10)$$

where $Sc = v_f/D_B$ is the Schmidt number, $Nb = \tau D_B\left(C_w - C_\infty\right)/v_f$ is the Brownian motion parameter, $Nt = \tau D_T/v_f$ is the thermophoresis parameter, $\gamma_s = h_s/k_f\sqrt{2/(m+1)x\,\mathrm{Re}_x^{-1/2}}$ is the conjugate parameter for Newtonian heating and *c/a* is the ratio of the constant of stretching/shrinking velocity and straining velocity, which corresponds to stretching in case of greater than zero (*c/a* > 0) and shrinking in case of less than zero (*c/a* < 0). The relations of skin friction coefficient, local Nusselt and Sherwood numbers are defined as

$$C_f = \frac{\tau_w}{\rho_f u_e^2}, \; Nu_x = \frac{xq_w}{k_f\left(T_w - T_\infty\right)}, Sh_x = \frac{xq_m}{D_B\left(C_w - C_\infty\right)}, \quad (6.11)$$

where τ_w is shear stress at the wall, q_w and q_m are the heat and mass fluxes from the wall respectively, which are written as

$$\tau_w = \mu_f\left(\frac{\partial u}{\partial y}\right)_{y=0}, \; q_w = -k_f\left(\frac{\partial T}{\partial y}\right)_{y=0}, q_m = -D_B\left(\frac{\partial C}{\partial y}\right)_{y=0}. \quad (6.12)$$

After using Eq. (6.12) into Eq. (6.11), the skin friction coefficient, local Nusselt number and local Sherwood number take the new form as follows

$$C_f \,\mathrm{Re}_x^{\frac{1}{2}} = \sqrt{\frac{m+1}{2}} f''(0),\ Nu_x \,\mathrm{Re}_x^{-\frac{1}{2}} = -\sqrt{\frac{m+1}{2}} \frac{\theta'(0)}{\theta(0)},\ Sh_x \,\mathrm{Re}_x^{-\frac{1}{2}} = -\sqrt{\frac{m+1}{2}} \varphi'(0).$$

6.2 Results and discussion

To obtain the numerical solution of the non-linear ordinary differential equations given in Eqs. (6.7-6.9) subject to the boundary conditions given in Eq. (6.10), a numerical method is applied known as Chebyshev spectral collocation method. The details of this method have been discussed in chapter 2. The effects of pertinent parameters namely suction, velocity ratio, Prandtl number, thermophoresis and Brownian motion, Newtonian heating and Schmidt number on the f' (velocity), θ (temperature), φ (nanoparticle concentration) profiles, $C_f \,\mathrm{Re}_x^{1/2}$ (skin friction coefficient), $Nu_x \,\mathrm{Re}_x^{-1/2}$ (local Nusselt number) and $Sh_x \,\mathrm{Re}_x^{-1/2}$ (Sherwood number) are computed and shown in terms of figures. Dual solution of the problem for a range of values of suction parameter γ are found by considering different η_∞ and initial guess and two distinct structure of boundary layer thicknesses are observed. The solid line represents the first solution and dotted line represents the second solution. For the validity of applied Chebyshev spectral collocation method, a comparison of the values of $f''(0)$, $\theta(0)$ and $-\theta'(0)$ with that of previous studies considered by Wang [29], Bachok et al. [69] and Mohammed et al. [110] are shown in Tables 6.1 and 6.2. This shows that the computed solutions are in good agreement and hence the solution scheme and code are accurate. Figs. 6.2–6.4 show the variation of $C_f \,\mathrm{Re}_x^{1/2}$, $Nu_x \,\mathrm{Re}_x^{-1/2}$ and $Sh_x \,\mathrm{Re}_x^{-1/2}$ against velocity ratio parameter c/a for some values of suction parameter γ with the fixed values of remaining parameters $m = 2$, $Sc = 1.5$, $\mathrm{Pr} = 7$, $\gamma_s = 1$ and $Nt = Nb = 0.3$. From these figures, it is seen that dual solutions exist for each positive value of c/a under the different values of suction parameter $\gamma = 2.5$, 3 and 3.5. However, for negative values of c/a, there exist critical values t_1 for which dual solution exists in the case ($c/a > t_1$) and no solution exists in the case ($c/a < t_1$), which are presented in Table 6.3. It is also seen that the region of c/a for which the dual solution exists increases with the increase of suction parameter γ. Zaimi et al. [103] found dual solutions for the same values of suction parameter $\gamma = 2.5$, 3 and 3.5 without considering stagnation point flow and they showed the critical values for which dual solutions exist, which are shown in Table 6.3. From Table 6.3, it is seen that the ranges of the dual solutions in the present study

are increased as compared to previous study due to stagnation point flow. This finding shows that stagnation point flow widens the ranges of dual solutions. A number of researchers like Weidman et al. [144] and Rosca and Pop [145] have discussed the stability analysis of multiple solutions. They have proved that the first solution as a stable solution and second solution as an unstable solution. Fig. 6.2 depicts that the values of $C_f \, \mathrm{Re}_x^{1/2}$ increase in stable solution (first solution) and decrease in unstable solution (second solution) by increasing the values of suction parameter γ. In Figs. 6.3 and 6.4 the local Nusselt number and Sherwood number are plotted against velocity ratio parameter c/a for some values of suction parameter $\gamma = 2.5$, 3.0 and 3.5. From these Figs. 6.3 and 6.4, it is noted that both $Nu_x \, \mathrm{Re}_x^{-1/2}$ and $Sh_x \, \mathrm{Re}_x^{-1/2}$ increase by increasing of suction parameter γ. In case of first solution, both the values of $Nu_x \, \mathrm{Re}_x^{-1/2}$ and $Sh_x \, \mathrm{Re}_x^{-1/2}$ decrease by reducing the values of c/a. The values of $Nu_x \, \mathrm{Re}_x^{-1/2}$ in first solution become smaller than that of the second solution and an opposite behavior is noticed for the values of $Sh_x \, \mathrm{Re}_x^{-1/2}$. Fig. 6.5 illustrates the variation of $Nu_x \, \mathrm{Re}_x^{-1/2}$ against c/a for some values of Pr. It is seen that $Nu_x \, \mathrm{Re}_x^{-1/2}$ increases with the increase of Pr, it is also seen that for the small value of Pr = 3, the first solution maintained a higher value of $Nu_x \, \mathrm{Re}_x^{-1/2}$ for $-3.565 < c/a < -0.15$, and after it, the second solution bisects the first solution. For large values of Prandtl number Pr, first solution has smaller values of $Nu_x \, \mathrm{Re}_x^{-1/2}$ than the second solution. Figs. 6.6(a) and 6.6(b) demonstrate the effects of γ (suction) on velocity profiles for shrinking and stretching cases respectively while other parameters are considered fixed. For the first solution in Fig. 6.6(a), velocity increases and momentum boundary layer thickness reduces by increasing of γ (suction). Because suction enhances the flow near the surface and reduces the momentum boundary layer thickness in case of shrinking sheet. Also for the second solution negative velocity gradient is found at the edge of the sheet and become positive away from the sheet. In Fig. 6.6(b), velocity reduces for first solution with the increase of suction parameter γ because suction is responsible for delay in fluid motion over a stretching sheet. In case of second solution velocity reduces by increasing suction parameter γ for the initial values of η and becomes an increasing function for large η. Figs. 6.7(a, b) and 6.8(a, b) illustrate temperature and nanoparticle concentration profiles against the thermophoresis parameter Nt. Figs. 6.7(a) and 6.7(b) reveal that variation of Nt from 0.1 to 0.7 enhances both temperature and thermal boundary layer thickness for first and second solutions respectively. But it is noticed that the magnitude of temperature difference and increase in boundary layer is almost negligible. It is further noticed that thermal boundary layer thickness is higher in case of

shrinking sheet as compared to that of stretching sheet. Figs. 6.8(a) and 6.8(b) depict that nanoparticle concentration increases with the increase of *Nt* for both first and second solutions, this is due to the physical mean that the thermophoresis increases the mass transfer of nanofluids. In Fig. 6.8(a), a positive concentration gradient $\varphi'(0)$ is obtained at the surface of the plate for the second solution when thermophoresis parameter is $Nt = 0.7$ and become negative for other values of $Nt = 0.4$ and 0.1. Also In Figs. 6.8(a, b) concentration boundary layer thickness is higher in second solution as compared to first solution. Figs. 6.9(a, b) and 6.10 (a, b) are plotted to show the effect of *Nb* (Brownian motion) on temperature and nanoparticle concentration profiles. Figs 6.9(a) and 6.9(b) demonstrate that variation of *Nb* from 0.1 to 0.3 enhances temperature and thermal boundary layer thickness for all solutions. This is due to the reason that the Brownian motion of nanoparticles enhances the temperature of the fluid. Figs. 6.10(a) and 6.10(b) illustrate that nanoparticle concentration decreases with the increase of Brownian motion parameter *Nb* for both solutions. Also for the second solution, the concentration boundary layer thickness in both shrinking and stretching cases is greater than that of the first solution. In Fig. 6.10(a), a positive concentration gradient $\varphi'(0)$ is obtained for $Nb = 0.1$ and negative concentration gradient $\varphi'(0)$ for other values of $Nb = 0.2$ and 0.3 is observed. The effects of Schmidt number on temperature profile and nanoparticle concentration profile are presented through Figs. 6.11(a, b) and 6.12(a, b) for both shrinking and stretching cases respectively. In Figs. 6.11(a) and 6.11(b), it is seen that temperature and thermal boundary layer thickness increase with increasing values of *Sc* for both solutions. On the other hand, nanoparticle concentration profile shows an opposite behavior by increasing *Sc* for both first and second solutions. From both Figs. 6.12(a) and 6.12(b), it is observed that concentration boundary layer thickness for $Sc = 2$ as predicted by the second solution are larger than that of the first solution in shrinking and stretching cases, which is responsible for instability of the second solution. The temperature and nanoparticle concentration profiles for different values of conjugate parameter γ_s are presented in Figs. 6.13(a, b) and 6.14(a, b). The effect of conjugate parameter γ_s on temperature profile by both first and second solutions shows that temperature and thermal boundary layer thickness increase with the increase of γ_s in both shrinking and stretching cases respectively. It is noted that when conjugate parameter γ_s is zero the temperature at the wall becomes zero i.e. insulated wall case and when $\gamma_s \to \infty$ the Newtonian heating condition becomes the condition of constant wall temperature. Physically it is due to the fact that the temperature becomes zero when conjugate parameter γ_s is zero, therefore, by increasing conjugate parameter γ_s the temperature enhances within the boundary

layer. The same behavior is observed in nanoparticle concentration profile but in second solution the boundary layer thickness is greater than that for the first solution.

Table 6.I: Numerical results of $f''(0)$ for some values of c/a with $m = 1$ and $\gamma = 0$.

c/a	Wang [29]	Bachok et al. [69]	Present study
2	-1.88731	-1.887307	-1.887307
1	0	0	0
0.5	0.71330	0.713295	0.713295
0	1.232588	1.232588	1.232588
-0.5	1.49567	1.495670	1.495670
-1	1.32882	1.328817	1.328817
	[0]	[0]	[0]
-1.15	1.08223	1.082231	1.082231
	[0.116702]	[0.116702]	[0.116702]
-1.2		0.932473	0.932473
		[0.233650]	[0.233650]
-1.2465	0.55430	0.584281	0.584282
		[0.554297]	[0.554296]

Table 6.2: Numerical results of $-\theta'(0)$ and $\theta(0)$ for some values of Pr when $m = \gamma_s = 1$ and $\gamma = c/a = 0$.

	Mohammed et al. [110]		Present result	
Pr	$\theta(0)$	$-\theta'(0)$	$\theta(0)$	$-\theta'(0)$
5	23.0239	24.0239	23.0239	24.0239
7	5.6062	6.6062	5.6062	6.6062
10	2.9516	3.9516	2.9516	3.9516
100	0.5034	1.5034	0.50327	1.5033
1000	0.1809	1.1809	0.1809	1.1809

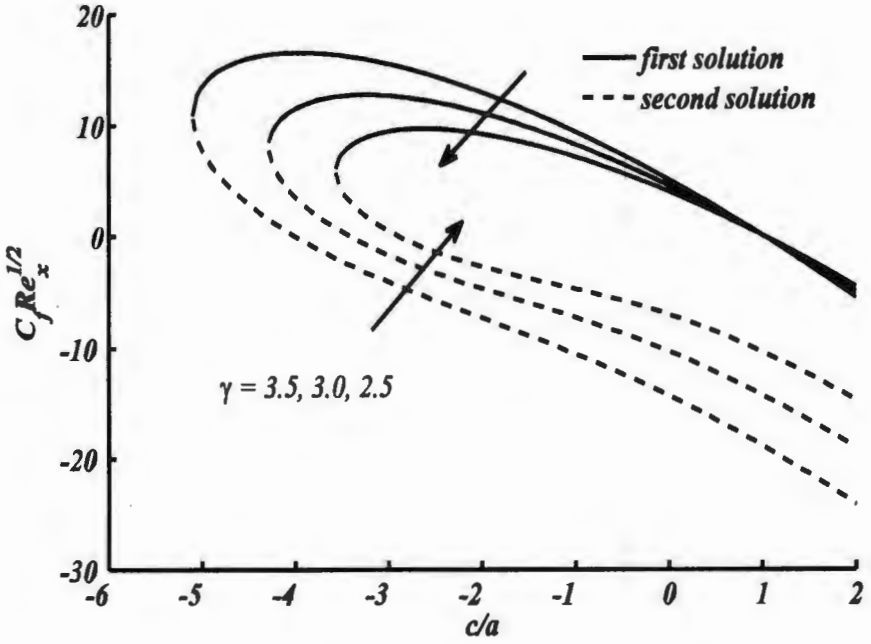

Figure 6.2: Skin friction coefficient against *c/a* for distinct values of suction parameter γ.

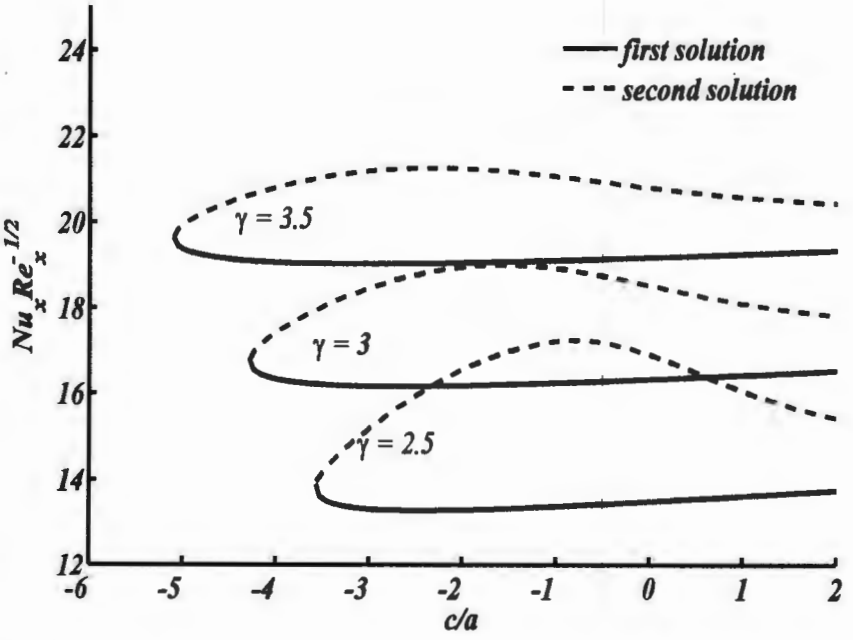

Figure 6.3: Local Nusselt number against *c/a* for distinct values of suction parameter γ.

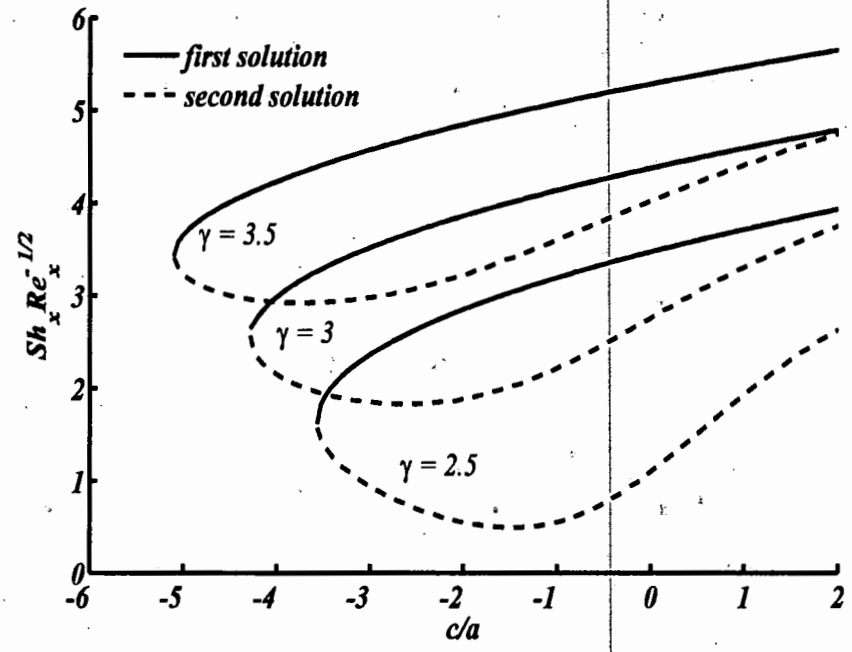

Figure 6.4: Sherwood number against *c/a* for distinct values of suction parameter γ.

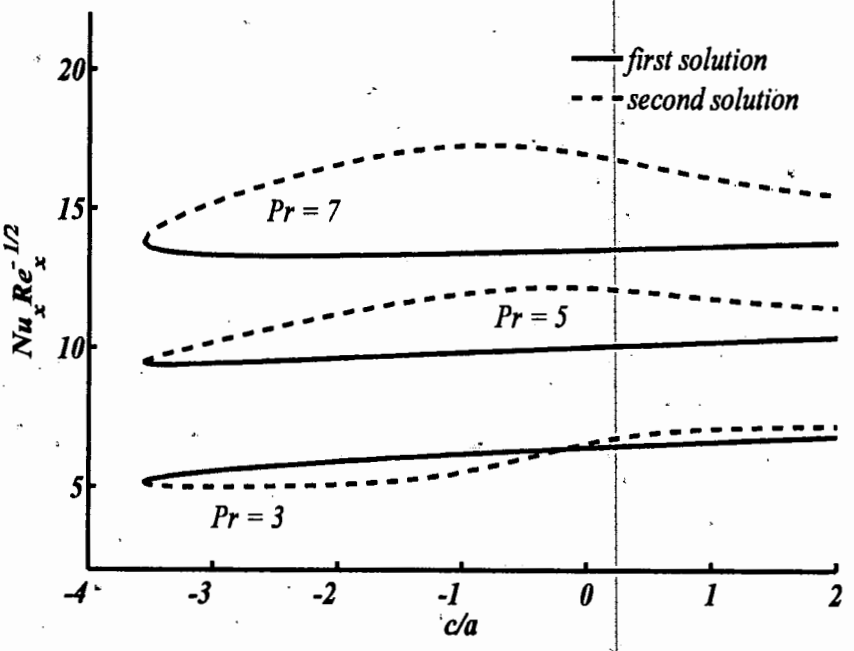

Figure 6.5: Local Nusselt number against *c/a* for distinct values of Prandtl number Pr.

(a)

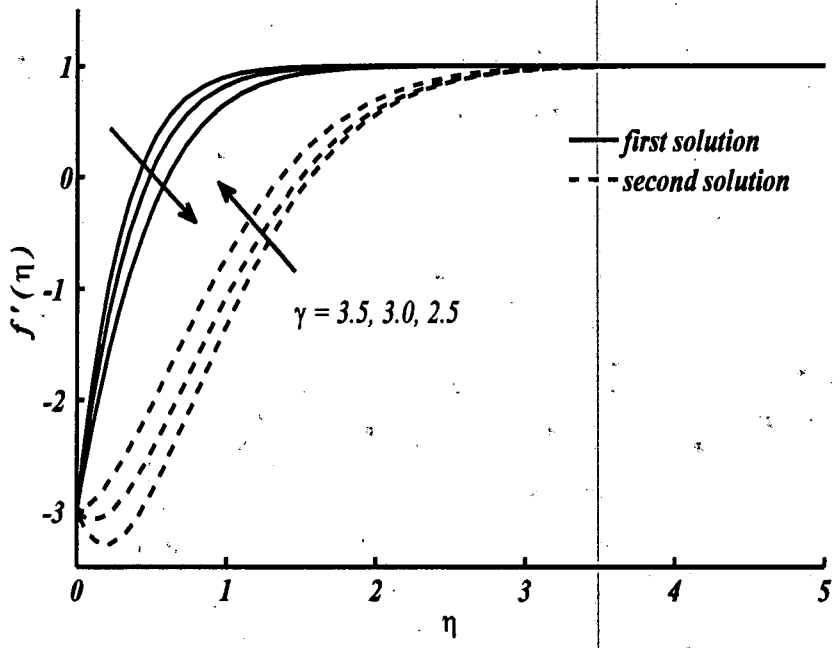

(b)

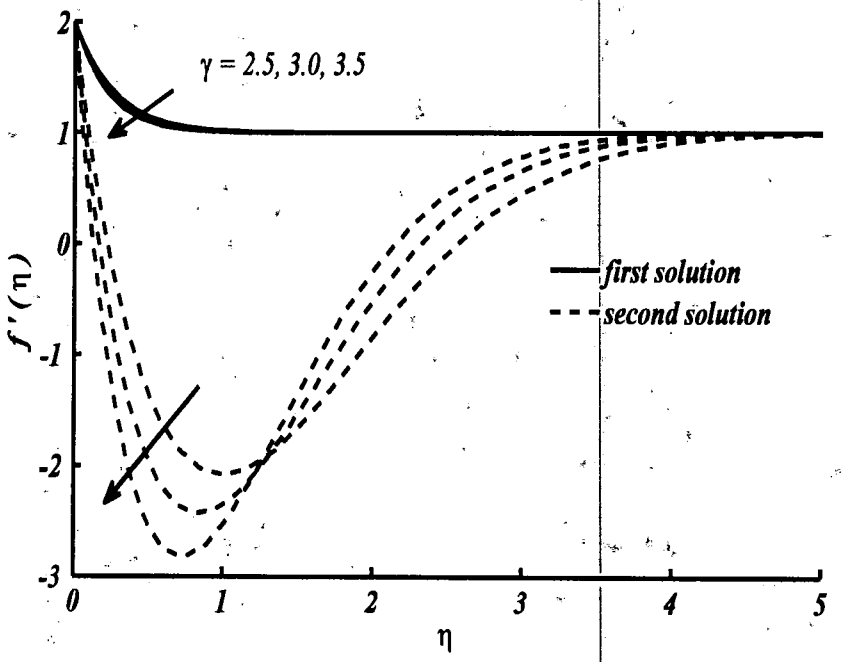

Figure 6.6(a, b): Velocity profile for distinct values of γ when $m = 2$, $Sc = 1.5$, $\Pr = 7$, $\gamma_s = 1$, $Nt = Nb = 0.3$ (a) shrinking sheet $c/a = -3$ (b) stretching sheet $c/a = 2$.

(a)

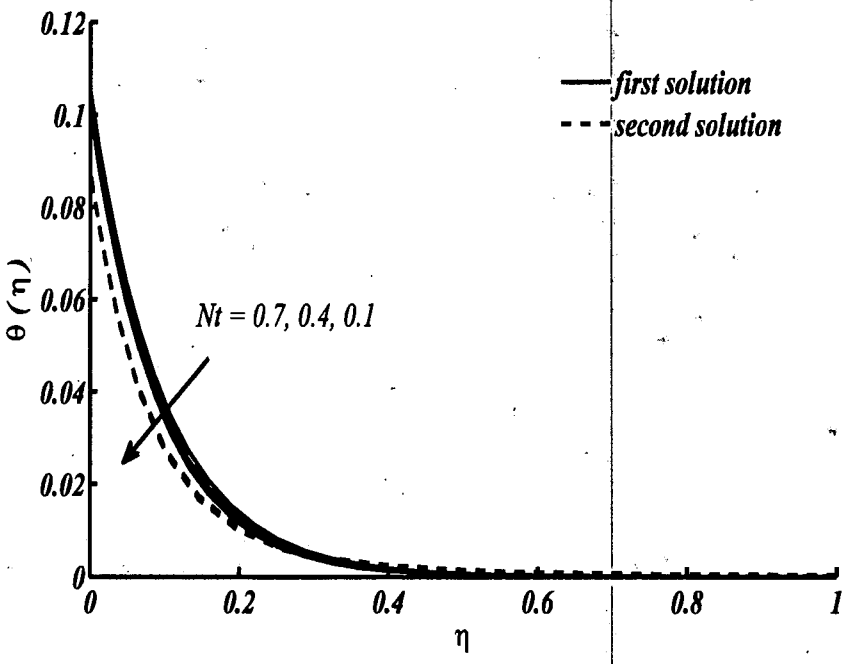

(b)

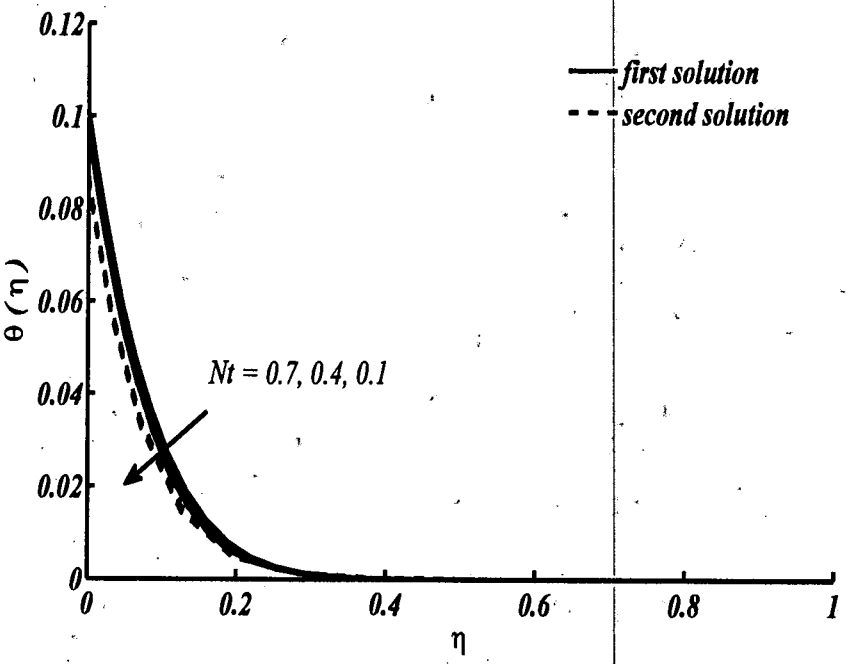

Figure 6.7(a, b): Temperature profile for distinct values of Nt when $m = 2$, $Sc = 1.5$, $\Pr = 7$, $\gamma_s = 1$, $Nb = 0.3$, $\gamma = 2.5$ (a) shrinking sheet $c/a = -3$ (b) stretching sheet $c/a = 2$.

(a)

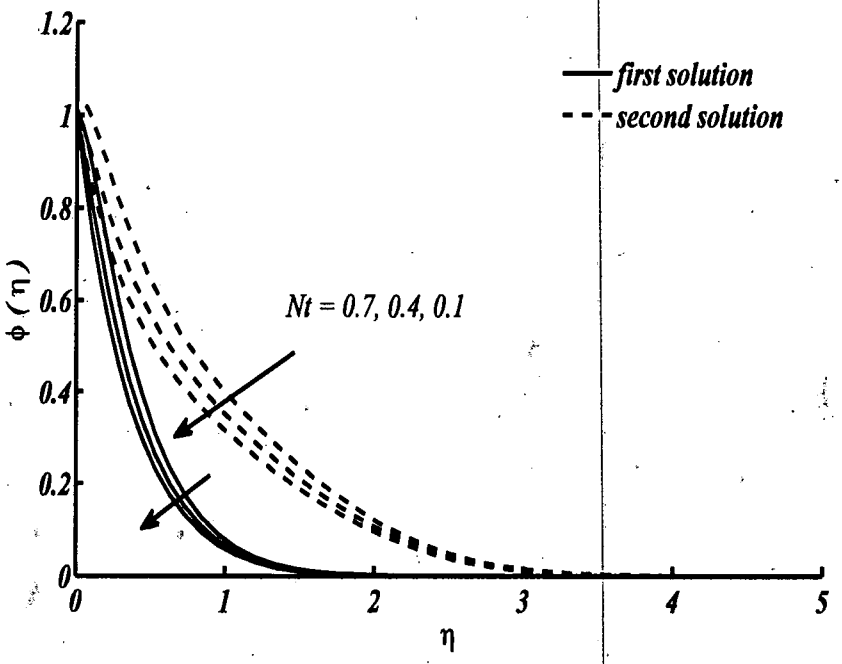

(b)

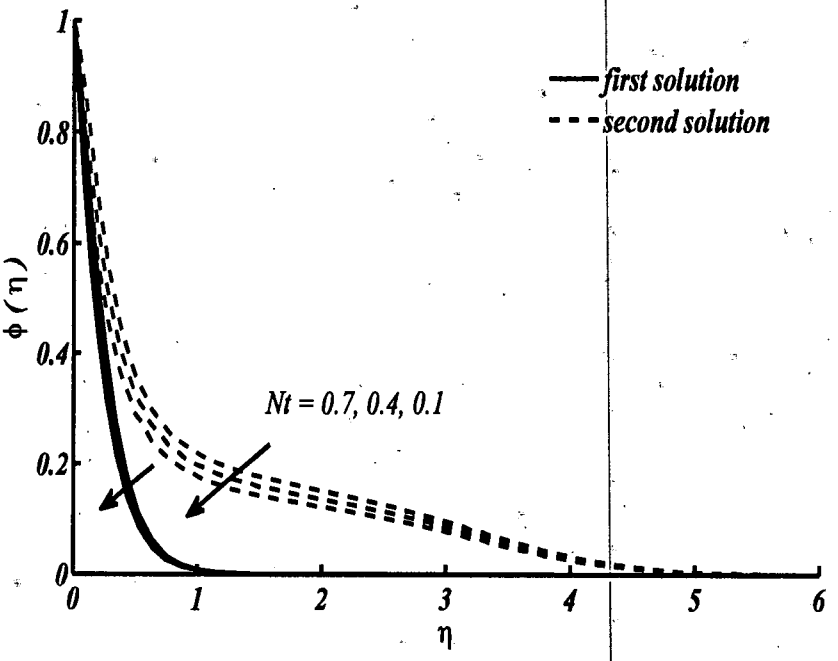

Figure 6.8(a, b): Nanoparticle concentration profile for distinct values of Nt when $m = 2$, $Sc = 1.5$, $\Pr = 7$, $\gamma_s = 1$, $Nb = 0.3$, $\gamma = 2.5$ (a) shrinking sheet $c/a = -3$ (b) stretching sheet $c/a = 2$.

(a)

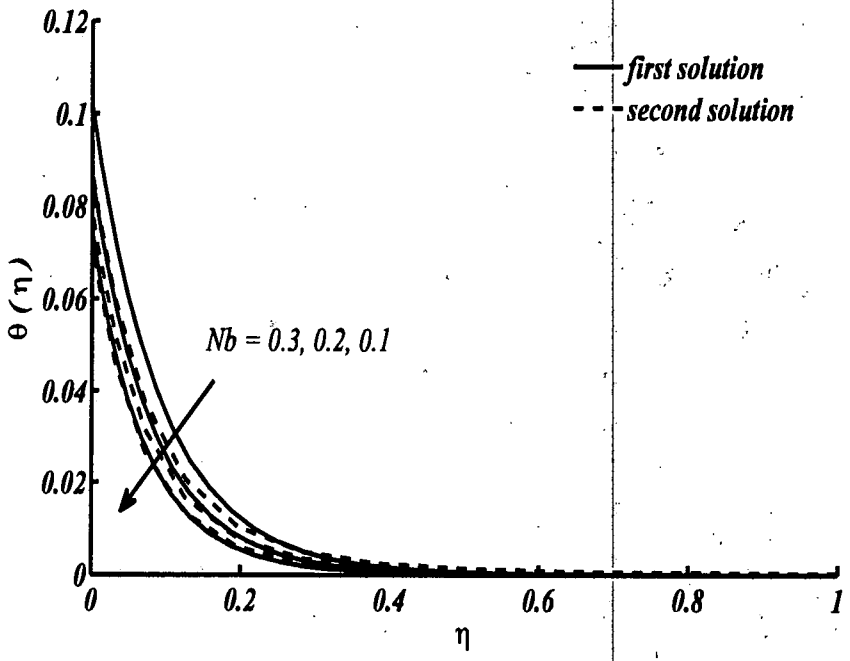

(b)

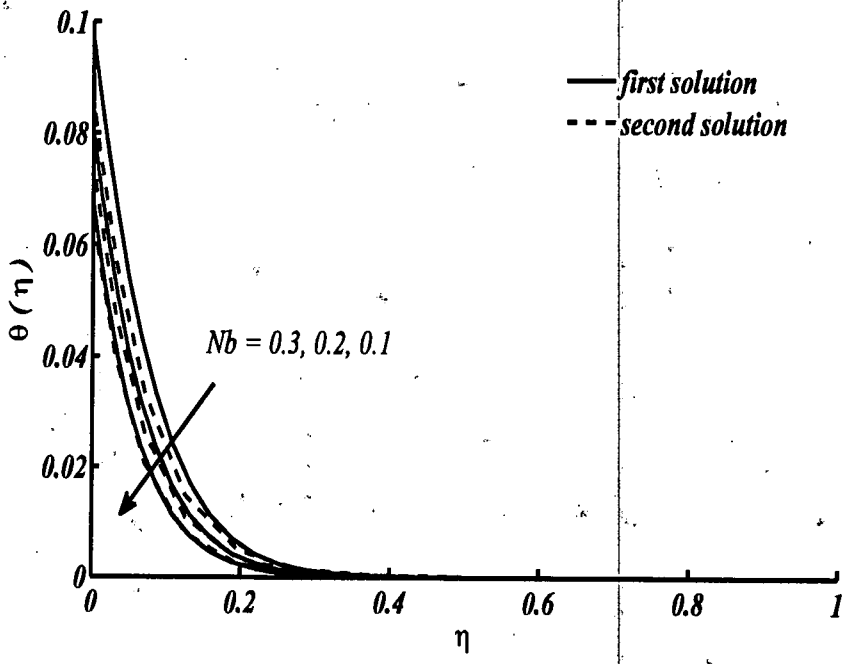

Figure 6.9(a, b): Temperature profile for distinct values of Nb when $m = 2$, $Sc = 1.5$, $\Pr = 7$, $\gamma_s = 1$, $Nt = 0.3$, $\gamma = 2.5$ (a) shrinking sheet $c/a = -3$ (b) stretching sheet $c/a = 2$.

(a)

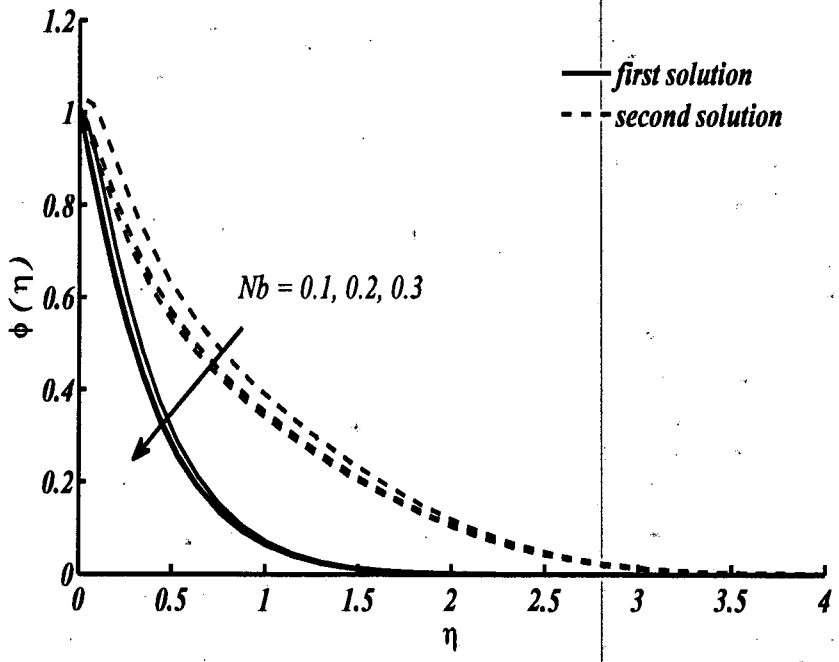

(b)

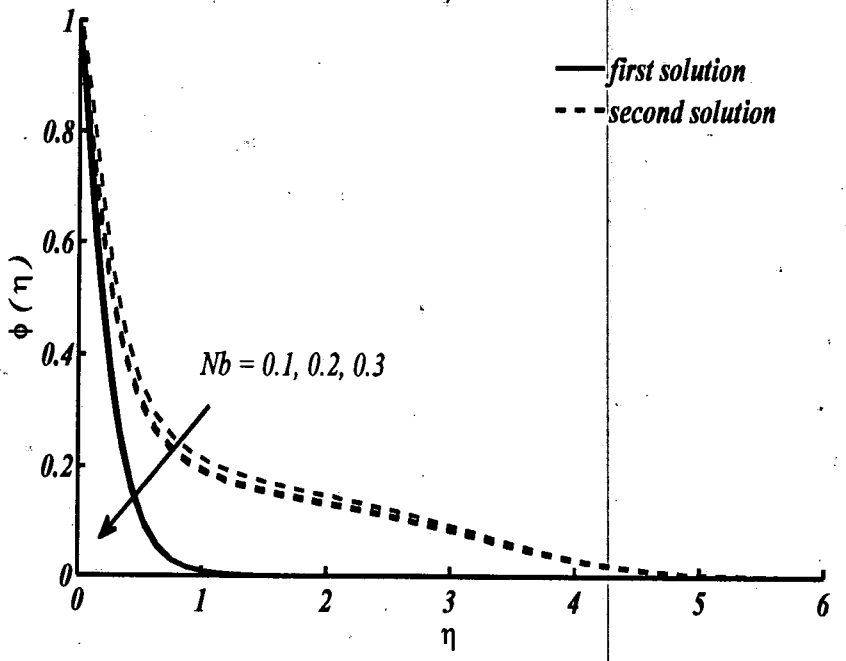

Figure 6.10(a, b): Nanoparticle concentration profile for distinct values of *Nb* when $m = 2$, $Sc = 1.5$, $\Pr = 7$, $\gamma_s = 1$, $Nt = 0.3$, $\gamma = 2.5$ (a) shrinking sheet $c/a = -3$ (b) stretching sheet $c/a = 2$.

(a)

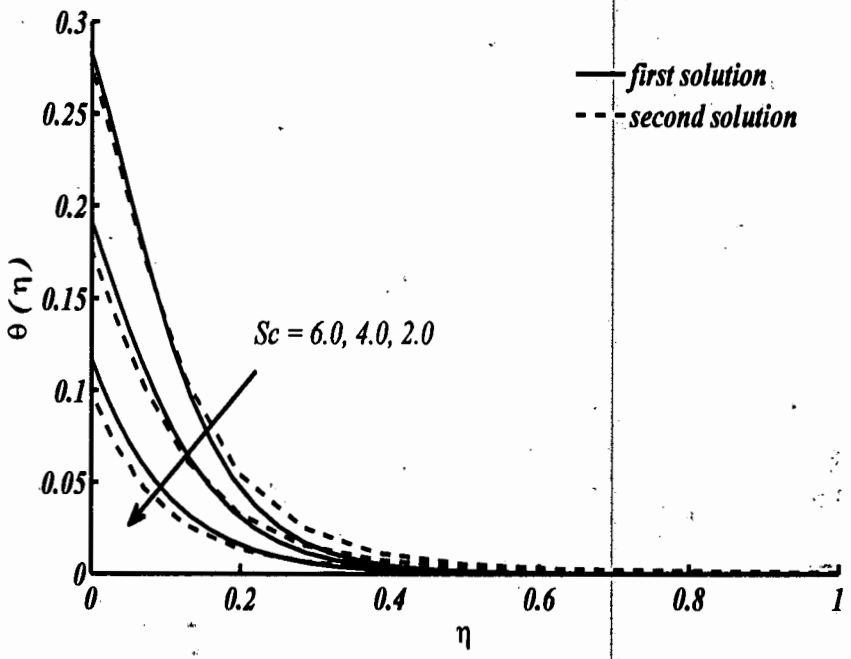

(b)

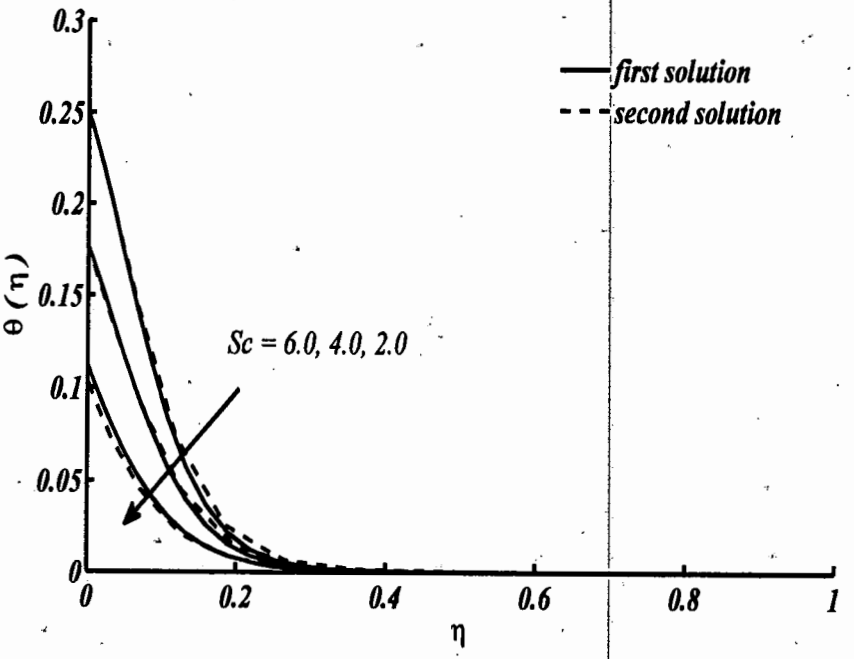

Figure 6.11(a, b): Temperature profile for distinct values of Sc when $m = 2$, Pr = 7, $\gamma_s = 1$, $Nt = Nb = 0.3$, $\gamma = 2.5$ (a) shrinking sheet $c/a = -3$ (b) stretching sheet $c/a = 2$.

(a)

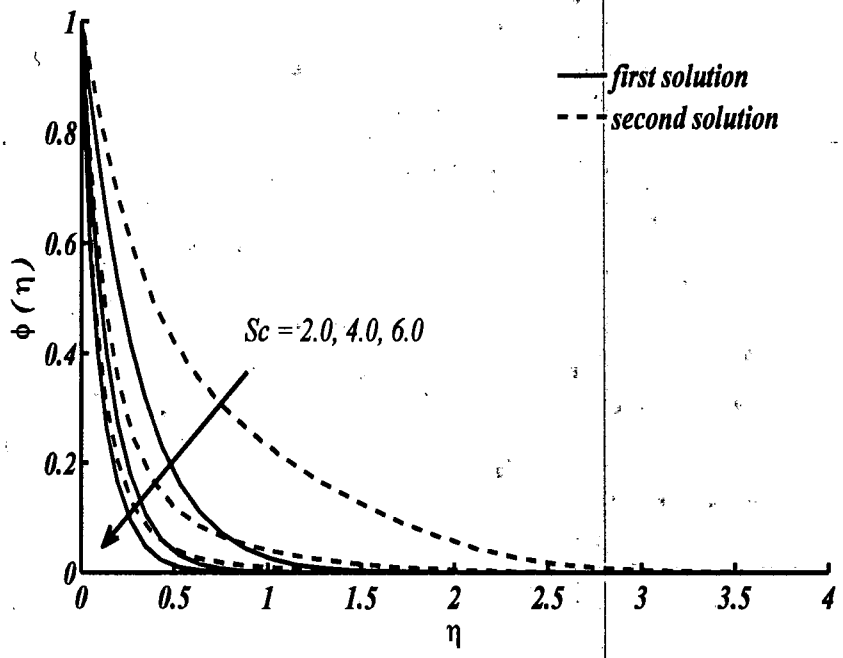

(b)

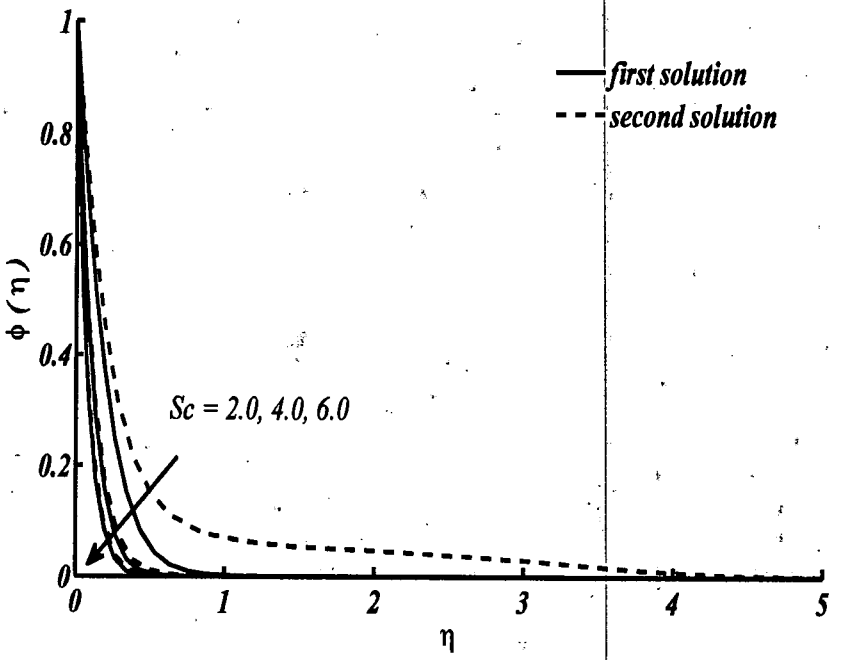

Figure 6.12(a, b): Nanoparticle concentration profile for distinct values of *Sc* when $m = 2$, Pr = 7, $\gamma_s = 1$, $Nt = Nb = 0.3$, and $\gamma = 2.5$ (a) shrinking sheet $c/a = -3$ (b) stretching sheet $c/a = 2$.

(a)

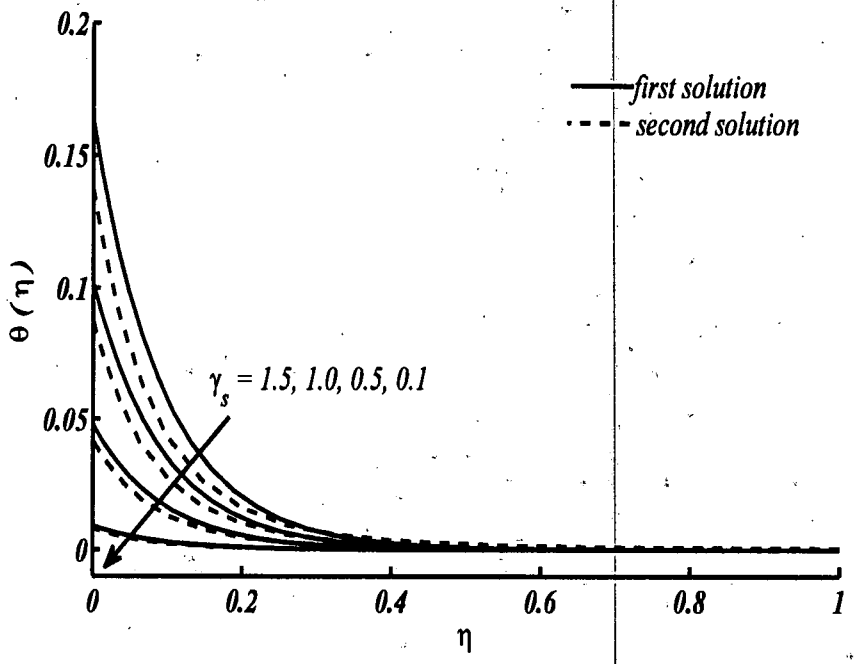

(b)

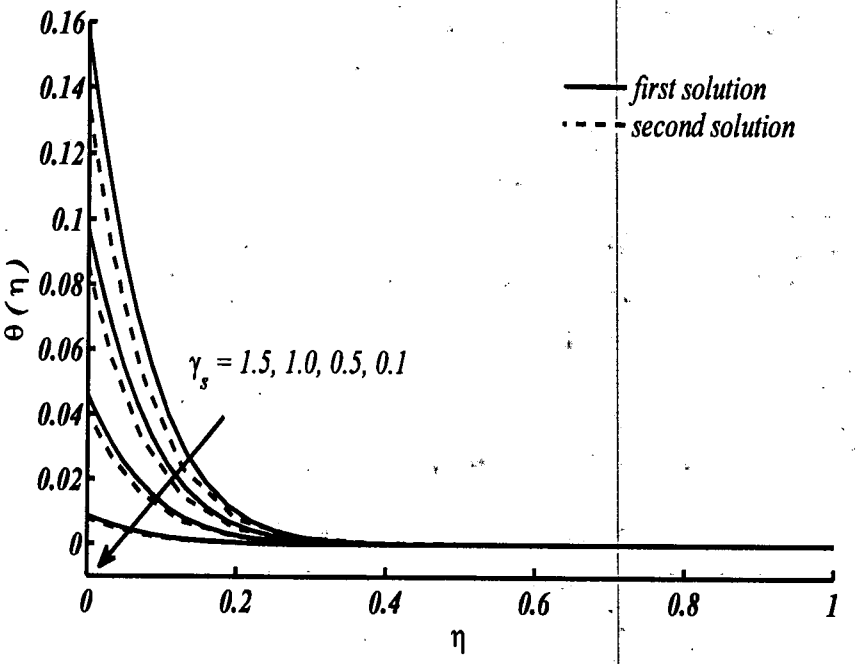

Figure 6.13(a, b): Temperature profile for distinct values of γ_s when $m = 2$, $Sc = 1.5$, $\mathrm{Pr} = 7$, $Nt = Nb = 0.3$, $\gamma = 2.5$ (a) shrinking sheet $c/a = -3$ (b) stretching sheet $c/a = 2$.

(a)

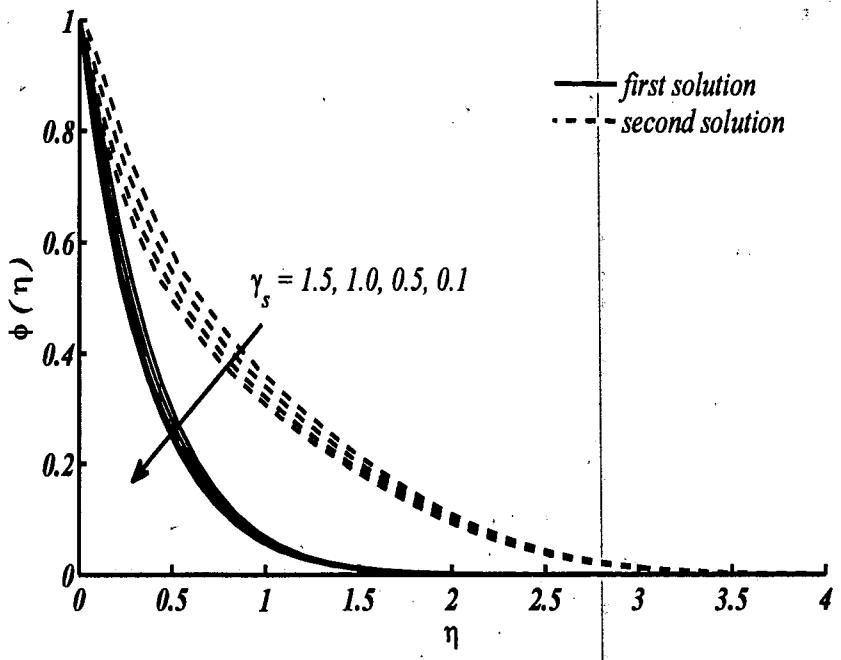

(b)

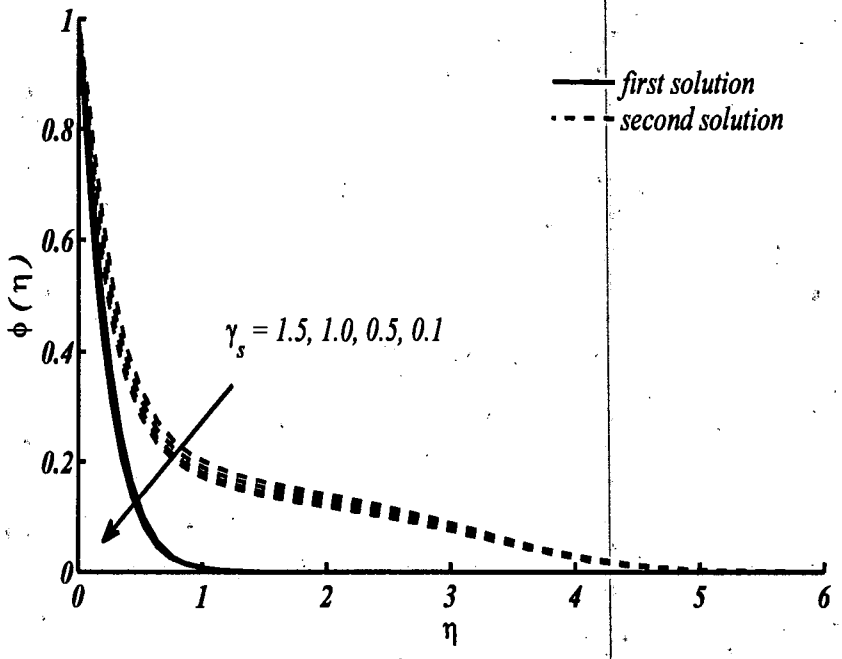

Figure 6.14(a, b): Nanoparticle concentration profile for distinct values of γ_s when $m = 2$, $Sc = 1.5$, $\Pr = 7$, $Nt = Nb = 0.3$, $\gamma = 2.5$ (a) shrinking sheet $c/a = -3$ (b) stretching sheet $c/a = 2$.

Table 6.3: The critical values t_1 of c/a for the some values of γ when $m = 2$.

	Zaimi et al. [103]	Present results
γ	t_1	t_1
2.5	-1.4278	-3.565
3.0	-2.0561	-4.286
3.5	-2.7986	-5.101

6.3 Conclusions

In this study, the heat transfer analysis in nanofluids flow near the stagnation point region over a non-linear permeable stretching/shrinking sheet is investigated. The governing equations of the flow problem are solved numerically by using a Chebyshev spectral collocation method and dual solutions are found for the specific ranges of suction parameter γ. The effects of pertinent parameters namely suction, velocity ratio, Prandtl number, thermophoresis and Brownian motion parameters, Schmidt number and Newtonian heating parameter γ_s on the velocity, temperature, nanoparticle concentration profiles in the boundary layer as well as the skin friction coefficient, local Nusselt number and local Sherwood number are examined through graphs. It is seen that temperature and concentration increase by increasing the values of Nt for both stretching and shrinking sheet cases. Also thermal and concentration boundary layer thicknesses are higher in shrinking case as compared to that of stretching case. By increasing the values of Nb and Schmidt number Sc temperature increases and concentration decreases for both stretching and shrinking sheet. Temperature and concentration profiles increase by increasing Newtonian heating parameter γ_s for both stretching and shrinking sheet. Skin friction coefficient increases in first solution and decreases in second solution with the increase of suction parameter γ and the values of first solution are higher than the values of second solution. The suction parameter γ widens the ranges of dual solutions. The local Nusselt number and Sherwood number increase by increasing γ for both first and second solutions. The values of first solution in $Nu_x \, \mathrm{Re}_x^{-1/2}$ are smaller than that of second solution and opposite behavior is observed in $Sh_x \, \mathrm{Re}_x^{-1/2}$.

Chapter 7

Heat transfer in mixed convection stagnation point flow of a third grade fluid on a vertical surface with slip effects

This chapter deals with the study of mixed convection stagnation point flow of a third grade fluid on a vertical surface with slip and viscous dissipation effects. The governing partial differential equations for third grade fluid are transformed into a coupled non-linear ordinary differential equations [146] by using similarity transformation and the resulting equations are solved numerically by using Chebyshev spectral collocation method. The effects of various parameters including Weissenberg number *We*, third grade parameter ε, local Reynolds number Re_x, Prandtl number Pr, Eckert number *Ec*, mixed convection parameter λ, velocity slip γ_v and thermal slip γ_t on velocity and temperature profiles, local skin friction coefficient and local Nusselt number are discussed through graphs for both assisting and opposing flow cases.

7.1 Mathematical formulation

Consider a steady laminar two dimensional mixed convection stagnation point flow of an incompressible third grade fluid on a vertical heated surface placed at $y = 0$. The geometry of the flow problem in which the fluid flow is occurring is shown in Fig. 7.1. It is assumed that the origin of the Cartesian coordinate system Oxy is taken at the center of the surface, however, the x-axis and y-axis are taken along and perpendicular to the surface. The velocity components of potential flow in the neighborhood of the stagnation point are $u_e = ax$ and $v_e = -ay$, where a being positive constant. In this study, only the heated surface case is studied which is valid for $T_w > T_\infty$. The governing boundary layer equations for the considered flow problem in the presence of viscous dissipation effect are written as

$$\frac{\partial u}{\partial x} + \frac{\partial v}{\partial y} = 0, \tag{7.1}$$

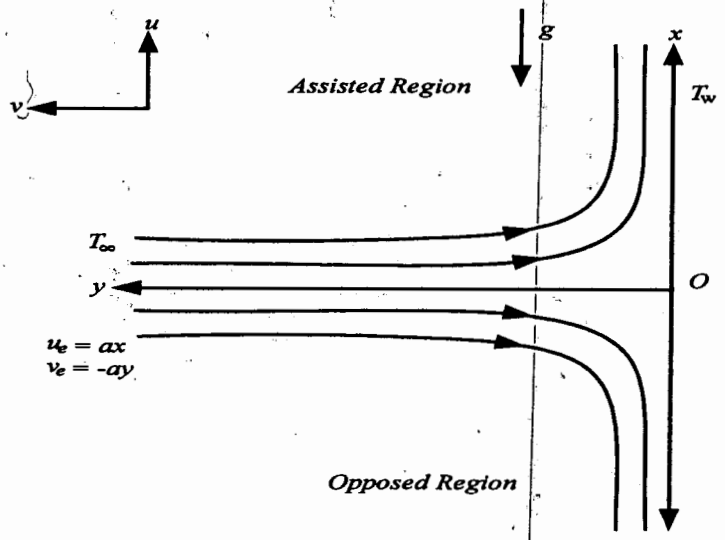

Figure 7.1: The physical description of the flow domain.

$$u\frac{\partial u}{\partial x}+v\frac{\partial u}{\partial y}=\frac{-1}{\rho_f}\frac{\partial p}{\partial x}+\frac{\mu_f}{\rho_f}\frac{\partial^2 u}{\partial y^2}+\frac{\alpha_1}{\rho_f}\left[u\frac{\partial^3 u}{\partial x\partial y^2}+\frac{\partial u}{\partial x}\frac{\partial^2 u}{\partial y^2}+3\frac{\partial u}{\partial y}\frac{\partial^2 u}{\partial x\partial y}+v\frac{\partial^3 u}{\partial y^3}\right]+ 2\frac{\alpha_2}{\rho_f}\frac{\partial u}{\partial y}\frac{\partial^2 u}{\partial x\partial y}+6\frac{\beta_3}{\rho_f}\left(\frac{\partial u}{\partial y}\right)^2\frac{\partial^2 u}{\partial y^2}\pm g\beta_f(T-T_\infty), \tag{7.2}$$

$$0=-\frac{\partial p}{\partial y}+(2\alpha_1+\alpha_2)\frac{\partial}{\partial y}\left(\frac{\partial u}{\partial y}\right)^2, \tag{7.3}$$

$$u\frac{\partial T}{\partial x}+v\frac{\partial T}{\partial y}=\frac{k_f}{(\rho c_p)_f}\frac{\partial^2 T}{\partial y^2}+\frac{\mu_f}{(\rho c_p)_f}\left(\frac{\partial u}{\partial y}\right)^2+\frac{\alpha_1}{(\rho c_p)_f}\left[u\frac{\partial u}{\partial y}\frac{\partial^2 u}{\partial x\partial y}+v\frac{\partial u}{\partial y}\frac{\partial^2 u}{\partial y^2}\right]+ 2\frac{\beta_3}{(\rho c_p)_f}\left(\frac{\partial u}{\partial y}\right)^4, \tag{7.4}$$

where u and v are the components of velocity in x and y directions respectively, α_1, α_2, β_3 are the material parameters of the fluid, g is acceleration due to gravity. The last term on the right hand side of Eq. (7.2) represents the presence of buoyancy force effects with +ve and -ve signs. The +ve sign is considered when surface extends in vertically upward direction called assisting flow case and -ve sign is considered when surface extends in vertically downward direction called opposing flow case.

From Eq. (7.3), a modified pressure is obtained as

$$p^* = p-(2\alpha_1+\alpha_2)\left(\frac{\partial u}{\partial y}\right)^2.$$

After using the above relation of modified pressure in Eqs. (7.2) and (7.3), the following equations [146] are obtained as

$$u\frac{\partial u}{\partial x}+v\frac{\partial u}{\partial y}=-\frac{1}{\rho_f}\frac{\partial p^*}{\partial x}+\frac{\mu_f}{\rho_f}\frac{\partial^2 u}{\partial y^2}+\frac{\alpha_1}{\rho_f}\left[u\frac{\partial^3 u}{\partial x\partial y^2}+\frac{\partial u}{\partial x}\frac{\partial^2 u}{\partial y^2}-\frac{\partial u}{\partial y}\frac{\partial^2 u}{\partial x\partial y}+v\frac{\partial^3 u}{\partial y^3}\right]+$$
$$6\frac{\beta_3}{\rho_f}\left(\frac{\partial u}{\partial y}\right)^2\frac{\partial^2 u}{\partial y^2}\pm g\beta_f(T-T_\infty), \tag{7.5}$$
$$\frac{\partial p^*}{\partial y}=0,$$

and upon using the potential flow velocity in Eq. (7.5), Eqs. (7.4) and (7.5) will become

$$u\frac{\partial u}{\partial x}+v\frac{\partial u}{\partial y}=u_e\frac{du_e}{dx}+\frac{\mu_f}{\rho_f}\frac{\partial^2 u}{\partial y^2}+\frac{\alpha_1}{\rho_f}\left[u\frac{\partial^3 u}{\partial x\partial y^2}+\frac{\partial u}{\partial x}\frac{\partial^2 u}{\partial y^2}-\frac{\partial u}{\partial y}\frac{\partial^2 u}{\partial x\partial y}+v\frac{\partial^3 u}{\partial y^3}\right]+$$
$$6\frac{\beta_3}{\rho_f}\left(\frac{\partial u}{\partial y}\right)^2\frac{\partial^2 u}{\partial y^2}\pm g\beta_f(T-T_\infty), \tag{7.6}$$

$$u\frac{\partial T}{\partial x}+v\frac{\partial T}{\partial y}=\frac{k_f}{(\rho c_p)_f}\frac{\partial^2 T}{\partial y^2}+\frac{\mu_f}{(\rho c_p)_f}\left(\frac{\partial u}{\partial y}\right)^2+\frac{\alpha_1}{(\rho c_p)_f}\left[u\frac{\partial u}{\partial y}\frac{\partial^2 u}{\partial x\partial y}+v\frac{\partial u}{\partial y}\frac{\partial^2 u}{\partial y^2}\right]+$$
$$2\frac{\beta_3}{(\rho c_p)_f}\left(\frac{\partial u}{\partial y}\right)^4. \tag{7.7}$$

Here Eq. (7.6) is of the same form as that of the study [146] after setting $Q_B=0$. The boundary conditions in the presence of velocity and thermal slips are given by

$$u=\frac{\gamma_1}{\mu_f}\tau_{xy}, v=0, T=T_w+\gamma_2\left(\frac{\partial T}{\partial y}\right) \quad \text{at } y=0, \tag{7.8}$$

$$u=u_e=ax, v=v_e=-ay, T=T_\infty \quad \text{as } y\to\infty, \tag{7.9}$$

where γ_1 and γ_2 are the velocity slip and thermal slip factors. The wall temperature which varies linearly along x is defined as $T_w=T_\infty+\Delta Tx$, where ΔT is the temperature difference. The governing Eqs. (7.6, 7.7) are nonlinear partial differential equations. After using the following similarity transformation

$$\eta=\sqrt{\frac{a}{\nu_f}}y, \quad u=axf'(\eta), \quad v=-\sqrt{a\nu_f}f(\eta), \quad \theta(\eta)=\frac{T-T_\infty}{T_w-T_\infty} \tag{7.10}$$

the governing equations are converted into coupled ordinary differential equations as follows [146]

$$\left.\begin{aligned} &f'''-f'^2+ff''+1+We(2ff'''-ff^{(iv)}-f''^2)+6\varepsilon\mathrm{Re}_x f''f''^2\pm\lambda\theta=0\\ &\theta''+\mathrm{Pr}(f\theta'-f'\theta)+\mathrm{Pr}\,Ec\left[f''^2+We(ff''^2-ff''f''')+2\varepsilon\mathrm{Re}_x f''^4\right]=0\end{aligned}\right\}, \tag{7.11}$$

where prime sign denotes the differentiation with respect to η, $We=a\alpha_1/\mu_f$ is the

Weissenberg number, $\varepsilon = \beta_3 a^2/\mu_f$ is the third grade parameter, $\lambda = Gr_x/\mathrm{Re}_x^2$ is a buoyancy or mixed convection parameter, when $\lambda = 0$ the flow corresponds to pure forced convection and when $\lambda \neq 0$ the flow corresponds to mixed convection flow and $Ec = a^2x^2/\left((c_p)_f(T_w - T_\infty)\right)$ is Eckert number which will be taken positive in the wall heating case $(T_w > T_\infty)$ and $(c_p)_f$ is specific heat.

The boundary conditions take the form as

$$\left.\begin{aligned} f(0) = 0, f'(0) = \gamma_v f''(0)[1 + 3We\, f'(0) + 2\varepsilon \mathrm{Re}_x (f''(0))^2] \\ f'(\infty) = 1, f''(\infty) = 0, \theta(0) = 1 + \gamma_t \theta'(0), \theta(\infty) = 0 \end{aligned}\right\}, \tag{7.12}$$

where $\gamma_v = \gamma_1\sqrt{\frac{a}{\nu_f}}$ and $\gamma_t = \gamma_2\sqrt{\frac{a}{\nu_f}}$ are dimensionless velocity and thermal slip parameters.

The local skin friction coefficient C_{fx} and the local Nusselt number Nu_x are

$$C_{fx} = \frac{\tau_w}{\rho_f u_e^2}, Nu_x = \frac{x q_w}{k_f(T_w - T_\infty)}, \tag{7.13}$$

τ_w and q_w are given by

$$\tau_w = \left[\begin{aligned} &\mu_f\left(\frac{\partial u}{\partial y} + \frac{\partial v}{\partial x}\right) + \alpha_1\left(u\frac{\partial^2 u}{\partial x \partial y} + u\frac{\partial^2 v}{\partial x^2} + v\frac{\partial^2 u}{\partial y^2} + v\frac{\partial^2 v}{\partial x \partial y} + 2\frac{\partial u}{\partial x}\frac{\partial u}{\partial y} + 2\frac{\partial v}{\partial x}\frac{\partial v}{\partial y}\right) \\ &+ \beta_3\left\{\left(\frac{\partial u}{\partial y} + \frac{\partial v}{\partial x}\right)\left(4\left(\frac{\partial u}{\partial x}\right)^2 + 2\left(\frac{\partial u}{\partial y}\right)^2 + 4\frac{\partial v}{\partial x}\frac{\partial u}{\partial y} + 2\left(\frac{\partial v}{\partial x}\right)^2 + 4\left(\frac{\partial v}{\partial y}\right)^2\right)\right\} \end{aligned}\right]_{y=0} \tag{7.14}$$

$$q_w = -k_f\left(\frac{\partial T}{\partial y}\right)_{y=0}.$$

In dimensionless form, Eq. (7.13) is reduced to

$$C_{fx}\,\mathrm{Re}_x^{1/2} = \left[f'' + We(3ff'' - ff''') + 2\varepsilon \mathrm{Re}_x f''^3\right]_{\eta=0}, \tag{7.15}$$

$$Nu_x/\mathrm{Re}_x^{1/2} = -\theta'(0). \tag{7.16}$$

In order to solve the coupled nonlinear system of ordinary differential Eqs. (7.11) subject to the boundary conditions (7.12), Chebyshev spectral collocation method is used [132], and the detail of this method is discussed in the next section.

7.2 Spectral collocation method

To solve highly nonlinear system of ordinary differential equations given in Eq. (7.11) subject to the boundary conditions Eq. (7.12) a Chebyshev spectral collocation method is used. In

which the solution $f(\xi)$ and $\theta(\xi)$ are written as a sum of N+1 basis functions $T_n(\xi)=\cos\left(n\cos^{-1}\xi\right)$ known as Chebyshev polynomial of degree n and defined in the interval $-1\le\xi\le 1$. The physical domain of the present flow problem is $[0,\infty)$, which is transformed into the domain of basis functions [-1, 1] by using the following transformation

$$\xi=2\frac{\eta}{\eta_\infty}-1, \tag{7.17}$$

After using the above transformation, the obtained boundary value problem will take the form

$$\begin{aligned}8\eta_\infty\frac{d^3f}{d\xi^3}+4{\eta_\infty}^2 f\frac{d^2f}{d\xi^2}+{\eta_\infty}^4+We\left\{32\frac{df}{d\xi}\frac{d^3f}{d\xi^3}-16f\frac{d^4f}{d\xi^4}-16\left(\frac{d^2f}{d\xi^2}\right)^2\right\}-\\ 4{\eta_\infty}^2\left(\frac{df}{d\xi}\right)^2+\frac{768}{{\eta_\infty}^3}\varepsilon\,\mathrm{Re}_x\left(\frac{d^2f}{d\xi^2}\right)^2\frac{d^3f}{d\xi^3}\pm{\eta_\infty}^4\lambda\theta=0,\end{aligned} \tag{7.18}$$

$$4\frac{d^2\theta}{d\xi^2}+2\,\mathrm{Pr}\,\eta_\infty\left(f\frac{d\theta}{d\xi}-\theta\frac{df}{d\xi}\right)+\mathrm{Pr}\,Ec\left[\begin{aligned}&\frac{16}{{\eta_\infty}^2}\left(\frac{d^2f}{d\xi^2}\right)^2+\frac{512\varepsilon\,\mathrm{Re}_x}{{\eta_\infty}^6}\left(\frac{d^2f}{d\xi^2}\right)^4\\&+\frac{32}{{\eta_\infty}^3}We\left\{\frac{df}{d\xi}\left(\frac{d^2f}{d\xi^2}\right)^2-f\frac{d^2f}{d\xi^2}\frac{d^3f}{d\xi^3}\right\}\end{aligned}\right]=0, \tag{7.19}$$

and boundary conditions become

$$\begin{aligned}f(\xi)=0,\frac{df}{d\xi}=\gamma_v\frac{2}{\eta_\infty}\frac{d^2f}{d\xi^2}\left[1+3We\frac{2}{\eta_\infty}\frac{df}{d\xi}+2\varepsilon\,\mathrm{Re}_x\frac{16}{{\eta_\infty}^4}\left(\frac{d^2f}{d\xi^2}\right)^2\right],\\ \theta(\xi)=1+\gamma_t\frac{2}{\eta_\infty}\frac{d\theta}{d\xi}\ \text{at}\ \xi=-1,\\ \frac{df}{d\xi}=\frac{\eta_\infty}{2},\frac{d^2f}{d\xi^2}=0,\theta(\xi)=0\,\text{at}\,\xi=1\end{aligned} \tag{7.20}$$

Substituting the assumed solutions Eqs. (2.18, 2.19) into Eqs. (7.18, 7.19), the following non-zero residues R_1 and R_2 are obtained as

$$\begin{aligned}R_1={\eta_\infty}^4+{\eta_\infty}^4\lambda\sum_{n=0}^{N}b_n\cos(n\cos^{-1}\xi)-4{\eta_\infty}^2\left(\sum_{n=0}^{N}\frac{na_n\sin(n\cos^{-1}\xi)}{\sqrt{1-\xi^2}}\right)^2+\\ \frac{8\eta_\infty}{\left(1-\xi^2\right)^{5/2}}\sum_{n=0}^{N}na_n\left(\begin{aligned}&-3n\xi\sqrt{1-\xi^2}\cos(n\cos^{-1}\xi)+\sin(n\cos^{-1}\xi)-n^2\sin(n\cos^{-1}\xi)\\&+2\xi^2\sin(n\cos^{-1}\xi)+n^2\xi^2\sin(n\cos^{-1}\xi)\end{aligned}\right)+\\ \frac{4{\eta_\infty}^2}{(-1+\xi^2)}\sum_{n=0}^{N}a_n\cos(n\cos^{-1}\xi)\sum_{n=0}^{N}na_n\left(n\cos(n\cos^{-1}\xi)-\xi\frac{\sin(n\cos^{-1}\xi)}{\sqrt{1-\xi^2}}\right)+\end{aligned}$$

$$\frac{768\varepsilon \operatorname{Re}_x}{\eta_\infty{}^3}\left(\sum_{n=0}^{N}\frac{na_n}{(-1+\xi^2)}\left(n\cos(n\cos^{-1}\xi)-\xi\frac{\sin(n\cos^{-1}\xi)}{\sqrt{1-\xi^2}}\right)\right)^2\times$$

$$\frac{1}{\left(1-\xi^2\right)^{5/2}}\sum_{n=0}^{N}na_n\begin{pmatrix}-3n\xi\sqrt{1-\xi^2}\cos(n\cos^{-1}\xi)+\\ \sin(n\cos^{-1}\xi)-n^2\sin(n\cos^{-1}\xi)+\\ 2\xi^2\sin(n\cos^{-1}\xi)+n^2\xi^2\sin(n\cos^{-1}\xi)\end{pmatrix}+$$

$$\frac{32We}{\left(1-\xi^2\right)^3}\sum_{n=0}^{N}na_n\sin(n\cos^{-1}\xi)\times\sum_{n=0}^{N}na_n\begin{pmatrix}-3n\xi\sqrt{1-\xi^2}\cos(n\cos^{-1}\xi)+\\ \sin(n\cos^{-1}\xi)-n^2\sin(n\cos^{-1}\xi)+\\ 2\xi^2\sin(n\cos^{-1}\xi)+n^2\xi^2\sin(n\cos^{-1}\xi)\end{pmatrix}-$$

$$16We\left(\sum_{n=0}^{N}\frac{na_n}{(-1+\xi^2)}\left(n\cos(n\cos^{-1}\xi)-\xi\frac{\sin(n\cos^{-1}\xi)}{\sqrt{1-\xi^2}}\right)\right)^2-16We\sum_{n=0}^{N}a_n\cos(n\cos^{-1}\xi)\times$$

$$\sum_{n=0}^{N}\begin{pmatrix}\frac{-15a_nn^2\xi^2\cos(n\cos^{-1}\xi)}{\left(1-\xi^2\right)^3}-\frac{4a_nn^2\cos(n\cos^{-1}\xi)}{\left(1-\xi^2\right)^2}+\frac{a_nn^4\cos(n\cos^{-1}\xi)}{\left(1-\xi^2\right)^2}+\\ \frac{15a_nn\xi^3\sin(n\cos^{-1}\xi)}{\left(1-\xi^2\right)^{7/2}}+\frac{9a_nn\xi\sin(n\cos^{-1}\xi)}{\left(1-\xi^2\right)^{5/2}}-\frac{6a_nn^3\xi\sin(n\cos^{-1}\xi)}{\left(1-\xi^2\right)^{5/2}}\end{pmatrix}$$

and

$$R_2=-2\Pr\eta_\infty\sum_{n=0}^{N}b_n\cos(n\cos^{-1}\xi)\sum_{n=0}^{N}\frac{na_n\sin(n\cos^{-1}\xi)}{\sqrt{1-\xi^2}}+$$

$$2\Pr\eta_\infty\sum_{n=0}^{N}a_n\cos(n\cos^{-1}\xi)\sum_{n=0}^{N}\frac{nb_n\sin(n\cos^{-1}\xi)}{\sqrt{1-\xi^2}}+4\sum_{n=0}^{N}\frac{nb_n}{-1+\xi^2}\begin{pmatrix}n\cos(n\cos^{-1}\xi)-\\ \xi\frac{\sin(n\cos^{-1}\xi)}{\sqrt{1-\xi^2}}\end{pmatrix}+$$

$$\Pr Ec\begin{pmatrix}\frac{16}{\eta_\infty{}^2}\left(\sum_{n=0}^{N}\frac{na_n}{(-1+\xi^2)}\left(n\cos(n\cos^{-1}\xi)-\xi\frac{\sin(n\cos^{-1}\xi)}{\sqrt{1-\xi^2}}\right)\right)^2+\\ \frac{512\operatorname{Re}_x\varepsilon}{\eta_\infty{}^6}\left(\sum_{n=0}^{N}\frac{na_n}{(-1+\xi^2)}\left(n\cos(n\cos^{-1}\xi)-\xi\frac{\sin(n\cos^{-1}\xi)}{\sqrt{1-\xi^2}}\right)\right)^4\end{pmatrix}-$$

$$\frac{32We\Pr Ec}{\eta_\infty{}^3}\sum_{n=0}^{N}a_n\cos(n\cos^{-1}\xi)\times\sum_{n=0}^{N}\frac{na_n}{(1-\xi^2)^{5/2}}\begin{pmatrix}-3n\xi\sqrt{1-\xi^2}\cos(n\cos^{-1}\xi)+\\ \sin(n\cos^{-1}\xi)-n^2\sin(n\cos^{-1}\xi)+\\ 2\xi^2\sin(n\cos^{-1}\xi)+n^2\xi^2\sin(n\cos^{-1}\xi)\end{pmatrix}\times$$

$$\sum_{n=0}^{N}\frac{na_n}{(-1+\xi^2)}\left(n\cos(n\cos^{-1}\xi)-\xi\frac{\sin(n\cos^{-1}\xi)}{\sqrt{1-\xi^2}}\right)+\frac{32We\Pr Ec}{\eta_\infty{}^3}\sum_{n=0}^{N}\frac{na_n\sin(n\cos^{-1}\xi)}{\sqrt{1-\xi^2}}\times$$

$$\left(\sum_{n=0}^{N}\frac{na_n}{(-1+\xi^2)}\left(n\cos(n\cos^{-1}\xi)-\xi\frac{\sin(n\cos^{-1}\xi)}{\sqrt{1-\xi^2}}\right)\right)^2.$$

For calculating the solution of unknown functions, the same procedure is used as discussed in chapter 2.

7.3 Results and discussion

The solution of highly non-linear coupled ordinary differential Eqs. (7.11) subject to the boundary conditions (7.12) is obtained by using Chebyshev spectral collocation method which is well established method and applicable for highly nonlinear system of ordinary differential equations. For verification, the results of Li et al. [147] and Hayat et al. [148] are reproduced in the absence of slip effects and is found in excellent agreement for different values of Weissenberg number *We* and Pr = 0.2 as shown in Table 7.1. After ensuring the validity and accuracy of the numerical method used, Figs. 7.2-7.11 are drawn for distinct values of the involving parameters. It is ensured that the value of numerical infinity is adjusted according to the value of parameters. It is, therefore, different values of infinity are chosen for different values of the parameters. Dashed lines represent the solution, when the parameters of velocity and thermal slips are fixed at zero i.e., for no slip case. Solid lines represent the solution showing slip effects which is the main focus in this chapter. Figs. 7.2-7.7 show the velocity and temperature profiles against η for involving parameters. Fig. 7.2(a, b) shows the velocity and temperature profiles for different values of λ ($\lambda > 0$ i.e. assisting flow), when Pr = 0.5, *Ec* = 0.05, *We* = 0.3, Re_x = 0.1and $\varepsilon = 1$ are fixed. It is observed that velocity increases and temperature decreases with the increase of mixed convection parameter λ. Further, it is seen that for $\lambda > 1$ velocity attains its maximum value near the surface which is even larger than the free stream and then ultimately approaches to the free stream velocity. The increasing of mixed convection parameter λ does not affect much on the momentum boundary layer thickness and thermal boundary layer thickness. Fig. 7.3(a, b) shows the velocity and temperature profiles for opposing case with the same values of parameters as considered in Fig. 7.2(a, b). In opposing case, the opposite behavior is observed as that in Fig. 7.2 with the increase of mixed convection parameter λ. Fig. 7.4(a, b) is drawn to show the effects of Prandtl number Pr, which is the ratio of the momentum diffusivity and thermal diffusivity on the velocity and temperature profiles. For the variation of Prandtl number, the values are chosen as Pr = 1, 2, 5 and 10 while

other parameters are kept fixed at $\lambda = 1, Ec = 0.05, We = 0.3, \varepsilon = 1$ and $\mathrm{Re}_x = 0.1$. The graphs are drawn for assisting flow case. It is seen that by increasing Pr the velocity profile $f'(\eta)$ and temperature profile $\theta(\eta)$ decrease, it is also seen that thermal boundary layer thickness decreases. Fig. 7.5(a, b) is drawn to show the effects of third grade parameter ε on the velocity profile $f'(\eta)$ and temperature profile $\theta(\eta)$ respectively for assisting flow case when $\lambda = 1, Ec = 0.05$, $We = 0.3, \mathrm{Re}_x = 0.1, \mathrm{Pr} = 0.5$ and $\varepsilon = 0$, 4, 8, 12. Dotted lines show the effects when no slip case is considered and it is observed that in this case the velocity profile starts from the surface and approaches free stream velocity uniformly. As soon as, velocity and thermal slips are considered, it is observed that initially for different values of ε velocity profile changes but near $\eta = 0.25$ the velocity profile becomes constant for all ε and after it the velocity profile starts changing with the change in ε. The variation of ε minimizes the change in temperature profile when the slips effect are considered. Although, it is comparatively active for no slip case. Third grade parameter is responsible for increase in boundary layer thickness, however, thermal boundary layer thickness remains ineffective with the variation of ε. Eckert number Ec produces increase in the velocity and temperature profiles for assisting flow case as shown in Fig. 7.6(a, b) when $\lambda = 1$, $\varepsilon = 1$, $We = 0.3$, $\mathrm{Re}_x = 0.1$ and Pr = 0.5 for both slip and no slip cases. The effect of velocity and thermal slips on velocity and temperature profiles are shown in Fig. 7.7(a, b) when $\lambda = 1$, $Ec = 0.05$, $We = 0.3$, $\mathrm{Re}_x = 0.1$, $\varepsilon = 1$ and Pr = 0.5. It is proved from Fig. 7.7(a, b) that by incorporating the slip effects velocity increases and temperature decreases at the wall, it is also observed that boundary layer thickness decreases. The variations of $C_{fx}\,\mathrm{Re}_x^{1/2}$ and $Nu_x\,\mathrm{Re}_x^{-1/2}$ against different parameters are shown through Figs. 7.8-7.11. The effects of $C_{fx}\,\mathrm{Re}_x^{1/2}$ and $Nu_x\,\mathrm{Re}_x^{-1/2}$ against velocity slip parameter γ_v and thermal slip parameter γ_t are shown in Fig. 7.8 when $\lambda = 1$, $Ec = 0.05$, $We = 0.3$, $\mathrm{Re}_x = 0.1$, $\varepsilon = 1$ and Pr = 0.5 are fixed. It is seen through these figures that both $C_{fx}\,\mathrm{Re}_x^{1/2}$ and $Nu_x\,\mathrm{Re}_x^{-1/2}$ decrease with the increase in their slip parameters. However, mixed convection parameter λ is responsible for increase in $C_{fx}\,\mathrm{Re}_x^{1/2}$ and $Nu_x\,\mathrm{Re}_x^{-1/2}$ for assisting flow case and $C_{fx}\,\mathrm{Re}_x^{1/2}$ and $Nu_x\,\mathrm{Re}_x^{-1/2}$ decrease for opposing flow case when $Ec = 0.05$, $We = 0.3$, $\mathrm{Re}_x = 0.1$, $\varepsilon = 1$ and Pr = 0.5 as shown in Fig. 7.9(a, b). The effects of Prandtl number on $C_{fx}\,\mathrm{Re}_x^{1/2}$ and $Nu_x\,\mathrm{Re}_x^{-1/2}$ are shown through Fig. 7.10(a, b) for slip and no slip cases

when $\lambda = 1.0$, $Ec = 0.05$, $\mathrm{Re}_x = 0.1$, $\varepsilon = 1.0$, $We = 0.3$ (for assisting flow). It is observed that when slip parameters are considered, local skin friction coefficient $C_{fx}\,\mathrm{Re}_x^{1/2}$ decreases and local Nusselt number $Nu_x\,\mathrm{Re}_x^{-1/2}$ increases. It is found that $C_{fx}\,\mathrm{Re}_x^{1/2}$ behaves as a decreasing function of Pr and $Nu_x\,\mathrm{Re}_x^{-1/2}$ behaves as an increasing function of Pr. The effects of Eckert number Ec on $C_{fx}\,\mathrm{Re}_x^{1/2}$ and $Nu_x\,\mathrm{Re}_x^{-1/2}$ are shown in Fig. 7.11(a, b) for slip and no slip cases. It is easily seen that $C_{fx}\,\mathrm{Re}_x^{1/2}$ is increasing function of Ec and $Nu_x\,\mathrm{Re}_x^{-1/2}$ as a decreasing function of Ec. It is further important to observe that $Nu_x\,\mathrm{Re}_x^{-1/2}$ crosses the zero line during the increase in Ec when $\lambda = 1$, $\mathrm{Pr} = 0.5$, $\mathrm{Re}_x = 0.1$, $\varepsilon = 1$ and $We = 0.3$.

Table 7.1: Comparison of $f''(0)$ and $-\theta'(0)$ for distinct values of We when $\mathrm{Pr} = \lambda = 0.2$ and $Ec = \mathrm{Re}_x = \varepsilon = \gamma_t = \gamma_v = 0$ with Hayat et al. [148] and Li et al. [147] for second grade fluid.

We	Li et al. [147]		Hayat et al. [148]		Present Result	
	Assisting flow	Opposing flow	Assisting flow	Opposing flow	Assisting flow	Opposing flow
			$f''(0)$			
0.0	1.35426	1.10711	1.3543	1.1072	1.35426	1.10711
0.5	0.98230	0.81854	0.9821	0.8184	0.98230	0.81854
1.0	0.81738	0.68434	0.8174	0.6844	0.81738	0.68434
1.5	0.71694	0.60129	0.7171	0.6015	0.71694	0.60129
2.0	0.64713	0.54310	0.6474	0.5435	0.64713	0.54310
			$-\theta'(0)$			
0.0	0.44198	0.42351	0.4420	0.4235	0.44198	0.42351
0.5	0.40990	0.39499	0.4097	0.3939	0.40990	0.39499
1.0	0.39189	0.37837	0.3920	0.3785	0.39189	0.37837
1.5	0.37922	0.36652	0.3793	0.3667	0.37922	0.36652
2.0	0.36944	0.35729	0.3698	0.3578	0.36944	0.35729

(a)

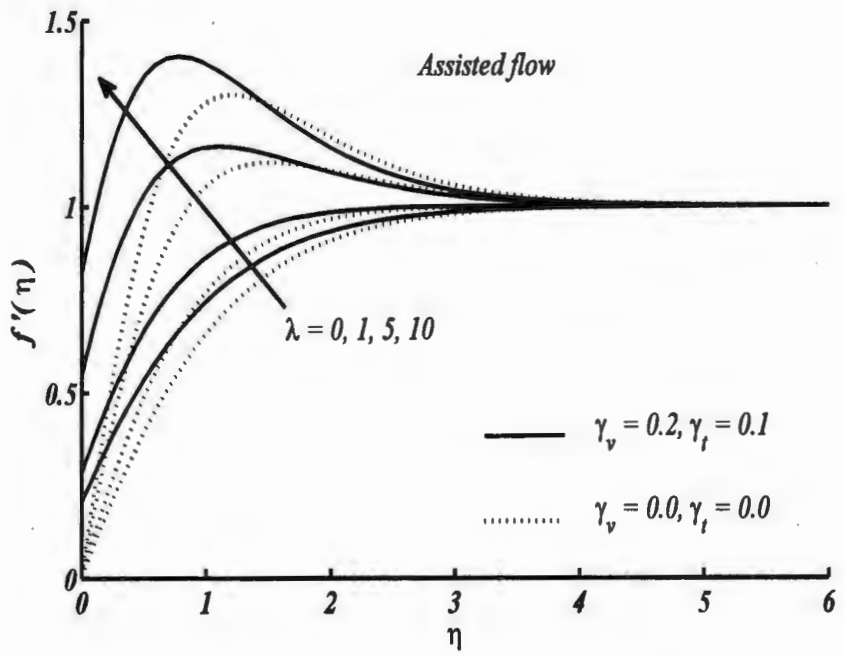

(b)

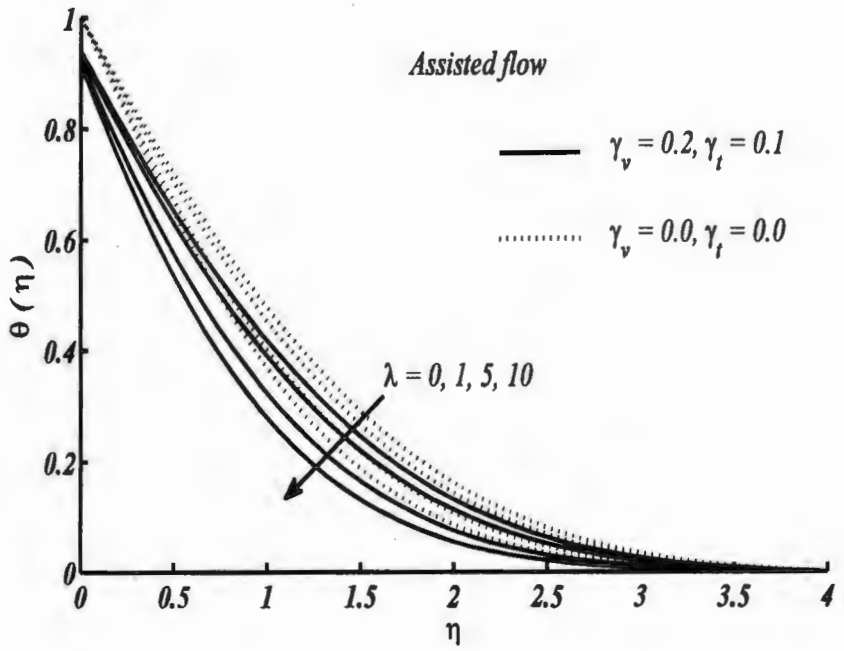

Figure 7.2(a, b): Velocity and temperature profiles for distinct values of λ.

(a)

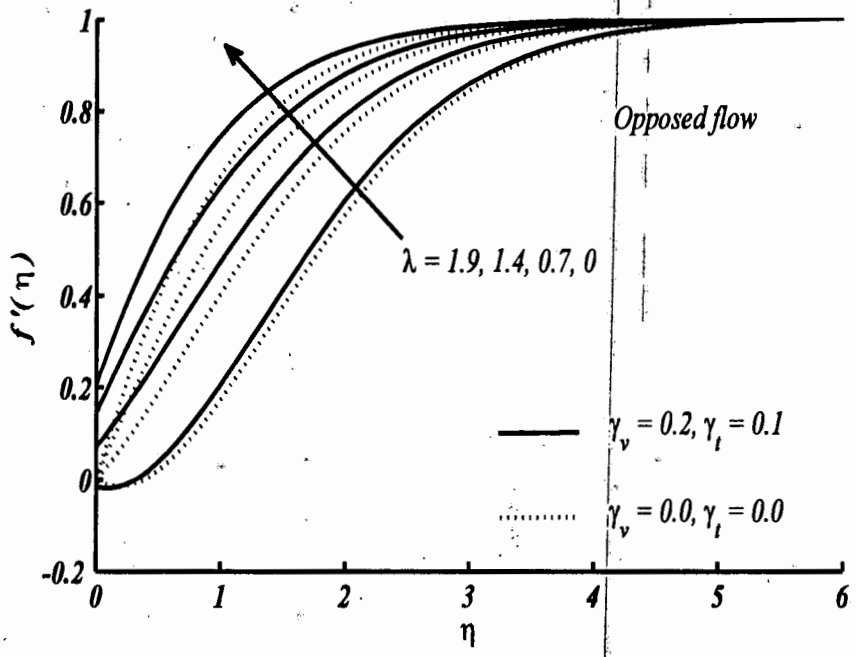

(b)

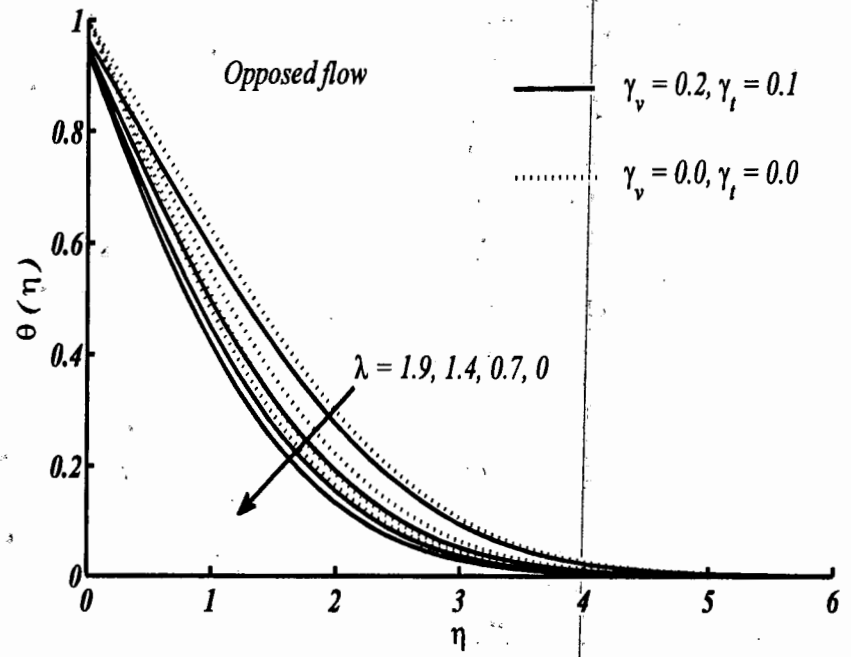

Figure 7.3(a, b): Velocity and temperature profiles for distinct values of λ.

(a)

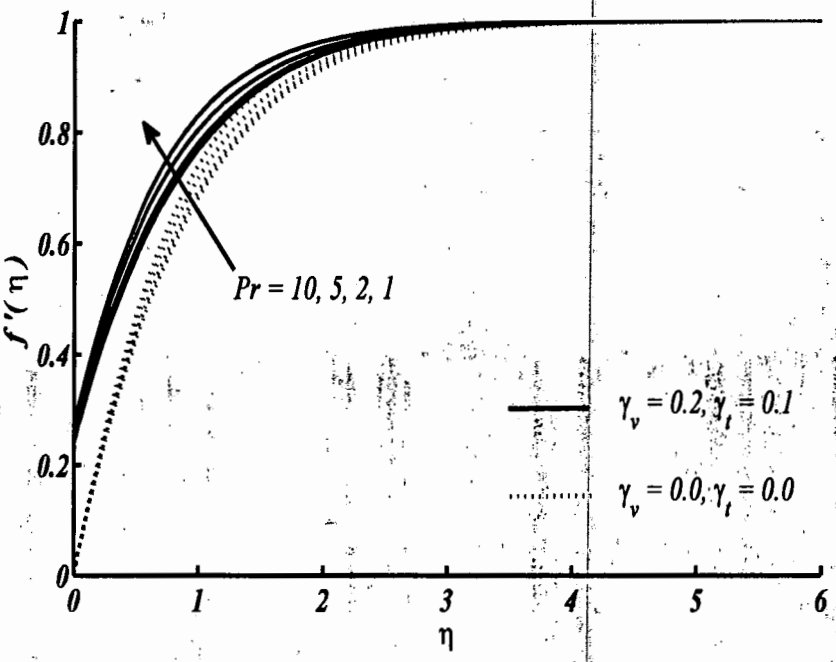

(b)

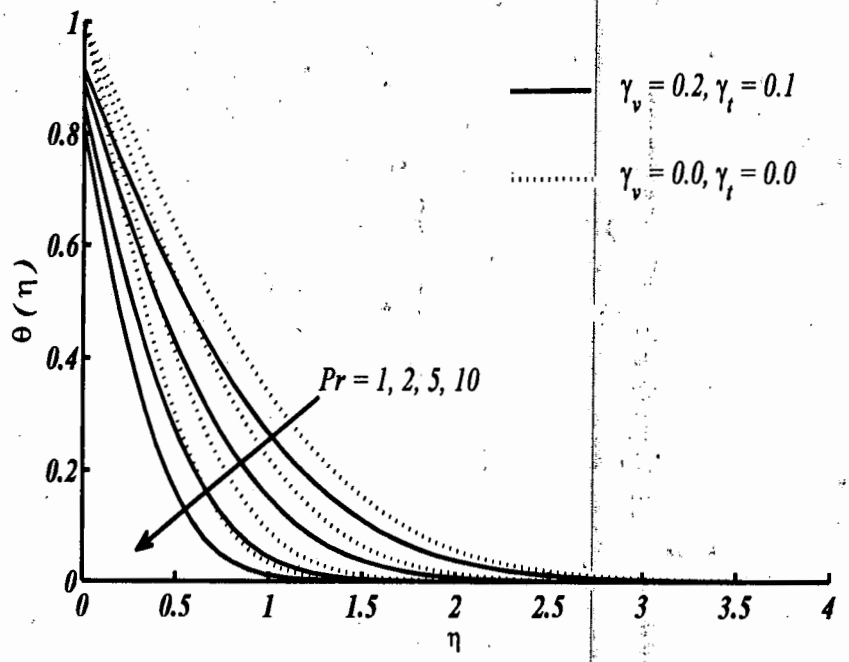

Figure 7.4(a, b): Velocity and temperature profiles for distinct values of Pr (assisting flow).

(a)

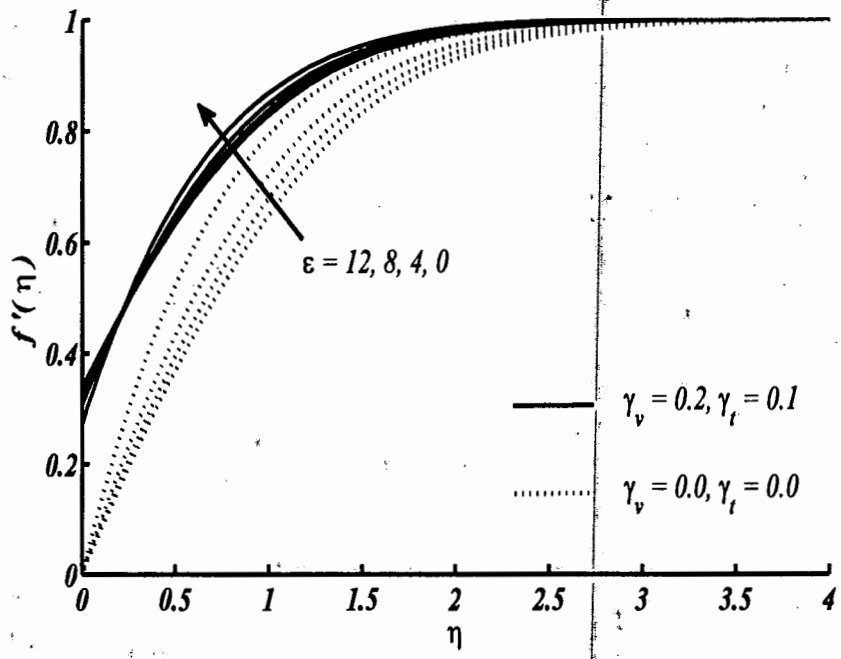

(b)

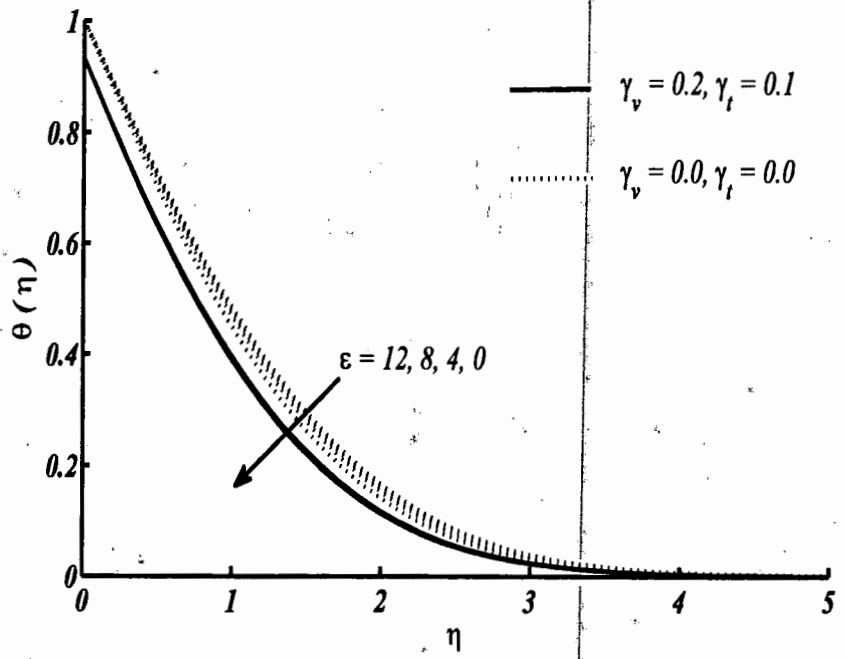

Figure 7.5(a, b): Velocity and temperature profiles for distinct values of ε (assisting flow).

(a)

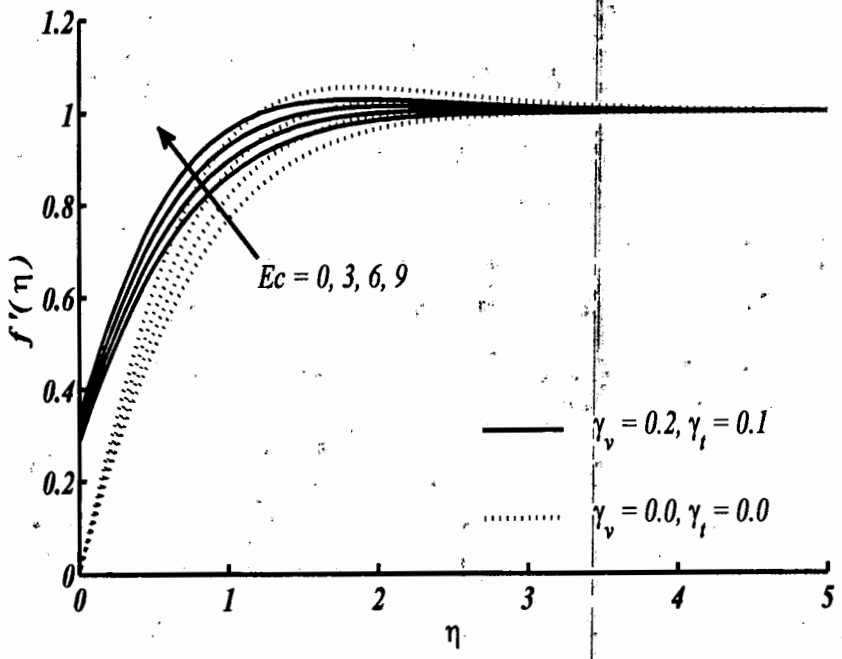

(b)

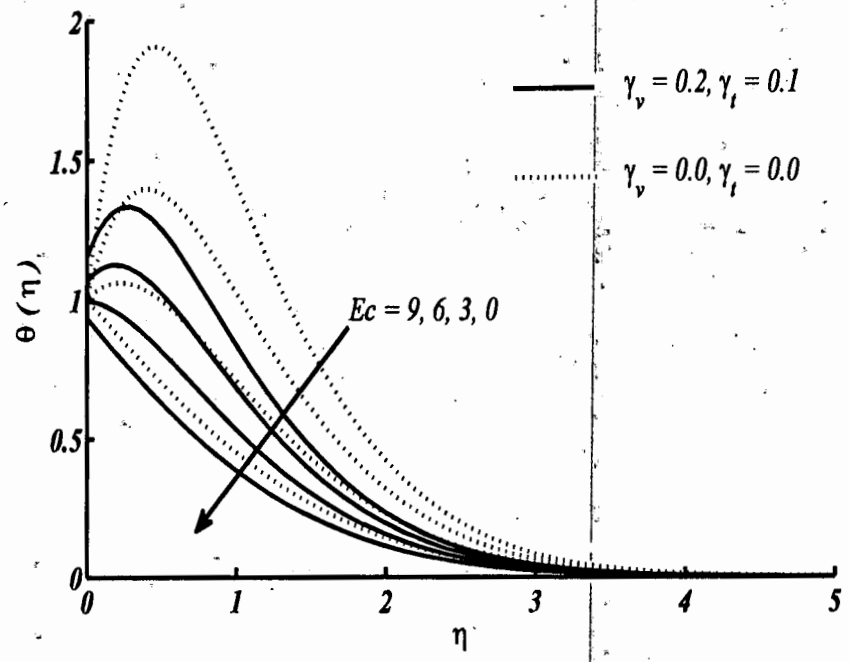

Figure 7.6(a, b): Velocity and temperature profiles for distinct values of *Ec* (assisting flow).

(a)

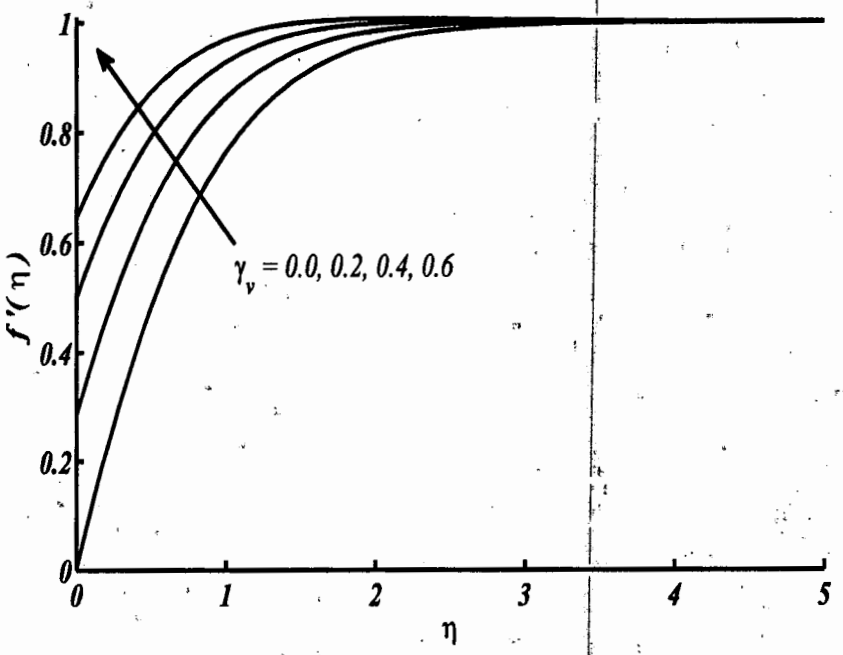

(b)

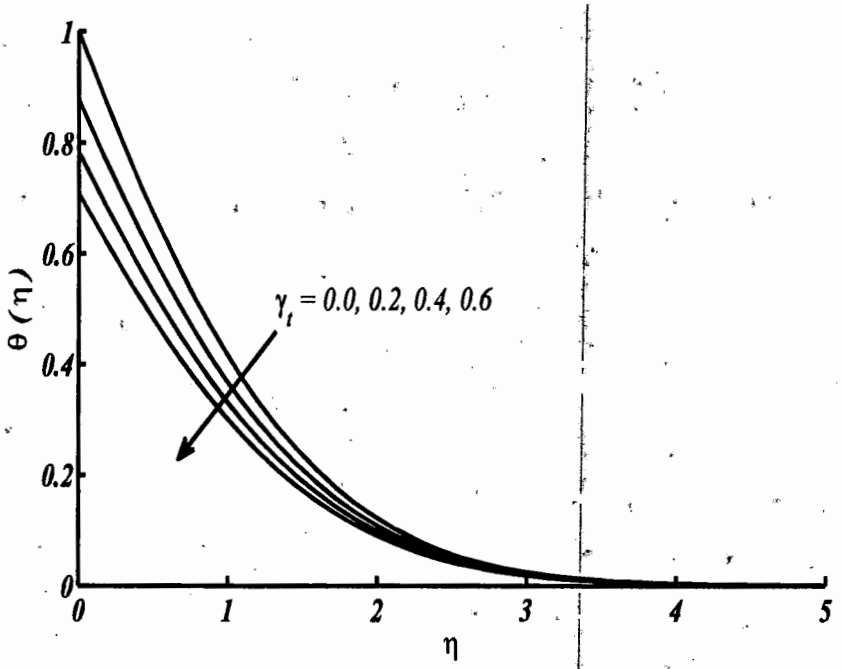

Figure 7.7(a, b): Velocity and temperature profiles for distinct values of slip parameters γ_t and γ_v (assisting flow).

(a)

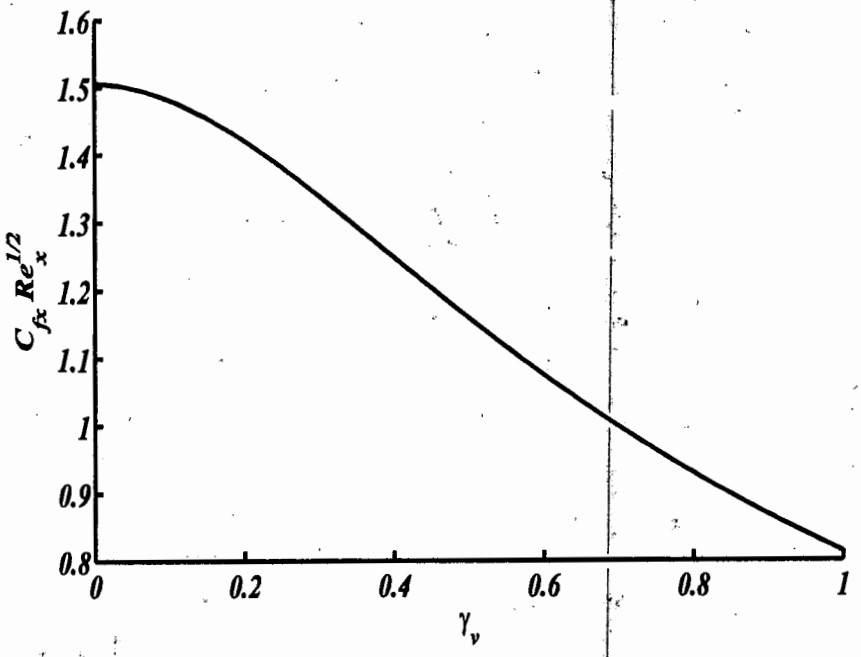

(b)

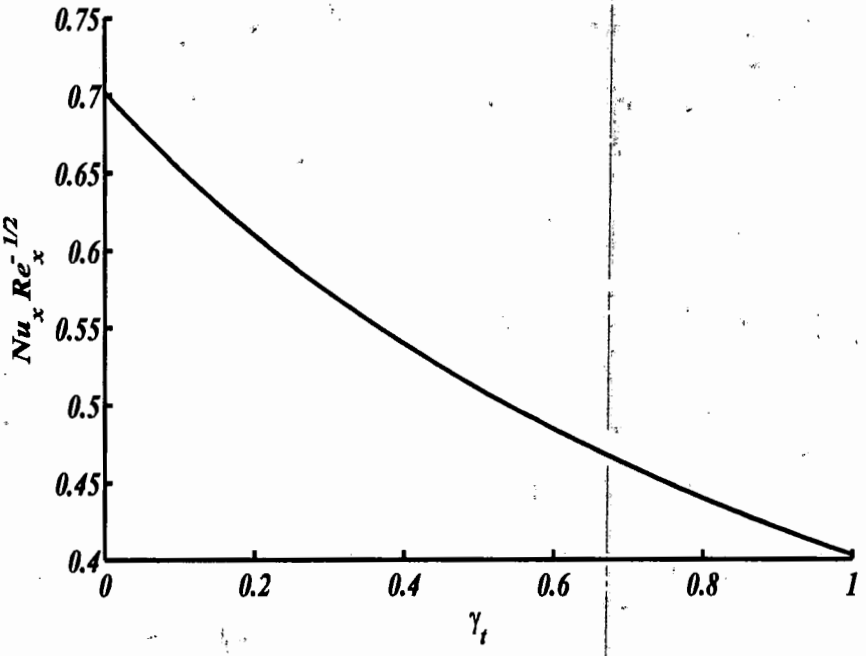

Figure 7.8(a, b): Variation of $C_{fx}\,\mathrm{Re}_x^{1/2}$ (skin friction coefficient) and $Nu_x\,\mathrm{Re}_x^{-1/2}$ (local Nusselt number) with slip parameters γ_v and γ_t (assisting flow).

(a)

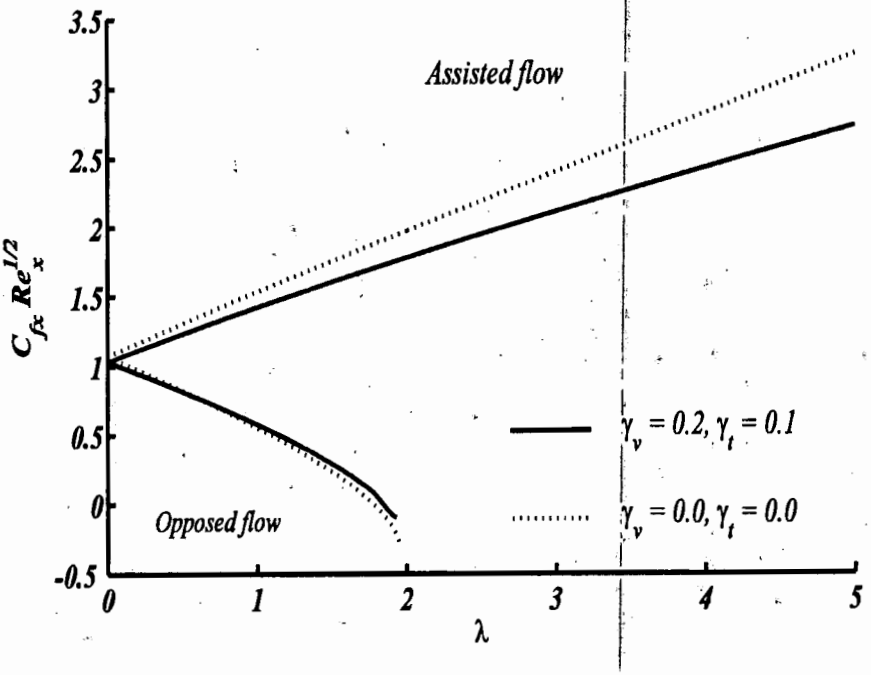

(b)

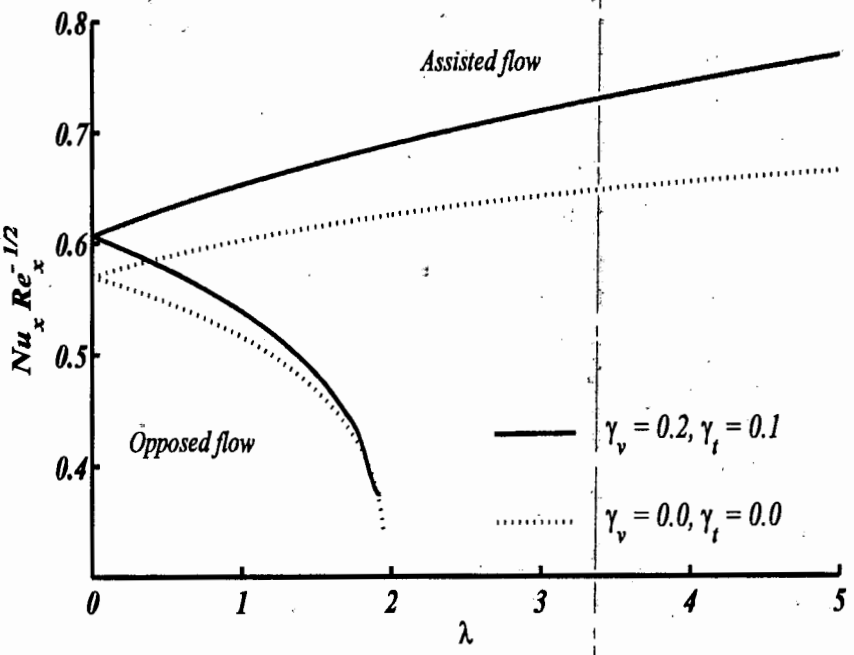

Figure 7.9(a, b): Variation of $C_{fx}\,\mathrm{Re}_x^{1/2}$ (skin friction coefficient) and $Nu_x\,\mathrm{Re}_x^{-1/2}$ (local Nusselt number) with mixed convection parameter λ.

(a)

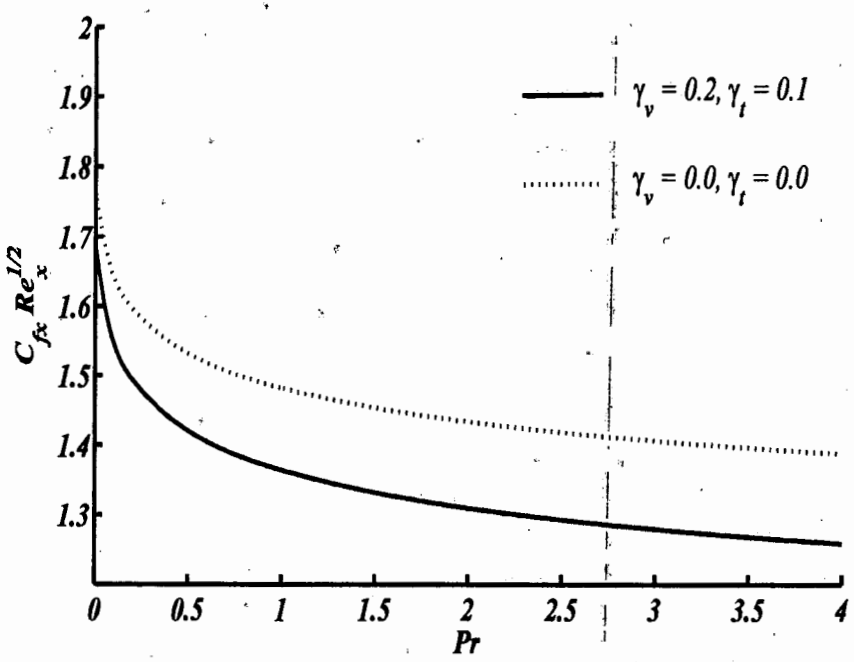

(b)

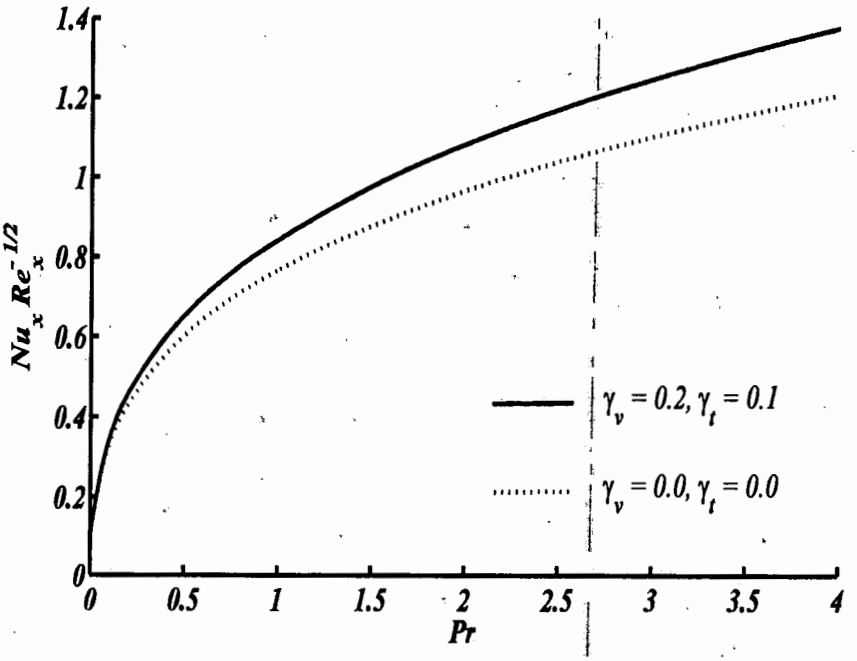

Figure 7.10(a, b): Variation of $C_{fx}\,\mathrm{Re}_x^{1/2}$ (skin friction coefficient) and $Nu_x\,\mathrm{Re}_x^{-1/2}$ (local Nusselt number) with mixed convection parameter Pr.

(a)

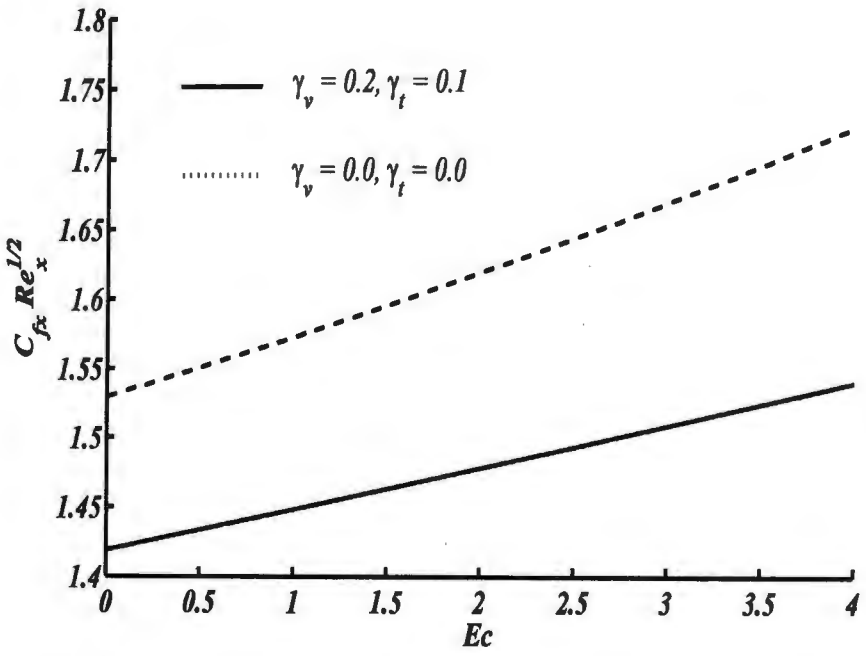

(b)

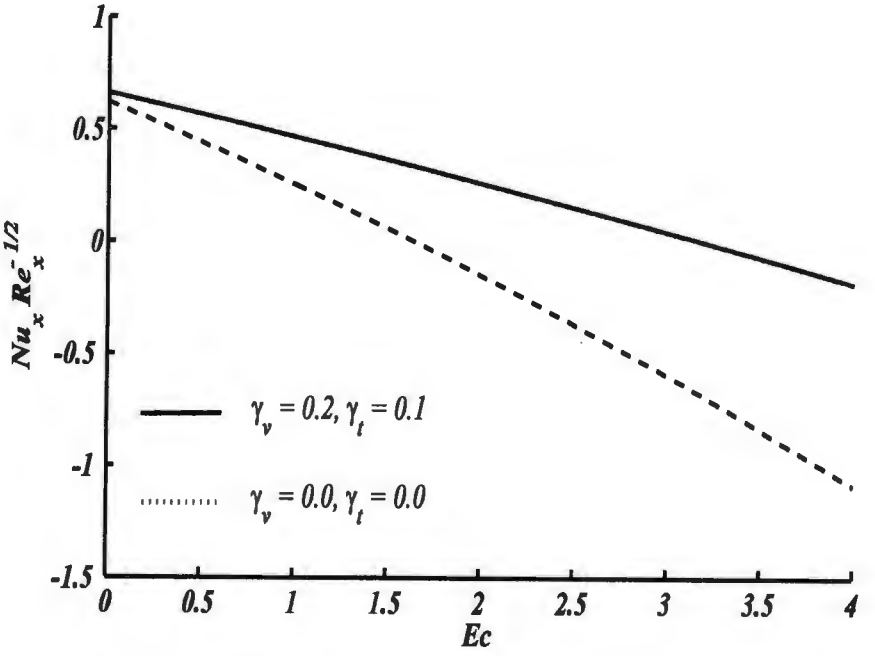

Figure 7.11(a, b): Variation of $C_{fx}\,\mathrm{Re}_x^{1/2}$ (skin friction coefficient) and $Nu_x\,\mathrm{Re}_x^{-1/2}$ (local Nusselt number) with Eckert number *Ec*.

7.4 Conclusions

In this chapter, the heat transfer analysis on mixed convection orthogonal stagnation point flow of a third grade fluid in presence of velocity and thermal slips on a vertical surface is investigated. The governing equations of the considered third grade fluid model are reduced in term of fourth and second order nonlinear ordinary differential equations. The Chebyshev spectral collocation method is again applied to obtain its solution. The effects of numerous important parameters on flow pattern in terms of velocity profile, temperature profile, skin friction coefficient and Nusselt number are seen and presented through graphs. It is noted that in assisting flow velocity enhances by increasing λ and reduces in opposing flow also the influence of mixed convection parameter λ on temperature profile shows an opposite behavior as noticed in velocity profile. In presence of slip effects on the surface velocity increases near the surface and reduces away from the surface by increasing ε. In assisting flow, velocity increases and temperature decreases by increasing velocity and thermal slip effects on the surface. For the effects of viscous dissipation Ec, it is noted that velocity and temperature increase with enhancing the effects of viscous dissipation. Local skin friction coefficient $C_{fx}\,\mathrm{Re}_x^{1/2}$ and local Nusselt number $Nu_x\,\mathrm{Re}_x^{-1/2}$ decrease with the increase in velocity and thermal slip parameters for assisting flow case. On the other hand, by increasing mixed convection parameter λ, local skin friction coefficient and local Nusselt number decrease for opposing flow case and increase in assisting flow case.

Bibliography

[1] E. Cao, Heat Transfer in Process Engineering, New York McGraw-Hill (**2010**).

[2] J.P. Holman, Heat transfer, New York McGraw-Hill (**1981**).

[3] R. Siegel and J.R. Howell, Thermal Radiation Heat Transfer, McGraw-Hill, New York, (**1987**).

[4] K.R. Rajagopal and T.Y. Na, On Stokes problem for a non-Newtonian fluid, Acta Mech., 48 (**1983**) 233–239.

[5] R.L. Fosdick and K.R. Rajagopal, Thermodynamics and stability of fluids of third grade, Proc. Roy. Soc. London Ser. A., 369 (**1980**) 351–377.

[6] K. Hiemenz, Die Grenzschicht an einem in den gleichförmigen Flüssigkeitsstrom eingetauchten geraden Kreiszylinder. Dingler's Polytech J., 326 (**1911**) 321–324.

[7] H. Schlichting and K. Bussmann, Exakte Losungen fur die Laminare Grenzchicht mit Absaugung und Ausblasen, Schri. Dtsch. Akad. Luftfahrtforschung, Ser., B 7, (**1943**) 25–69.

[8] E.R. G Eckert, Die Berechnung desWä rmeü berganges in der laminaren Grenzschicht um stromter Korper, VDI Forchungs-heft. Berlin, (**1942**) 416–418.

[9] B.C. Sakiadis, Boundary layer behaviour on continuous solid surface: I. Boundary layer equations for two dimensional and axisymmetric flow, AIChE J., 7 (**1961**) 26–28.

[10] B.C. Sakiadis, Boundary layer behaviour on continuous solid surface: II. Boundary layer equations for two dimensional and axisymmetric flow, AIChE J., 7 (**1961**) 221–225.

[11] L.J. Crane, Flow past a stretching plate, Z. Angew. Math. Phys., 21 (**1970**) 645–647.

[12] C.Y. Wang, Fluid flow due to a stretching cylinder, Phys. Fluids, 31 (**1988**) 466–468.

[13] A. Ishak, R. Nazar and I. Pop, Uniform suction/blowing effect on flow and heat transfer due to a stretching cylinder, Appl. Math. Model., 32 (**2008**) 2059–2066.

[14] A. Ishak and R. Nazar, Laminar boundary layer flow along a stretching cylinder, Eur. J. Sci. Res., 36 (**2008**) 22–29.

[15] A. Ishak, R. Nazar and I. Pop, Magnetohydrodynamic (MHD) flow and heat transfer due to a stretching cylinder, Energ. convers. Manage., 49 (**2008**) 3265–3269.

[16] K. Vajravelu, K.V. Prasad and S.R. Santhi, Axisymmetric magnetohydrodynamic (MHD) flow and heat transfer at a non-isothermal stretching cylinder, Appl. Math. Comput., 219 (**2012**) 3993–4005.

[17] R.R. Rangi and N. Ahmad, Boundary layer flow past a stretching cylinder and heat transfer with variable thermal conductivity, Appl. Math., 3 (**2012**) 205–209.

[18] N. Bachok and A. Ishak, Flow and heat transfer over a stretching cylinder with prescribed surface heat flux, Malays. J. Math. Sci., 4 (**2010**) 159–169.

[19] S. Mukhopadhyay, MHD boundary layer slip flow along a stretching cylinder, Ain Shams Eng. J., 4 (**2013**) 317–324.

[20] Z. Abbas, A. Majeed and T. Javed, Thermal radiation effects on MHD flow over a stretching cylinder in a porous medium, Heat transf. Res., 44 (**2013**) 703–718.

[21] M. Miklavcic and C.Y. Wang, Viscous flow due a shrinking sheet, Q. Appl. Math., 64 (**2006**) 283–290.

[22] T. Fang, Boundary layer flow over a shrinking sheet with power-law velocity, Int. J. Heat Mass Tran., 51 (**2009**) 5543–5838.

[23] T. Fang and J. Zhang, Closed-form exact solution of MHD viscous flow over a shrinking sheet, Commun. Nonlinear Sci. Numer. Simul., 14 (**2009**) 2853–2857.

[24] M. Sajid, T. Hayat, and T. Javed, MHD rotating flow of a viscous fluid over a shrinking surface, Nonlinear Dyn., 51 (**2008**) 259–265.

[25] N.F.M. Noor, S.A. Kechil, and I. Hashim, Simple non-perturbative solution for MHD viscous flow due to a shrinking sheet, Commun. Nonlinear Sci. Numer. Simul., 15 (**2010**) 144–148.

[26] S. Yao, T. Fang, and Y. Zhong, Heat transfer of a generalized stretching/shrinking wall problem with convective boundary conditions, Commun. Nonlinear Sci. Numer. Simul., 16 (**2011**) 752–760.

[27] U. Mishra and G. Singh, Dual solutions of mixed convection flow with momentum and thermal slip flow over a permeable shrinking cylinder. Comp. Fluids, 93 (**2014**) 107–115.

[28] T.C. Chiam, Stagnation point flow towards a stretching plate, J. Phys. Soc. Jpn., 63 (**1994**) 2443–2444.

[29] C.Y. Wang, Stagnation flow towards a shrinking sheet, Int. J. Non. Lin. Mech., 43 (**2008**) 377–382.

[30] N. Bachok, A. Ishak and I. Pop, Melting heat transfer in boundary layer stagnation-point flow towards a stretching/shrinking sheet, Phys. Lett. A, 374 (**2010**) 4075–4079.

[31] K. Bhattacharyya, Dual solutions in boundary layer stagnation-point flow and mass transfer with chemical reaction past a stretching/shrinking sheet, Int. Commun. Heat Mass Tran., 38 (**2011**) 917–922.

[32] N.A. Yacob, A. Ishak and I. Pop, Melting heat transfer in boundary layer stagnation-point flow towards a stretching/shrinking sheet in a micropolar fluid, Comput. Fluids, 47 (**2011**) 16–21.

[33] M. Turkyilmazoglu and I. Pop, Exact analytical solutions for the flow and heat transfer near the stagnation point on a stretching/shrinking sheet in a Jeffrey fluid, Int. J. Heat Mass Tran., 57 (**2013**) 82–88.

[34] P.D. Weidman and M.E. Ali, Aligned and nonaligned radial stagnation flow on a stretching cylinder, Eur. J. Mech. B Fluids, 30 (**2011**) 120–128.

[35] Y.Y. Lok and I. Pop, Wang's shrinking cylinder problem with suction near a stagnation point, Phys. Fluids, 23 (**2011**) Article ID 083102.

[36] Y.Y. Lok, J.H. Merkin and I. Pop, Mixed convection flow near the axisymmetric stagnation point on a stretching or shrinking cylinder, Int. J. Therm. Sci., 59 (**2012**) 186–194.

[37] N. Najib, N. Bachok, N.M. Arifin and A. Ishak, Stagnation point flow and mass transfer with chemical reaction past a stretching/shrinking cylinder, Appl. Math. Chem. Eng., 4 (**2014**) 1–7.

[38] S. Munawar, A. Mehmood and A. Ali, Unsteady flow of viscous fluid over the vacillate stretching cylinder, Int. J. Numer. Meth. Fluids, 70 (**2012**) 671–681.

[39] T. Fang, J. Zhang, Y. Zhong and H. Tao, Unsteady viscous flow over an expanding stretching cylinder, Chin. Phys. Lett., 28 (**2011**) DOI: 10.1088/0256-307x/28/12/124707.

[40] W. Zaimi, A. Ishak and I. Pop, Unsteady viscous flow over a shrinking cylinder, J. King Saud Univ. Sci., 25 (**2013**) 143–148.

[41] J.H. Merkin, Mixed convection from a horizontal circular cylinder, Int. J. Heat Mass Tran., 20 (**1977**) 73–77.

[42] R. Nazar, N. Amin and I. Pop, Mixed convection boundary layer flow a horizontal circular cylinder with a constant surface heat flux, Heat Mass Tran., 40 (**2004**) 219–227.

[43] S. Ahmad, N.M. Arifin, R. Nazar and I. Pop, Mixed convection boundary layer flow past an isothermal horizontal circular cylinder with temperature dependent viscosity, Int. J. Therm. Sci., 48 (**2009**) 1943–1948.

[44] R. Nazar, A. Norsarahaida and I. Pop, Mixed convection boundary layer flow from a horizontal circular cylinder in micropolar fluids: Case of Constant Wall Temperature, Int. J. Numer. Method H., 13 (**2003**) 86–109.

[45] I. Anwar, N. Amin and I. Pop, Mixed convection boundary layer flow of a viscoelastic fluid over a horizontal circular cylinder, Int. J. Nonlinear Mech., 43 (**2008**) 814–821.

[46] A.T. Srinivas, R.P. Bharti and R.P. Chhabra, Mixed convection heat transfer from a cylinder in power-law fluids: Effect of Aiding Buoyancy, Ind. Eng. Chem. Res., 48 (**2009**) 9735–9754.

[47] S. Bhowmick, M.M. Molla and L.S. Yao, Non-Newtonian mixed convection flow along an isothermal horizontal circular cylinder, Numer. Heat Tr. A-Appl., 66 (**2014**) 509–529.

[48] J.H. Merkin, Free convection boundary layers on cylinders of elliptic cross section, J. Heat Tran., 99 (**1977**) 453–457.

[49] C.Y. Cheng, A boundary layer analysis of heat transfer by free convection from permeable horizontal cylinders of elliptic cross section in porous media using a thermal non-equilibrium model, Int. Commun. Heat Mass, 34 (**2007**) 613–622.

[50] S. Ahmad, N.M. Arifin, R. Nazar and I. Pop, Free convection boundary layer flow over cylinders of elliptic cross section with constant surface heat flux, Eur. J. Sci. Res., 23 (**2008**) 613–625.

[51] C.Y. Cheng, Natural convection heat transfer from a horizontal isothermal elliptical cylinder with internal heat generation, Int. Commun. Heat Mass, 36 (**2009**) 346–350.

[52] S. Kaprawi and D. Santoso, Convective heat transfer from a heated elliptic cylinder at uniform wall temperature, IJEE, 4 (**2013**) 133–140.

[53] S.J.D.D'Alessio, Steady and Unsteady forced convection past an inclined elliptic cylinder, Acta Mech., 123 (**1997**) 99–115.

[54] M.L. Williams, Analytic Study of unsteady free convection from an inclined elliptic cylinder, M. Math. thesis, Waterloo University, Waterloo, Ont., (**2004**).

[55] M.K. Jaman and M.A. Hossain, Effect of fluctuating surface temperature on natural convection flow over cylinders of elliptic cross section, Int. J. Transp. Phenom., 2 (**2010**) 35–47.

[56] M. Jamaludin, M.N. Farahain, S. Sharidan and A. Anati, Unsteady mixed convection flow over a cylinder of elliptic cross section near forward stagnation point, Matematika, 28 (**2012**) 109–125.

[57] S.U.S. Choi, Enhancing thermal conductivity of fluids with nanoparticles, Proc. Int. Mech. Eng. Congress, San Francisco, USA, ASME, FED 231/MD 66 (**1995**) 99–105.

[58] J. Buongiorno, Convective transport in nanofluids, ASME J. Heat Tran., 128 (**2006**) 240–250.

[59] E. Abu-Nada, Application of nanofluids for heat transfer enhancement of separated flows encountered in a backward facing step, Int. J. Heat Fluid Fl., 29 (**2008**) 242–249.

[60] R.J. Tiwari and M.K. Das, Heat transfer augmentation in a two sided lid driven differentially heated square cavity utilizing nanofluids, Int. J. Heat Mass Tran., 50 (**2007**) 2002–2018.

[61] S.E.B. Maïga, S.J. Palm, C.T. Nguyen, G. Roy and N. Galanis, Heat transfer enhancement by using nanofluids in forced convection flows, Int. J. Heat Fluid Fl., 26 (**2005**) 530–546.

[62] H.F. Oztop and E. Abu-Nada, Numerical study of natural convection in partially heated rectangular enclosures filled with nanofluids, Int. J. Heat Fluid Fl., 29 (**2008**) 1326–1336.

[63] A.V. Kuznetsov and D.A. Nield, Natural convective boundary layer flow of a nanofluid past a vertical plate, Int. J. Therm. Sci., 49 (**2010**) 243–247.

[64] D.A. Nield and A.V. Kuznetsov, The Cheng–Minkowycz problem for the double-diffusive natural convective boundary layer flow in a porous medium saturated by a nanofluid, Int. J. Heat Mass Tran., 54 (**2011**) 374–378.

[65] Y. Jaluria, O. Manca, D. Poulikakos, K. Vafai, and L. Wang, Heat transfer in nanofluid, Adv. Mech. Eng., (**2012**) 1–2 Article ID 972973.

[66] O. Mahian, A. Kianifar, S.A. Kalogirou, I. Pop and S. Wongwises, A review of the applications of nanofluids in solar energy, Int. J. Heat Mass Tran., 57 (**2013**) 582–594.

[67] M. Mustafa, T. Hayat, I. Pop, S. Asghar and S. Obaidat, Stagnation point flow of a nanofluid towards a stretching sheet, Int. J. Heat Mass Tran., 54 (**2011**) 5588–5594.

[68] R. Nazar, M. Jaradat, N.M. Arifin and I. Pop, Stagnation point flow past a shrinking sheet in a nanofluid, Cent. Eur. J. Phys., 9 (**2011**) 1195–1202.

[69] N. Bachok, A. Ishak and I. Pop, Stagnation-point flow over a stretching/shrinking sheet in a nano-fluid, Nanoscale Res. Lett., 6 (**2011**) 623.

[70] Ch.K. Kumar and S. Bandari, Melting heat transfer in boundary layer stagnation point flow of a nanofluid towards a stretching shrinking sheet, Can. J. Phys., 92 (**2014**) 1703–1708.

[71] S. Khalili, S. Dinarvand, R. Hosseini, I.R. Dehkordi and H. Tamim, Stagnation-point flow and heat transfer of a nanofluid adjacent to linearly stretching/shrinking sheet: A Numerical Study, Res. J. Appl. Sci. Eng. Tech., 7 (**2014**) 83–90.

[72] K. Zaimi, A. Ishak and I. Pop, Stagnation-point flow toward a stretching/shrinking sheet in a nanofluid containing both nanoparticles and gyrotactic microorganisms, J. Heat Tran., 136 (**2014**) DOI: 10.1115/1.4026011.

[73] W. Ibrahim, B. Shankar and M.M. Nandeppanavar, MHD stagnation point flow and heat transfer due to nanofluid towards a stretching sheet, Int. J. Heat Mass Tran., 56 (**2013**) 1–9.

[74] S. Khalili, S. Dinarvand, R. Hosseini M. Saber and I. Pop, Magnetohydrodynamic stagnation point flow toward stretching/shrinking permeable plate in porous medium filled with a nanofluid, Proc. Inst. Mech. Eng. E J. Process Mech. Eng., 228 (**2014**) 309–319.

[75] O.D. Makinde, W.A. Khan and Z.H. Khan, Buoyancy effects on MHD stagnation point flow and heat transfer of a nanofluid past a convectively heated stretching/shrinking sheet, Int. J. Heat Mass Tran., 62 (**2013**) 526–533.

[76] M.E. Yazdi, A. Moradi and S. Dinarvand, MHD mixed convection stagnation point flow over a stretching vertical plate in porous medium filled with a nanofluid in the presence of thermal radiation, Arab. J. Sci. Eng., 39 (**2014**) 2251–2261.

[77] H. Tamim, S. Dinarvand, R. Hosseini, S. Khalili and A. Khalili, Mixed convection boundary layer flow of a nanofluid near stagnation point on a vertical plate with effects of buoyancy assisting and opposing flows, Res. J. Appl. Sci. Eng. Tech., 6 (**2013**) 1785–1793.

[78] R.E. Rosensweig, Ferrohydrodynamics, Cambridge Univ Press, Cambridge, London (**1985**).

[79] S.S. Papell, Low viscosity magnetic fluid obtained by the colloidal suspension of magnetic particles, United States Patent office Filed, 315 (**1963**) 096.

[80] E.K. Ruuge and A.N. Rusetski, Magnetic fluids as drug carriers, Targeted transport of drugs by a magnetic field, J. Magn. Magn. Mater., 122 (**1993**) 335–339.

[81] S. Goodwin, C. Peterson, C. Hoh and C. Bittner, Targeting and retention of magnetic targeted carriers (MTCs) enhancing intra-arterial chemotherapy, J. Magn. Magn. Mater., 194 (**1999**) 132–139.

[82] D.B. Hathway, Use of ferrofluid in moving-coil loudspeakers, dB-Sound, Engg. Mag., 13 (**1979**) 42–44.

[83] F. Wu, C. Wu, F. Guo and D. Li, Acoustically controlled heat transfer of ferromagnetic fluid, Int. J. Heat Mass Tran., 44 (**2001**) 4427–4432.

[84] M. Motozawa, J. Chang, T. Sawada, and Y. Kawaguchi, Effect of magnetic field on heat transfer in rectangular duct flow of a magnetic fluid, Phys. Procedia, 9 (**2010**) 190–193.

[85] C. Yang, X. Bian, J. Qin, X. Zhao, K. Zhang and Y. Bai, An investigation of a viscosity-magnetic field hysteretic effect in nano-ferrofluid, J. Mol. Liq., 196 (**2014**) 357–362.

[86] Z.H. Khan, W.A. Khan, M. Qasim and I.A. Shah, MHD stagnation point ferrofluid flow and heat transfer toward a stretching sheet, IEEE Trans., 13 (**2014**) 35–40.

[87] P. Ram, A. Bhandari and K. Sharma, Axi-symmetric ferrofluid flow with rotating disk in a porous medium, Int. J. Fluid Mech., 2 (**2010**) 151–161.

[88] P. Ram, K. Sharma and A. Bhandari, Effect of porosity on ferrofluid flow with rotating disk, Int. J. Appl. Math. Mech., 6 (**2010**) 67–76.

[89] P. Ram, K. Sharma and A. Bhandari, Effect of porosity on revolving ferrofluid flow with rotating disk, Int. J. Fluids Eng., 3 (**2011**) 261–271.

[90] P. Ram and K. Sharma, On the revolving ferrofluid flow due to rotating disk. Int. J. Nonlinear Sci., 13 (**2012**) 317–324.

[91] P. Ram and K. Sharma, Effect of rotation and MHD viscosity on ferrofluid flow with rotating disk, Indian J. Pure Appl. Phys., 52 (**2014**) 87–92.

[92] K. Vajravelu, Viscous flow over a nonlinearly stretching sheet, Appl. Math. Comput., 124 (**2001**) 281–288.

[93] K. Vajravelu and J.R. Cannon, Fluid flow over a nonlinear stretching sheet, Appl. Math. Comput., 181 (**2006**) 609–618.

[94] R. Cortell, Viscous flow and heat transfer over a nonlinearly stretching sheet. Appl. Math. Comput., 184 (**2007**) 864–873.

[95] R.C. Bataller, Similarity solutions for flow and heat transfer of a quiescent fluid over a nonlinearly stretching surface, J. Mater. Process. Tech., 203 (**2008**) 176–183.

[96] T. Hayat, T. Javed and Z. Abbas, MHD flow of a micropolar fluid near a stagnation-point towards a non-linear stretching surface, Nonlinear Anal. Real World Appl., 10 (**2009**) 1514–1526.

[97] N. Bachok and A. Ishak, Similarity solutions for the stagnation-point flow and heat transfer over a nonlinearly stretching/shrinking sheet, Sains Malays., 40 (**2011**) 1297–1300.

[98] R.N. Jat and A. Neemawat, Similarity solution for MHD stagnation point flow and heat transfer over a non-linear stretching sheet, IJCRR, 3 (**2012**).

[99] N.A. Yacob and A. Ishak, Stagnation-point flow over a nonlinearly stretching/shrinking sheet in a micropolar fluid, AIP Conference Proceedings, 1602 (**2014**) 266-272.

[100] K. Zaimi and A. Ishak, Stagnation-point flow and heat transfer over a nonlinearly stretching/shrinking sheet in a micropolar fluid, Abstr. Appl. Anal., (**2014**), DOI:/10.1155/2014/261630.

[101] P. Rana and R. Bhargava, Flow and heat transfer of a nanofluid over a nonlinearly stretching sheet: A numerical study, Commun. Nonlinear Sci. Numer. Simulat., 17 (**2012**) 212–226.

[102] F.M. Hady, F.S. Ibrahim, S.M. Abdel–Gaied and M.R. Eid, Radiation effect on viscous flow of a nanofluid and heat transfer over a nonlinearly stretching sheet, Nanoscale Res. Lett., 7 (**2012**) Article ID 229.

[103] K. Zaimi, A. Ishak and I. Pop, Boundary layer flow and heat transfer over a nonlinearly permeable stretching/shrinking sheet in a nanofluid, Scientific Reports 4, DOI:10.1038/srep04404.

[104] N. Bachok, A. Ishak and I. Pop, Boundary layer stagnation-point flow and heat transfer over an exponentially stretching/shrinking sheet in a nanofluid, Int. J. Heat Mass Tran., 55 (**2012**) 8122–8128.

[105] A. Malvandi, F. Hedayati and G. Domairry, Stagnation point flow of a nanofluid toward an exponentially stretching sheet with non-uniform heat generation/absorption, J. Thermodyn., (**2013**) DOI:/10.1155/2013/764827.

[106] I. Anwar, S. Shafie and M.Z. Salleh, Radiation effect on MHD stagnation-point flow of a nanofluid over an exponentially stretching sheet, Walailak J. Sci. & Tech., 11 (**2014**) DOI: 10.14456/WJST.

[107] M.Z. Salleh, R. Nazar and I. Pop, Forced convection boundary layer flow at a forward stagnation point with newtonian heating, Chem. Eng. Comm., 196 (**2009**) 987–996.

[108] J.H. Merkin, R. Nazar and I. Pop, The development of forced convection heat transfer near a forward stagnation point with Newtonian heating, J. Eng. Math., 74 (**2012**) 53–60.

[109] M.Z. Salleh, R. Nazar and I. Pop, Boundary layer flow and heat transfer over a stretching sheet with Newtonian heating, J. Taiwan Inst. Chem. Eng., 41 (**2010**) 651–655.

[110] M.K.A. Mohammed, M.Z. Salleh, R. Nazar and A. Ishak, Stagnation point flow over a stretching sheet with Newtonian heating, Sains Malays., 41 (**2012**) 1467–1473.

[111] N. Bachok, A. Ishak and I. Pop, Stagnation point flow toward a stretching/shrinking sheet with a convective surface boundary condition, J. Franklin Inst., 350 (**2013**) 2736–2744.

[112] N.A. Yacob, A. Ishak, I. Pop and K. Vajravelu, Boundary layer flow past a stretching/shrinking surface beneath an external uniform shear flow with a convective surface boundary condition in a nanofluid, Nanoscale Res. Lett., 6 (**2011**) DOI: 10.1186/1556-276X-6-314.

[113] O.D. Makinde, W.A. Khan, and Z.H. Khan, Buoyancy effects on MHD stagnation point flow and heat transfer of a nanofluid past a convectively heated stretching/shrinking sheet, Int. J. Heat Mass Tran., 62 (**2013**) 526–533.

[114] M.M. Rahman and I.A. Eltayeb, Radiative heat transfer in a hydromagnetic nanofluid past a non-linear stretching surface with convective boundary condition, Meccanica, 48 (**2013**) 601–615.

[115] G.S. Beavers and D.D. Joseph, Boundary conditions at a naturally permeable wall, Int. J. Fluid Mech., 30 (**1967**) 197-207.

[116] H.I. Andersson, Slip flow past a stretching surface, Acta Mech., 158 (**2002**) 121-125.

[117] F. Labropulu and D. Li, Stagnation point flow of a second grade fluid with slip, Int. J. Non-Linear Mech., 43 (**2008**) 941-947.

[118] K. Cao and J. Baker, Slip effects on mixed convective flow and heat transfer from a vertical plate, Int. J. Heat Mass Tran., 52 (**2009**) 3829-3841.

[119] S.D. Harris, D.B. Ingham and I. Pop, Mixed convection boundary-layer flow near the stagnation point on a vertical surface in a porous medium: Brinkman model with slip, Transp. Porous Med., 77 (**2009**) 267-285.

[120] K. Bhattacharyya, S. Mukhopadhyay and G.C. Layek, Similarity solution of mixed convective boundary layer slip flow over a vertical plate, Ain Shams Eng. J., 4 (**2013**) 299-305.

[121] F. Aman, A. Ishak and I. Pop, Mixed convection boundary layer flow near stagnation point on vertical surface with slip, Appl. Math. Mech. Engl. Ed., 32 (**2011**) 1599-1606.

[122] K. Das, Slip effects on MHD mixed convection stagnation point flow of a micropolar fluid towards a shrinking vertical sheet, Comput. Math. Appl., 63 (**2012**) 255-267.

[123] K.R. Rajagopal, T.Y. Na and A.S. Gupta, Flow of a viscoelastic fluid over a stretching sheet, Rheol. Acta, 23 (**1984**) 213-215.

[124] P.D. Ariel, MHD flow of a viscoelastic fluid past a stretching sheet with suction, Acta Mech., 105 (**1994**) 49–56.

[125] H.I. Andersson, MHD flow of a viscoelastic fluid past a stretching sheet, Acta Mech., 95 (**1992**) 227–230.

[126] I.C. Liu, Flow and heat transfer of an electrically conducting fluid of second grade over a stretching sheet subject to a transverse magnetic field, Int. J. Heat Mass Trans., 47 (**2004**) 4427–4437.

[127] B. Sahoo and H.G. Sharma, Existence and uniqueness theorem for flow and heat transfer of a non-Newtonian fluid over a stretching sheet, J. Zhej. Univ. Sci. A, 8 (**2007**) 766–771.

[128] R. Cortell, Similarity solutions for flow and heat transfer of a viscoelastic fluid over a stretching sheet, Int. J. Non-Linear Mech., 29 (**1994**) 155-161.

[129] C. Truesdell and W. Noll, The Nonlinear Field Theories of Mechanics, 3rd ed., Springer, (**2004**).

[130] J.E. Dunn and K.R. Rajagopal, Fluids of differential type: critical review and thermodynamic analysis, Int. J. Eng. Sci., 33 (**1995**) 689–729.

[131] T. Cebeci and P. Bradshaw, Physical and Computational Aspects of Convective Heat Transfer, Springer, New York, (**1984**).

[132] C. Canuto, M.Y. Hossaini, A. Quartcroni and T.A. Zang, Spectral Methods in Fluid Dynamics, Springer, Berlin, (**1987**).

[133] Y. Jaluria, Computer Methods for Engineering, Allyn and Bacon Inc., Boston, (**1988**).

[134] N. Riley and P.D. Weidman, Multiple solutions of the Falkner-Skan equation for flow past a stretching boundary, SIAM J. Appl. Math., 49 (**1989**) 1350–1358.

[135] G. Wilks and J.S. Bramley, Dual solutions in mixed convection, Proceedings of the Royal Society of Edinburgh, 87 (**1981**) 349–358.

[136] J.H. Merkin, On dual solutions occurring in mixed convection in a porous medium, J. Eng. Math., 20 (**1985**) 171–179.

[137] S.J.D.D'Alessio, Steady, unsteady and linear stability of flow past an elliptic cylinder, Can. Appl. Math. Q., 4 (1996) 341–379.

[138] A. Ali, N. Amin and I. Pop, Unsteady mixed convection boundary layer from a circular cylinder in a micropolar fluid, Int. J. Chem. Eng., (**2010**) DOI: 10.1155/2010/417875.

[139] D.B. Ingham and J.H. Merkin, Unsteady mixed convection from an isothermal circular cylinder, Acta Mech., 38 (**1981**) 55–69.

[140] H.C. Brinkman, The viscosity of concentrated suspensions and solution, J. Chem. Phys., 20 (**1952**) 571–581.

[141] J.C. Maxwell Garnett, Colours in metal glasses and in metallic films, Philos. Trans. R. Soc. Lond., A, 203 (**1904**) 385–420.

[142] M. Turkyilmazoglu, MHD fluid flow and heat transfer due to a stretching rotating disk, Int. J. Therm. Sci., 51 (**2012**) 195–201.

[143] B. Weidenfeller, M. Hofer, and F. Schilling, Thermal and electrical properties of magnetite filled polymers, Composit. A, Appl. Sci. Manuf., 33 (**2002**) 1041–1053.

[144] P.D. Weidman, D.G. Kubitschek and A.M.J. Davis, The effect of transpiration on self-similar boundary layer flow over moving surfaces, Int. J. Eng. Sci., 44 (**2006**) 730–737.

[145] A.V. Rosca and I. Pop, Flow and heat transfer over a vertical permeable stretching/shrinking sheet with a second order slip, Int. J. Heat Mass Tran., 60 (**2013**) 355–364.

[146] M. Pakdemirli, The boundary layer equations of third grade fluids, Int. J. Non-Linear Mech., 27 (**1992**) 785-793.

[147] D. Li, F. Labropulu and I. Pop, Mixed convection flow of a viscoelastic fluid near the orthogonal stagnation-point on a vertical surface, Int. J. Therm. Sci., 50 (**2011**) 1698-1705.

[148] T. Hayat, Z. Abbas and I. Pop, Mixed convection in the stagnation point flow adjacent to a vertical surface in a viscoelastic fluid, Int. J. Heat Mass Tran., 51 (**2008**) 3200-3206.